Structure and Diffraction Properties of Disordered Systems

David H. Wojtas

Department of Electrical and Computer Engineering

A thesis presented for the degree of
Doctor of Philosophy

University of Canterbury
Christchurch, New Zealand
September 2010

To my mother, Marie

Contents

Acknowledgements

I will always be indebted to my supervisor, Prof. Rick Millane for the opportunity to work on this thesis. Your guidance, intuition and extensive knowledge were invaluable to my work and have inspired me towards future academic pursuits. I would like to thank my co-supervisor, Prof. Peter Smith, for your useful input. I would also like to thank Prof. Phil Bones, Assoc. Prof. Mike Reid and Dr. Surujhdeo Seunarine of the University of Canterbury and Prof. Peter Ahnelt, Vienna Medical University, Prof. John Squire, University of Bristol and Prof. Veit Elser of Cornell University for useful discussions.

I am grateful to the University of Canterbury and the Department of Electrical and Computer Engineering for financial support.

Many thanks to my colleagues and friends in our Computational Imaging Group; Jeffrey Hsiao, Alan Hunter, Victor Lo, Bing Wu, Chunhong Yoon and Amanda Zhang. Thank you to the technical staff in our department for their assistance. Special thanks to my friends dispersed across the globe for the good memories, namely those of the Physoc Beer Society, BWCUCC Gold/Navy, the "Young Panthers", Topsy's G.C. and the talented people at 7/14 Kirkwood Ave.

It is my family who have supported me the most in my studies. To my parents Mum and John, Dad and Toni, I cannot thank you enough. Mum, you have motivated me to achieve my goals so I dedicate this thesis to you. A big thank you to my older brother, Marc, and to my younger siblings Johnny, William, Sarah and Anna for their support. Finally, a big thank you to my girlfriend Emma, whose encouragement and patience motivated me during these final months.

Abstract

In many systems of interest, both physical and biological, disorder inhibits the organization and cooperative properties of the system. Disorder can originate from a variety of system defects and the degree of disorder also varies. Geometric frustration introduces disorder into a system in which all the preferred interactions between the elements of the system cannot be satisfied due to the topology of an underlying lattice that describes the position of these elements. Recently, geometric frustration has been recognized as an important organizing principle in a diverse range of systems from superconducting networks to neural computation. The correlation behavior of such systems is often complicated and poorly understood. The myosin lattice of higher vertebrate muscle is a geometrically frustrated system, and the presence of this kind of disorder has prevented a rigorous interpretation of X-ray diffraction patterns from muscle fibres for the purposes of studying muscle molecular structure.

This thesis investigates the correlation behavior of two geometrically frustrated systems, the triangular Ising antiferromagnet (TIA) and the fully frustrated square Ising model (FFS), and its use to interpret X-ray fibre diffraction patterns. A combination of numerical evaluation of exact expressions and Monte Carlo simulation is used to study a number of aspects of the two-point correlation function of the TIA and FFS. In the case of the TIA, a simple functional expression is developed that allows accurate calculation of the correlation function. Theory is developed for calculating diffraction by polycrystalline fibres of helical molecules, in which the constituent crystallites contain correlated substitution disorder. The theory was used to study the characteristics of diffraction by fibres with TIA-type substitution disorder statistics. A quantitative model of the disorder in the myosin filament array is developed and the above theory is used to calculate X-ray fibre diffraction from low resolution models of the myosin filament array in higher vertebrate muscle. The calculated diffraction is compared to measured diffraction data, showing good agreement.

Preface

The work presented in this thesis was motivated by efforts to develop methods for interpreting X-ray fibre diffraction data from vertebrate muscle. X-ray diffraction is an important tool for molecular structure determination and its application to muscle has led to important discoveries on its structure. In higher vertebrates such as humans, disorder within the arrays of myosin filaments that compose a muscle fibre inhibits the interpretation of diffraction data. This disorder was first identified by Luther and Squire [LS80] and has recently been characterized in terms of the statistics of triangular Ising antiferromagnet (TIA) by Yoon [Yoo09]. Analytical results that partially describe the correlation behavior of the TIA have been developed by Stephenson [Ste70]. Similar results have been obtained for another geometrically frustrated system, the fully frustrated square Ising model (FFS) by Wolff and Zittartz [WZ82]. Methods have been developed by Stroud and Millane [SM96a, SM96b] for calculating the diffraction from polycrystalline fibres with short-range order. This thesis extends and synthesizes all of these various results to allow calculation of X-ray fibre diffraction patterns from the disordered myosin array of higher vertebrate muscle and comparison with experimental diffraction patterns.

The thesis addresses three topics related to the above problem; (1) The accuracy of existing asymptotic results for the two-point correlation functions, and the convenient and accurate computation of all correlations for the TIA and FFS. (2) Methods for calculating the diffraction from fibres that allow for complicated correlation statistics between scatterers. (3) Determining the effects of the kind of disorder found in higher vertebrate muscle on fibre diffraction patterns. Material relevant to these topics is reviewed in Chapter 1, and original work is presented in Chapters 2-5.

Chapter 1 contains a review of background material relevant to the thesis. It discusses equilibrium statistical physics, statistical disorder, the Ising model, geometric frustration, known correlation properties of the TIA and FFS, Monte Carlo simulation, X-ray crystallography, diffraction from polycrystalline fibres, vertebrate muscle structure and myosin filament disorder.

Chapter 2 addresses shortcomings in current knowledge of the correlation properties of the TIA. Methods for computing general (off-axis) correlations and a new sublattice partitioning of the correlation function is presented. A rotationally invariant expression is developed that allows accurate calculation of correlation coefficients.

Chapter 3 investigates the correlation properties of the FFS. Exact results are reviewed and the precision of existing approximations is evaluated. Symmetry relationships and a sublattice description for the general correlation function are derived, and rotational invariance is studied as a function of temperature.

Chapter 4 develops theory for calculating the cylindrically averaged diffraction by polycrystalline fibres with correlated substitution disorder. This theory is then used to study the characteristics of X-ray diffraction patterns from fibres with correlated substitution disorder with TIA-type statistics.

In Chapter 5, the myosin lattice disorder in higher vertebrate muscle is modelled using the high-precision results for the two-point correlation function of the TIA from Chapter 2. Using a low resolution model of myosin filament and the theory developed in Chapter 4, X-ray fibre diffraction patterns are calculated and compared with experimental data.

A summary of key results from this thesis with directions for future research are given in Chapter 6.

Some results from this thesis have been published and presented:

D. H. Wojtas and R. P. Millane, "Two-point correlation function for the triangular Ising antiferromagnet", Phys. Rev. E, 79, 041123, 2009.

D. H. Wojtas and R. P. Millane, "Two-point correlation function for the fully frustrated square Ising model", Under review by Physical Review E.

D. H. Wojtas, C. H. Yoon, R. P. Millane and J. M. Squire, "Modelling X-ray Diffraction From The Myosin Superlattice Of Vertebrate Muscle", Biophysical Journal, 96, supplement 1, 615a-616a, 2009.

D. H. Wojtas, C. H. Yoon and R. P. Millane, "Cylindrically averaged diffraction by disordered polycrystalline fibres with correlated substitution disorder", in preparation.

Chapter 1

Introduction

1.1 Statistical disorder

1.1.1 Equilibrium statistical mechanics

The field of statistical mechanics is concerned with deriving the thermodynamic properties of macroscopic systems from a description of the behaviour of their microscopic components, typically atoms or molecules [LLP80, PB89]. The number of microscopic components is usually extremely large, so that the system has many degrees of freedom, only a few of which are measurable. Probabilistic methods are required to relate the thermodynamics of the system to the microscopic variables.

A macroscopic system of d spatial dimensions, consisting of N particles in thermal equilibrium has $2dN$ degrees of freedom described by the coordinates $q_1, \ldots, q_j, \ldots, q_{dN}$ and the momenta $p_1, \ldots, p_j, \ldots, p_{dN}$. These coordinates obey the classical Hamiltonian equations of motion

$$\dot{q}_j = -\frac{\partial H(\{q_j, p_j\})}{\partial q_j}, \tag{1.1a}$$

$$\dot{p}_j = \frac{\partial H(\{q_j, p_j\})}{\partial p_j}, \tag{1.1b}$$

with $j = 1, 2, \ldots, dN$, $\{q_j, p_j\} = \{q_1, \ldots, q_{dN}, p_1, \ldots, p_{dN}\}$ and $H(\{q_j, p_j\})$ the Hamiltonian of the system, given by

$$H(\{q_j, p_j\}) = \sum_{i=1}^{N} \frac{p_i^2}{2m} + \sum_{i=1}^{N} \left[U(q_i) + \sum_{j=1}^{N} V(q_i, q_j) \right], \tag{1.2}$$

where $U(q_i)$ is the particle potential energy and $V(q_i, q_j)$ is the two-particle interaction

energy. The first term in Eq. (1.2) is referred to as the kinetic term and the second sum over i is the potential term. This system is closed, at a fixed temperature and is said to be a canonical Hamiltonian system. Hamiltonian systems have a number of conserved quantities, the total energy, E, of the system being the most obvious. If an N particle system is fully integrable, there exist N mutually independent constants of motion $f(q_j(t), p_j(t))$ which commute with the Hamiltonian under the Poisson bracket [GPS01], i.e.

$$\frac{\partial f}{\partial q}\frac{\partial H}{\partial p} - \frac{\partial f}{\partial p}\frac{\partial H}{\partial q} = 0, \tag{1.3}$$

and its motion can be expressed in terms of $2dN$ constants. The state of the system can be represented by the $2dN$-dimensional vector $\{q_j, p_j\}$ [Par88]. Given the energy is fixed, the system's motion is then confined to the $(2dN-1)$-dimensional surface $\Upsilon(E)$ defined by

$$H(\{q_j, p_j\}) = E. \tag{1.4}$$

An ensemble is a collection of system configurations over a period of time t. The ensemble average of an observable $A(\{q_i(t), p_i(t)\})$ is then defined by

$$\langle A \rangle = \lim_{t\to\infty} \frac{1}{t} \int_0^t A(\{q_j(t'), p_j(t')\}) \mathrm{d}t'. \tag{1.5}$$

The limit $t \to \infty$ is taken to ensure all states of the $2dN$-dimensional phase space are represented with the appropriate frequency in the average. A more useful approach is to define the equilibrium probability density $P(\{q_j, p_j\})$ for a phase point $\{q_j, p_j\}$ to be occupied by the ensemble and average over the $2dN$-dimensional phase space,

$$\langle A \rangle = \int \prod_{i=1}^{N} \mathrm{d}^d q_i \int \prod_{j=1}^{N} \mathrm{d}^d p_j A(\{q_j, p_j\}) P(\{q_j, p_j\}). \tag{1.6}$$

The probability density $P(\{q_j, p_j\})$ is by definition always positive and satisfies the normalization condition

$$\int \prod_{i=1}^{N} \mathrm{d}^d q_i \int \prod_{j=1}^{N} \mathrm{d}^d p_j P(\{q_j, p_j\}) = 1. \tag{1.7}$$

The hypothesis central to equilibrium statistical mechanics is that $P(\{q_j, p_j\})$ follows a canonical probability distribution

$$P(\{q_j, p_j\}) = \frac{\exp(-\beta H(\{q_j, p_j\}))}{Z}, \tag{1.8}$$

where Z is the canonical partition function and $\beta = 1/k_B T$ with Boltzmann's constant, $k_B = 1.38 \times 10^{-23} JK^{-1}$ and T is the temperature [Gib02]. For simplicity, energies shall be

measured in Kelvins by using a rescaled temperature parameter

$$\widetilde{T} = k_B T, \tag{1.9}$$

and, for brevity, $\widetilde{T}$ is rewritten as T and β rescales to $\beta = 1/T$. The canonical partition function, or simply the partition function, is defined as

$$Z = \int \prod_{i=1}^{N} \mathrm{d}^d q_i \int \prod_{j=1}^{N} \mathrm{d}^d p_j \exp(-\beta H(\{q_j, p_j\})). \tag{1.10}$$

It is dependent on the temperature and the energies of the different states, and contains a vast amount of information about the system. A number of important thermodynamic quantities can be derived from the partition function including the internal energy, entropy, Helmholtz free energy and specific heat.

The system's entropy is a useful quantity for characterizing the degree of disorder of a canonical distribution. The entropy $S[P]$ is defined as

$$\begin{aligned} S[P] &= -\langle \log\left(P(\{q_j, p_j\})\right)\rangle \\ &= -\int \prod_{i=1}^{N} \mathrm{d}^d q_i \int \prod_{j=1}^{N} \mathrm{d}^d p_j P(\{q_j, p_j\}) \log\left(P(\{q_j, p_j\})\right). \end{aligned} \tag{1.11}$$

If the density $P(\{q_j, p_j\})$ is localised in a region of phase space, as in Fig. 1.1(a), the calculated entropy will be small and indicates a well-ordered system. A uniform density that is spread out evenly over phase space [Fig. 1.1(b)] gives a large entropy, indicating a disordered system.

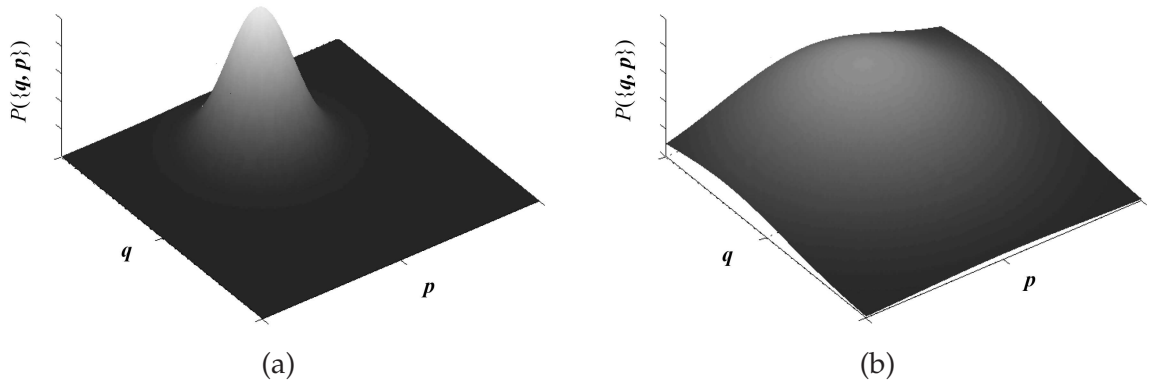

(a) (b)

Figure 1.1 The density $P(\{q_j, p_j\})$ over phase space where (a) the density is localised to a region of phase space, and (b) where the density is spread out over phase space.

1.1.2 Discrete formalism

In a classical mechanical system the positions and momenta of the microscopic components vary continuously and the set of states in phase space is uncountable. In systems with distinguishable constituent particles such as crystallites or polymer chains, each component can be indexed by their position on a lattice or chain structure. The degrees of freedom of the lattice model situate on the lattice vertices, shown in Fig. 1.2, and can be continuous or discrete. The integral representation of the partition function then reduces to a discrete sum over state dependent factors [Hua63]. If the individual state energies of a system are calculable, the partition function can be calculated exactly as can the associated thermodynamic quantities derivable from the partition function.

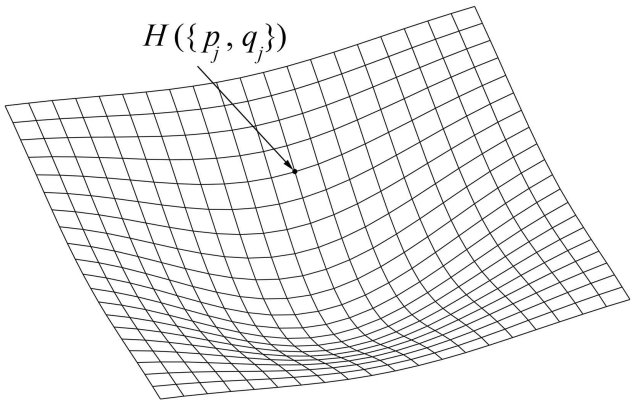

Figure 1.2 The confined motion of the Hamiltonian defined on a lattice.

The different configurations of a discrete configuration space, $C = \{C_1, C_2, \ldots, C_{\mathcal{N}}\}$ where the number of allowed configurations $\mathcal{N}$ can be infinite, can be indexed by the integers $\mu \in \mathbb{Z}^+$ such that

$$C_\mu = \{q_1^\mu, \ldots, q_{dN}^\mu, p_1^\mu, \ldots, p_{dN}^\mu\},$$

where q_i^μ and p_i^μ denote the displacement q_i and momentum p_i in configuration μ. The quantities in Eqs. (1.6), (1.8), (1.10) and (1.11) now become

$$\langle A \rangle = \sum_\mu P(C_\mu) A(C_\mu), \tag{1.12a}$$

$$P(C_\mu) = \frac{\exp(-\beta H(C_\mu))}{Z}, \tag{1.12b}$$

$$Z = \sum_\mu \exp(-\beta H(C_\mu)), \tag{1.12c}$$

$$S[P] = -\sum_{\mu} P(C_\mu) \log P(C_\mu). \tag{1.12d}$$

In a discretized space, the Hamiltonian $H(C_\mu)$ retains the same general form as Eq. (1.2).

Another statistical property of significance is the two-point correlation function (a.k.a. pair, spatial or spin-spin correlation function) defined by

$$\begin{aligned}
\rho_{ij} &= \frac{1}{Z}\sum_{\mu} q_i^\mu q_j^\mu \exp(-\beta H(C_\mu)) \\
&\quad - \left\{\frac{1}{Z}\sum_{\mu} q_i^\mu \exp(-\beta H(C_\mu))\right\}\left\{\frac{1}{Z}\sum_{\mu} q_j^\mu \exp(-\beta H(C_\mu))\right\} \\
&= \langle q_i q_j\rangle - \langle q_i\rangle\langle q_j\rangle \\
&= \langle (q_i - \langle q_i\rangle)(q_j - \langle q_j\rangle)\rangle.
\end{aligned} \tag{1.13}$$

The correlation function is a measure of the range over which particles in one region of space influence those in another region. The correlation $\langle q_i q_j\rangle$ between the i-th and j-th particle positions is zero when the positions are uncorrelated and equal to unity when they are completely correlated. If the systems statistics are translationally invariant or "stationary", the correlation function is invariant with position, i.e. depends only on $q_i - q_j$. For large separation $r_{ij} = q_i - q_j$, the two-point correlation function can be parameterized by the expression

$$\rho_{ij}(T) \sim \frac{\exp(-r_{ij}/\xi)}{r_{ij}^{d-2+\eta}} \tag{1.14}$$

where $\xi(T)$ is the correlation length which gives a measure of the range of order across the lattice, and η is a critical exponent characteristic of the system being studied [PB89].

1.1.3 Disordered systems

In reality, most systems of interest to practical applications possess some degree of statistical disorder [Zim79]. Only inorganic compounds such as metals and ionic crystals of materials possess near perfect crystallinity, hence a deeper understanding of the properties of disordered systems is necessary for practical applications. Many of the challenging problems currently being studied in condensed matter physics are connected in some way to disorder.

The spatial arrangement in which atoms and molecules assemble within a material can be characterised by the degree of regularity. Shown in Fig. 1.3 are four main states of regularity a material may have; crystalline, disordered, plastic crystalline and amorphous. The components of a crystal can be either atoms, atomic groups, ions or molecules but, for simplicity, crystal components will collectively be referred to as molecules. Crystals

that consist of identical molecules exhibiting a high degree of regularity are so-called ideal crystals and are said to be crystalline [Fig. 1.3(a)]. The opposite to crystalline is the amorphous state in which, not necessarily identical, molecules are arranged with no correlation between their positions [Fig. 1.3(d)]. In between these two extremes are the disordered [Fig. 1.3(b)] and plastic [Fig. 1.3(c)] crystal states. In the plastic crystal state, molecules situate on a perfect lattice but are permitted to rotate, weakening the intermolecular bonds and giving the characteristic of plasticity [KK05]. The disordered state describes materials which exhibit a variety of types and degrees of disorder, without being in the completely disordered amorphous state.

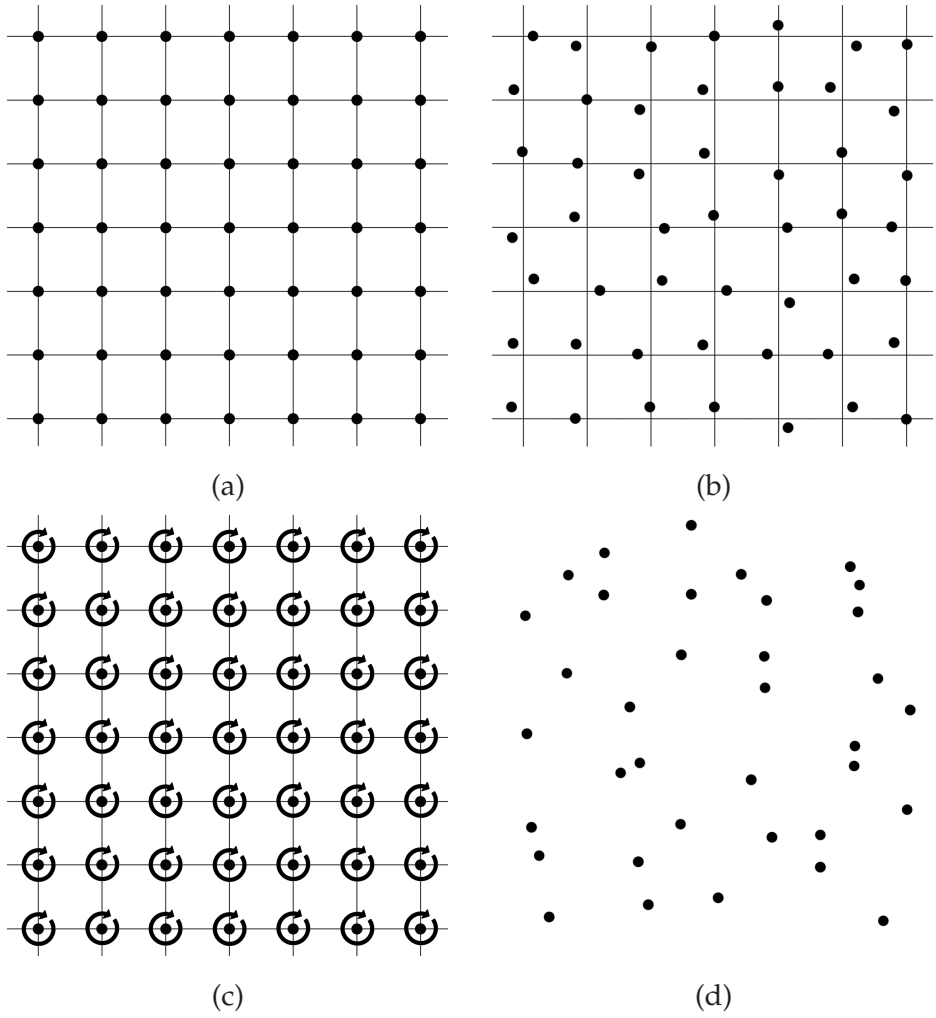

Figure 1.3 The four states of regularity; (a) crystalline, (b) disordered, (c) plastic and (d) amorphous.

Two characteristics of crystalline distortions are lattice and substitution disorder [Str93]. Lattice disorder refers to distortions of the underlying crystalline lattice, whereas substitution disorder refers to variations in the entities at the lattice sites. Lattice disorder has traditionally been classed as either of the first or second kind depending on the kind of irregularity [HB62], although modern descriptions of disorder avoid these terms [Wel04].

There are a number of causes for lattice disorder and their effects are shown in Fig. 1.4. Lattice disorder of the first kind can be described as a perturbation from perfect crystalline order in which the statistical average of all molecular positions correspond to lattice points in a perfect crystal. In Fig. 1.4(a) thermal vibrations cause continual displacements in the molecular positions about their equilibrium position, i.e. the lattice points of the ideal crystal [HB62]. Fig. 1.4(b) shows a frozen structure which has non-zero molecular displacements due to thermal vibrations frozen at a certain instant. For first kind disorder the distortions at different lattice sites are uncorrelated.

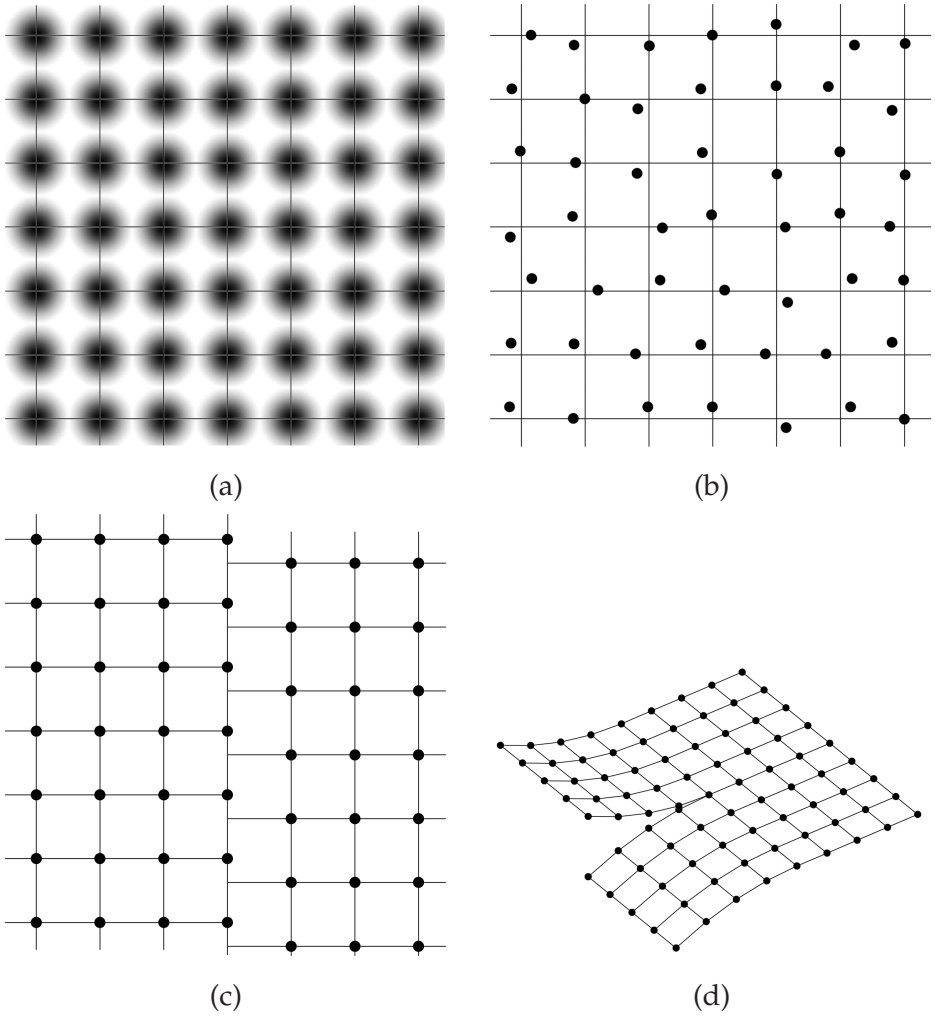

Figure 1.4 The effects of various types of lattice disorder namely (a) thermal disorder, (b) frozen state disorder, (c) edge and (d) screw dislocations.

Materials exhibiting lattice disorder of the second kind signify a further departure from crystalline order, resembling the amorphous state more than the crystalline state. Statistical averages of molecular positions deviate significantly from the ideal lattice positions. Crystallinity is only observed over a short range and long range order is not observed as is the case for the amorphous state. The distortions from the ideal lattice points are corre-

lated, as a result of a distortion at one site affecting the distortion at adjacent sites. This is generally expected to be the case in close-packed systems [WB95].

Although the classifications of "first kind" and "second kind" lattice disorder have been traditionally used and are in widespread use, a more comprehensive model is the "perturbed lattice" model where each site of the distorted lattice is related to a site of a regular lattice by a random displacement [WMC80, WC82, Wel04]. The perturbed lattice model is well-defined in one dimension, but consistent correlation functions in more than one dimension are complex and not completely understood [WMC80]. However, in practice, good approximations can be made by using an imposed correlation field [dG89, SM96b].

Substitution disorder refers to variations in the objects occupying each lattice site and can be either compositional or orientational in nature. Materials exhibiting compositional disorder are an admixture of two or more component molecules substituted at various lattice sites in a crystal, as shown in Fig. 1.5(a). Vacancies and interdigitation are also a form of compositional disorder where molecules are missing at certain lattice cites [Fig. 1.5(b)] or interdigitated as extra molecules between regular lattice sites [Fig. 1.5(c)]. Orientational disorder, shown in Fig. 1.5(d), refers to a particular molecule type within the crystal being allowed one of a number of rotations at each lattice site.

Substitution disorder is relatively easily characterized for a one-dimensional system using a Markov chain or one-dimensional Ising model (the two descriptions being, in fact, equivalent) [Wel04]. In two dimensions, however, the situation is much more complicated and completely general exact results do not exist. This is due in large part to the properties of spatially interacting random variables in two or more dimensions being imperfectly understood. A simple generalization of the Markov chain in two dimensions are two-dimensional growth-disorder models, although solutions can be obtained only in special cases [WG73, WG75, Wel77]. Pickard [Pic77, Pic78, Pic80] has developed symmetric growth-disorder models for which, under appropriate restrictions, the resulting distributions are stationary Markov random fields allowing the form of the correlation field to be determined. Overall, however, general substitution disorder in two dimensions is poorly understood.

Crystalline disorder can be classified as either uncorrelated or correlated. Within closely packed crystals, the distortions at one lattice site can significantly affect crystal distortions at a contiguous site on the lattice. In these cases, the distortions at contiguous lattice sites are correlated, and this is referred to here as correlated lattice disorder. Likewise, the particular rotation or the molecule type occupying one lattice site may be probabilistically dependent on the orientation of molecules at contiguous sites so that substitution disorder may also be correlated. Of course uncorrelated disorder is a special case of correlated

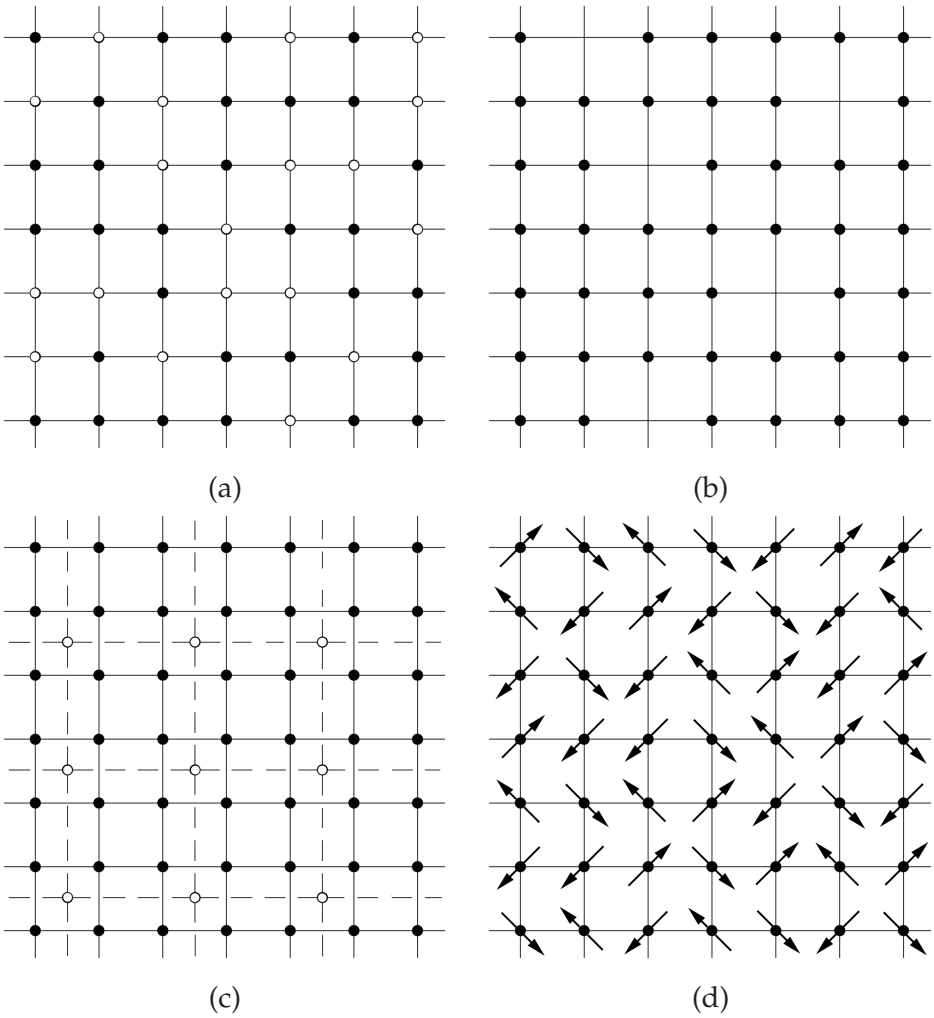

Figure 1.5 The effects of various types of substitution disorder namely (a) compositional disorder, (b) vacancies, (c) interdigitations and (d) orientational disorder.

disorder when the correlation coefficients are zero. In this thesis, disorder is described in terms of correlated distortions from ideal crystallinity and the classification as first and second kind disorder is not used.

1.2 The Ising model

1.2.1 General

In recent developments of condensed matter physics, models have played a crucial role in relating experimental data to physical theory [Bax82]. To quantitatively study complex solid state systems it is often necessary to consider only degrees of freedom relevant to the question or phenomenon being studied. This is done by using a simplified model with a reduced effective Hamiltonian written as a function of the relevant degrees of freedom. Constructing an effective Hamiltonian, H_{eff} of the model system usually involves a compromise between analytical simplicity and maintaining a realistic representation of the system. Often, existing exactly solvable models are used as the starting point in such models. Studies are then carried out on systems with effective Hamiltonians that match the Hamiltonian of the model. This holds particularly true for spin models, as a number of important analytical solutions exist for this class of models.

Spin models are a specialized case of the discrete formalism in which the degrees of freedom correspond to magnetic moments, **S**. This property occurs naturally in magnetic systems consisting of molecules with unpaired electronic spins located on lattice sites. In many magnetic materials, strong short-range exchange interactions orient the magnetic moments approximately in one of two directions. The Ising model assumes magnetic moments can have one of two orientations, referred to as up or down, and assumes a simplified description of particle interactions. Magnetic moments have scalar values $+1$ and -1 corresponding to the up and down orientations, respectively, and are denoted by the scalar quantity s_i. Ising models on a number of various lattice types are exactly solvable. That is, the configuration space can summed to calculate the partition function, Eq. (1.12c), at any given energy level, $H(C_\mu) = E$.

1.2.2 The one-dimensional Ising model

The simplest example of an Ising model is a one-dimensional linear chain of N magnetic moments in zero external magnetic field with the Hamiltonian

$$H = -J \sum_{x=0}^{N-1} s_x s_{x+1}, \tag{1.15}$$

where the sign of the coupling strength J dictates whether the bonds are ferromagnetic $(+)$ or antiferromagnetic $(-)$. The partition function of Eq. (1.12c) with the Hamiltonian Eq (1.15) has the form

$$Z = \sum_{s_0=\pm 1} \sum_{s_1=\pm 1} \cdots \sum_{s_{N-1}=\pm 1} \exp\left(\beta J \sum_{x=0}^{N-1} s_x s_{x+1}\right), \tag{1.16}$$

where $s_x = \pm 1$ and cyclic boundary conditions have been assumed such that $s_N = s_0$ [Hua63]. This model was solved by Ernst Ising in his 1924 Ph.D thesis [Isi24], after whom the model takes its name and is illustrated in Fig. 1.6. Expanding the argument of the exponent and recollecting terms, and denoting

$$\sum_{\{s\}} = \sum_{s_0=\pm 1} \sum_{s_1=\pm 1} \cdots \sum_{s_{N-1}=\pm 1},$$

Eq. (1.16) becomes

$$Z = \sum_{\{s\}} \prod_{x=0}^{N-1} \exp(-\beta J s_x s_{x+1}), \tag{1.17}$$

where $s_N = s_0$. Eq. (1.17) has the form of the Leibniz formula for the determinant of an $N \times N$ matrix [PB89]. It therefore is convention, although trivial in this simple case, to introduce the transfer matrix

$$\mathbf{P} = \begin{bmatrix} P_{11} & P_{1,-1} \\ P_{-1,1} & P_{-1,-1} \end{bmatrix}, \tag{1.18}$$

where

$$\begin{aligned} P_{11} &= P_{-1,-1} = \exp(\beta J), \\ P_{1,-1} &= P_{-1,1} = \exp(-\beta J). \end{aligned} \tag{1.19}$$

The partition function Eq. (1.17) then takes the form

$$\begin{aligned} Z &= \sum_{s_i} P_{s_0,s_1} P_{s_1,s_2} \dots P_{s_{N-1},s_0} \\ &= \text{Tr}\,\left(\mathbf{P}^N\right), \end{aligned} \tag{1.20}$$

where $\text{Tr}(\cdot)$ is the trace. The transfer matrix $\mathbf{P}$ can be diagonalized with eigenvalues λ_1 and λ_2 given by the roots of the determinant

$$|\mathbf{P} - \lambda \mathbf{I}| = 0. \tag{1.21}$$

Likewise, the matrix $\mathbf{P}^N$ can be diagonalized by the eigenvalues λ_1^N and λ_2^N and Eq. (1.20) is the sum of the eigenvalues,

$$\begin{aligned} Z = \lambda_1^N + \lambda_2^N &= [\exp(\beta J) + \exp(-\beta J)]^N \\ &= [2\cosh(\beta J)]^N . \end{aligned} \tag{1.22}$$

Substitution of the solution Eq. (1.22) into Eq. (1.12b) and Eq. (1.12a) gives exact solutions to physically measurable quantities. Similarly the systems entropy Eq. (1.12d) per site is given by

$$\frac{S}{N} = \frac{1}{N}\left[\log 2 + \log\left(\cosh(\beta J)\right) - \beta J \tanh(\beta J)\right]. \tag{1.23}$$

Eq. (1.23) is a monotonic continuous function, indicating that the system undergoes no phase transition.

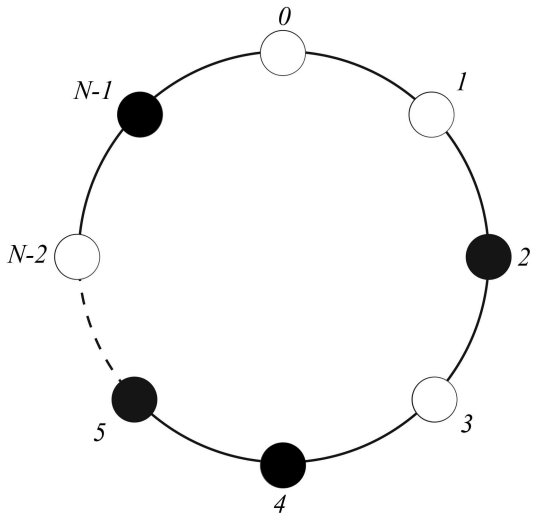

Figure 1.6 The one-dimensional Ising model on a ring. The two spin orientations are represented by black and white circles.

The two-point correlation function is stationary so that Eq. (1.13) can be written

$$\rho_x = \langle s_0 s_x \rangle - \langle s_0 \rangle \langle s_x \rangle. \tag{1.24}$$

In a long chain, the populations of each spin orientation are equal so that $\langle s_x \rangle = 0$, giving

$$\begin{aligned} \rho_x &= \langle s_0 s_x \rangle \\ &= \frac{1}{Z} \sum_{\{s\}} s_0 s_x \exp\left(-\beta J \sum_{j=0}^{N-1} s_j s_{j+1} \right), \end{aligned} \tag{1.25}$$

where Z is given by Eq. (1.22). Inserting the product $(s_1)^2.(s_2)^2 \ldots (s_{x-1})^2 = 1$, Eq. (1.25)

can be reduced to the closed form

$$\begin{aligned}\rho_x &= \frac{1}{Z}\sum_{\{s\}}(s_0s_1)(s_1s_2)\ldots(s_{x-1}s_x)\exp\left(-\beta J\sum_{j=0}^{N-1}s_js_{j+1}\right)\\ &= \frac{1}{Z\beta^x}\frac{\partial Z(J)}{\partial J}\\ &= [\tanh(\beta J)]^x\,. \end{aligned} \tag{1.26}$$

In the ferromagnetic case where $\beta J < 1$, the correlation length ξ is defined as

$$\xi = -\frac{1}{\log\left(\tanh(\beta J)\right)}. \tag{1.27}$$

Eq. (1.26) can be written in the form

$$\rho_x = \exp(-x/\xi), \tag{1.28}$$

where $\xi > 0$. As $T \to 0$, the correlation length $\xi \to \infty$, and as $T \to \infty$, i.e. the system becomes completely disordered due to thermal vibration, $\xi \to 0$. The correlation function Eq. (1.28) over the range $0 \le x \le 10$ is shown in Fig. 1.7 for the temperatures $T = 0$, 1.0, 2.0 and ∞. At the $T = 0$, all correlations equal unity and $T = \infty$ all correlations are zero for $x > 0$. Between these two temperatures the correlation function is shown to decay exponentially with x. In the antiferromagnetic case, the correlation function Eq. (1.28) is modified by a prefactor of $(-1)^x$, i.e. for odd separations the correlation function is negative.

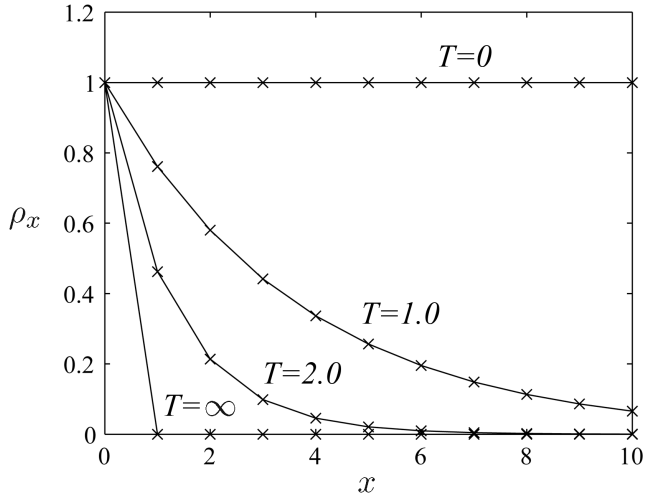

Figure 1.7 The two-point correlation function of the ferromagnetic one-dimensional Ising model at T =0,1.0, 2.0 and ∞.

1.2.3 The square lattice Ising model

The square lattice (SL) Ising model in zero external magnetic field was the first two-dimensional Ising model to be analytically solved, making it one of the most studied models in condensed matter physics. New analytical methods have often been developed for this model and later applied to more complicated models [Bax82]. The SL Ising model consisting of N magnetic moments has the Hamiltonian

$$H = -\sum_{x=0}^{m-1}\sum_{y=0}^{n-1}(J_1 s_{xy}s_{x+1,y} + J_2 s_{xy}s_{x,y+1}) \tag{1.29}$$

where $s_{xy} = \pm 1$ are the Ising spins and (x, y) index the sites on an $m \times n$ lattice of square plaquettes, referred to as the square lattice. The model consists of up and down spins on a square lattice, shown in Fig. 1.8, and is said to be ferromagnetic if $J_i > 0$ and antiferromagnetic if $J_i < 0$. The solution to the model was found by Onsager in 1944 [Ons44] by diagonalizing the transfer matrix and finding an irreducible matrix algebra representation to calculate the free energy of the system. His calculation famously showed discontinuities in derived functions for temperature dependent quantities, indicating the presence of a finite temperature phase transition at a normalized Curie temperature of $T_C = 2.27$. This drew attention from much of the physics community, and is widely considered as one of the most important calculations of the 20^{th} century, being the first exact solution of a system which underwent a phase transition. However, Onsager's method was mathematically complex and, as a result, more transparent analytical solutions were later developed.

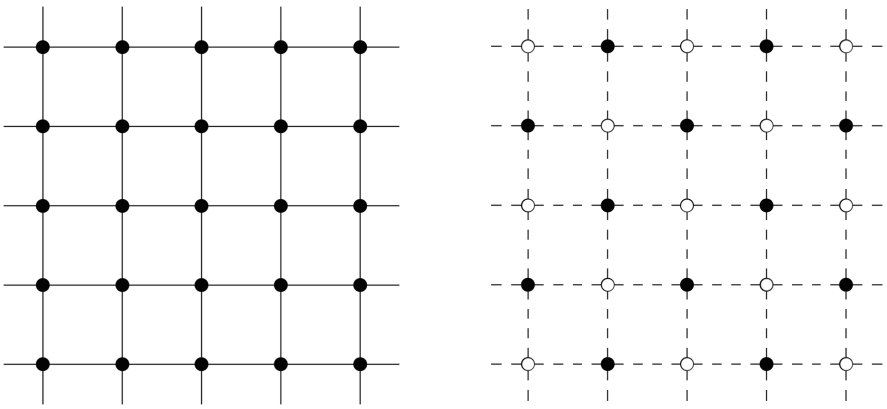

(a) (b)

Figure 1.8 Ground states of the square lattice Ising model with (a) ferromagnetic bonds (full lines) and (b) antiferromagnetic bonds (broken lines). Black and white circles represent up and down spins.

In 1949, Onsager's Ph.D student Bruria Kaufmann showed that the transfer matrix formulated by Onsager belongs to the group of spinor operators allowing simplifications to be made in the calculation [KO49]. Alternative formulations of the transfer matrix have been developed by Schultz et al. [SML64], Thompson [Tho65], Stephen and Mittag [SM72] providing simpler techniques for analytical solution. An alternative approach not requiring the use of a transfer matrix was developed by Kac and Ward [KW52] in 1952 and Potts and Ward [PW55] in 1955, who used combinatorics to construct the partition function as a determinant. This approach was later implemented by Hurst and Green in 1960 [HG60] and Kasteleyn in 1963 [Kas63], utilizing a number of topological theorems to reduce the calculation of the partition function to a problem of counting dimer coverings, the combinatorics of which can be described by a mathematical object known as a Pfaffian. A brief account of this method applied to the SL Ising model is given in Appendix A.

The partition function of the Ising model on a two-dimensional square lattice is given by

$$\begin{aligned} Z &= \sum_{\{s\}} \prod_{x=0}^{m-1} \prod_{y=0}^{n-1} \exp\left(K_1 s_{xy} s_{x+1,y} + K_2 s_{xy} s_{x,y+1}\right), \\ &= \sum_{\{s\}} \prod_{x=0}^{m-1} \prod_{y=0}^{n-1} \left[(\cosh K_1 + s_{xy} s_{x+1,y} \sinh K_1)(\cosh K_2 + s_{xy} s_{x,y+1} \sinh K_2)\right] \\ &= (\cosh K_1 \cosh K_2)^N \sum_{\{s\}} \prod_{x=0}^{m-1} \prod_{y=0}^{n-1} \left[(1 + z_1 s_{xy} s_{x+1,y})(1 + z_2 s_{xy} s_{x,y+1})\right], \end{aligned} \tag{1.30}$$

where $K_i = -\beta J_i$, $z_i = \tanh K_i$ and

$$\sum_{\{s\}} = \sum_{s_{00}=\pm 1} \cdots \sum_{s_{m-1,0}=\pm 1} \sum_{s_{01}=\pm 1} \cdots \sum_{s_{m-1,1}=\pm 1} \cdots \sum_{s_{0,n-1}=\pm 1} \cdots \sum_{s_{m-1,n-1}=\pm 1}.$$

By constructing a Pfaffian as in Eq. (A.1), Kasteleyn showed that in the thermodynamic limit in which the system size $N \to \infty$ [Kas63], the partition function has the solution

$$N^{-1} \ln Z \sim \ln 2 + \int_{-\pi}^{\pi} \int_{-\pi}^{\pi} \ln(\cosh 2K_1 \cosh 2K_2 - \sinh 2K_1 \cos\phi_2 - \sinh 2K_2 \cos\phi_1) \mathrm{d}\phi_1 \mathrm{d}\phi_2, \tag{1.31}$$

where ϕ_1 and ϕ_2 are as defined in Appendix A. Eq. (1.31) is exactly the expression derived by Onsager [Ons44] for the system .

Another advantage of the combinatorial Pfaffian approach is that it admits a straightforward calculation of the two-point correlation function. The two-point correlation function

between the pair of spins at sites $(0,0)$ and $(x,0)$ is given by

$$\rho_{x0} \equiv \langle s_{00}s_{x0}\rangle = \frac{1}{Z}(\cosh K_1 \cosh K_2)^N \sum_{\{s\}} s_{00}s_{x0} \prod_{j=0}^{m-1}\prod_{k=0}^{n-1}(1+z_1 s_{jk}s_{j+1,k})(1+z_2 s_{jk}s_{j,k+1}). \tag{1.32}$$

By implementing the Pfaffian approach (as shown in Appendix A) Montroll et al. [MPW63] reduced the calculation of the correlation function to the evaluation of a Toeplitz determinant given by Eqs. (A.34)-(A.37). In the ferromagnetic case, the positive sign in Eq. (A.34) is selected so that the correlations are positive. Similarly, in the antiferromagnetic case the negative sign is selected. A similar result obtained by Kaufmann and Onsager [KO49] using spinor algebra was shown to be equivalent to the result Eq. (A.34) by Montroll et al. [MPW63], although the analysis is considerably more complicated. The transfer matrix formalism of Schultz et al.[SML64] admits a result which can be shown to be identical to Eqs. (A.34).

At $T = T_C$, the integral Eq. (A.35) can be calculated explicitly [KO49]. For large spin separation x, Kaufmann and Onsager [KO49] give the approximate form

$$\rho_{x0} \simeq \prod_{s=1}^{x} \frac{\Gamma(s)\Gamma(s)}{\Gamma(s+1/2)\Gamma(s-1/2)}, \tag{1.33}$$

which can be approximated by

$$\rho_{x0} \simeq \frac{B_0}{x^{1/4}}, \tag{1.34}$$

with $B_0 \simeq 0.7034$ [Fis59, Fis63]. By utilizing a similarity between Toeplitz determinants and Wiener-Hopf sums, Wu [Wu66] determined the asymptotic behaviours of Toeplitz determinants in some limiting cases. The calculation utilizes Szego's theorem which provides limiting behaviour of Eq. (A.34) as the separation $x \to \infty$. The on-axis two-point correlation behaviour was determined in the limit of large separation in the cases where $T < T_C$ and $T > T_C$. Results have the form of an asymptotic expansion in x and T, the leading terms of which provide valuable information about the correlation behaviour about the critical temperature T_C. The analysis was sufficiently general that analogous calculations could be carried for a number of other systems.

Adapting the Pfaffian technique to the calculation of off-axis correlations has proven to be a non-trivial task, as foreseen by Montroll et al. [MPW63]. Even so, asymptotic information has been obtained for the square Ising model [CW67]. Alternative approaches to the transfer matrix and combinatorial methods for calculating correlations have been developed for the square Ising model, most utilizing connections between statistical physics and quantum field theory [WMTB76, DD83, Bax82, Ple88]. As no results using such techniques exist for the systems studied in this thesis, they will not be discussed further.

1.2.4 The triangular Ising antiferromagnet

The anisotropic Ising model consisting of N Ising spins on a triangular lattice with nearest-neighbor interactions is defined by the Hamiltonian

$$H = -\sum_x \sum_y \left(J_1 s_{xy} s_{x+1,y} + J_2 s_{xy} s_{x,y+1} + J_3 s_{xy} s_{x+1,y+1} \right), \tag{1.35}$$

where $s_{xy} = \pm 1$ are the Ising spins, (x, y) index sites on the triangular lattice and J_i are the bond strength between nearest neighbour spins [Fig. 1.9(a)]. When all three bonds are antiferromagnetic ($J < 0$) the system is referred to as the triangular Ising antiferromagnet (TIA). Each spin interacts with each of its six nearest-neighbours with a bond energy that depends on whether the two spins are the same or different. For an antiferromagnetic system the bond energy is smaller for unlike neighbours than for like neighbours. The system adopts configurations that minimise the total free energy so that unlike nearest-neighbour spins are preferred. At a temperature T of absolute zero the internal energy is minimised and the number of unlike adjacent spins is maximised. As the temperature increases, thermal fluctuations mean that the preference for unlike adjacent states is reduced and the system becomes more random. It becomes completely random for $T \to \infty$. The partition function, given by

$$\begin{aligned} Z &= (\cosh K_1 \cosh K_2 \cosh K_3)^N \\ &\quad \times \sum_{s_{xy}=\pm 1} \prod_{x=0}^{N-1} \prod_{y=0}^{N-1} \left[(1 + z_1 s_{xy} s_{x+1,y})(1 + z_2 s_{xy} s_{x,y+1})(1 + z_3 s_{xy} s_{x+1,y+1}) \right], \end{aligned} \tag{1.36}$$

where $K_i = -\beta J_i$ and $z_i = \tanh K_i$, was first evaluated in the thermodynamic limit [Wan50, Hou50, HS50, New50] by including diagonal interactions in the transfer matrix diagonalization method of Onsager [Ons44]. It was shown that the partition function takes the form

$$\begin{aligned} N^{-1} \log Z &= \log 2 + \frac{1}{2(2\pi)^2} \int_{-\pi}^{\pi} \int_{-\pi}^{\pi} \log \Big\{ \cosh 2K_1 \cosh 2K_2 \cosh 2K_3 \\ &\quad + \sinh 2K_1 \sinh 2K_2 \sinh 2K_3 - \sinh 2K_1 \cos(\phi_1) - \sinh 2K_2 \cos(\phi_2) \\ &\quad + \sinh 2K_3 \cos(\phi_1 + \phi_2) \Big\}, \end{aligned} \tag{1.37}$$

in the thermodynamic limit. A typical ground-state configuration shown in Fig. 1.9(b).

The TIA does not undergo a finite temperature phase transition, effectively having a Curie temperature at $T_c = 0$. The TIA was shown [Wan50, Hou50, MC06] to have a non-zero

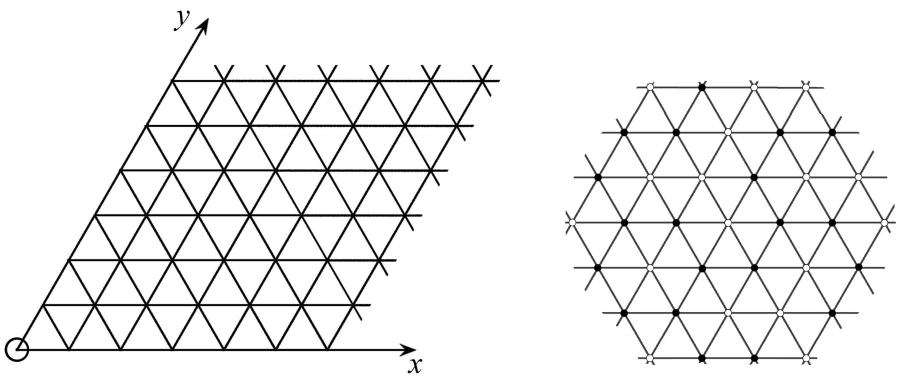

(a) (b)

Figure 1.9 The TIA lattice, shown in (a), and (b) a ground-state configuration of the TIA with black and white circles represent up and down spins. Full lines represent antiferromagnetic bonds.

ground state entropy given by

$$\begin{aligned} S &= R\frac{2}{\pi}\int_0^{\pi/3}\log(2\cos\omega)\mathrm{d}\omega \\ &\sim (0.3231)R. \end{aligned} \tag{1.38}$$

Note that the numerical values given by Wannier [Wan50, MC06] is incorrect. This residual ground state entropy indicates that the TIA does not achieve antiferromagnetic ordering, and has a highly degenerate ground state at absolute zero. Such a system is said to be "frustrated". The frustration results from the inability of a system to satisfy all bonds due to the topology of the underlying lattice, and this kind of frustration is termed "geometric" frustration [Pau35, Lie86, Gre01]. Geometric frustration is increasingly being recognised as an important organizing principle in systems from a diverse range of areas, including coding theory, spin glasses, superconducting networks, quantum dynamics, protein folding and neural computation [AC97, DKR$^+$97, MS01, Ram03, Mez03, WNF$^+$06]. Fig. 1.10 shows a single plaquette of the TIA consisting of three mutually interacting spins with bond strength J. If antiferromagnetism is imposed on the plaquette with nearest neighbour spins preferring opposite orientations, it is impossible to minimize the energy of all three interactions. Given two spin orientations, the plaquette is frustrated regardless of the orientation of the third spin. There are in fact 6 configurations that minimize the energy on a triangular plaquette. There are therefore a large number of minimum energy states at absolute zero.

Stephenson [Ste64] applied the combinatorial method of Kasteleyn [Kas63], as detailed for the square lattice (SL) Ising model in Appendix A, to represent the partition function by a Pfaffian such that

$$Z^2 = (2\cosh K_1\cosh K_2\cosh K_3)^{2N}|\mathbf{A}|, \tag{1.39}$$

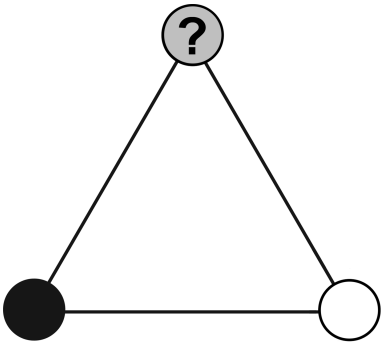

Figure 1.10 Nearest-neighbouring spins on a triangular plaquette, shown to be frustrated independent on the orientation of the unknown spin. Black and white circles represent the up and down states.

with the K_i defined as in Eq. (1.36). The skew-symmetric matrix $\mathbf{A}(x, y; x, y)$ is a $6N \times 6N$ matrix where the elements are 6×6 submatrices, analogous to the SL Ising model. By following the procedures presented in Appendix A for the SL Ising model, the result analogous to Eq. (A.11) is obtained with

$$\begin{aligned} |\mathbf{A}(\phi_1, \phi_2)| &= (1+z_1^2)(1+z_2^2)(1+z_3^2) + 8z_1z_2z_3 \\ &\quad -2z_1(1-z_2^2)(1-z_3^2)\cos\phi_1 - 2z_2(1-z_3^2)(1-z_1^2)\cos\phi_2 \\ &\quad -2z_3(1-z_1^2)(1-z_2^2)\cos(\phi_1+\phi_2), \end{aligned} \tag{1.40}$$

with the z_i defined as in Eq. (1.36). By substituting Eq. (1.40) into Eq. (1.39) and considering the thermodynamic limit, the solution of the partition function Eq. (1.37) is obtained.

Stephenson also performed an analogous calculation to Montroll et al. [MPW63] presented in Appendix A for the two-point correlation function between the pair of spins at sites $(0, 0)$ and $(x, 0)$ of the TIA given by

$$\begin{aligned} \rho_{x0} &= \frac{1}{Z}(\cosh K_1 \cosh K_2 \cosh K_3)^N \sum_{s_{jk}=\pm 1} s_{00}s_{x0} \\ &\quad \times \prod_{j=0}^{m-1}\prod_{k=0}^{n-1}(1+z_1 s_{jk}s_{j+1,k})(1+z_2 s_{jk}s_{j,k+1})(1+z_3 s_{jk}s_{j+1,k+1}). \end{aligned} \tag{1.41}$$

The inverse matrix $\mathbf{A}^{-1}(\phi_1, \phi_2)$ of Eq. (1.40) was determined, allowing analogous expressions to Eqs. (A.25) and (A.26) to be determined. As a result, a Toeplitz determinant of the form of Eq. (A.34) is obtained, with the function $\varphi(\omega)$ of Eq. (A.35) for the TIA given by

$$\varphi(\omega) = \left(\frac{a - be^{i\omega} + ce^{-i\omega}}{a - be^{-i\omega} + ce^{i\omega}}\right)^{1/2}, \tag{1.42}$$

where,

$$\begin{aligned} a &= 2z_3(1+z_1^2)(1+z_2^2)+4z_1z_2(1+z_3^2), \\ b &= z_3^2(1-z_1^2)(1-z_2^2), \\ c &= (1-z_1^2)(1-z_2^2). \end{aligned} \tag{1.43}$$

Note that by selecting $J_3 = 0$ such that $z_3 = 0$, the Hamiltonian Eq. (1.35) reduces to the SL Ising model Hamiltonian Eq. (1.29) and the results Eqs. (A.34) - (A.37) are obtained.

At the critical point ($T = 0$), the elements Eq. (A.35) simplify considerably and can be evaluated explicitly when isotropy is assumed, i.e. $J_i = J$. In this case Eq. (1.42) simplifies, allowing the integral Eq. (A.35) to be evaluated giving [Ste64]

$$a_0 = -1/3, \tag{1.44a}$$

$$a_n = -\frac{[2\sin(2\pi n/3)]}{\pi n}. \tag{1.44b}$$

which can be written,

$$a_n = \begin{cases} -1/3, & n = 0 \\ 0, & n = 3r \\ \sqrt{3}/(\pi n), & n = 3r-1 \\ -\sqrt{3}/(\pi n), & n = 3r-2, \end{cases} \tag{1.45}$$

where $r = 1, 2, \ldots$. Exact correlation values can then be calculated by substituting Eq. (1.45) into Eq. (A.34) and evaluating the determinant.

An interesting result of the above calculation is that any given lattice site is negatively correlated to its first and second nearest neighbours on an axis and positively correlated to its third nearest neighbour on an axis. This pattern then repeats along the axis such that every third spin is positively correlated with the origin spin. By numerical fitting of exact correlation values calculated from Eq. (A.34), Stephenson [Ste64] obtained the asymptotic approximations

$$\rho_{x0} \simeq \begin{cases} \epsilon_0 x^{-1/2} + \epsilon_2 x^{-5/2} + \cdots, & x = 0, 3, 6 \ldots \\ (-\epsilon_0/2)x^{-1/2} + \epsilon_1 x^{-3/2} + \cdots, & x = 1, 4, 7 \ldots, \quad x \to \infty \\ (-\epsilon_0/2)x^{-1/2} - \epsilon_1 x^{-3/2} + \cdots, & x = 2, 5, 8 \ldots \end{cases} \tag{1.46}$$

where $\epsilon_0 = 0.632226(2)$, $\epsilon_1 = 0.32(2)$ and $\epsilon_2 = -0.187(5)$. The form of Eq. (1.46) indicates that the on-axis sites can be partitioned into three sublattices, each of three times the lattice spacing, with the correlations in each sublattice being described by the 3 expressions in

Eq. (1.46). The sublattice that contains the origin has positive correlations and the other two have negative correlations. For large x, all correlations decay as $x^{-1/2}$ and the two sets of negative correlations have the same form. To leading order then, all on-axis correlations can be expressed as

$$\rho_{x0} \simeq \epsilon_0 x^{-1/2} \cos\left(\frac{2\pi x}{3}\right), \tag{1.47}$$

where the cosine takes the value $+1$ or $-1/2$ depending on whether the sublattice to which x belongs contains the origin or does not, respectively. Hence, to leading order, the two sublattices that do not contain the origin become degenerate and the correlation coefficient falls into one of two classes.

At finite temperature, Eq. (A.35) is not solvable except in a few limiting cases where it may be reduced to a form in terms of elliptic integrals [Cho84]. Utilizing the theory of Toeplitz determinants developed by Wu [Wu66] for the SL Ising model, Stephenson also obtained asymptotic information on the on-axis correlation function for finite temperatures [Ste70]. Stephenson [Ste70] obtained an asymptotic expansion in x for the correlation function ρ_{x0} at finite temperature,

$$\begin{aligned}
\rho_{x0}(T) \quad \sim \quad & \left(\frac{\pi}{2}\sin\theta\right)^{-1/2} z^x x^{-1/2} \Bigg\{ \cos\left(x\theta + \frac{\theta}{2} - \frac{\pi}{4} - \phi\right) \\
& -(4x)^{-1}\left[\frac{3}{2} + (2\sin\theta)^{-1}\cos\left(x\theta + \frac{3\theta}{2} + \frac{\pi}{4} - \phi\right)\right. \\
& +z^2(1-z^2)^{-1}\cos\left(x\theta + \frac{\theta}{2} - \frac{\pi}{4} - \phi\right) \\
& \left.+z^2\rho^2\cos\left(x\theta + \frac{5\theta}{2} - \frac{\pi}{4} - 3\phi\right)\right]\Bigg\}, \quad x \to \infty
\end{aligned} \tag{1.48}$$

where

$$\theta = \cos^{-1}[(1+\exp 4K)/2], \tag{1.49}$$

$$\rho = (1 - 2z^2\cos 2\theta + z^4)^{-1/4}, \tag{1.50}$$

and

$$\phi = \arg(1 - z^2\cos 2\theta + iz^2\sin 2\theta)/2. \tag{1.51}$$

The calculation utilizes the similarity between a Toeplitz determinant and the Wiener-Hopf sum equation which only holds when x (and hence, the size of the Toeplitz determinant) is large, and when $T \gg 0$. By the use of Szego's theorem [GS58], the asymptotic behaviour of the Toeplitz determinant as $x \to \infty$ can be inferred. Eq. (1.48) is therefore expected to break down for small x, and also for $T \to 0$. Eq. (1.48) exhibits the same on-axis correlation behaviour as was observed at $T = 0$.

1.2.5 The fully frustrated square Ising model

The fully frustrated square (FFS) Ising model with nearest neighbour couplings was originally formulated by Villain [Vil77] as a simple model for a spin glass with non-random interactions. The model consists of up or down spins on a square lattice with ferromagnetic horizontal bonds and alternating columns of ferromagnetic and antiferromagnetic vertical bonds, shown in Fig. 1.11. The FFS model is defined by the Hamiltonian

$$H = -J \sum_x \sum_y \left(s_{xy} s_{x+1,y} + (-1)^x s_{xy} s_{x,y+1} \right), \tag{1.52}$$

where $s_{xy} = \pm 1$ are the Ising spins, (x, y) indexes the sites on the square lattice and $J > 0$ is the magnitude of the bond strength between nearest neighbour spins. Note that we have followed the more conventional notation [Vil77, For80, LO80] in taking the ferromagnetic bonds as horizontal in contrast to Wolff and Zittartz [WZ82] who take them as vertical. These bond rules make the system periodic, allowing for the possibility of exact solutions. The partition function was determined by Villain [Vil77] using the combinatorial method of Kasteleyn [Kas63] giving

$$\begin{aligned} N^{-1} \log Z &= \log(2 \cosh 2K) \\ &\quad + \frac{1}{4\pi^2} \int_0^\pi \int_0^\pi \log \left([1 + z^2]^2 - 2z^2 \cos \phi_1 - 2z^2 \cos \phi_2 \right) \mathrm{d}\phi_1 \mathrm{d}\phi_2. \end{aligned} \tag{1.53}$$

The FFS model is related to the checkerboard model by a simple gauge transformation [PAY06] and shares many of the same statistical properties.

The FFS Ising model undergoes no finite temperature phase transition and has a critical point at $T = 0$, as is the case for the TIA of Section 1.2.4. Andre et al. [ABC$^+$79] showed that the FFS Ising model has non-zero ground state entropy of $S = 0.2916$, indicating that the configurations of the system do not achieve an ordered state at $T_C = 0$ and it is geometrically frustrated. Consider a plaquette of the FFS Ising model consisting of four mutually nearest-neighbour spins, as shown in Fig. 1.12. With a single antiferromagnetic bond in the vertical direction and three ferromagnetic bonds, it is not possible to minimize the energy of all four interactions. Given any three orientations, the fourth cannot be chosen such that the plaquette is satisfied. There are 4 configurations in total that minimize the energy on a triangular plaquette. Degeneracy in the plaquettes minimal energy state gives the system a highly degenerate ground state and a residual ground state entropy.

Correlation properties of the FFS were studied by Forgacs [For80] by mapping the system onto a special case of the 8-vertex Baxter model and using traditional Pfaffian techniques [WHZ81]. It was shown that ground state correlations along the horizontal axis exhibit power law decay with a critical exponent $\eta = 0.5$, as is the case for the triangular Ising

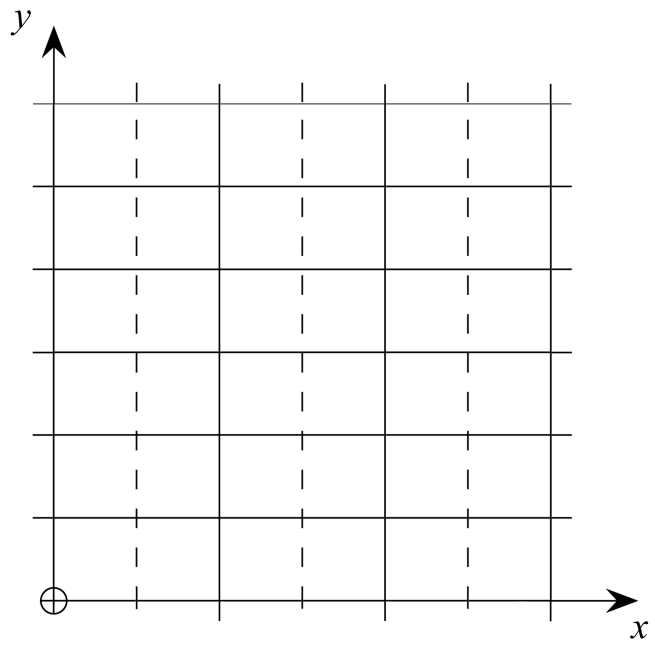

Figure 1.11 The FFS Ising model with ferromagnetic and antiferromagnetic bonds shown by full and broken lines, respectively. Note that the origin is defined as being on a ferromagnetic column.

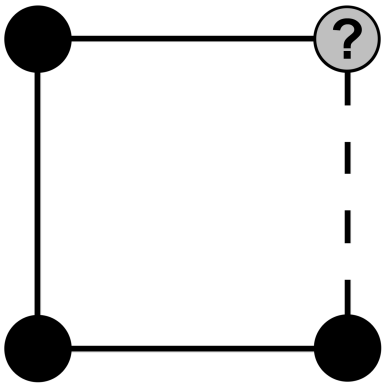

Figure 1.12 Nearest-neighbouring spins on a square plaquette of the FFS with ferromagnetic and antiferromagnetic bonds shown by full and broken lines, respectively. The plaquette is frustrated independent on the orientation of the unknown spin.

antiferromagnet (TIA) [Hou50, Wan50, Ste64]. Peschel [Pes82] later showed by a mapping onto the quantum XY-chain that the FFS, the TIA and the 'Union-Jack' model share the same critical exponent of 0.5.

The correlation functions ρ_{x0} and ρ_{xx} are used here to denote the horizontal and diagonal correlation functions, respectively, and the set $\{\rho_{x0}, \rho_{xx}\}$ are referred to here as the axial correlation functions. The definition of the Hamiltonian Eq. (1.52) implies that the origin of the lattice is on a ferromagnetic column (Fig. 3.1). Using transfer matrix techniques developed by Schultz et al. [SML64] and developed further by Hoever et al. [HWZ81, WHZ81, HZ81], Wolff and Zittartz [WZ82] expressed the axial correlation functions as a Toeplitz determinant of the form of Eq. (A.34) where $n = x$ for ρ_{x0} or ρ_{xx}. The elements a_n are given by Eq. (A.35) where the form of $\varphi(\omega)$ depends on whether the correlation function is horizontal or diagonal. The diagonal correlations ρ_{xx} take the simplest form, and $\varphi(\omega)$ is given by

$$\varphi(\omega) = e^{-i\omega} \frac{(1 + z_0^2 \exp(2i\omega))}{(1 + z_0^2 \exp(-2i\omega))}, \tag{1.54}$$

where $z_0 = 1/(\alpha + \sqrt{\alpha^2 - 1})$, with $\alpha = \coth^2(2K)$ and $K = 1/T$. For the horizontal correlation function ρ_{x0}, $\varphi(\omega)$ is given by

$$\varphi(\omega) = e^{-i\omega} \left[\frac{(1 - z_1^2 \exp(2i\omega))(1 + z_2 \exp(i\omega))(1 - z_2 \exp(-i\omega))}{(1 - z_1^2 \exp(-2i\omega))(1 + z_2 \exp(-i\omega))(1 - z_2 \exp(i\omega))} \right]^{\frac{1}{2}}, \tag{1.55}$$

where $z_1 = \sqrt{\alpha} - \sqrt{\alpha - 1}$ and $z_2 = \sqrt{1 + \alpha} - \sqrt{\alpha}$.

At $T = 0$, $\alpha = 1$ so that Eq. (1.54) for the diagonal correlations simplifies to

$$\varphi(\omega) = \text{sign}(\cos q), \tag{1.56}$$

allowing the integral to be evaluated, giving

$$a_n = \begin{cases} 0, & n = 2m \\ 2/\pi n, & n = 4m - 1 \\ -2/\pi n, & n = 4m + 1, \end{cases} \tag{1.57}$$

where $m \in \mathbb{Z}$. Substituting Eq. (1.57) into Eq. (A.34) and evaluating the determinant gives [WZ82]

$$\rho_{xx} = \begin{cases} 0, & x = 2m - 1 \\ \left[\prod_{s=1}^{x/2} \frac{\Gamma^2(s)}{\Gamma(s-\frac{1}{2})\Gamma(s+\frac{1}{2})} \right]^2, & x = 2m, \end{cases} \tag{1.58}$$

where $m \in \mathbb{Z}^+$. The spins are therefore uncorrelated with neighbours separated by an odd

diagonal distance, and correlate positively with neighbours with even separation. Using an asymptotic evaluation of the determinant Eq. (A.34) at $T = 0$, allowed Wolff and Zittartz to derive the leading order asymptotic behaviour for the horizontal and diagonal correlation functions [WZ82]. For large x the leading order behaviour at $T = 0$ is [WZ82]

$$\rho_{xx} \sim \begin{cases} 0, & x = 2m-1 \\ (0.6450)^2 2^{1/2} x^{-1/2}, & x = 2m. \end{cases} \tag{1.59}$$

At $T = 0$, Eq. (1.55) for the horizontal correlations simplifies to

$$\varphi(\omega) = -i\,[\text{sign}(\omega)] \left[\frac{(1+z_2\xi)(1-z_2\xi^{-1})}{(1+z_2\xi^{-1})(1-z_2\xi)}\right]. \tag{1.60}$$

An explicit expression for ρ_{x0}, while potentially obtainable using Eqs. (1.60), (A.35) and (A.34), has not been determined although Wolff and Zittartz [WZ82] inferred the asymptotic behaviour using isotropy at $T = 0$ for large separations, giving

$$\rho_{x0} \sim \begin{cases} (0.6450)^2 2^{1/4} x^{-1/2}, & x = 2m-1 \\ (0.6450)^2 2^{3/4} x^{-1/2}, & x = 2m. \end{cases} \tag{1.61}$$

Eq. (1.61) shows that the horizontal correlations ρ_{x0} are smaller for odd separations than for even separations, and the ratio (odd/even) is $1/\sqrt{2}$ for large separations. Note that the assumption of isotropy above ensures that

$$\rho_{xx} \sim \rho_{x'0}\big|_{x'=\sqrt{2}\,x}, \quad x = 2m \tag{1.62}$$

where $\rho_{x'0}$ is evaluated using Eq. (1.61) as if x' were even, i.e. for large x the correlation is a function of physical distance in the lattice. Note that horizontal and vertical correlations are simply related through symmetry arguments (described in detail in Chapter 3).

At finite temperature, the integral Eq. (A.35) cannot be evaluated for either the diagonal or horizontal form of the integrand. A leading order asymptotic description of the correlation behaviour was obtained by applying the techniques of Wu [Wu66]. Using asymptotic properties of the integrands Eq. (1.54) and Eq. (1.55) for $T > 0$, Wolff and Zittartz [WZ82] obtained the leading order asymptotic behaviour for the correlation functions $\rho_{xx}(T)$ and $\rho_{x0}(T)$ at finite temperature [WZ82], showing

$$\rho_{x0}(T) \sim \begin{cases} (2/\pi)^{1/2}\,\alpha^{3/4}\,(1+\alpha)^{-1/4}\,x^{-1/2} z_1^x, & x = 2m-1 \\ (2/\pi)^{1/2}\,\alpha^{1/4}\,(1+\alpha)^{1/4}\,x^{-1/2} z_1^x, & x = 2m. \end{cases} \tag{1.63}$$

and

$$\rho_{xx}(T) \sim \begin{cases} 0, & x = 2m-1 \\ (2/\pi)^{1/2}\, x^{-1/2} z_0^x, & x = 2m, \end{cases} \tag{1.64}$$

respectively.

1.3 Monte Carlo simulation

1.3.1 Ergodicity and the detailed balance

Monte Carlo simulation is a class of stochastic methods used to generate a subset of sample configurations of a large but finite many-bodied system, chosen at random from the configuration space, according to the Boltzmann distribution [MU49, NB99]. Thermal expectation values of observables are obtained by numerical averaging over measurements made on the configurations. A key application of Monte Carlo simulation is to investigate phase transitions and critical phenomena in classical many-body models in which configurations are typically particle positions or spin directions [LB05]. The set of configurations in such systems can be continuous or discrete and infinite or finite in number. As well as the traditional applications in statistical physics, Monte Carlo simulation has been used extensively in areas outside of physics ranging from biology to economics [Liu02, LB05].

A Monte Carlo simulation begins with an arbitrary configuration $C_{\mu(0)}$ from which a sequence of configurations $C_{\mu(0)}$, $C_{\mu(1)}$, ..., $C_{\mu(Q)}$ is stochastically generated. The aim is for the distribution of configurations to closely match the distribution of Eq. (1.12b) in order to get a good approximation to the expectation values being calculated. The number of configurations Q usually needs to be large in order to acquire a representation of the distribution function $P(C_\mu)$.

By definition, a Monte Carlo simulation is a Markov process and must satisfy the requirements of ergodicity and the detailed balance [GRS96, Nor97]. A stochastic process generates a subsequent configuration $C_{\mu(k+1)}$ by making some sort of random change to the configuration $C_{\mu(k)}$. These two configurations are said to constitute a Markov chain if the transition probability to go from $C_{\mu(k)}$ to $C_{\mu(k+1)}$ is independent of the processes required to produce $C_{\mu(k)}$, i.e.

$$P\left(C_{\mu(k+1)}|C_{\mu(0)}, C_{\mu(1)}, \ldots C_{\mu(k)}\right) = P\left(C_{\mu(k+1)}|C_{\mu(k)}\right). \tag{1.65}$$

To satisfy ergodicity, each configuration in the configuration space must be accessible from the current configuration.

The conditions imposed by the detailed balance on the transition probabilities can be shown by considering an ensemble of configurations. The number of times $N_0(C_\mu)$ the configuration C_μ occurs within the ensemble is directly proportional to the equilibrium occupation probability $W(C_\mu)$. If a stochastic process is implemented to change the ensemble of configurations, the number of configurations of C_μ afterwards is equal to $N_0(C_\mu)$ plus the number of configurations that were changed into and out of C_μ, i.e.

$$\begin{aligned} N_1(C_\mu) &= N_0(C_\mu) + \sum_{\nu\neq\mu} \big[N_0(C_\nu) P\left(C_{\mu(1)} = C_\mu | C_{\mu(0)} = C_\nu\right) \\ &\quad - N_0(C_\mu) P\left(C_{\mu(1)} = C_\nu | C_{\mu(0)} = C_\mu\right) \big]. \end{aligned} \tag{1.66}$$

The transition probability $P(X_1 = C_\nu | X_0 = C_\mu)$ states the likelihood of transitioning from the configuration C_μ to C_ν which, for brevity, will be denoted by $P(C_\mu \to C_\nu)$. It is clear that for the remaining ensemble of configurations to distribute according to $P(C_\mu \to C_\nu)$ that the sum over ν term in Eq. (1.66) must satisfy

$$\sum_{\nu\neq\mu} \left[N_0(C_\nu) P\left(C_\nu \to C_\mu\right) - N_0(C_\mu) P\left(C_\mu \to C_\nu\right) \right] = 0, \tag{1.67}$$

or equivalently,

$$\sum_{\nu\neq\mu} \left[W(C_\nu) P\left(C_\nu \to C_\mu\right) - W(C_\mu) P\left(C_\mu \to C_\nu\right) \right] = 0. \tag{1.68}$$

A unique solution to Eq. (1.68) can be obtained by satisfying the sum term-by-term, giving

$$W(C_\nu) P\left(C_\nu \to C_\mu\right) = W(C_\mu) P\left(C_\mu \to C_\nu\right). \tag{1.69}$$

The equilibrium distribution of probabilities is a Boltzmann distribution with occupation probabilities given by Boltzmann weights of the form

$$W(C_\mu) = \exp(-\beta E_\mu). \tag{1.70}$$

It follows from Eqs. (1.69) and (1.70) that the ratio of transition probabilities between two states must satisfy

$$\frac{P\left(C_\mu \to C_\nu\right)}{P\left(C_\nu \to C_\mu\right)} = \frac{W(C_\nu)}{W(C_\mu)} = \exp(-\beta[E_\nu - E_\mu]). \tag{1.71}$$

Eq. (1.71) is known as the condition of detailed balance.

It is useful to write the transition probability $P(C_\mu \to C_\nu)$ as a product of the probability to select the configuration $P^s(C_\mu \to C_\nu)$ and the probability to accept a configuration

$P^a(C_\mu \to C_\nu)$

$$P(C_\mu \to C_\nu) = P^s(C_\mu \to C_\nu) \times P^a(C_\mu \to C_\nu). \tag{1.72}$$

The probability of selecting a particular configuration to transition to is uniform such that

$$P^s(C_\mu \to C_\nu) = P^s(C_\nu \to C_\mu) = \frac{1}{N}. \tag{1.73}$$

Equation (1.71) then simplifies to a ratio of the acceptance probabilities

$$\frac{P^a\left(C_\mu \to C_\nu\right)}{P^a\left(C_\nu \to C_\mu\right)} = \exp(-\beta[E_\nu - E_\mu]), \tag{1.74}$$

which allows complete freedom in choosing the acceptance probabilities.

1.3.2 Equilibration, decorrelation and critical slowing down

In practice, a Monte Carlo simulation initiates a Markov chain from an arbitrary state which could be an improbable state for a given Boltzmann distribution [NB99]. Given that detailed balance and ergodicity are satisfied, the correct distribution of configurations will be obtained after many transitions. This can be seen in Eq. (1.66) where, if $N_0(C_\mu)$ is too large in an ensemble, there must be a deficit in other configurations. Subsequent transitions will then involve more configurations moving out of C_μ than into it. The ensemble of configurations sampled initially in a simulation would be a poor representation of the systems probability density function, Eq. (1.12b), as illustrated in Fig. 1.13(a). A sufficient number of Monte Carlo steps must therefore be performed before the ensemble of sampled configurations resembles the probability density function [Fig. 1.13(b)]. This period of correctly redistributing the ensemble is referred to as thermal equilibration (or thermalization) and is a crucial step in Monte Carlo simulation before observables can be measured.

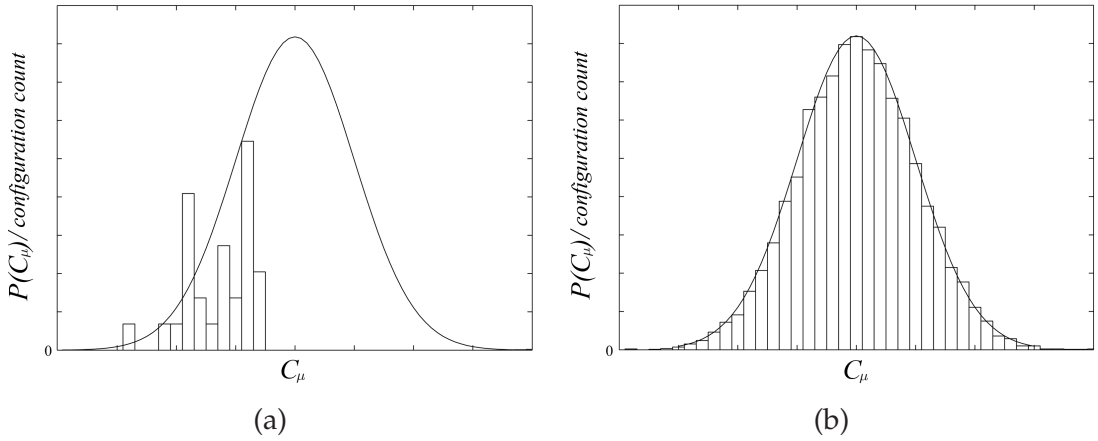

Figure 1.13 Histogram showing the sampled configurations (a) early in a simulation and (b) once thermal equilibration is achieved. The full line is the probability density function and the bars are binned counts of simulated configurations.

In a real system, the observables are dynamic and are functions of time. The Ising model has no kinetic energy term and has no in-built dynamics so a useful quantity to consider is the equilibration time, τ_{eq} for a system to approach equilibrium. An observable $A(t)$ relaxes to its equilibrium value A_{eq} in the time τ_{eq} defined by

$$\tau_{\text{eq}} = \frac{\int_0^\infty \mathrm{d}t\ t[A(t) - A_{eq}]}{\int_0^\infty \mathrm{d}t[A(t) - A_{eq}]}. \tag{1.75}$$

The Markov chain of generated configurations from a Monte Carlo simulation does not represent the real-time evolution of the spin system being modelled. Time in Monte Carlo simulations is measured in "sweeps", a sweep consisting of N attempts, or "steps", to change the current configuration. The equilibration time, τ_{eq} is then an indication of the number of sweeps required to correctly redistribute the ensemble before sampling of configurations can begin. In Monte Carlo simulation, τ_{eq} is defined to be the number of sweeps for the value of an observable $A(t)$ to stabilize within one standard deviation of the mean $\langle A(t)\rangle$.

With equilibrium achieved, measurements on observables can be made. Statistical independence between successively sampled configurations is required to ensure measurements are unbiased. It is useful to calculate a decorrelation time τ_{decorr} that gives the number of Monte Carlo sweeps required for a statistically independent configuration to be generated. The time autocorrelation function is defined as

$$\begin{aligned} c(t) &= \langle (A_0 - \langle A_0\rangle)(A_t - \langle A_t\rangle)\rangle \\ &= \langle A_0 A_t\rangle - \langle A_t\rangle^2. \end{aligned} \tag{1.76}$$

If two configurations separated by t Monte Carlo sweeps are truly independent, $\langle A_0 A_t\rangle = \langle A_0\rangle\langle A_t\rangle = \langle A_0\rangle^2$ and the value of $c(t)$ is zero. Ergodicity must be preserved in a Monte Carlo simulation and so as $t \to \infty$, $c(t) \to 0$. The approach of $c(t)$ to zero is usually exponentially decaying such that, for large t

$$c(t) \sim \exp(-t/\tau_{\text{decorr}}), \tag{1.77}$$

where, by definition $c(0) = 1$. By subtracting $\log(c(0))$ from $\log(c(t))$, the decorrelation time τ_{decorr} can be computed as

$$\tau_{\text{decorr}} = -\left\langle \frac{t}{\log\left|\frac{c(t)}{c(0)}\right|} \right\rangle, \tag{1.78}$$

where the average is over all configurations in the ensemble [NB99]. From Eq. (1.78) it also

follows that

$$\begin{aligned}\int_0^\infty c(t) &= \int_0^\infty \mathrm{d}t c(0)\exp(-t/\tau_{\text{decorr}})\mathrm{d}t \\ &= \tau_{\text{decorr}} c(0). \end{aligned} \tag{1.79}$$

In a finite ensemble, the integral $\int_0^\infty c(t)\mathrm{d}t$ reduces to the discrete sum $\sum_{t=0} c(t)$ and so an alternative measure of the decorrelation time can be calculated as

$$\tau_{\text{decorr}} = \sum_{t=0} \frac{c(t)}{c(0)}. \tag{1.80}$$

To avoid confusion, this decorrelation time is referred to as the "integration" decorrelation time, whereas Eq. (1.78) is referred to as the "exponential" decorrelation time. Monte Carlo simulations typically generate a large ensemble of configurations and it is not desirable to save each one. The decorrelation times are usually calculated as the simulation is running and configurations are sampled at sweep intervals of τ_{decorr}.

Near the critical temperature T_C of a system, the equilibration and decorrelation times τ_{eq} and τ_{decorr} become very long and, in the thermodynamic limit, diverge to infinity. This divergence is known as "critical slowing" which greatly inhibits the applicability of a Monte Carlo method in numerical studies of systems close to their critical point. To describe how τ_{decorr} diverges as $T \to T_C$ it is useful assume the lattice is approximately isotropic such that the J_i are approximately equal and $N = L^d$, and to use the definition

$$\tau_{\text{decorr}} \sim \xi^z. \tag{1.81}$$

The quantity ξ is the correlation length, introduced in Section 1.1.2, which has the asymptotic form

$$\xi \sim \frac{1}{|T - T_C|}, \tag{1.82}$$

where $\xi \to \infty$ as $T \to T_C$. The exponent z of Eq. (1.81) is the so-called the "dynamic critical exponent" and is dependent on the Monte Carlo method and the system being studied. The value of z provides a useful measure of the efficiency of a Monte Carlo method, a lower value indicating a more efficient algorithm. The calculation of z follows from the observation that, although the correlation length $\xi \to \infty$ as $T \to T_C$, the maximum possible value for ξ in a finite system of N spins is L, the length of the system. By obtaining measurements of some observable $A(t)$, calculating Eq. (1.76) and substituting into Eq. (1.80) for simulations using different lattice sizes, the value of z can be determined by calculating the gradient of the plot $\log \tau_{\text{decorr}}$ vs. $\log L$.

1.3.3 Metropolis algorithm

The Metropolis algorithm, developed by Metropolis *et al.* [MRR+53] in 1951, is the first example of a Monte Carlo algorithm that uses the more efficient method of thermal "importance" sampling. Rather than randomly sampling configurations and weighting by appropriate Boltzmann weights, states of the system are sampled with a probability proportional to the Boltzmann weights and weighted evenly. Therefore, by using the Metropolis algorithm, an ensemble of configurations which approximate a system's overall probability distribution, for which random sampling might be too difficult or time-consuming, can be obtained. Metropolis *et al.* [MRR+53] initially specialized the algorithm to numerically calculate the equation of state for a system of rigid spheres in two dimensions. The algorithm was later extended to the general case by Hastings [Has70] in 1970, and remains the most widely used Monte Carlo algorithm today.

The Metropolis algorithm operates by choosing a new configuration C_ν and accepting or rejecting it according to the relevant acceptance probability. The Metropolis acceptance probability is given by

$$P^a(C_\mu \to C_\nu) = \min\left[\frac{W(C_\nu)}{W(C_\mu)}, 1\right], \tag{1.83}$$

which states that if the new configuration weight $W(C_\nu)$ is higher than $W(C_\mu)$ it is always accepted, but if it is lower it is accepted with probability equal to the ratio of new and old weights [Pes73]. If the configuration is accepted, the transition to C_ν is made. If the configuration is rejected, no transition is made and the Markov chain remains at C_μ. To implement the acceptance probability when $P^a(C_\mu \to C_\nu) < 1$, a random number $r \in [0, 1)$ can be used such that if $r < P^a(C_\mu \to C_\nu)$ then the new configuration is accepted. One application of the accept/reject procedure comprises one Monte Carlo step. This definition of the acceptance probability Eq. (1.83) can be shown to satisfy the detailed balance as follows. If $W(C_\nu) > W(C_\mu)$ then with the definition Eq. (1.83), Eq. (1.74) reduces to

$$\frac{P^a\left(C_\mu \to C_\nu\right)}{P^a\left(C_\nu \to C_\mu\right)} = 1 \times \left[\frac{1}{W(C_\mu)/W(C_\nu)}\right] = \frac{W(C_\nu)}{W(C_\mu)}. \tag{1.84}$$

If $W(C_\nu) < W(C_\mu)$, Eq. (1.74) becomes

$$\frac{P^a\left(C_\mu \to C_\nu\right)}{P^a\left(C_\nu \to C_\mu\right)} = \frac{W(C_\nu)}{W(C_\mu)} \times \frac{1}{1} = \frac{W(C_\nu)}{W(C_\mu)}, \tag{1.85}$$

showing that detailed balance is satisfied.

The Metropolis algorithm is easily specialized to simulate Ising systems. Updating a configuration corresponds to selecting a spin at random and flipping its orientation with probability given by Eq. (1.83). The two-dimensional ferromagnetic SL Ising model with the

Hamiltonian Eq. (1.29), for example, has a Boltzmann weight factor Eq. (1.70) given by

$$W(C_\mu) = \exp\left(\beta \sum_x \sum_y [J_1 s_{xy} s_{x+1,y} + J_2 s_{xy} s_{x,y+1}]\right). \tag{1.86}$$

A single spin flip of a randomly selected spin at site (x, y) gives a new configuration with a weight factor $W(C_\nu)$. The weight ratio of Eq. (1.83) becomes

$$\frac{W(C_\nu)}{W(C_\mu)} = \exp\left(2\beta s'_{xy}\left[J_1(s_{x-1,y} + s_{x+1,y}) + J_2(s_{x,y-1} + s_{x,y+1})\right]\right), \tag{1.87}$$

where $s'_{xy} = -s_{xy}$ is the new value after flipping. Implementing one Monte Carlo step reduces to flipping a randomly selected spin to produce a new configuration, calculating the ratio Eq. (1.87), then comparing it to a randomly generated number and accepting or rejecting the configuration, appropriately. The quantities $E_\nu - E_\mu$ and $P^a(E_\nu - E_\mu)$ are considered for a number spin-flip procedures in Fig. 1.14.

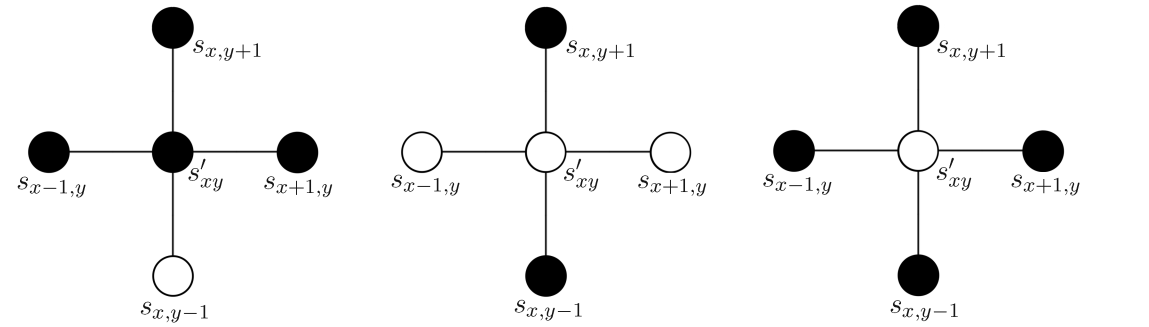

Figure 1.14 Several single Metropolis spin-flip procedures with (a) and (b), $P^a(E_\nu - E_\mu) = 1$ and (c), $P^a(E_\nu - E_\mu) < 1$.

A large configuration ensemble, and therefore a large number of Monte Carlo steps, is usually required to obtain precise averages of physical quantities measured on each configuration. Quantities of interest in Ising model simulations are the magnetization per spin,

$$\langle m \rangle = \frac{1}{MNQ} \sum_\mu^Q \sum_x^M \sum_y^N s^\mu_{xy}, \tag{1.88}$$

and the magnetic susceptibility,

$$\chi = \frac{1}{MNT}\left(\langle m^2 \rangle - \langle m \rangle^2\right), \tag{1.89}$$

where Q is the total number of configurations. Two-point correlations in spin orientations are calculated similarly, given by

$$\rho_{x0} = \frac{1}{Q}\frac{1}{\lfloor M/2 \rfloor}\frac{1}{\lfloor N/2 \rfloor}\sum_{\mu}^{Q}\sum_{j}^{\lfloor M/2 \rfloor}\sum_{k}^{\lfloor N/2 \rfloor} s_{jk}^{\mu} s_{j+x,k}^{\mu}, \tag{1.90}$$

where $\lfloor X/2 \rfloor$ denotes the value of $X/2$ rounded down to the nearest integer.

In simulations of the two-dimensional square Ising model, the Metropolis algorithm has a dynamic critical exponent of $z \simeq 2.1$ [SW87]. The correlation length on a lattice is restricted to $\xi \leq L$, so Eq. (1.81) for the Metropolis algorithm scales like $\tau_{\text{decorr}} \sim \xi^{2.1} \sim L^{2.1} \sim N$ for a two-dimensional lattice. Therefore, the number of Monte Carlo steps to generate a new configuration scales like $N\tau \sim N^2 = L^4$. If the lattice size increases by some factor $L \to aL$, the computation time increases as $t \to a^4 t$. At a given temperature, the choice of lattice size must be $L \sim 2\xi$ in order to avoid finite size effects, so implementing the Metropolis algorithm near the critical temperature can require extremely large computation times.

1.3.4 Swendsen-Wang algorithm

The obstacle of critical slowing motivated the development of a class of Monte Carlo algorithms known as cluster Monte Carlo. Numerous such algorithms exist [Wol89, PS01, Eve03] however the Swendsen-Wang algorithm [SW87] is of particular importance to the work in this thesis. The algorithm operates by simultaneously flipping large groups of contiguous spins, termed "clusters", rapidly evolving the lattice configuration. Decorrelation times measured from simulations of the two-dimensional square Ising model at critical temperature are shown in Fig. 1.15 for various lattice sizes implementing the Metropolis and Swendsen-Wang algorithms. Decorrelation times are significantly smaller for the Swendsen-Wang algorithm in comparison to the Metropolis algorithm, with the dynamic critical exponent of $z = 0.35$ for two-dimensional Ising model. As a result, critical slowing is significantly reduced.

A single Monte Carlo step of the Swendsen-Wang algorithm consists of two parts. For the first part, all nearest neighbour bonds are labelled "frozen". All spins on the lattice are then cycled through and "freeze" and "delete" decisions are made on the bonds. A bond is deleted with probability $P_d = 1$ if the parity of the connected spins does not satisfy the coupling criteria, i.e. like orientations for ferromagnetic coupling and opposing orientations for antiferromagentic coupling. A bond that satisfies the coupling criteria is frozen with probability $P_f = 1 - \exp(-2|J|/T)$ and deleted with probability $P_d = \exp(-2|J|/T)$. What remains is a segmented network of frozen bonds, as shown in Fig. 1.16 for a configuration of the two-dimensional Ising model with ferromagnetic bonds. Spins connected by frozen

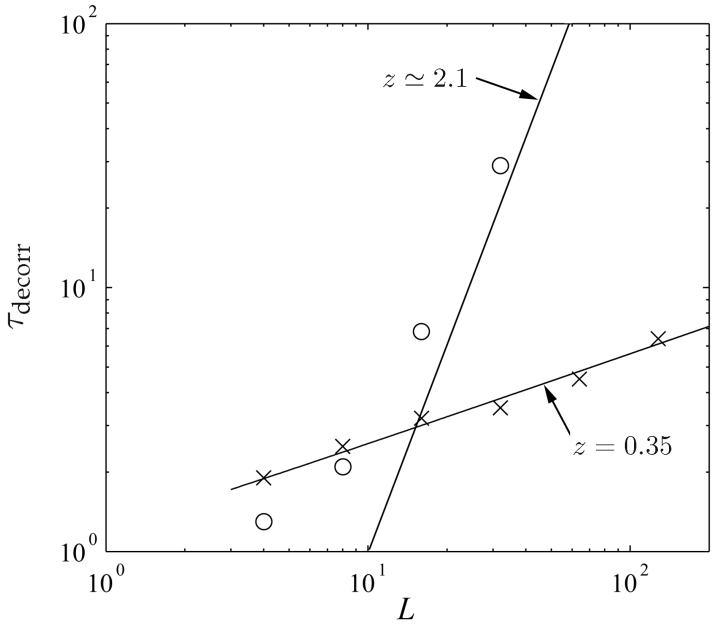

Figure 1.15 Correlation times τ_{decorr} of the SL Ising model at critical temperature for various L calculated using the Metropolis ($\circ$) and Swendsen-Wang ($\times$) algorithms [SW87].

bonds form a interconnected network of spins referred to as a "cluster". Clusters vary in mean size and number depending on the systems temperature and lattice size being simulated. Note that a single spin not connected to a larger cluster is itself considered a cluster so that every spin on the lattice is assigned to a cluster.

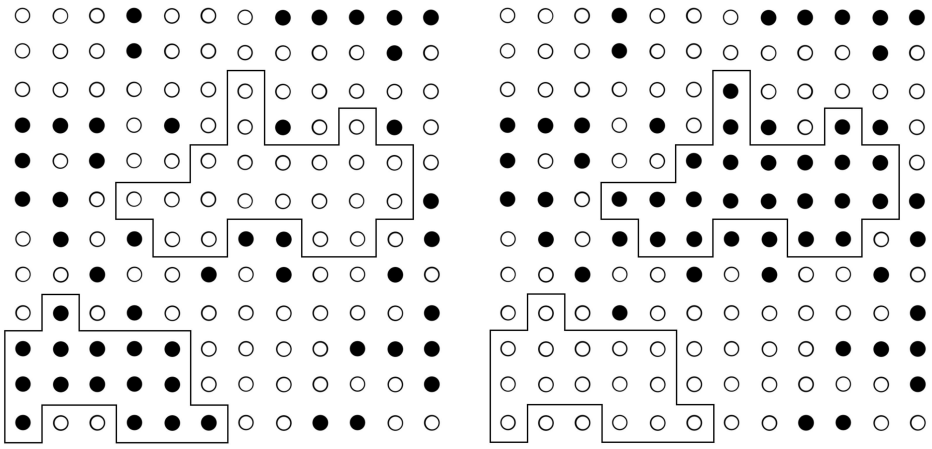

Figure 1.16 Flipping two clusters, outlined in (a), in Monte Carlo simulation of the SL Ising model using the Swendsen-Wang algorithm to produce the new configuration shown in (b). Black and white circles indicate up and down spins.

The second part of the Swendsen-Wang algorithm is to systematically subject each cluster to a "flipping" test. For each cluster a random variable $r \in [0, 1)$ is generated and compared

to the flipping probability P_{flip}. If $r < P_{\text{flip}}$ then the flipping criteria is satisfied for a cluster and all constituent spins are reversed. Typically, a value of $P_{\text{flip}} = 1/2$ is used, however this choice is arbitrary and is shown to satisfy the detailed balance below.

The Swendsen-Wang algorithm can be shown to be ergodic and satisfy the condition of detailed balance. The former can be realised by noticing that there is always a finite chance that no cluster networks will be formed. Subsequent flipping of the single spin clusters is equivalent to choosing a new state at random for the entire system, so in theory it is possible to go from one state to any other in one sweep. To show the Swendsen-Wang algorithm satisfies detailed balance, let the number of bonds deleted and frozen in updating a configuration be denoted n_d and n_f, respectively. The energy change after the update is then

$$E_\nu - E_\mu = 2|J|(n_d - n_f). \tag{1.91}$$

Similarly, if the reverse transition is performed the energy change is

$$E_\mu - E_\nu = 2|J|(n_f - n_d). \tag{1.92}$$

The transition probabilities for choosing a particular set of bonds differ between the update and the reverse transition only at the places where bonds are deleted or frozen. The ratio of transition probabilities between the two configurations is then

$$\frac{P(C_\mu \to C_\nu)}{P(C_\nu \to C_\mu)} = (1 - P_f)^{(n_d - n_f)}. \tag{1.93}$$

By choosing $P_f = 1 - \exp(-2\beta|J|)$ ensures that the transition probability is independent of n_d and n_f. Using this definition of P_f and Eq. (1.91), Eq. (1.93) becomes

$$\begin{aligned} \frac{P(C_\mu \to C_\nu)}{P(C_\nu \to C_\mu)} &= [1 - 1 + \exp(-2\beta|J|)]^{(n_d - n_f)} \\ &= \exp(-\beta[E_\nu - E_\mu]), \end{aligned} \tag{1.94}$$

which is exactly Eq. (1.74). Therefore any change, such as flipping all clusters with probability $1/2$, is the same for the update or reverse transition and detailed balance is satisfied.

1.4 X-ray crystallography

X-ray crystallography is a technique used to determine the relative spatial positions of the constituent atoms in a molecule [WHf95]. A crystalline specimen of the molecule is illuminated by an x-ray beam and the intensity of the radiation scattered in different directions is measured. These measurements are used to determine the atomic coordinates of the molecule. Various methods are used to do this depending on the kind of specimen. X-

ray crystallography can also be applied to partially crystalline materials (specimens). The primary effect of the disorder is on the diffracted x-ray intensities.

1.4.1 X-ray scattering

X-rays are electromagnetic waves in the $1 - 100$Å wavelength range of the electromagnetic spectrum [Gui63]. The wave nature of X-rays causes the shell electrons of the atoms of objects through which they pass to vibrate. Electronically charged particles such as electrons when accelerated (e.g. in a vibration) emit secondary radiation. This secondary emission is stimulated by the electric field component of the incident X-rays, and is therefore synchronous with it, having an identical wavelength to the incident X-rays. This type of coherent scattering is referred to as Thompson scattering and is the main contribution in X-ray diffraction. In laboratory experiments X-rays can be generated using a number of techniques such as sealed tube devices and synchrotrons [Cul78].

A laboratory sealed tube or rotating anode device involves accelerating electrons generated from a heated filament into anode atoms using a large potential difference, as illustrated in Fig. 1.17(a). Incoming electrons excite atomic electrons in the anode to higher atomic energy levels which emit radiation at characteristic X-ray wavelengths when transitioning back to lower energy levels. This process is very inefficient with $< 1\%$ of the input energy being converted to X-rays and the remainder in heat.

A synchrotron, shown in Fig. 1.17(b), consists of a ring of magnets used to constrain high-energy electrons in a circular path. The accelerated electrons emit radiation confined in the direction of the electrons motion. This type of radiation is termed *bremmstrahlung* (braking radiation) and consists of a wide spectrum of wavelengths including X-ray radiation confined to a narrow horizontal plane. This horizontal "fan" of radiation is divided up into "beam-lines" used to supply several experiments situated at different sites along the circular path. Along these beam-lines extra devices such as "wigglers" are inserted to give very bright sources optimized for particular wavelengths.

The high intensity, collimated, monochromatic X-ray beam irradiates the crystalline specimen and undergoes Thompson scattering, producing a diffraction pattern of periodic intensity peaks called "reflections". X-rays diffract in directions determined by the spacing of the scatterers within the crystalline specimen. Reflections are recorded as a function of scattering angle by a screen of photographic film, an area detector or a charged-coupled device (CCD). The specimen is rotated through a range of angles, and reflections recorded at each rotation.

X-ray crystallography is an important tool for molecular structure determination. Protein

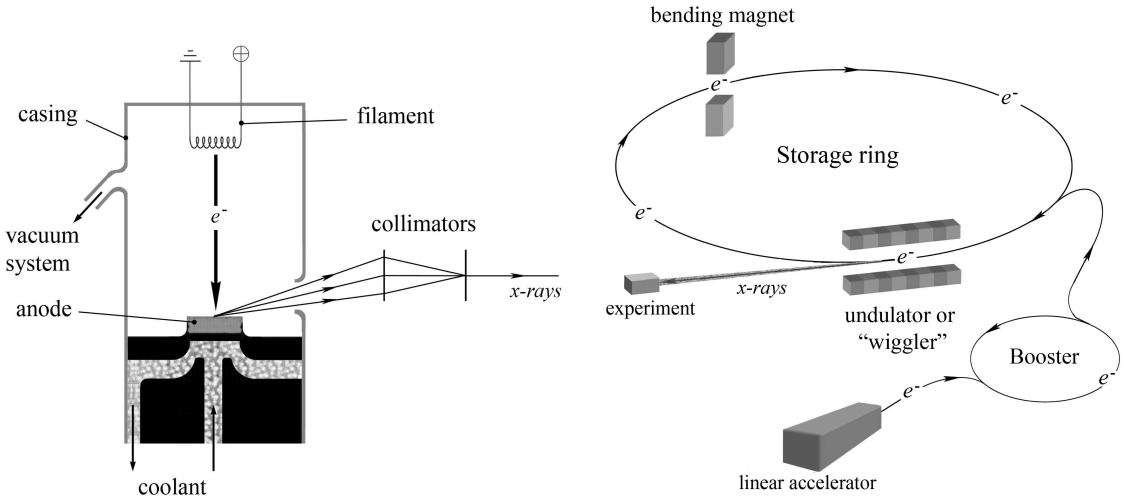

(a) (b)

Figure 1.17 X-ray sources used in X-ray diffraction experiments. (a) A sealed tube device and (b) a synchrotron.

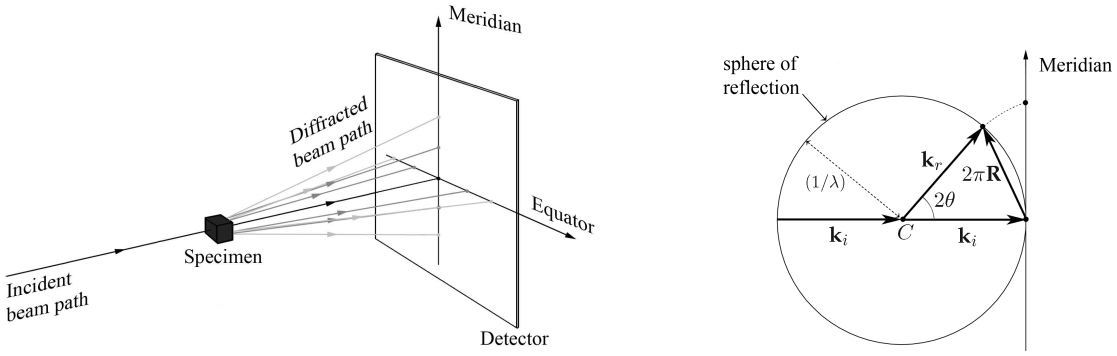

(a) (b)

Figure 1.18 (a) The experimental setup for an X-ray crystallography experiment, and (b) wavevectors $\mathbf{k}_i$ and $\mathbf{k}_r$ diffracting from a scattering point C at an angle 2θ.

crystallographers and material scientists have been able to make significant discoveries in their respective areas. As of the 21st September 2010 the Protein Data Bank (PDB) registers 68139 structures, 59072 ($\approx 87\%$) of which have been determined by X-ray diffraction, illustrating the importance of this technique for studying molecular structures.

1.4.2 Fourier analysis

The diffraction of X-rays from matter is conveniently described using Fourier analysis. In Fig. 1.18(b) a monochromatic collimated beam of incident X-rays scatters off a scattering centre C, e.g. an electron, at an angle 2θ to the incident direction. The incident and diffracted wavevectors are $\mathbf{k}_i = (2\pi/\lambda)\hat{\mathbf{r}}_i$ and $\mathbf{k}_r = (2\pi/\lambda)\hat{\mathbf{r}}_r$ where λ is the wavelength and $\hat{\mathbf{r}}_i$ and $\hat{\mathbf{r}}_r$ are unit vectors in the incident and diffraction directions, respectively. The scattering point C is displaced by the vector $\mathbf{r}$ from the origin O, and the phase of waves scattered at the origin is taken to be zero. The phase difference, $\Delta\phi$ between X-ray waves scattered at position C to those scattered at the origin is

$$\begin{aligned} \Delta\phi &= \mathbf{r}\cdot(\mathbf{k}_r - \mathbf{k}_i) \\ &= 2\pi\mathbf{R}\cdot\mathbf{r}, \end{aligned} \tag{1.95}$$

this being the definition of the "reciprocal space vector" $\mathbf{R} = (1/2\pi)(\mathbf{k}_r - \mathbf{k}_i)$. The amplitude of the incident wave is assumed to equal unity and the scattering amplitude from a point at the origin is

$$A(\mathbf{R}) = \exp(i2\pi\mathbf{R}\cdot\mathbf{r}). \tag{1.96}$$

The above analysis considers scattering from a stationary point. Electrons in an atom are in perpetual motion in a continuous electron "cloud" surrounding the atomic nucleus. The probability of finding an electron in the volume element $\mathrm{d}V$, $\rho_{\text{atom}}(\mathbf{r})\mathrm{d}V$, where $\rho_{\text{atom}}(\mathbf{r})$ is the electron density, about the nucleus centre is given by the absolute square of the continuous atomic wavefunction, $\Psi(\mathbf{r})\Psi^*(\mathbf{r})$. The atomic scattering factor $f_{\text{atom}}(\mathbf{R})$ is then scattering by the the atomic electron density, i.e.

$$f_{\text{atom}}(\mathbf{R}) = A_e \int \rho_{\text{atom}}(\mathbf{r}) \exp(-i2\pi\mathbf{R}\cdot\mathbf{r})\mathrm{d}\mathbf{r}. \tag{1.97}$$

The scattering amplitude from a single atomic electron is given by

$$A_e = \left[(7.90\times10^{-26})I_0\frac{1}{R^2}\frac{1+\cos^2 2\theta}{2}\right]^{1/2}, \tag{1.98}$$

where I_0 is the intensity of the incident beam. In general, the electron density of a free atom is assumed to have spherical symmetry and $f_{\text{atom}}(\mathbf{R})$ reduces to a function dependent only

on the magnitude $|\mathbf{R}|$.

Consider now a system of N scatterers (atoms) located at positions $\mathbf{r}_j$ with atomic scattering factors $f_j(\mathbf{R})$. The total scattering amplitude is the summation of the contributions by each scatterer, given by

$$A(\mathbf{R}) = \sum_{j=1}^{N} f_j(\mathbf{R}) \exp(i2\pi\mathbf{R}\cdot\mathbf{r}). \tag{1.99}$$

This can be generalized to give the scattering amplitude $A(\mathbf{R})$ from a continuous medium of scatterers so that

$$A(\mathbf{R}) = \int \rho(\mathbf{r}) \exp(i2\pi\mathbf{R}\cdot\mathbf{r})\mathrm{d}\mathbf{r}, \tag{1.100}$$

with the scattering density $\rho(\mathbf{r})$ describing the electron density at the point $\mathbf{r}$ in the medium. Eq. (1.100) states that the amplitude of the wave scattered from a continuous medium is given by the Fourier transform of the scattering density, denoted $\mathcal{F}[\rho(\mathbf{r})]$ [Bra78]. It follows that the scattering density is given by the inverse Fourier transform,

$$\begin{aligned} \rho(\mathbf{r}) &= \mathcal{F}^{-1}[A(\mathbf{R})] \\ &= \int A(\mathbf{R}) \exp(-i2\pi\mathbf{R}\cdot\mathbf{r})\mathrm{d}\mathbf{r}, \end{aligned} \tag{1.101}$$

which, in theory, can be reconstructed from the scattered amplitude.

1.4.3 Diffraction by a crystal

A crystal is a periodic structure and can be characterised by one period, referred to as the unit cell, with unit-cell vectors $(\mathbf{a}, \mathbf{b}, \mathbf{c})$ [Fig. 1.19(a)]. Within a reference unit cell, the position of the jth atom is given by

$$\mathbf{r}_j = x_j\mathbf{a} + y_j\mathbf{b} + z_j\mathbf{c}, \tag{1.102}$$

with $0 \leq x_j, y_j, z_j < 1$, referred to as the atomic "fractional coordinates". The group of atoms within the unit cell has an electron density denoted $\rho_{cell}(\mathbf{r})$. The electron density of an entire crystal is given by the convolution of the electron density in one unit cell of the crystal with an array of three-dimensional delta functions defining the crystal lattice $l(\mathbf{r})$ where

$$l(\mathbf{r}) = \sum_{m=0}^{N_1-1} \sum_{n=0}^{N_2-1} \sum_{p=0}^{N_3-1} \delta(\mathbf{r} - \mathbf{r}_{mnp}), \tag{1.103}$$

where $\delta(\mathbf{r})$ is the Dirac delta function,

$$\mathbf{r}_{mnp} = m\mathbf{a} + n\mathbf{b} + p\mathbf{c}, \tag{1.104}$$

$\{m, n, p\} \in \mathbb{Z}$ and $\{m, n, p\} = 0$ is defined as the origin. The quantities N_1, N_2 and N_3 give the number of unit cells in the **a**, **b** and **c** directions, respectively, of the crystal. For a real crystal N_1, N_2 and N_3 are extremely large. A crystal's electron density can then be written as

$$\rho(\mathbf{r}) = \rho_{cell}(\mathbf{r}) \otimes l(\mathbf{r}), \tag{1.105}$$

where $\otimes$ denotes convolution.

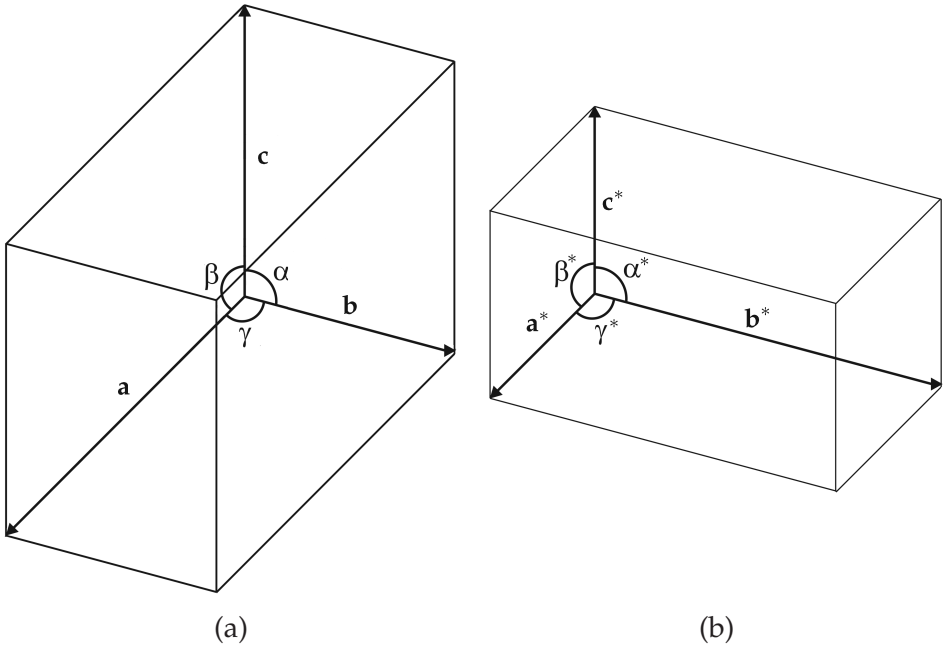

Figure 1.19 A unit cell in (a) real space, and (b) reciprocal space.

The convolution theorem of Fourier transforms states that the Fourier transform of the convolution of two functions is equal to the product of the Fourier transforms of the individual functions, i.e.

$$\mathcal{F}[f(x) \otimes g(x)] = \mathcal{F}[f(x)]\mathcal{F}[g(x)]. \tag{1.106}$$

It follows that the scattering amplitude from the crystal can be written as

$$A(\mathbf{R}) = F(\mathbf{R})L(\mathbf{R}), \tag{1.107}$$

where

$$F(\mathbf{R}) = \int \rho_{\text{cell}}(\mathbf{r}) \exp(i2\pi\mathbf{R} \cdot \mathbf{r}) \mathrm{d}\mathbf{r}, \tag{1.108}$$

is the scattering from a unit cell. The Fourier transform of Eq. (1.103), $L(\mathbf{R}) = \mathcal{F}[l(\mathbf{R})]$ gives

$$\begin{aligned} L(\mathbf{R}) &= \sum_{m=0}^{N_1-1}\sum_{n=0}^{N_2-1}\sum_{p=0}^{N_3-1}\exp(i2\pi\mathbf{R}\cdot\mathbf{r}_{mnp}) \\ &= \prod_{v=1}^{3}\sum_{w=0}^{N_v}\exp(i2\pi w\mathbf{R}\cdot\mathbf{u}_v) \\ &= \prod_{v=1}^{3}\left[\frac{1-\exp(i2\pi N_v\mathbf{R}\cdot\mathbf{u}_v)}{1-\exp(i2\pi\mathbf{R}\cdot\mathbf{u}_v)}\right] \\ &= \prod_{v=1}^{3}\left[\frac{\sin(\pi N_v\mathbf{R}\cdot\mathbf{u}_v)}{\sin(\pi\mathbf{R}\cdot\mathbf{u}_v)}\right]\exp(i\pi[N_v-1]\mathbf{R}\cdot\mathbf{u}_v), \end{aligned} \tag{1.109}$$

where $\mathbf{u}_1 = (m\mathbf{a}, 0, 0)$, $\mathbf{u}_2 = (0, n\mathbf{b}, 0)$ and $\mathbf{u}_3 = (0, 0, p\mathbf{c})$. As $N_v \to \infty$, the trigonometric ratio in Eq. (1.109) is non-zero only when the dot products satisfy

$$\mathbf{R}\cdot\mathbf{a} = h, \tag{1.110a}$$

$$\mathbf{R}\cdot\mathbf{b} = k, \tag{1.110b}$$

$$\mathbf{R}\cdot\mathbf{c} = l, \tag{1.110c}$$

with $h, k, l \in \mathbb{Z}$. The solution of this system of equations is given by

$$\mathbf{R}_{hkl} = h\mathbf{a}^* + k\mathbf{b}^* + l\mathbf{c}^*, \tag{1.111}$$

where

$$\mathbf{a}^* = \frac{\mathbf{b}\times\mathbf{c}}{V_{\text{cell}}}, \tag{1.112a}$$

$$\mathbf{b}^* = \frac{\mathbf{c}\times\mathbf{a}}{V_{\text{cell}}}, \tag{1.112b}$$

$$\mathbf{c}^* = \frac{\mathbf{a}\times\mathbf{b}}{V_{\text{cell}}}, \tag{1.112c}$$

are the unit vectors of Fourier or "reciprocal" space [Fig. 1.19(b)], with the unit cell volume $V_{\text{cell}} = |\mathbf{c}\cdot(\mathbf{a}\times\mathbf{b})|$. The Fourier transform of the lattice function $l(\mathbf{r})$ in the limit $N_v \to \infty$, denoted $L_\infty(\mathbf{R})$, then takes the form of another lattice

$$L_\infty(\mathbf{R}) = \sum_{h=0}^{\infty}\sum_{k=0}^{\infty}\sum_{l=0}^{\infty}\delta(\mathbf{R}-\mathbf{R}_{hkl}), \tag{1.113}$$

called the reciprocal lattice. With this definition Eq. (1.107) becomes

$$A(\mathbf{R}) = F(\mathbf{R})L_\infty(\mathbf{R}). \tag{1.114}$$

Eq. (1.114) shows that the diffracted amplitude for a large crystal is discrete and is the amplitude diffracted by one unit cell sampled at the reciprocal lattice sites $\mathbf{R}_{hkl}$. The complex diffraction amplitudes (sampled Fourier transform) are called the "structure factors" in crystallography and are denoted F_{hkl}, i.e. $F_{hkl} = F(\mathbf{R}_{hkl})$. The complex amplitude diffracted by an infinite crystal is then given by

$$A(\mathbf{R}) = \frac{1}{V_{\text{cell}}} \sum_h \sum_k \sum_l F_{hkl} \delta(\mathbf{R} - \mathbf{R}_{hkl}), \tag{1.115}$$

where, from Eq. (1.108),

$$F_{hkl} = \int \rho_{\text{cell}} \exp(i2\pi \mathbf{R}_{hkl} \cdot \mathbf{r}) \mathrm{d}\mathbf{r}. \tag{1.116}$$

Since $\rho(\mathbf{r})$ is periodic, it can be expressed by the Fourier series

$$\rho(\mathbf{r}) = \frac{1}{V_{\text{cell}}} \sum_h \sum_k \sum_l F_{hkl} \exp(i2\pi(hx + ky + lz)), \tag{1.117}$$

which, in principle, allows the electron density in the unit cell (from which the molecular structure can be inferred) to be reconstructed from the complex diffraction amplitudes F_{hkl}.

In x-ray diffraction experiments however it is the diffracted intensity $|F_{hkl}|^2$ that is measured and the phase information is lost. The phase of F_{hkl} therefore needs to be determined before Eq. (1.101) can be evaluated. This is referred to as the "phase problem" and has been extensively studied in the context of X-ray crystallography as well as other areas of imaging from measurements of diffracted radiation [Mil90, Dre94, MD01].

The indices (h, k, l), referred to as Miller indices [Bal71], identify points in the reciprocal lattice but also identify different sets of equally spaced parallel planes in the crystal lattice. Each set is characterised by the plane closest to the origin that passes through the points $(\mathbf{a}/h, 0, 0)$, $(0, \mathbf{b}/k, 0)$ and $(0, 0, \mathbf{c}/l)$. Points lying on the plane labelled (hkl) are spaced by a distance

$$\mathbf{d}_{hkl} = \frac{1}{|\mathbf{R}_{hkl}|}, \tag{1.118}$$

with the vector $\mathbf{R}_{hkl}$ perpendicular to this set of planes. Shown in Fig. 1.20 are the a selection of planes for the two dimensional triangular lattice.

Crystals in reality are of finite size and the external form of the crystal is conveniently described by the "shape function" $s(\mathbf{r})$ (rather than the number of unit cells N_1, N_2 and N_3 above), defined by

$$s(\mathbf{r}) \quad = \quad \begin{cases} 1, & r_{mnp} \in \Omega \\ 0, & r_{mnp} \notin \Omega, \end{cases} \tag{1.119}$$

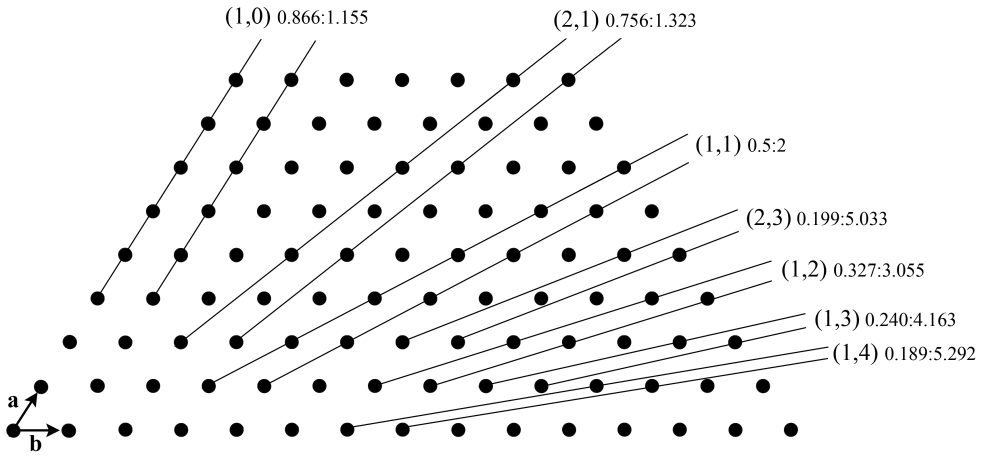

Figure 1.20 Miller planes on a triangular lattice $a = b = 1$ indicated by the indices (h, k) and the distances $d_{hkl} : R_{hkl}$ to 3.d.p.

where Ω is the set of all lattice sites within the crystal. The electron density of a real crystal, depicted in Fig. 1.21, can then be written in the form

$$\rho(\mathbf{r}) = [\rho_{cell}(\mathbf{r}) \otimes l(\mathbf{r})]s(\mathbf{r}). \tag{1.120}$$

The corresponding scattering amplitude is

$$A(\mathbf{R}) = [F(\mathbf{R})L_{\infty}(\mathbf{R})] \otimes S(\mathbf{R}), \tag{1.121}$$

where $S(\mathbf{R})$ is the Fourier transform of $s(\mathbf{r})$. The convolution of the diffraction by an infinite crystal Eq. (1.114) with $S(\mathbf{R})$ has the effect of blurring the sharp scattering amplitudes into small regions of Fourier space characterized by $S(\mathbf{R})$, i.e.

$$A(\mathbf{R}) = \frac{1}{V_{\text{cell}}} \sum_h \sum_k \sum_l F_{hkl} S(\mathbf{R} - \mathbf{R}_{hkl}). \tag{1.122}$$

1.4.4 Diffraction by disordered crystals

The variety of the forms of disorder discussed in Section 1.1.3 produce irregularities in a crystal. The effect of disorder in diffraction patterns is to introduce diffuse scattering intensity which generally needs to be accounted for before analysis of the diffraction can be performed. The scattering amplitude from a crystal with varying types of scatterers (each corresponding to $\rho_{\text{cell}}(\mathbf{r})$ above) perturbed off the crystal lattice can be written in the form

$$A(\mathbf{R}) = \sum_m \sum_n \sum_p s(\mathbf{r}_{mnp}) F_{mnp}(\mathbf{R}) \exp\left(i2\pi\mathbf{R} \cdot [\mathbf{r}_{mnp} + \mathbf{d}_{mnp}]\right), \tag{1.123}$$

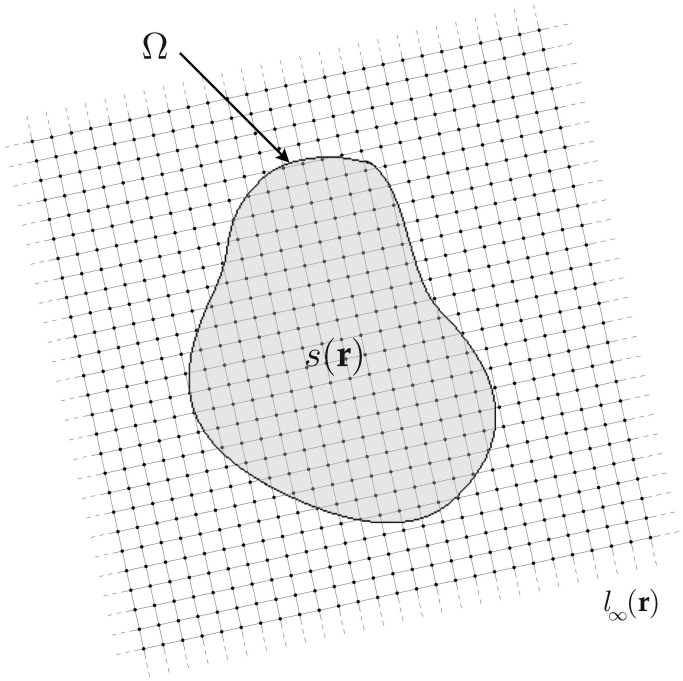

Figure 1.21 The shape function $s(\mathbf{r})$ defining the boundary of a real crystal on an infinite square lattice $l_\infty(\mathbf{r})$.

where the distortion vector $\mathbf{d}_{mnp}$ is the displacement of the scatterer at site (m, n, p) away from the lattice site $\mathbf{r}_{mnp}$ (lattice disorder) and $F_{mnp}(\mathbf{R})$ is now the scattering function of the scatterer at that site (substitution disorder).

The specimen is assumed to consist of many small crystallite domains (crystallites) defined by $s(\mathbf{r})$ that are randomly positioned. The scattering from each domain then adds incoherently and the measured intensity $I(\mathbf{R})$ is the ensemble average of the intensity over all disordered configurations of the scatterers [Str93], given by

$$\begin{aligned} I(\mathbf{R}) &= \left\langle \left| \sum_m \sum_n \sum_p s(\mathbf{r}_{mnp}) F_{mnp}(\mathbf{R}) \exp\left(i2\pi\mathbf{R}\cdot[\mathbf{r}_{mnp}+\mathbf{d}_{mnp}]\right)\right|^2 \right\rangle_d \\ &= \sum_m \sum_n \sum_p \sum_{m'} \sum_{n'} \sum_{p'} s(\mathbf{r}_{mnp}) s(\mathbf{r}_{m'n'p'}) \exp\left(i2\pi\mathbf{R}\cdot[\mathbf{r}_{mnp}-\mathbf{r}_{m'n'p'}]\right). \\ &\quad \times \left\langle F_{mnp}(\mathbf{R}) F^*_{m'n'p'}(\mathbf{R}) \exp\left(i2\pi\mathbf{R}\cdot[\mathbf{d}_{mnp}-\mathbf{d}_{m'n'p'}]\right)\right\rangle_d, \end{aligned} \tag{1.124}$$

where $\langle\ \ \rangle_d$ denotes the ensemble averaging. Typically the statistics of the perturbations are assumed to stationary and with the variable rescaling

$$\mathbf{r}_{mnp} = \mathbf{r}_{m'+m,n'+n,p'+p} - \mathbf{r}_{m',n',p'}, \tag{1.125}$$

the diffracted intensity in Eq. (1.124) simplifies to

$$\begin{aligned} I(\mathbf{R}) &= N \sum_m \sum_n \sum_p t(\mathbf{r}_{mnp}) \exp\left(i2\pi \mathbf{R} \cdot \mathbf{r}_{mnp}\right) \\ &\quad \times \left\langle F_{000}(\mathbf{R}) F^*_{mnp}(\mathbf{R}) \exp\left(i2\pi \mathbf{R} \cdot [\mathbf{d}_{mnp} - \mathbf{d}_{000}]\right)\right\rangle_d , \end{aligned} \tag{1.126}$$

where N is the number of sites in the crystallite, and

$$t(\mathbf{r}_{mnp}) = \frac{1}{N} \sum_{m'} \sum_{n'} \sum_{p'} s(\mathbf{r}_{m+m',n+n',p+p'}) s(\mathbf{r}_{m'n'p'}), \tag{1.127}$$

is the autocorrelation of the shape function.

1.5 X-ray Fibre diffraction

Fibre diffraction refers to crystallography applied to specimens of long slender molecules such as polymers that form fibre specimens as opposed to regular crystals. A polycrystalline fibre consists of crystallite domains, or crystallites, that aggregate parallel to the fibre axis. These domains are randomly positioned in the lateral plane and randomly rotated about the fibre axis, as shown by the transverse cross-section in Fig. 1.22. Each crystallite contains molecules that generally align with the crystallographic c-axis, which is aligned with the fibre axis, and the molecules are periodic in that direction with period c. Using cylindrical polar coordinates (r, ϕ, z) and (R, ψ, Z) in real and reciprocal space respectively, the intensity diffracted by an individual crystallite is denoted $I(\mathbf{R}) \equiv I(R, \psi, Z = l/c)$. The intensity $I_l(R)$ diffracted by the fibre is then the cylindrical average of the intensity diffracted by an individual crystallite [SM95], i.e.

$$I_l(R) = \frac{1}{2\pi} \int_0^{2\pi} I(R, \psi, l/c) \mathrm{d}\psi. \tag{1.128}$$

1.5.1 Diffraction by helical structures

The oriented, periodic molecules within a fibre specimen often adopt helical symmetry. Molecules lacking helical symmetry corresponding to a one-fold helix. A molecular helix can be characterized by two numbers, the number of repeating units (residues) u in one c-repeat and the number of turns v of the helix in one c-repeat. Such a helix is said to have u_v symmetry, with a 7_2 helix illustrated in Fig. 1.23. The projected distance between helical turns is called the pitch, P, so that $c = vP$. The repeating unit is a group of atoms from which the whole molecule can be generated by helix symmetry operations. Adjacent units

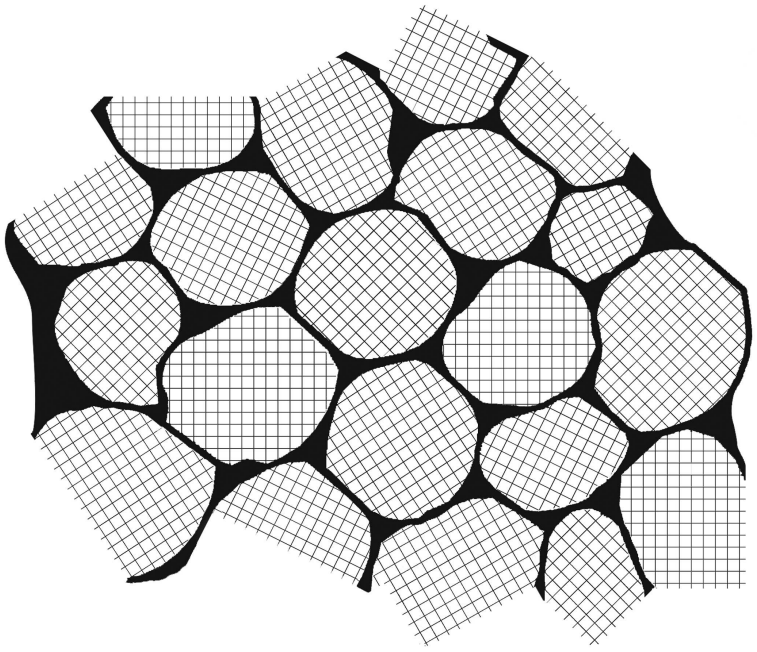

Figure 1.22 Cross-section of a polycrystalline fibre showing composite crystallites random in position, orientation and shape.

differ by a translation δz parallel to the fibre axis of

$$\delta z = \frac{c}{u}, \tag{1.129}$$

and a rotation $\delta\phi$ about the fibre axis of

$$\delta\phi = \frac{2\pi v}{u}. \tag{1.130}$$

It follows that the electron density $\rho(r, \phi, z)$ is a periodic function in ϕ and z and

$$\rho(r, \phi, z) = \rho(r, \phi + m\delta\phi, z + m\delta z), \tag{1.131}$$

where $m \in \mathbb{Z}$.

To calculate the diffracted amplitude from a molecular helix, denoted $F(\mathbf{R})$, first consider the diffracted amplitude from a continuous helix of pitch P, infinite length, radius r and infinitesimal thickness, shown in Fig. 1.24(a). With uniform electron density in the **z**-direction of unit magnitude and noting that the diffracted amplitude is non-zero only when $Z = n/P$ where $n \in \mathbb{Z}$, Eq. (1.100) can be written

$$F_{\text{helix}}(R, \psi, n/P)) = \int_0^P \exp(i2\pi\mathbf{R} \cdot \mathbf{r})\mathrm{d}z. \tag{1.132}$$

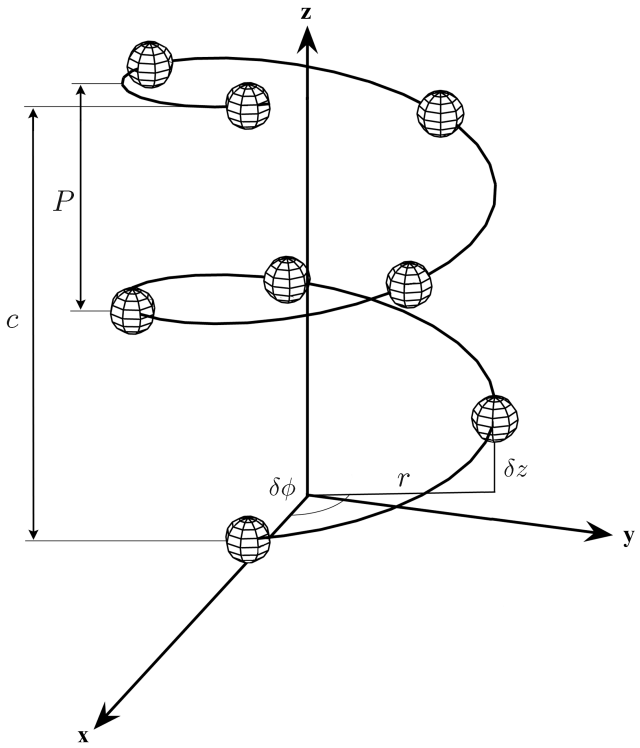

Figure 1.23 A single c-repeat of a helical structure with 7_2 symmetry. The c-repeat, pitch (P) and helical radius r are shown. Also shown are the axial and rotational shifts, δz and $\delta\phi$, between repeating units are also shown.

With Cartesian coordinates $\mathbf{r} = (r\cos\phi, r\sin\phi, z)$ and $\mathbf{R} = (R\cos\psi, R\sin\psi, Z)$, the dot product $\mathbf{R}\cdot\mathbf{r}$ reduces to

$$\begin{aligned}\mathbf{R}\cdot\mathbf{r} &= Rr\cos\psi\cos\phi + Rr\sin\psi\sin\phi + zn/P \\ &= Rr\cos(\phi-\psi) + zn/P. \end{aligned} \tag{1.133}$$

Inserting Eq. (1.133) into Eq. (1.132) and noting $\phi = 2\pi z/P$,

$$F_{\text{helix}}(R,\psi,n/P)) = \int_0^P \exp(i2\pi Rr\cos(2\pi z/P-\psi))\exp(i2\pi zn/P)\mathrm{d}z. \tag{1.134}$$

Multiplying both sides by $\exp(-in\psi)$ and using the definition of the n-th order Bessel function of the first kind [Bow38], gives

$$\begin{aligned}F_{\text{helix}}(R,\psi,n/P))\exp(-in\psi) &= \int_0^P \exp(i2\pi Rr\cos(2\pi z/P-\psi))\exp(in[2\pi z/P-\psi])\mathrm{d}z \\ &= \int_0^{2\pi}\exp(i2\pi r\cos\varphi)\exp(in\varphi)\mathrm{d}\varphi \\ &= i^n J_n(2\pi rR). \end{aligned} \tag{1.135}$$

Noting $i^n = \exp(in\pi/2)$, the diffracted amplitude of a continuous helix is then

$$F_{\text{helix}}(R,\psi,n/P) = J_n(2\pi Rr)\exp(in[\pi/2+\psi]). \tag{1.136}$$

The absolute amplitude $|F_{\text{helix}}(R,0,n/P)|$ is illustrated in Fig. 1.24(d). The diffraction pattern is non-zero only for $Z = n/P$, cylindrically symmetric i.e. independent of ψ, and described by Bessel functions of increasing order n. The Bessel function of order zero has a first maximum at $R = 0$, and higher order bessel functions have a first maximum that occurs at values of R which increase with n. The form of the diffracted amplitude is of a cross centered at the origin, referred to as the "helix cross pattern".

A helix of point scatterers is a set of points situated on a continuous helix, u points every v turns, with vertical spacing δz, as shown in Fig. 1.24(c). It can be represented by the product of the electron density of a continuous helix [Fig. 1.24(a)] with an infinite set of planes

$$H_\infty(\mathbf{r}) = \sum_{m=-\infty}^{\infty}\delta(z-m\delta z), \tag{1.137}$$

shown in Fig. 1.24(b). The Fourier transform is given, using the convolution theorem Eq. (1.106), so that the diffracted amplitude is

$$F(R,\psi,Z) = \mathcal{F}[\rho(\mathbf{r}).H_\infty(\mathbf{r})] = F_{\text{helix}}(R,\psi,n/P)\otimes\mathcal{F}[H_\infty(\mathbf{r})], \tag{1.138}$$

where $F_{\text{helix}}(R, \psi, n/P)$ is given by Eq. (1.136). The Fourier transform of Eq. (1.137) is

$$\mathcal{F}[H_\infty(\mathbf{r})] = \delta(R) \sum_{m=-\infty}^{\infty} \delta\left(z - \frac{m}{\delta z}\right), \tag{1.139}$$

i.e. a set of points spaced by $1/\delta z$ along the Z-axis shown in Fig. 1.24(e). The convolution Eq. (1.138) implies, using Eq. (1.129), that

$$F(R, \psi, Z) = \sum_{m=-\infty}^{\infty} F_{\text{helix}}\left(R, \psi, z + \frac{mu}{c}\right). \tag{1.140}$$

Since $F(R, \psi, Z)$ is non-zero only for $Z = l/c$ and $F_{\text{helix}}(R, \psi, Z)$ is non-zero only for $Z = n/P$, Eq. (1.140) implies that there is a non-zero diffracted amplitude only for $l/c = um/c + vn/c$, or that m and n can only have values that satisfy the condition

$$l = um + vn, \tag{1.141}$$

referred to as the "helix selection rule" [CCV52, Mil91]. The diffracted amplitude is given by

$$F(R, \psi, l/c) = \sum_{n=-\infty}^{\infty} F_{\text{helix}}(R, \psi, vn/c), \tag{1.142}$$

where the sum is over values of n that satisfy Eq. (1.141). The absolute diffracted amplitude $|F(R, 0, l/c)|$ is illustrated in Fig. 1.24(f). The diffraction pattern can be described as the summation of helix cross patterns centered at points $(0, 0, Z = um/c)$, where m is any integer.

The simplest helical molecule is one consisting of monatomic repeating units, assumed to have spherical symmetry. This can be described as the convolution of a single atom with a helix of points. From the convolution theorem, the diffracted amplitude is given by the product of Eq. (1.142) with the transform of the atom, the atomic scattering factor $f_0(|\mathbf{R}|)$, and using Eq. (1.136) gives

$$F(R, \psi, l/c) = f_0(|\mathbf{R}|) \sum_n J_n(2\pi R r_0) \exp(in[\pi/2 + \psi]). \tag{1.143}$$

A real helical molecule contains many atoms within a repeating unit. A helical molecule with a repeating unit consisting of s atoms can be considered as s helices of atoms with equivalent c-repeat and helical symmetry but with varying displacement coordinates (r_s, ϕ_s, z_s) from the origin and atomic scattering factors $f_s(|\mathbf{R}|)$. For these helices, the dot product of Eq. (1.133) is then modified such that

$$\mathbf{R} \cdot \mathbf{r}_s = R r_s \cos(\phi_s - \psi) + z_s l/c. \tag{1.144}$$

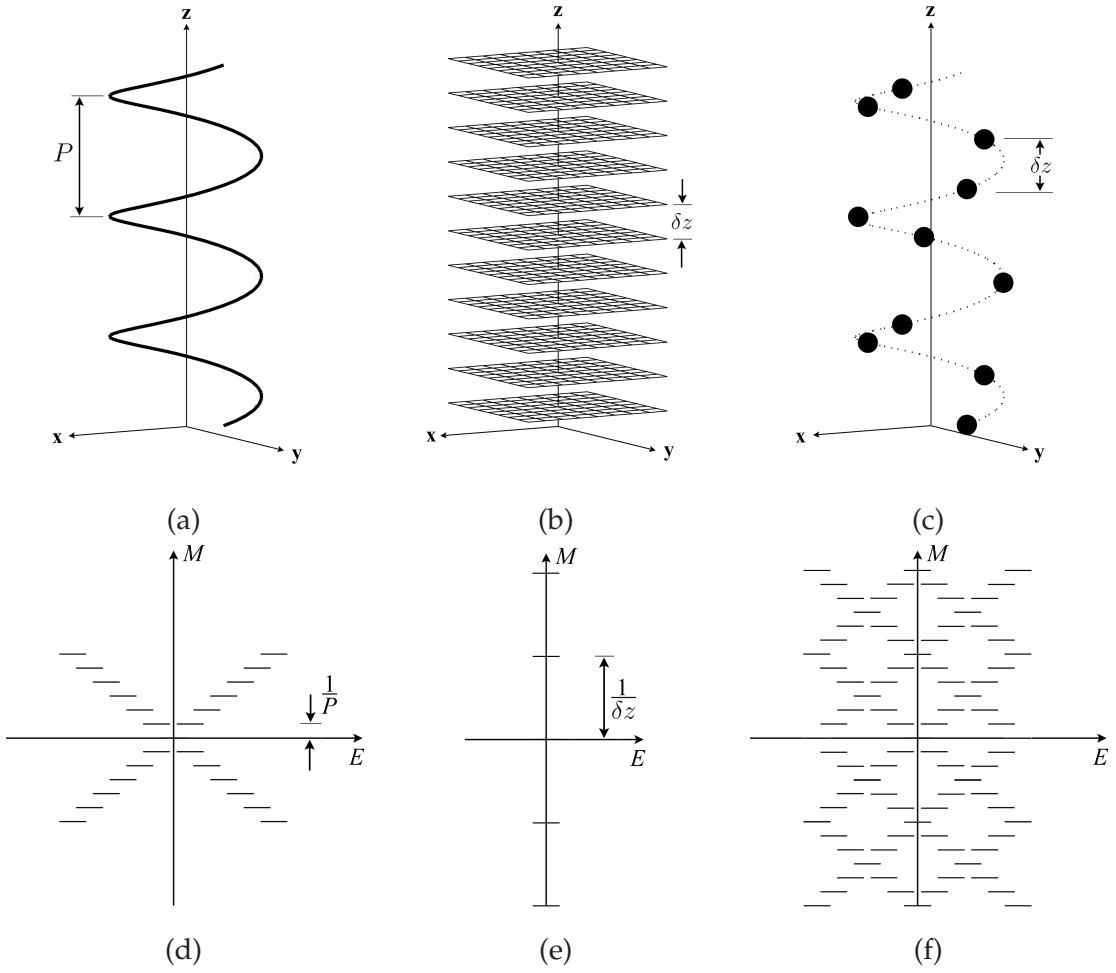

Figure 1.24 A discontinuous helix (c) can be represented as the product of the electron density of a continuous helix (a) with an infinite set of planes (b). The helical path is shown by a dotted line in (c). Using the convolution theorem, the diffracted amplitude of the discontinuous helix (f) is given by the convolution of the Fourier transform of the continuous helix (d) with the Fourier transform of the set of planes (e).

The total diffracted amplitude from a helical molecule is then given by

$$F(R,\psi,l/c)=\sum_n G_{nl}(R)\exp\left(in[\psi+\pi/2]\right), \tag{1.145}$$

where $G_{nl}(R)$ are the "Fourier-Bessel structure factors" defined by

$$G_{nl}(R)=\sum_s f_s(|\mathbf{R}|)J_n(2\pi Rr_s)\exp\left(i[(2\pi z_s l/c)-n\phi_s]\right). \tag{1.146}$$

Equations (1.145) and (1.146) then give the amplitude diffracted by a molecular helix. For a fibre made up of orientated, randomly positioned and randomly rotated helical molecules, the diffracted intensity is given by Eq. (1.128) and substituting Eq. (1.145) gives

$$I_l(R)=\sum_n |G_{nl}(R)|^2. \tag{1.147}$$

1.5.2 Polycrystalline fibres

The intensity diffracted by a crystallite is $I(\mathbf{R})=|A(\mathbf{R})|^2$, so that, using Eq. (1.122),

$$I(\mathbf{R})=\left|\frac{1}{V_{\text{cell}}}\sum_h\sum_k\sum_l F_{hkl}S(\mathbf{R}-\mathbf{R}_{hkl})\right|^2. \tag{1.148}$$

The shape function transform $S(\mathbf{R})$ is, in general, significant over a region that is small compared to the reciprocal lattice spacing so that Eq. (1.148) can be written

$$I(\mathbf{R})=\frac{1}{V_{\text{cell}}^2}\sum_h\sum_k\sum_l |F_{hkl}|^2|S(\mathbf{R}-\mathbf{R}_{hkl})|^2. \tag{1.149}$$

Substituting Eq. (1.149) into Eq. (1.128) shows that the intensity diffracted by a fibre is

$$I(R,Z)=\frac{1}{2\pi V_{\text{cell}}^2}\sum_h\sum_k\sum_l |F_{hkl}|^2\int_0^{2\pi}|S(\mathbf{R}-\mathbf{R}_{hkl})|^2\mathrm{d}\psi. \tag{1.150}$$

The cylindrically averaged intensity is therefore the sum of all reflections cylindrically projected onto the $\psi=0$ axis. As a consequence, some information from Eq. (1.149) is lost since independent reflections that lie at cylindrical radii differing by less than the half-widths of the reflections will record as a composite overlapping reflection. The symmetry of the crystallite lattice significantly affects the way in which reflections overlap.

The transform of the shape function $S(\mathbf{R})$ can be factorized as

$$S(\mathbf{R})=S_{\text{lat}}(R,\psi)S_{\text{axial}}(Z), \tag{1.151}$$

where $S_{\text{lat}}(R,\psi)$ is the transform of the shape function $s_{\text{lat}}(r,\phi)$ describing the cross-section of the crystallite in the plane perpendicular to the fibre axis and $S_{\text{axial}}(Z)$ is the transform of the shape function along the fibre axis. The intensity diffracted from a polycrystalline fibre can then be written as

$$I(R,Z) = \sum_l I_l(R)|S_{\text{axial}}(Z-l/c)|^2, \tag{1.152}$$

with the layer line intensities given by

$$I_l(R) = \frac{1}{2\pi V_{\text{cell}}^2}\sum_h\sum_k |F_{hkl}|^2 \int_0^{2\pi} |S_{\text{lat}}(R-R_{hk},\psi-\psi_{hk})|^2 \mathrm{d}\psi, \tag{1.153}$$

where $(R_{hk},\psi_{hk},l/c)$ are the coordinates of the reciprocal lattice point. Eq. (1.153) can be written in the from

$$I_l(R) = \frac{1}{V_{\text{cell}}^2}\sum_h\sum_k |F_{hkl}|^2 S_{\text{rad}}(R-R_{hk}), \tag{1.154}$$

where $S_{\text{rad}}(R)$ is the shape function of reflections in the radial direction.

1.5.3 Disordered fibres

If the individual crystallites in the fibre are disordered then the effects of the disorder described in Section 1.4.4 must be included before the cylindrical averaging, i.e. Eq. (1.128) is replaced by

$$I_l(R) = \frac{1}{2\pi}\int_0^{2\pi} \langle I(R,\psi,l/c)\rangle_d \, \mathrm{d}\psi. \tag{1.155}$$

The molecules in a fibre are generally considered rigid bodies so the disorder is limited to the lateral plane so that a single crystallite is characterized by the configuration of molecules in the lateral cross-section. Therefore, referring to Eqs. (1.126) and (1.127) the ensemble averaged intensity is given by

$$\begin{aligned}\langle I(\mathbf{R})\rangle_d &= \langle N\rangle \sum_h\sum_k t(\mathbf{r}_{hk}) \exp\left(i2\pi\mathbf{R}\cdot\mathbf{r}_{hk}\right) \\ &\quad \times \langle F_{00}(\mathbf{R})F_{hk}^*(\mathbf{R})\rangle_d \left\langle \exp\left(i2\pi\mathbf{R}\cdot[\mathbf{d}_{hk}-\mathbf{d}_{00}]\right)\right\rangle_d ,\end{aligned} \tag{1.156}$$

where $t(\mathbf{r}_{hk})$ is the normalised ($t(0)=1$) autocorrelation of the lateral shape function given by

$$t(\mathbf{r}_{hk}) = \sum_{h'}\sum_{k'} s_{\text{lat}}(\mathbf{r}_{h+h',k+k'}) s_{\text{lat}}(\mathbf{r}_{h'k'}), \tag{1.157}$$

and $\langle N\rangle$ is the average number of the lattice sites per crystallite [SM96a]. The intensity diffracted by a disordered polycrystalline fibre is then given by substituting Eq. (1.156) into Eq. (1.155).

1.5.4 Coherence length and disorientation

In a real fibre, the average length over which a helical molecule adopts a regular helix symmetry is restricted by disorder in the fibre. This finite length is referred to as the "coherence length" of the helical molecule, and is denoted l_c. The electron density of the fibre is the product of the electron density of an infinite molecule with the "axial" shape function, defined as

$$s_{\text{axial}}(z) = \begin{cases} 1, & |z| \leq l_c/2 \\ 0, & |z| > l_c/2. \end{cases} \tag{1.158}$$

For a polycrystalline fibre, the coherence length corresponds to the axial dimensions of the crystallites and the effect on the diffraction is through the layer line profile $S_{\text{axial}}(Z)$ as described in Section 1.5.3. For a range of crystallite dimensions in a specimen, the profile of a layer line can be approximated by [Stu74]

$$|S_{\text{axial}}(Z)|^2 \sim \exp(-\pi l_c^2 Z^2), \tag{1.159}$$

and Eq. (1.152) becomes

$$I(R, Z) = \sum_l I_l(R) \exp(-\pi l_c^2 [Z - l/c]^2). \tag{1.160}$$

This has the effect of broadening the layer-line intensities in the Z direction so that they have a finite width.

The molecular or crystallite axes in a real fibre are not perfectly aligned with the fibre axis, and are described by an orientation density function $N(\alpha)$ where α is the angle of inclination to the fibre axis. The form of $N(\alpha)$ is usually unknown, however the assumption that it has a Gaussian distribution generally provides a good match to measured profiles [HL74, Mak78]. With this assumption $N(\alpha)$ is written

$$N(\alpha) = \frac{1}{2\pi\alpha_0^2} \exp\left(-\frac{\alpha^2}{2\alpha_0^2}\right), \tag{1.161}$$

where α_0 is referred to as the "disorientation". With imperfect molecule orientation within a fibre, it is more convenient to write the diffracted intensity as function of spherical polar coordinates (ρ, ψ, σ) where σ is the angle to the meridian in the (R, Z)-plane. For small α_0, the diffracted intensity $I(\rho, \sigma)$ can be related to the diffracted intensity $I_p(\rho, \sigma)$, where perfect orientation is assumed, by [HL74]

$$I(\rho, \sigma) = \int_0^\pi I_p(\rho, \sigma') \exp\left(-\frac{[\sigma - \sigma']^2}{2\alpha_0^2}\right) i_0\left(\frac{\sin\sigma \sin\sigma'}{\alpha_0^2}\right) \sin\sigma' \mathrm{d}\sigma', \tag{1.162}$$

with the function $i_0(x)$ given by

$$i_0(x) = \exp(-x)K_0(x), \tag{1.163}$$

where $K_0(x)$ is the zeroth-order modified Bessel function of the second kind. With the assumption of a large coherence length l_c, Eq. (1.162) can be approximated by [HL74, Stu74]

$$I(\rho, \sigma) \simeq \sum_l \frac{I_l(R)}{\alpha_0 \rho \sqrt{2\pi}} \exp\left(-\frac{[\sigma - \sigma_l]^2}{2\alpha_0^2}\right), \tag{1.164}$$

where $\sigma_l = \cos^{-1}(l/(c\rho))$ is the polar angle at the centre of a layer line, i.e. $R = \rho \sin \sigma_l$. The effects of disorientation are assumed to dominate over those of a finite coherence length, with exception to along the meridian, so that Eq. (1.160) and Eq. (1.164) can be combined to give [MA86, MD01]

$$I(\rho, \sigma) \simeq \sum_l \frac{I_l(R)}{2\pi\alpha_0 l_c \rho} \exp\left(-\frac{[\sigma - \sigma_l]^2}{2\beta^2}\right), \tag{1.165}$$

where

$$\beta^2 = \alpha_0^2 + 1/(2\pi l_c^2 \rho^2 \sin^2 \sigma_l). \tag{1.166}$$

The effect of disorientation on a fibre diffraction pattern is to blur layer-line intensities along arcs centered at the origin of the diffraction pattern. This limits the resolution to which data can be collected since it introduces overlap between adjacent layer lines.

1.6 Vertebrate muscle

1.6.1 Muscle structure hierarchy

Vertebrate muscle is a hierarchical assembly of millions of basic contractile units called sarcomeres, illustrated in Fig. 1.25 [SAKKL05]. Muscle tissue is composed of parallel muscle fasciculi, each enclosed in a protective sheath of connective tissue called the epimysium [Fig. 1.25(a)]. Each muscle fasciculus is a bundle of thousands of muscle fibers ensheathed by a connective tissue called the endomysium [Fig. 1.25(b)]. In turn, each muscle fiber is a multinucleate cell composed of numerous cross-striated myofibrils [Fig. 1.25(c)]. Fibres typically vary between 50-100 μm in diameter, containing several hundred myofibrils that vary in cross-sectional size and shape. The outer membrane of the fiber is called the sarcolemma and spaces between myofibrils are filled by sarcoplasm [CP04]. Myofibrils are end-to-end arrangements of Sarcomeres [Fig. 1.25(d)], reaching lengths of up to $\sim$0.1 m in humans. Myofibril cross-sections measure from 2-5 μm across and consist of crystalline arrays of myosin filaments. Each myofibril is at a random orientation about the fibre axis

and is randomly positioned in the lateral plane.

A single sarcomere, illustrated in Fig. 1.26, consists of the region between successive Z-bands in the myofibril chain [SAKKL05]. A sarcomere is approximately 2.2 μm - 2.3 μm in length but this can vary significantly depending on whether the muscle is in a relaxed or contracted state. Each sarcomere consists of two principal types of contractile proteins, actin and myosin filaments. Myosin filaments in vertebrate muscle are 1.6 μm in length, ~ 15 nm in diameter and are arranged on a triangular array with a spacing of 45 nm [SLM90], with actin filaments interdigitated within the myosin array. Each myosin filament consists of approximately 250 myosin type II molecules, golf club shaped molecules that are two-chain, coiled-coil, α-helical rods measuring 150 nm in length and 2 nm in diameter. A globular head, referred to as the myosin subfragment-1 region [RHW$^+$93] or the myosin "head", is attached to the end of each chain as shown in Fig. 1.27(a). The globular head consists of a motor domain which contains the actin binding sites, and a lever arm which positions the motor domain along the actin filament [Hux57, Hux74]. Its three-dimensional structure has been determined using protein X-ray crystallography to a resolution of 0.28 nm, it has a molecular size of ~ 130 kD (1.3×10^5 atomic mass units), with 1157 identifiable residues (amino acids) [RHW$^+$93]. The myosin molecule rods of these molecules form the stem of the filament. The globular heads protrude from the stem and are arranged in a 3-stranded, 9_1 helix with an axial c-repeat of $c = 128.7$ nm [Squ72][Fig. 1.27(b)]. Actin filaments consist of a 2-stranded 13_7 helix of globular-α actin monomers and the regulatory proteins, troponin and tropomyosin [EEO69][Fig. 1.27(c)].

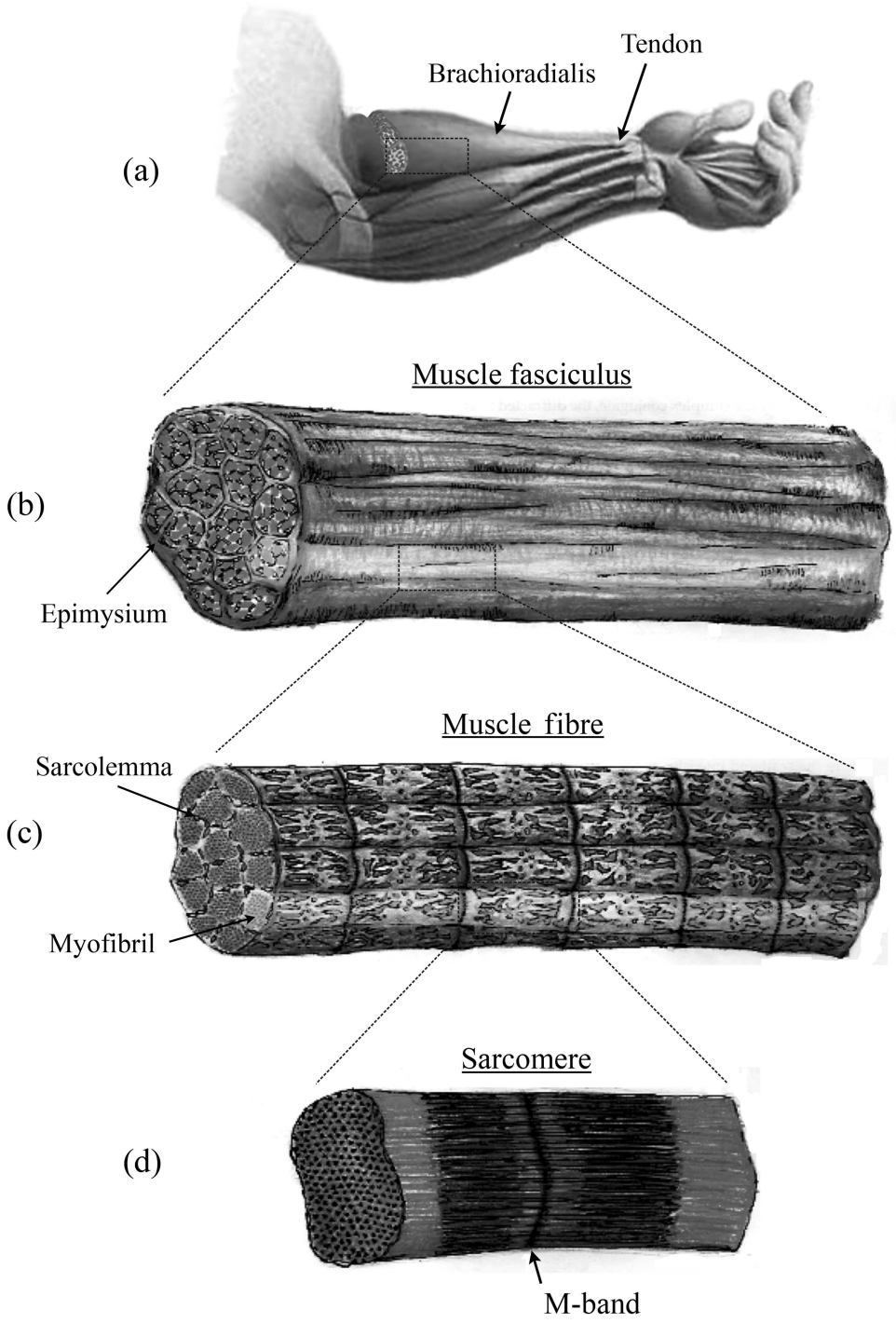

Figure 1.25 The hierarchical structure of muscle. The brachioradialis muscle is shown in (a) and, decreasing in scale, (b) muscle fasciculus, (c) muscle fibres of myofibrils and (d) muscle sarcomere. (Figure redrawn from [Yoo09]).

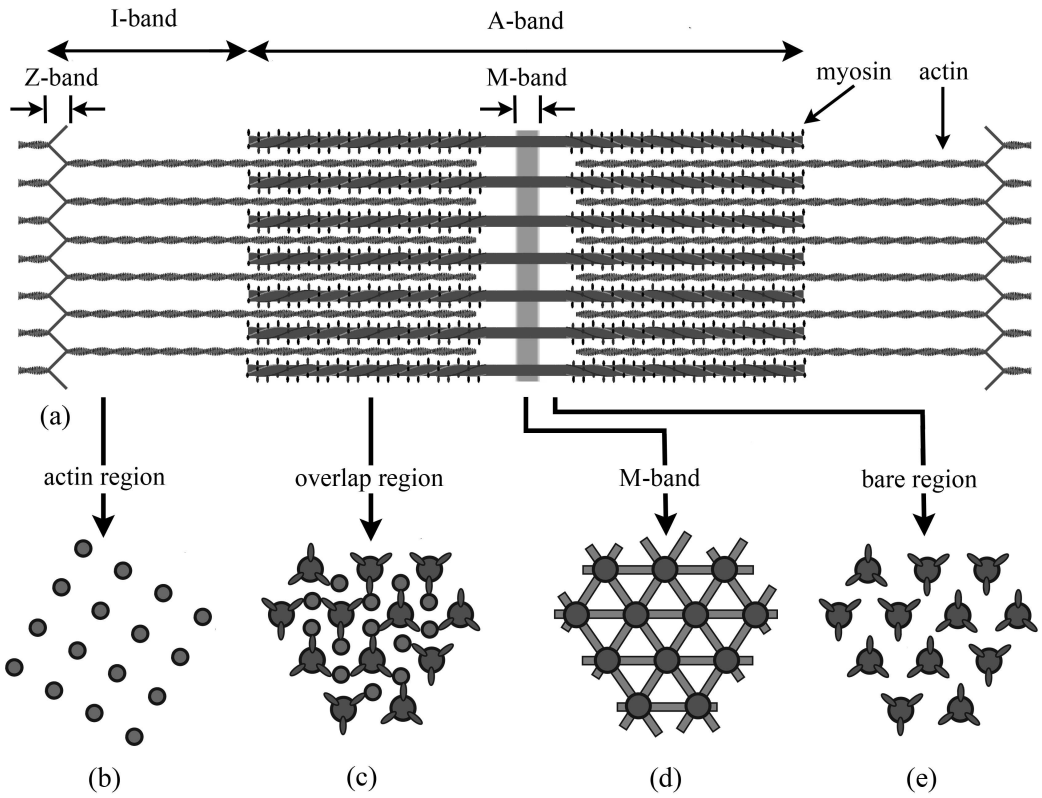

Figure 1.26 Diagram showing the muscle sarcomere structure. (a) A single sarcomere defined as the region between successive Z-bands with overlapping myosin and actin filaments, the cross-linking M-band and the bare region of the A-band shown schematically. Cross-sections through the sarcomere show (b) the square lattice of actin filaments in the I-band, (c) the overlap region of the A-band where the triangular myosin array is interdigitated by actin filaments, (d,e) the bare region of the A-band absent of myosin heads and actin filaments where (d) cross-linking between myosin filaments occurs in the M-band. (Figure redrawn from [SAKKL05]).

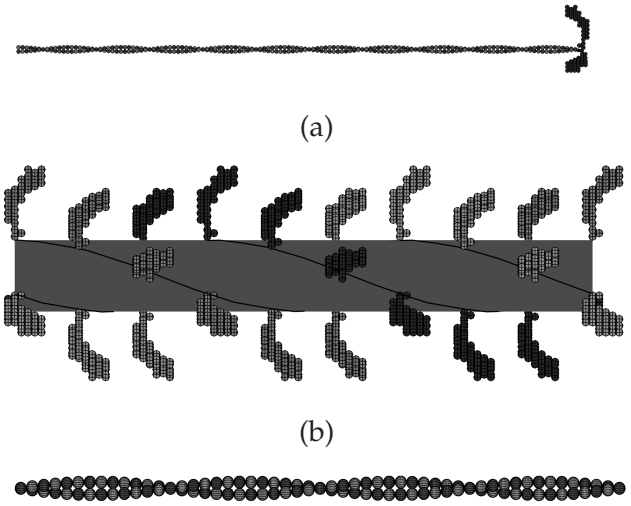

Figure 1.27 (a) The myosin II molecule with the rod and myosin heads. The contractile proteins (b) the myosin filament and (c) the actin filament, where only one myosin head per pair is shown for clarity in (b).

1.6.2 Contraction

At rest, myosin heads are not bound to actin filaments. During contraction, myosin heads attach to actin binding sites, forming the acto-S1 rigor complex [HAK$^+$03]. A contraction is activated within a muscle fiber when the brain delivers an impulse in the form of a nerve action potential via an attached nerve axon (or motor neuron). A single nerve axon stems from a larger nerve network, referred to as a motor unit, which stimulates a number of muscle fibers not necessary adjacent to one another. This action potential depolarizes the outer fiber membrane, the sarcolemma. The sarcomere envelopes the muscle fiber with periodic transverse tubules, or T-tubules, invaginating the inner fiber region. The action potential travels into these T-tubules and is distributed to other regions of the terminal cisternae (TC) regions of the sarcolemma. Depolarization of the TC region causes the sarcoplasmic reticulum (SR) to release calcium Ca^{2+} ions into local myofibrils. The sequestered Ca^{2+} ions in a myofibril interact with the regulatory protein called troponin. Each troponin protein complex is associated with a single tropomyosin filament, a two-stranded, coiled-coil, α-helical rod that runs along an actin chain. The absorbtion of Ca^{2+} ions initiates a conformational change in the troponin-tropomyosin assembly, exposing the actin binding sites and allowing the attachment-detachment process of the myosin heads to actin [GH05]. A sarcomere in the contracted and relaxed states are shown in Fig. 1.28(a) and (b), respectively.

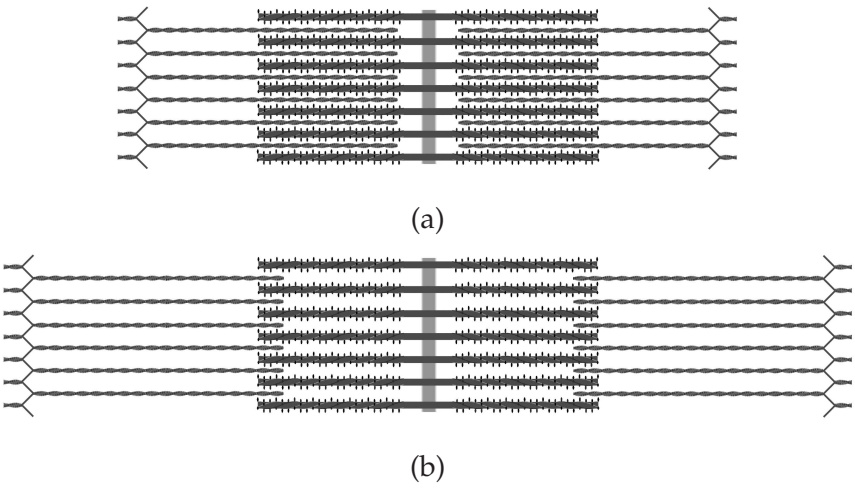

(a)

(b)

Figure 1.28 The muscle sarcomere in (a) the contracted and (b) relaxed states. (Figure redrawn from [HS97]).

1.6.3 Muscle imaging techniques

The dimensions of the repeating units and the c-repeats of myosin and actin filaments are such that imaging techniques require spatial resolutions of 1-50 nm for structural studies. Structural and molecular events that generate the muscular contraction force occur in time intervals of milliseconds or less. Studies of the molecular events that occur in muscular contraction require time resolutions of this order. Two imaging techniques with appropriate spatial resolution are electron microscopy and x-ray crystallography [WH81, HS97]. Both techniques have been used to make important discoveries in determining the structure of the muscle fibre, and both have their own advantages.

The key advantage of electron microscopy is that actual images are obtained, as opposed to diffraction patterns that require interpretation. Electron microscopy of a specimen is performed in a vacuum so that, in order to withstand the vacuum, the specimen has to be fixed by chemical fixation, embedding in resin or cryogenic freezing [Har90, SSL$^+$91]. The fixation procedure eliminates the possibility of time-resolved studies and can introduce undesired artifacts, and radiation damage from the electron beam can affect the specimen. An obvious concern then is whether the recorded images represent the native structure of the specimen. Despite these drawbacks, electron microscopy has proved a valuable technique. Electron micrographs of thin transverse sections show the myosin filaments packing [LS80, LSF96], and "tilt series" micrographs can be used to produce low resolution (~ 1.5 nm) three-dimensional images [HAK$^+$03].

One main advantage of X-ray diffraction lies in fast time-resolved studies of intact living tissue. X-ray diffraction can be used to study the structural state of the myosin filaments in the relaxed and contracted states. The resolution of X-ray diffraction is potentially higher

than that of electron microscopy, extending down to 1 nm and beyond [HDM$^+$96], but it requires interpretation of the diffraction data. Furthermore, the myofibrils are randomly rotated in the transverse plane so that methods of fibre diffraction must be used, requiring modelling of the molecular system. In addition, inherent disorder in the myosin filament packing further complicates the interpretation of the diffraction data. Characterisation of this disorder and its effect on X-ray fibre diffraction patterns is the topic of this thesis. X-ray diffraction has also been used for high resolution structural studies of the head portion, or subfragment-1, of the myosin type II molecule using single crystal X-ray diffraction [RHW$^+$93]

1.6.4 The myosin superlattice

X-ray fibre diffraction studies of teleost, primitive and some cartilaginous fish muscle show reflections from the hexagonal array of the myosin filaments [LSF96, SAKKL05]. Many X-ray diffraction studies of living muscle specimens use frog muscle due to the similarity in the arrangement of contractile proteins to that found in higher vertebrate muscle of other reptiles, mammals, birds and some species of cartilaginous fish [LSF96]. Thus, studies of frog muscle are motivated by their direct relevance to the determination of human muscle structure and function. Initial studies of X-ray fibre diffraction patterns from frog sartorius muscle, a long muscle that runs down the length of the thigh of vertebrate, showed, as well as reflections from the hexagonal array, the presence of additional reflections accompanied by diffuse scattering [HB67]. These reflections appear periodic, leading Huxley and Brown to conjecture the existence of a larger scale periodicity within the myosin array.

Myosin filaments in craniate skeletal muscle are now known to be arranged on a hexagonal array in two basic ways within the A-band, the simple-lattice [LMS81] and superlattice arrangements [LS80, LSF96]. For the simple-lattice arrangement there is one orientation of the myosin filament in the unit cell shown by the dashed line in Fig. 1.29(a). For the superlattice arrangement the myosin filaments can adopt one of two rotations in the unit cell. Filaments of like rotation tend to occur at the vertices of superlattice lattice cells with a spacing $\sqrt{3}$ times larger than the lattice unit cell as shown by the dashed line in Fig. 1.29(b). The effects of myosin superlattice disorder were categorized by Luther and Squire [LMS81] by studying electron micrographs of transverse sections. The ordering of filament orientations was observed to generally satisfy two rules; three filaments on a triangular plaquette usually do not all have the same orientation (rule 1) and three adjacent filaments along a row do not all have the same orientation (rule 2). These rules, referred to as the "no-three-alike" rules, are obeyed semi-systematically across the myosin array and are related to the formation of the superlattices. Is is expected that this disorder is related to the nature of the myosin head-actin interactions in the overlap region, and hence has implications for the mechanism of muscle contraction. It has been proposed that the superlattice structure

leads to an efficient sharing of actin binding sites by myosin heads [LS80, LSF96].

Methods for automated analysis of electron micrographs have recently been developed [YBK$^+$09], allowing Yoon [Yoo09] to estimate the frequencies of rule violations in frog sartorius muscle. By considering every set of 3 filaments, referred to as "cliques", that each rule can be assessed on, rule 1 was violated 5% of the time and rule 2 was violated 9% of the time. Frequencies of 25% for both rule violations are obtained for a random system. Based on a number of similarities between the disordered myosin lattice and the TIA, Yoon [Yoo09] characterized the disorder in terms of the statistics of the TIA. The automated analysis program also allowed for efficient calculation of two-point correlations from electron micrographs. Measured correlations were compared to values from the asymptotic expression Eq. (1.48) over a range of temperatures. Good agreement was obtained at a temperature of $T_{\text{eff}} = 1.1$ [Yoo09], where T_{eff} denotes the effective TIA temperature of the myosin lattice.

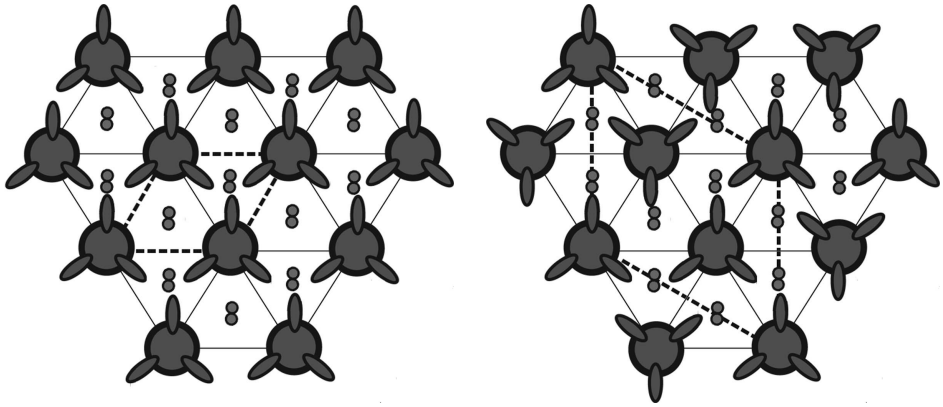

(a) (b)

Figure 1.29 The (a) simple lattice and (b) superlattice myosin filament arrangements. Unit cells of each arrangement are identified by the dashed lines. (Figure redrawn from [SAKKL05]).

Chapter 2

The two-point correlation function for the triangular Ising antiferromagnet

2.1 Introduction

The classical triangular Ising antiferromagnet (TIA), introduced in Section 1.2.4, is of considerable interest as it is an archetypical geometrically frustrated system. Geometric frustration inhibits the organization and cooperative properties of a system. The correlation behavior of the TIA provides a basic description of its cooperative properties, and an accurate description of the correlation function is useful in some applications. The few exact results available and the existing on-axis approximations were reviewed in Section 1.2.4. Despite considerable study however, a number of aspects of the correlation function of the TIA, including convenient and accurate computation, are poorly understood.

For on-axis pairs of sites and at zero temperature, the elements of the Toeplitz determinant are easily evaluated to give Eq. (1.45) and accurate approximations to the determinant have been developed [Ste64], given by Eqs. (1.46) and (1.47). For non-zero temperatures, the elements of the determinant are not easily evaluated, and although asymptotic expansions have been developed, their precision has not been investigated. At zero temperature the on-axis correlation function can be partitioned into three sublattices with smoothly varying dependence on separation in each. To leading order, the correlation functions on two of the sublattices become degenerate. For non-zero temperature, the leading order degenerate behaviour is evident only for sufficiently small temperatures. The higher order non-degenerate behaviour, although certainly present, has not been shown to follow from the asymptotic expansions.

For pairs of sites not on a lattice axis, much less is known rigourously. Adapting the Pfaffian technique to the calculation of off-axis correlations has proven to be a non-trivial task, as foreseen by Montroll et al. [MPW63]. Even so, asymptotic information has been obtained for the square Ising model [CW67]. Alternative approaches to calculating correlations have been developed for the square Ising model, most utilizing connections between statistical physics and quantum field theory [WMTB76, DD83, Ple88]. However, little progress has been made in adapting these methods to the triangular lattice. Results for the triangular solid-on-solid (SOS) model [NHB84] and structure factor calculations [JF97] indicate that the correlation function is rotationally invariant to leading order and for sufficiently small temperatures. (This is in contrast to, for example, the brick lattice for which the correlations are anisotropic [YNS86].) These results only address the leading order degenerate sublattice case however. There are no results for the off-axis correlation function at higher order that are necessary to accurately describe correlation coefficients for small separations. Furthermore, there are no results for off-axis correlations at higher temperatures.

In this chapter, some of the shortcomings in current knowledge of the correlation function for the TIA are addressed. This is achieved through a combination of known exact results for the on-axis case at $T = 0$, numerical integration of known analytic expressions at finite temperature, and through Monte Carlo simulation for off-axis separations. In Section 2.2 the precision of existing approximations for the on-axis case at zero and finite temperatures is evaluated. The off-axis case is examined in some detail in Section 2.3. It is noted that the sublattice description that has been employed to partition the correlation function at leading order is not suitable for a higher order description of the correlation function. Rotational invariance is studied and evaluated as a function of temperature. The region of separation-temperature space in which correlations are significant is identified in Section 2.4, and expressions are developed that allow accurate calculation of correlation coefficients within this region. Concluding remarks are made in Section 2.5.

2.2 On-axis correlation function

The anisotropic TIA with nearest-neighbor interactions is defined by Eq. (1.35). In this chapter, isotropy in the lattice bonds is assumed such that all antiferromagnetic bond strengths J_i are equal. Each spin then interacts with each of its 6 nearest-neighbours with equal bond strengths and bond energies minimized such that unlike nearest-neighbours are preferred. The Hamiltonian Eq. (1.35) can then be written

$$H = -J \sum_x \sum_y \left(s_{xy} s_{x+1,y} + s_{xy} s_{x,y+1} + s_{xy} s_{x+1,y+1} \right). \tag{2.1}$$

Throughout this chapter the rescaled temperature parameter Eq. (1.9) is used.

2.2.1 Numerical integration

The on-axis correlation coefficients for $T > 0$ were calculated by writing Eq. (A.35) in real form for the purposes of numerical integration and evaluating the determinant Eq. (A.34). Eq. (1.42) can be written in the form

$$\begin{aligned}\varphi(\omega) &= \left[\frac{A(\omega)}{A^*(\omega)}\right]^{1/2} \\ &= \left[\frac{A^2(\omega)}{A^*(\omega)A(\omega)}\right]^{1/2} \\ &= \frac{A(\omega)}{|A(\omega)|},\end{aligned} \tag{2.2}$$

where

$$A(\omega) = a - b\exp(i\omega) - c\exp(-i\omega), \tag{2.3}$$

with the coefficients a, b and c defined by Eq. (1.43). Substituting the form Eq. (2.2) into Eq. (A.35) gives

$$a_n = \frac{1}{2\pi}\int_0^{\pi}\exp(-in\omega)\frac{A(\omega)}{|A(\omega)|}\mathrm{d}\omega + \frac{1}{2\pi}\int_{-\pi}^{0}\exp(-in\omega)\frac{A(\omega)}{|A(\omega)|}\mathrm{d}\omega. \tag{2.4}$$

Substituting $\omega \to -\omega'$ in the second integral in Eq. (2.4) gives

$$\frac{1}{2\pi}\int_{-\pi}^{0}\exp(in\omega')\frac{A(-\omega')}{|A(-\omega')|}(-\mathrm{d}\omega') = \frac{1}{2\pi}\int_0^{\pi}\exp(in\omega')\frac{A^*(\omega')}{|A(\omega')|}\mathrm{d}\omega', \tag{2.5}$$

where $A(\omega) = A^*(-\omega)$ and $|A(\omega)| = |A(-\omega)|$ have been used. Relabelling $\omega' \to \omega$, Eq. (2.4) becomes

$$\begin{aligned}a_n &= \frac{1}{2\pi}\int_0^{\pi}\frac{\exp(-in\omega)A(\omega) + \exp(in\omega)A^*(\omega)}{|A(\omega)|}\mathrm{d}\omega \\ &= \frac{1}{2\pi}\int_0^{\pi}\frac{\cos(n\omega)\left[A^*(\omega) + A(\omega)\right] + i\sin(n\omega)\left[A^*(\omega) - A(\omega)\right]}{|A(\omega)|}\mathrm{d}\omega \\ &= \frac{1}{\pi}\int_0^{\pi}\frac{\cos(n\omega)\Re[A(\omega)] + \sin(n\omega)\Im[A(\omega)]}{|A(\omega)|}d\omega,\end{aligned} \tag{2.6}$$

taking a real form.

In the case of the TIA, $A(\omega)$ is given by Eq. (2.3), such that

$$\Re[A(\omega)] = a - b\cos(\omega) - c\cos(\omega), \tag{2.7a}$$

$$\Im[A(\omega)] = -b\cos(\omega) + c\cos(\omega), \tag{2.7b}$$

$$|A(\omega)| = [a^2 + b^2 + c^2 - 2ab\cos\omega - 2ac\cos\omega + 2bc\cos(2\omega)]^{1/2}. \tag{2.7c}$$

Substituting these quantities into Eq. (2.6) gives

$$a_n = \frac{1}{\pi}\int_0^\pi \frac{\cos(n\omega)(a - b\cos\omega - c\cos\omega) + \sin(n\omega)(-b\sin\omega + c\sin\omega)}{[a^2 + b^2 + c^2 - 2ab\cos\omega - 2ac\cos\omega + 2bc\cos(2\omega)]^{1/2}} d\omega, \tag{2.8}$$

which is straight forward to integrate numerically. Note that for $n = 1$, Eq. (2.8) can be evaluated in terms of complete elliptic integrals [Cho84], although the resulting expression is not convenient for numerical evaluation.

Numerical integration was performed using an adaptive Gauss-Lobatto quadrature algorithm described in Ref. [GG00]. Adaptive quadrature evaluates the definite integral of interest using two different methods. If the difference in the two values is within an imposed tolerance, the values are accepted. If the tolerance is not satisfied, the interval is subdivided, and the integration procedure is repeated over each subdivided interval. This is repeated recursively until the tolerance is satisfied, or the algorithm fails to achieve the imposed tolerance after a set number of iterations. The Gauss-Lobatto quadrature approximates the integral on the interval [a,b] by

$$\int_a^b f(x)dx \approx \frac{h}{6}\left\{f(a) + f(b) + 5[f(m - \beta h) + f(m + \beta h)]\right\}, \tag{2.9}$$

where $h = (b - a)/2$, $h = (a + b)/2$ and $\beta = (1/5)^{-1/2}$. In an adaptive implementation of this quadrature method, a Kronrod extension of Eq. (2.9) is constructed to estimate the relative error which is then compared to a required tolerance [GG00]. If the tolerance is not satisfied, the interval is divided into two and the two respective integrals are computed individually. This process is repeated until the tolerance is satisfied. Calculations were repeated using various tolerance values and the results showed that the error tolerance value of 1×10^{-6} is sufficient. For a good review on adaptive quadrature algorithms in general, and the Gauss-Lobatto quadrature method, the reader is referred to Ref. [GG00].

2.2.2 Approximations

Before results from numerical integration are presented, the qualitative information available from the variation of the coefficients a,b, and c of Eq. (1.43) with T is discussed, which is shown in Fig. 2.1. Inspection of the figure shows that for T less than about 0.3 there is little variation in their values. This suggests that there will be little variation in the correlation function in the interval $0 \leq T \lesssim 0.3$. As $T \to \infty$, $z \to 0$, so that $a \to 0$, $b \to 0$ and $c \to 1$. Substituting into Eq. (A.35) shows that $a_n \to 0$ and from Eq. (A.34) $\rho_{x0} \to 0$, i.e. the system is completely disordered, as expected.

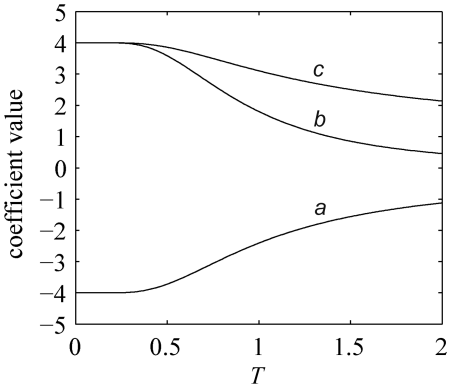

Figure 2.1 Coefficients a,b, and c versus temperature.

The correlation function at $T = 0$ was calculated on the interval $1 \leq x \leq 20$ using Eqs. (A.34) and (1.45) and is shown by the filled circles in Fig. 2.2. These values will be referred to as "exact." The positive and negative correlations as described above are evident. Close inspection of the figure shows that for small x, the negative correlations fall on two smooth curves as described above, but the difference between the two curves is small for $x \gtrsim 10$. The approximation Eq. (1.47) was calculated and is shown as the crosses in Fig. 2.2. The maximum absolute error of the approximation is 0.03 and the maximum relative error 0.15. Both errors decrease with increasing x and therefore, for small x, higher order terms are significant.

It is useful to examine the behaviour of Eq. (1.48) for $T \to 0$. With $T = 0$, $z = -1$, $\theta = \pi/3$, $\rho = 3^{-1/4}$ and $\phi = -\pi/12$. Substitution into Eq. (1.48) shows that the term of order $x^{-3/2}$ diverges as a result of the factor $(1 - z^2)^{-1}$. The first term remains finite however, and to leading order Eq. (1.48) reduces to

$$\begin{aligned} \rho_{x0} &\sim \left(2\pi^{-1/2}3^{-1/4}\right) x^{-1/2} \cos\left(\frac{2\pi x}{3}\right) \\ &\sim (0.8753)\, x^{-1/2} \cos\left(\frac{2\pi x}{3}\right). \end{aligned} \tag{2.10}$$

Comparison with Eq. (1.47) shows the same functional form but a discrepancy between the prefactors of 0.8753 versus $\epsilon_0 = 0.632226$. The approximation Eq. (2.10) was also calculated and was found to be less accurate than Eq. (1.47). The prefactor 0.8753 derived for finite temperatures is therefore inappropriate for the ground state. Including the second order terms in Eq. (1.46) gives a better approximation with a maximum error of about 0.01.

The correlation function ρ_{x0} at $T = 0$ was also calculated using numerical integration of Eq. (2.8) and the results agree with the exact values with an error of less than 3×10^{-5}. This indicates that the adaptive quadrature method is suitable for calculating accurate correlation functions for $T > 0$ where the a_n cannot be determined analytically. Since high precision values of ρ_{x0} may be useful for other studies, the values of ρ_{x0} calculated by numerical integration are listed Table 2.1. Note in passing that the correlation coefficients presented in Table II of Ref. [Ste64] are in error, although the estimate of ϵ_0 is correct.

	$\rho_{x0}(T)$[1]			$\rho_{xx}(T)$[2]
x	$T = 0$	$T = 0.5$	$T = 1.0$	$T = 0$
0	1	1	1	1
1	-0.33333	-0.33243	-0.31038	0.487
2	-0.19285	-0.18652	-0.10865	0.344
3	0.35852	0.34387	0.19067	0.282
4	-0.16561	-0.15734	-0.08130	0.241
5	-0.13362	-0.12079	-0.03266	0.219
6	0.25682	0.22977	0.06288	0.199
7	-0.12320	-0.10900	-0.02898	0.184
8	-0.10801	-0.09003	-0.01100	0.173
9	0.21026	0.17335	0.02308	0.163
10	-0.10225	-0.08333	-0.01125	0.154
11	-0.09302	-0.07094	-0.00388	0.147
12	0.18227	0.13749	0.00888	0.140
13	-0.08925	-0.06656	-0.00454	0.135
14	-0.08290	-0.05756	-0.00139	0.131
15	0.16311	0.11205	0.00351	
16	-0.08020	-0.05449	-0.00188	
17	-0.07549	-0.04756	-0.00050	
18	0.14893	0.09288	0.00141	
19	-0.07344	-0.04532	-0.00079	
20	-0.06977	-0.03978	-0.00018	

[1] The precision of ρ_{x0} is 3×10^{-5}
[2] The precision of ρ_{xx} is 5×10^{-3}

Table 2.1 Values of ρ_{x0} for $T = 0$, 0.5, 1.0 and ρ_{kk} for $T = 0$.

For finite temperature, the correlation function was calculated using Eq. (A.34) and numerical integration of Eq. (2.8). Given the precision of the numerical integration, these results are treated as exact. Results are shown by the filled circles in Fig. 2.3 for $T = 0.5$

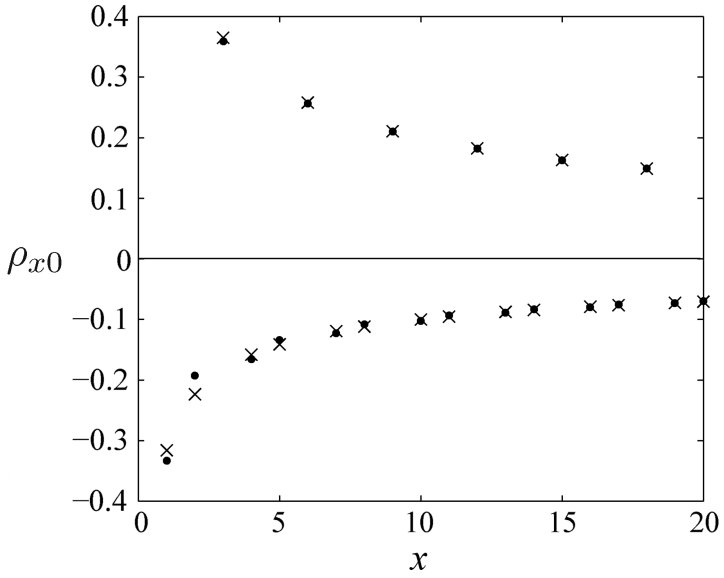

Figure 2.2 On-axis correlation function at $T = 0$ calculated using Eq. (A.34) and Eq. (1.45) (•), and using the approximation Eq. (1.47) (×).

and $T = 1.0$. The negative correlations fall on two smooth curves here also. The correlation coefficient falls off more rapidly with x for increasing T as expected. The short-range correlations are shown versus temperature in Fig. 2.4. They are seen to be approximately constant for $T \leq 0.3$ as anticipated above. The correlations were also calculated using the first term of the asymptotic expansion Eq. (1.48) and are shown by the crosses in Fig. 2.3. The maximum absolute error is 0.11 and the maximum relative error 0.48 for $T = 0.5$, and are larger for smaller temperatures, as expected. Note however, particularly for $T = 1.0$, that the approximate expression also describes two smooth curves for the negative correlations, in distinction to the leading order Eq. (1.47) for $T = 0$. Including the second term, of order $\mathcal{O}(x^{-3/2})$, in Eq. (1.48) gives a less accurate approximation, particularly for small T, as anticipated above. Eq. (1.48) is therefore unsuitable for high precision calculation of the correlation function. The values of ρ_{x0} calculated by numerical integration for $T = 0.5$ and 1.0 are listed in Table 2.1.

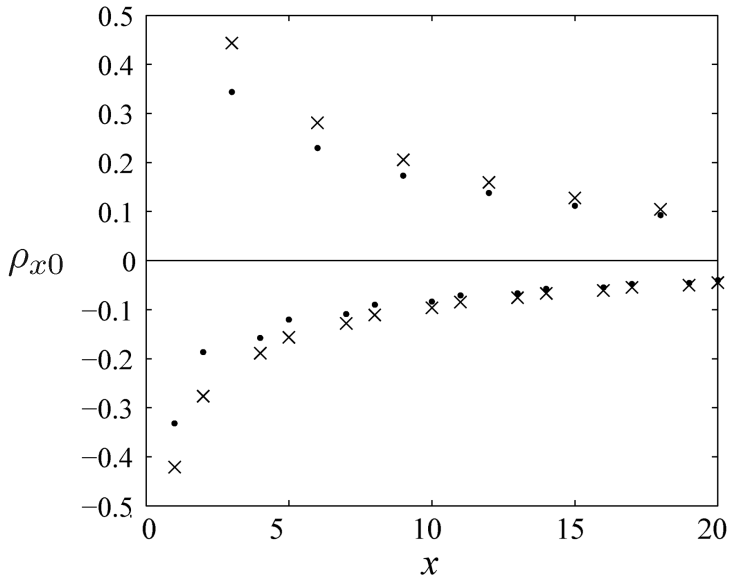

(a)

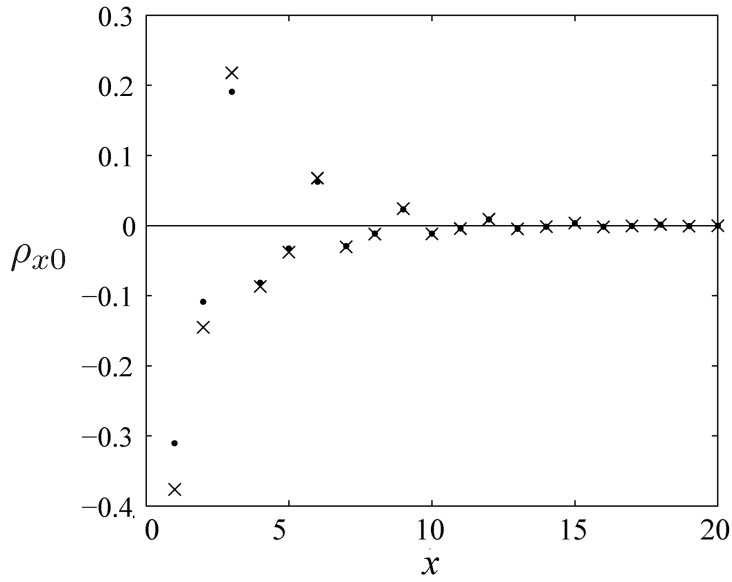

(b)

Figure 2.3 On-axis correlation function calculated exactly by numerical integration (•) and from the first term of Eq. (1.48) (×) for (a) $T = 0.5$ and (b) $T = 1.0$.

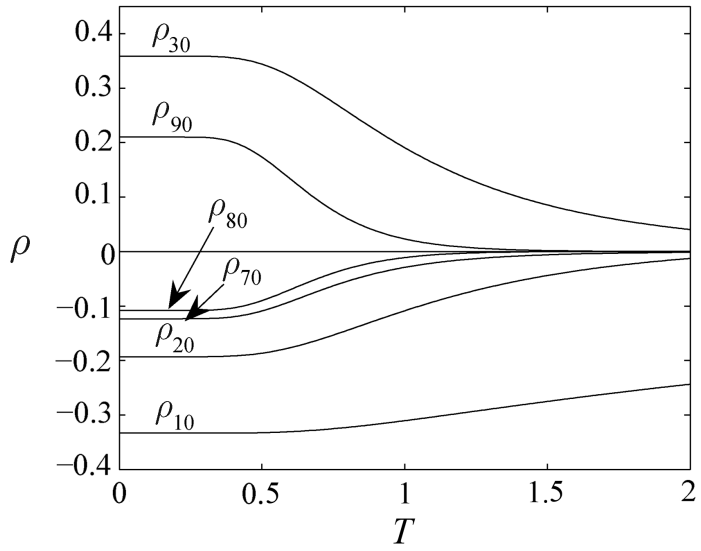

Figure 2.4 Low-order on-axis correlation coefficients versus temperature.

2.3 Off-axis correlation function

The correlation coefficient for two sites, not necessarily lying on a lattice axis, is denoted by $\rho_{xy} = \langle s_{00} s_{xy} \rangle$. Little is known rigourously concerning the coefficients ρ_{xy}. An important question is the extent to which ρ_{xy} is rotationally invariant, i.e. depends only on the distance,

$$r_{xy} = \left(x^2 + y^2 + xy\right)^{1/2}, \tag{2.11}$$

between the sites $(0, 0)$ and (x, y). Some information on the nature of ρ_{xy} has been obtained by Nienhuis et al. [NHB84] who mapped the TIA with a staggered field onto a period-6 spin wave operator of the triangular solid-on-solid model. Their work indicates that at $T = 0$, and for $r_{xy} \gg 1$, ρ_{xy} is expected to follow Eq. (1.47) with the separation x replaced by r_{xy} and the cosine term replaced by a weight factor equal to $+1$ when (x, y) belongs to a sublattice of the form $(3m + n, n)$, for all integers m and n, and $-1/2$ otherwise. This behaviour can be described by partitioning the triangular lattice into three sublattices, labelled 0, 1 and 2, as shown in Fig. 2.5(a), fixing the origin on sublattice 0, and partitioning the correlation function ρ_{xy} into two sets, one for which the site (x, y) is on sublattice 0, and the other for which it is on sublattice 1 or 2. The sublattices 0, 1 and 2 can be indexed by the sites $(3m + n, n)$, $(3m - 1 + n, n)$ and $(3m + 1 + n, n)$, respectively, for all integers m and n. Since the form of the off-axis correlation function as described above is identical on sublattices 1 and 2, it is said that it is degenerate with respect to these two sublattices. Monte Carlo calculations of structure factors support this contention for sufficiently small

temperatures [JF97]. The off-axis correlation function for larger temperatures has not been studied.

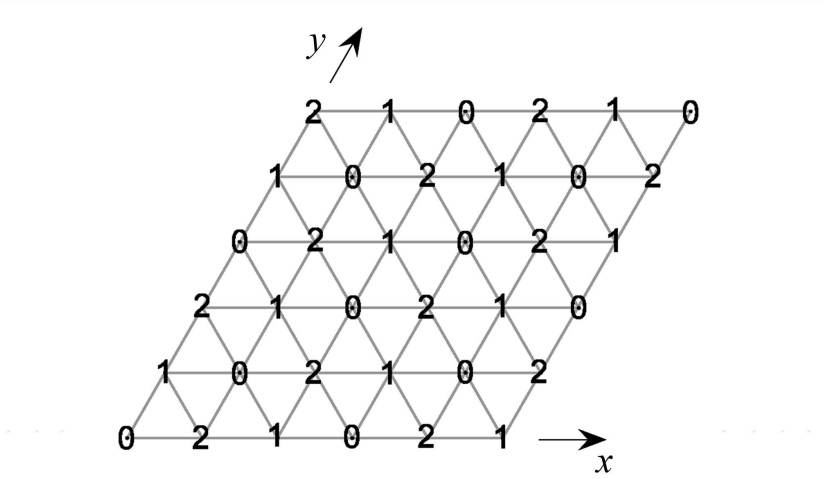

(a)

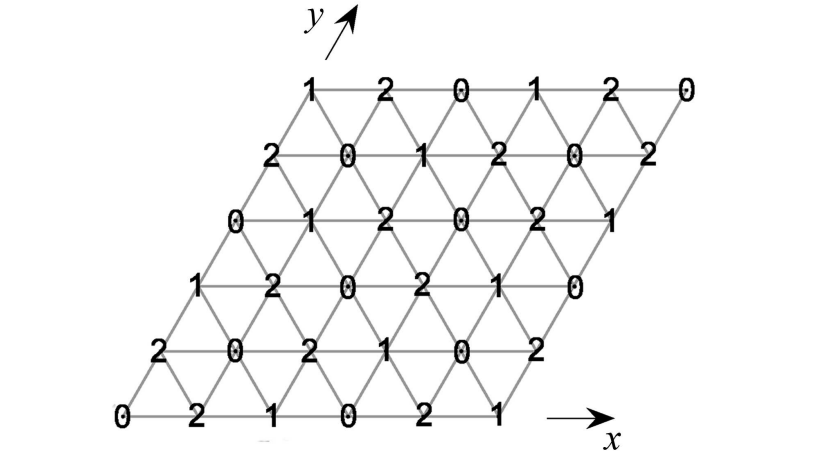

(b)

Figure 2.5 The sublattice partitioning implied by (a) Eq. (1.47) and (b) Eq. (1.46).

The results described above address only the leading order behaviour of the off-axis correlation function. In this section, the structure of the off-axis correlations using high precision Monte Carlo calculations, and the degree to which they are rotationally invariant, are studied.

2.3.1 Monte Carlo simulation

Since analytical results are not available for calculating the off-axis correlation coefficients for the TIA, they were calculated using Monte Carlo (MC) simulation. Since MC simulation near the ground state and for frustrated systems can be difficult, the methods used are briefly outlined here.

The TIA is a challenging model for MC simulation due to the complicated structure of the ground state, with standard simulation techniques becoming extremely inefficient or trivial. The metropolis algorithm gets trapped in metastable regions of configuration space and equilibriates very slowly. For example, simulations of the three-dimensional spin glass with the Metropolis algorithm have a dynamic critical exponent of $z \simeq 6$ [BY86]. Cluster algorithms such as the Swendsen-Wang [SW87], Wolff [WZ82] and multigrid [KDR$^+$88] end up freezing the whole lattice into a single cluster allowing only trivial global flips of the system. The problem occurs because the freeze-delete decision on a bond are made using information on the states of the two spins that the bond connects. Longer range correlations must be taken into account when the freeze-delete decisions are made. This idea inspired the development for a new framework for cluster MC simulation developed by Kandel, Ben-Av and Domany for zero-temperature MC simulation of the fully frustrated square Ising model [KBAD90]. MC simulation was performed using an algorithm developed specifically for the TIA model [CH94, ZY94] which employs the Kandel, Ben-Av and Domany (KBD) framework. The algorithm is outlined briefly here and the reader is referred to Ref. [ZY94] for more details.

The KBD cluster algorithm developed for the TIA [CH94, ZY94] combines elements of the Metropolis and Swendsen-Wang algorithms. First, the lattice is partitioned into two sets of triangular plaquettes, one of which is chosen at random for each Monte Carlo step. Bonds between spins are then labelled as frozen or deleted depending on the orientation of spins in the plaquette and strict criteria to satisfy the condition of detailed balance. A frozen bond is added to a cluster of connected bonds, and a deleted bond is not. If all three bonds in a plaquette are unsatisfied, all three bonds are deleted. If two bonds are satisfied, then all three bonds are deleted with probability $p = \exp(4K)$. If this does not occur, then one of the two satisfied bonds is chosen with probability $p = 1/2$ and then frozen with probability $p = 1-\exp(4K)$, while the other two bonds are deleted. Clusters of connected frozen bonds are then flipped in a Swendsen-Wang manner, bringing about large steps in configuration space. A Metropolis sweep is then performed to ensure that the simulation is ergodic.

On large lattices, clusters can be large in both number and size so efficiently identifying and labelling clusters can be a complicated process. The Hoshen-Kopelman (HK) cluster-labelling algorithm [HK76] was used to perform this task. The key ideas underlying this

algorithm are relatively straightforward to understand but are somewhat difficult to program. For a given configuration, each spin in the lattice is considered systematically, moving sequentially through $s_{0y}, s_{1y}, \ldots, s_{my}$, then $s_{0,y+1}, s_{1,y+1}, \ldots, s_{m,y+1}$ etc. For each spin s_{xy}, the set $\mathcal{N} = \{s_{x-1,y}, s_{x,y-1}, s_{x-1,y-1}\}$ of nearest-neighbour spins already visited by the algorithm is considered. If no spins in $\mathcal{N}$ are connected to s_{xy} by frozen bonds, s_{xy} is assigned a unique cluster label l_{xy} larger than all labels assigned previously. If one spin from $\mathcal{N}$ is connected by a frozen bond to s_{xy}, l_{xy} is assigned the label value of this connected spin. If a subset $\mathcal{N}_1 \subseteq \mathcal{N}$ of spins are connected to s_{xy} by frozen bonds, but the labels of the connected spins are different, $l_{xy} = \min\{l \in \mathcal{N}_1\}$. Because the spins in $\mathcal{N}_1$ and also s_{xy} belong to the same cluster, it is possible for a cluster to be assigned more than one label. A cluster only has one proper label, the minimum value of all labels assigned to its constituent spins, and all the others are improper. To determine the proper label the HK algorithm catalogues each label in an array $A[l]$ and classifies each as proper or improper. Entries in the array are indexed by the label value such that, when a new label is created for l_{xy} and classified as proper, $A[l] = l_{xy}$. When $\mathcal{N}_1$ is non-empty the array values of the larger labels are set equal to the smallest label value $A[l_{x'y'}] = \min\{l_{x'y'} \in \mathcal{N}_1\}$. Thus any label for which $A[l] \neq l_{xy}$ is improper and l_{xy} should be set to $A[l]$.

A random number generator of L'Ecuyer [L'E88], as implemented in Ch. 7 of Ref. [PTVF92], was used to generate a uniform pseudorandom deviate. The algorithm combines two multiplicative linear congruential generators such that the period is common multiple of the individual periods. A Bays-Durham shuffle [BD76] was performed to alleviate regularities in the pseudorandom number sequence generated by the L'Ecuyer algorithm. This combination generated a uniform deviate in the interval $(0, 1)$ with a sufficiently long period of $> 2 \times 10^{18}$.

The TIA was simulated on an $L \times L$ lattice, shown in Fig. 2.6(a), with toroidal boundary conditions such that the vertices at corner lattice sites $(0, 0)$, $(0, L-1)$, $(L-1, 0)$ and $(L-1, L-1)$ form a square plaquette, as shown in Fig. 2.6(b). The value of L used was a multiple of 6 to avoid dislocations in sublattice configurations across the boundaries, and generally $L = 300$. Thermalization times used were generally 1×10^5 sweeps. Decorrelation times τ_{decorr} were calculated and correlation values calculated by sampling every τ_{decorr} sweeps and averaging over 2×10^4 samples. Standard deviations of correlation coefficients calculated from the MC simulations were typically about 5×10^{-4}. Comparison of on-axis correlation coefficients with those calculated by numerical integration gave a maximum absolute difference of 3×10^{-3}. The algorithms presented here were written in C++ coding language and executed on an AMD OpteronTM based Linux Beowulf cluster with 152 cores and 188G RAM.

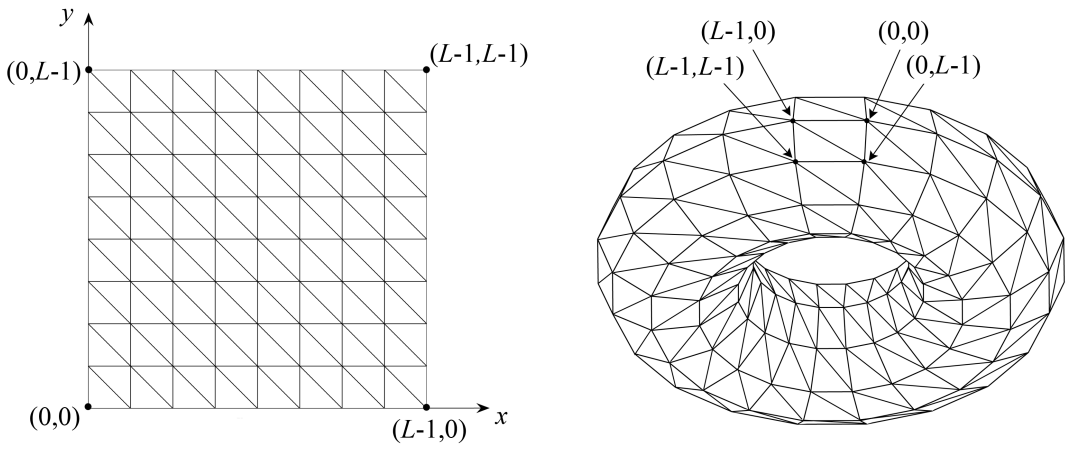

Figure 2.6 TIA on a lattice (a), with toroidal boundary conditions imposed in (b). The corner sites $(0,0)$, $(0,L-1)$, $(L-1,0)$ and $(L-1,L-1)$ are labelled.

2.3.2 Rotational invariance

The degree to which ρ_{xy} is rotationally invariant is of fundamental interest, and is also of interest because it would simplify the description of the correlation function. Note first that the correlation function must satisfy the symmetry relationships

$$\rho_{xy} = \rho_{yx} = \rho_{-y,x} = \rho_{y,-x} = \rho_{-x,-y}. \tag{2.12}$$

It is therefore sufficient to study ρ_{xy} in the sector $S = \{(x,y) : x \geq 0, 0 \leq y \leq x\}$, illustrated in Fig. 2.7, as all other values can be generated from these using Eq. (2.12).

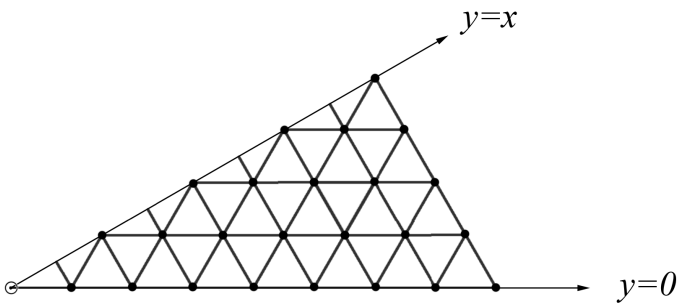

Figure 2.7 Sector of the lattice $S = \{(x,y) : x \geq 0, 0 \leq y \leq x\}$ on which the correlation function is unique with the origin indicated by the $\circ$.

Rotational invariance is first assessed by interpolating the on-axis correlation coefficients, calculated in Section 2.2, as a function of r_{xy} within each of the three sublattice groups and comparing the off-axis correlations calculated by MC simulation with the interpolated val-

ues at the same value of r_{xy}. Spline interpolation of the on-axis correlation coefficients was performed using cubic splines with "not-a-knot" end conditions, discussed in Appendix C. The results are shown for three temperatures in Fig. 2.8 and the off-axis values are seen to fit well to the interpolated values. This indicates that the on- and off-axis correlations can probably be quite accurately described by three functions of the distance r_{xy} between sites. This is addressed further in Section 2.4. Inspection of Fig. 2.8 shows that the off-axis correlations fall onto the three curves defined by the on-axis correlations. Inspection of the indices (x, y) corresponding to points on the three curves shows that they correspond to the three sublattices described above, but only within the sector S. Note that now, because the functional form of the correlation is different on sublattices 1 and 2, the off-axis correlations are not degenerate with respect to these two sublattices. Therefore, to describe the correlation function outside the sector S, the symmetry relationships Eq. (2.12) must be applied to the partitioning in S, which gives the full partitioning shown in Fig. 2.5(b). This partitioning describes the correlations relative to an origin on sublattice 0. Note the difference between Figs. 2.5(a) and (b). Although the partitions 1 and 2 in Fig. 2.5(b) do not have translational symmetry, they are referred to, for convenience, as sublattices. The correlations are therefore determined not by being "on" or "off" a sublattice, but by their membership of sublattice 0, 1 or 2, relative to an origin on sublattice 0. The sublattices can be described in terms of sets of hexagons as shown in Fig. 2.9. The values of ρ_{xx} for $T = 0$ and out to $r_{xx} = 20$ are listed in Table 2.1.

Since ρ_{xy} is a function of the discrete variables x and y, strict rotational invariance would imply that for a particular T, $\rho_{xy} = \rho_{x'y'}$ for all (x, y) and (x', y') belonging to the same sublattice and for which $r_{xy} = r_{x'y'}$. The degree to which the correlations are rotationally invariant was therefore further studied by calculating and comparing correlation coefficients for pairs of sites (x, y) and (x', y') with the same radius and on the same sublattice. Eight such pairs listed in Table 2.2 were tested and the difference $\Delta\rho = \rho_{xy} - \rho_{x'y'}$ between the correlation coefficients in each pair are plotted versus temperature in Fig. 2.10. Increasing the lattice size beyond $L = 300$ made no significant difference to the values of $\Delta\rho$. The results show that although rotational invariance is not satisfied exactly, deviations from rotational invariance are less than 2×10^{-3}. The results in Fig. 2.10 are suggestive of the nature of the deviations from rotational invariance but this will not be pursued here.

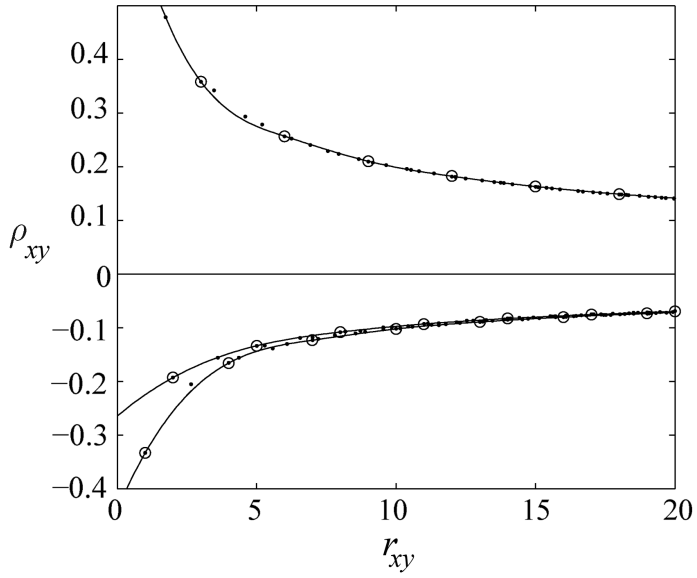
0.4
0.3
0.2
0.1
0
−0.1
−0.2
−0.3
−0.4
ρ_{xy}
0
5
10
15
20
r_{xy}

(a)

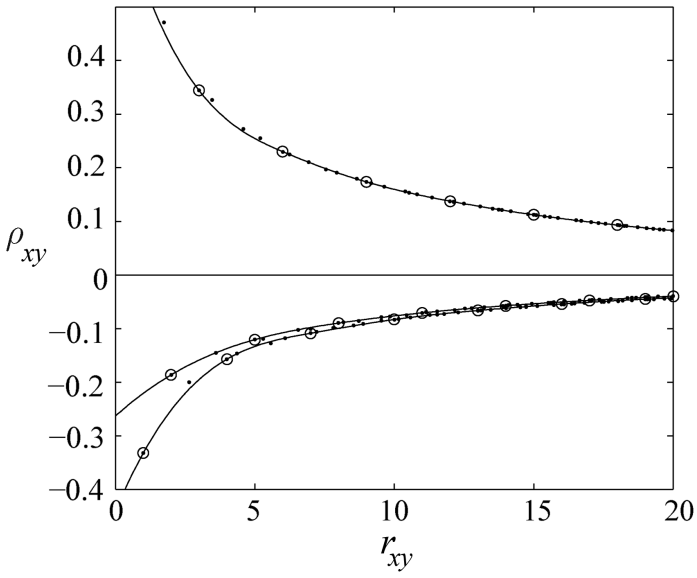
0.4
0.3
0.2
0.1
0
−0.1
−0.2
−0.3
−0.4
ρ_{xy}
0
5
10
15
20
r_{xy}

(b)

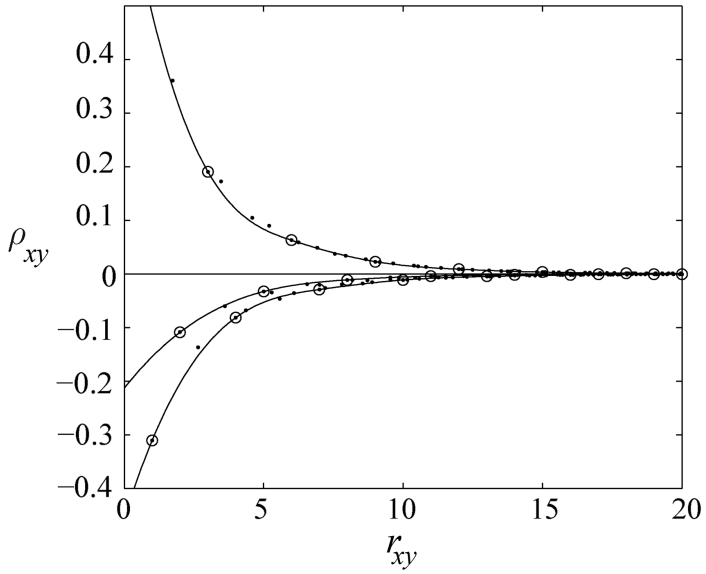

(c)

Figure 2.8 On-axis correlation coefficients ⊙ with spline interpolation (-), and off-axis correlation coefficients calculated by MC simulation, (•), for (a) $T = 0$, (b) $T = 0.5$ and (c) $T = 1.0$. The three curves are for the three sublattices.

Label	sublattice	r_{xy}^2	(x, y)	$(x^{'}, y^{'})$
A	0	147	(11,2)	(7,7)
B	2	169	(13,0)	(8,7)
C	2	217	(13,3)	(9,8)
D	0	273	(16,1)	(11,8)
E	1	301	(15,4)	(11,9)
F	0	399	(17,5)	(13,10)
G	1	403	(19,2)	(14,9)
H	0	441	(21,0)	(15,9)

Table 2.2 Pairs (x, y) and (x', y') that lie on the same sublattice and such that $r_{xy} = r_{x'y'}$, used to study rotational invariance.

2.4 Functional approximation

The results in the previous section indicate that ρ_{xy} can be written approximately in the form

$$\rho_{xy} \simeq \tilde{\rho}(r_{xy}, \sigma_{xy}), \tag{2.13}$$

where σ_{xy} depends *only* on the sublattice to which (x, y) belongs. They also indicate that the off-axis correlation coefficients can be obtained by interpolation from the on-axis coefficients. The latter can be obtained by evaluating Eqs. (A.34) and (2.8), although this is

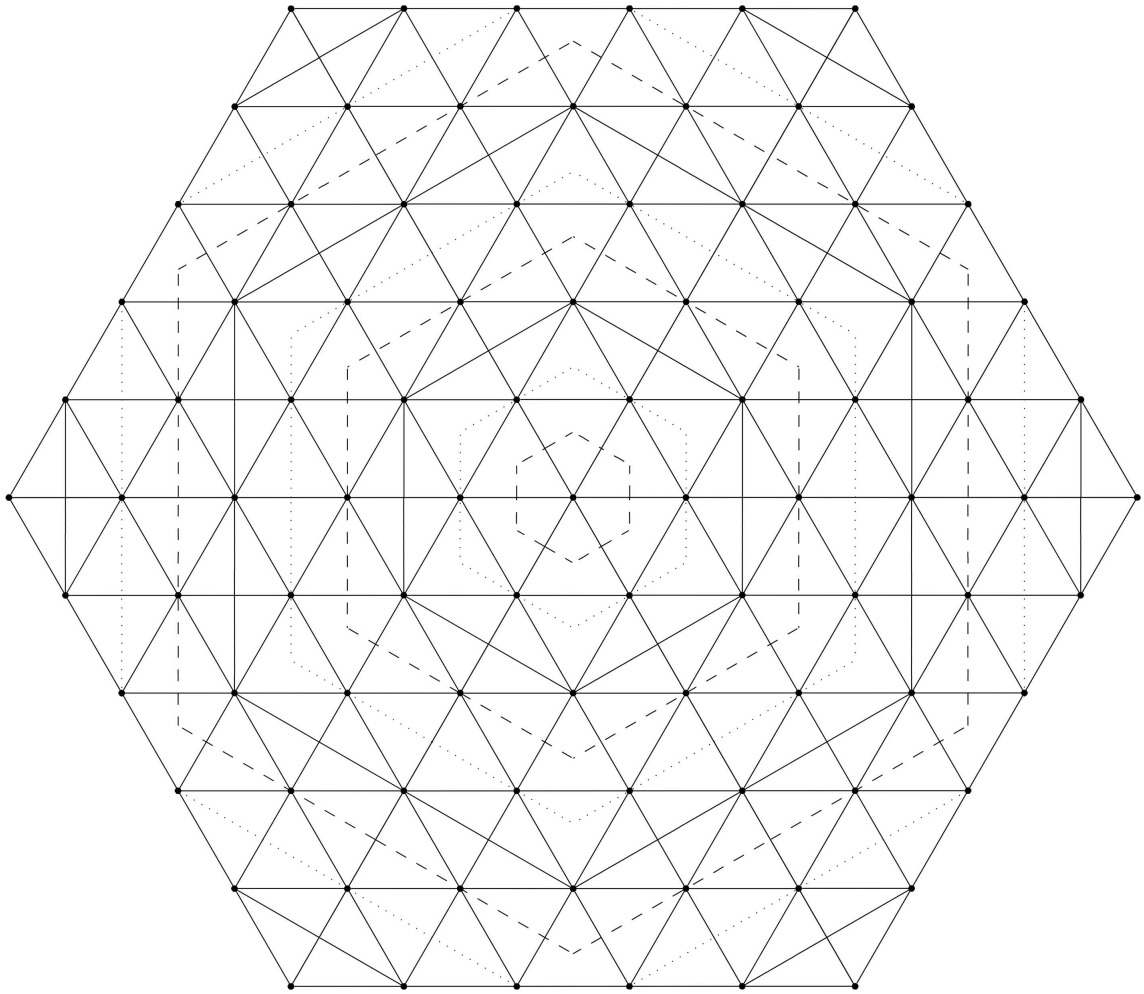

Figure 2.9 A representation of the sublattice structure of the TIA corresponding to Fig. 2.5(b) that describes the correlations of the TIA. The full-line hexagons pass through the sites of the 0-sublattice, and the dash-dot hexagon through the sites of the 1-sublattice, and the dashed line hexagon through the sites of the 2-sublattice.

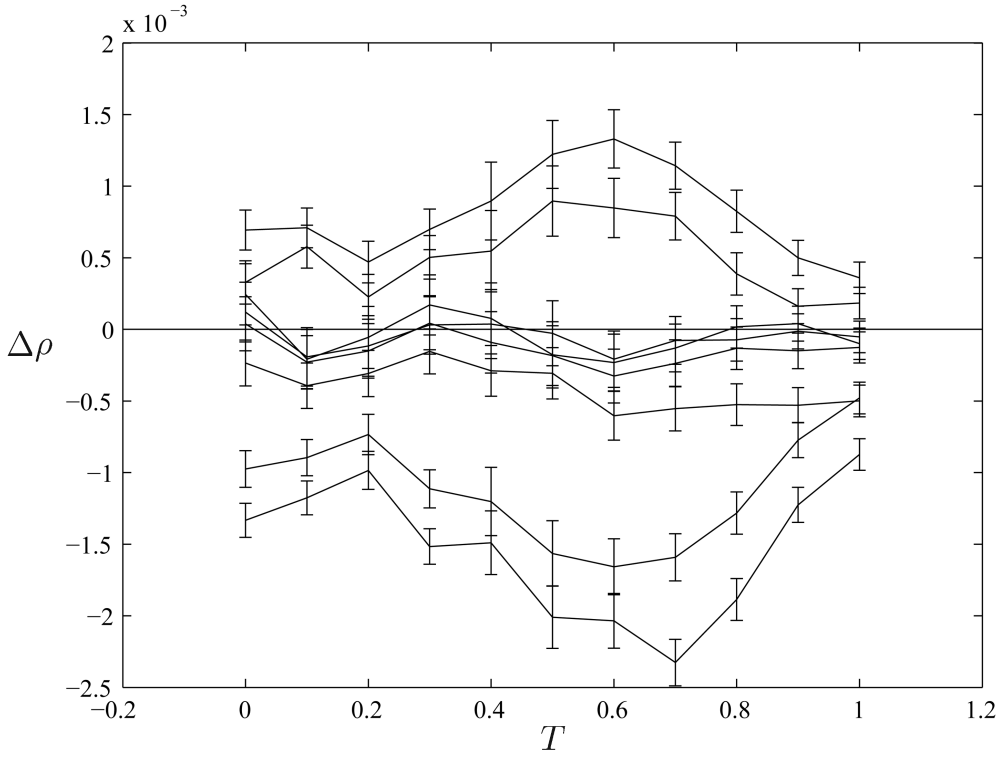

Figure 2.10 Differences in correlation coefficients for different lattice separations with the same radial distance as described in the text. Vertical bars show ± 1 standard deviation. The different curves are defined in Table 2.2.

not particularly convenient. Here simple expressions are developed that can be used to calculate the correlation function over a range of values of x and T. Since the correlation function is largest on the 0 sublattice, the range of values of x and T for which the correlation has significant value is determined by calculating $\rho_{3x,0}$ versus x and T. The results are shown as a contour plot in Fig. 2.11. The region for which $\rho_{xy}(T) > 0.02$ was chosen (arbitrarily) to describe $\rho_{xy}(T)$. This is done by developing suitable functions $\rho(r_{xy}, T)$ and fitting them to the on-axis values obtained from Eqs. (A.34), (1.45) and (2.8), for each sublattice. Off-axis correlations are then obtained by evaluating these expressions for the appropriate value of r_{xy}. A suitable expression was developed as follows.

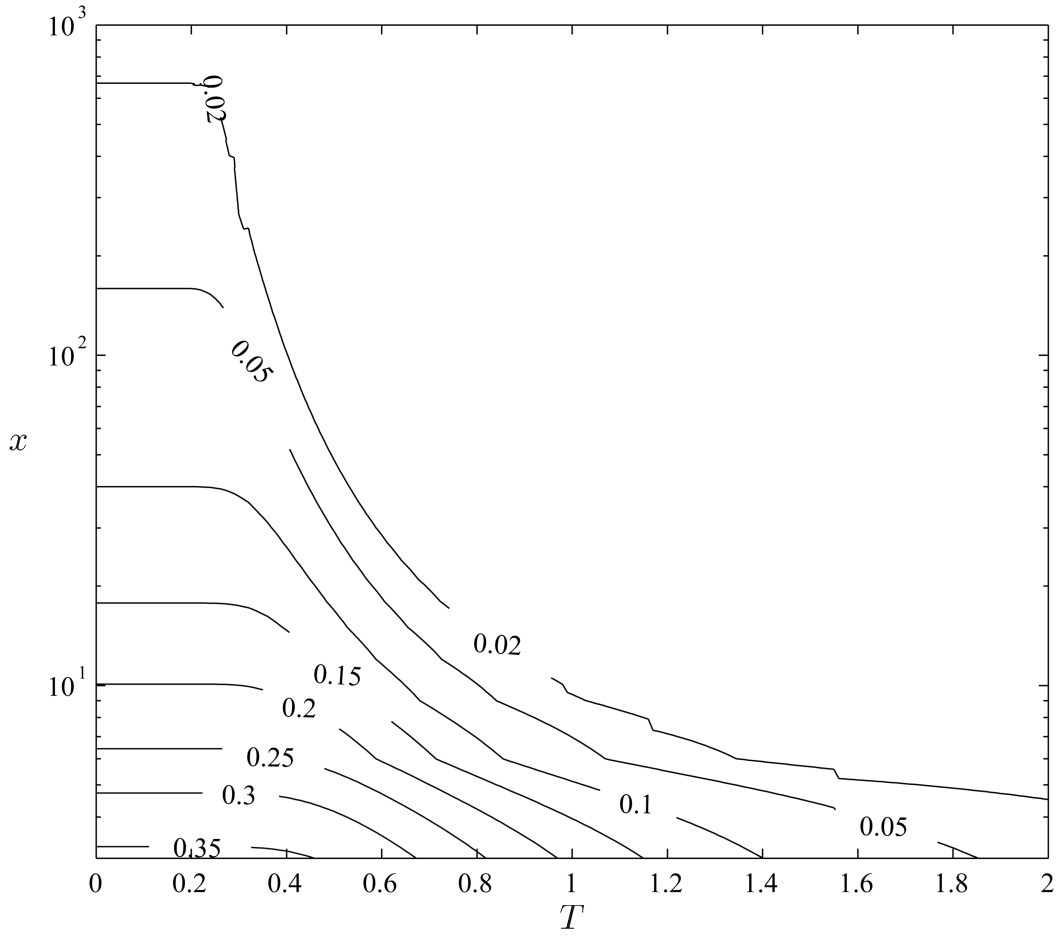

Figure 2.11 Contour plot of $\rho_{3x,0}$ versus x (on a log scale) and T.

For $T = 0$ the on-axis correlation function behaves approximately as $x^{-1/2}$. Although the leading order behaviour is not particularly accurate for small x, this can potentially be improved by allowing the prefactor ϵ_0 in Eq. (1.47) to vary between the sublattices. For finite

temperature, to leading order [Eq. (1.48)], in addition to the $x^{-1/2}$ dependence, there is an exponential decay through the factor z^x. The temperature dependence is primarily through the temperature dependence of z, but there is also an effect on the prefactor through the cosine term in Eq. (1.48). It was found that the form z^x was insufficient to accurately describe the temperature dependence, so z was replaced by a general function of T. In summary then, an expression of the form

$$\rho(r,T) = \alpha_i(T) r^{-1/2} \left[\beta(T)\right]^r , \tag{2.14}$$

is used as a tentative description of the correlation function, where for convenience r_{xy} has been replaced by r, the coefficients α_i and β depend on temperature, and α_i depends on the sublattice i. As $T \to 0$, it is expected that $\beta \to 1$ and α_0 to approach ϵ_0. Note that the cosine factor in Eqs. (1.47) and (1.48) has been absorbed into α_i. Note also that writing Eq. (2.14) in the form $\rho(r,T) = \alpha_i(T) r^{-1/2} e^{-r/\xi(T)}$ shows that $\xi(T) = -1/\ln(\beta(T))$ is a correlation length, and that $\xi(T) \to \infty$ as $T \to 0$. The coefficients $\alpha_i(T)$ and $\beta(T)$ were determined by making a least-squares fit of Eq. (2.14) to the on-axis correlation function over $0 \le r \le 700$ (for which the correlation function is less than 0.02) for $0 \le T \le 1.5$ with an interval of 0.1.

The resulting coefficients are listed in Table 2.3. The mean and maximum absolute errors in the fit for all the correlations (on-axis and off-axis) are 5×10^{-3} and 0.017, respectively. The maximum relative error in the fit is 0.11. For intermediate temperatures, linear interpolation of the coefficients in Table 2.3 gives equivalent precision. For interest, the correlation length $\xi(T)$ is also listed in Table 2.3. Because of the precision with which β can be estimated, only a lower bound can be obtained for ξ for $T \le 0.2$. Of course the correlation length continues to grow throughout this temperature range. In summary, Eq. (2.14), together with the coefficients listed in Table 2.3, allows convenient and accurate calculation of the on- and off-axis correlation function in the region specified above.

	$\alpha_i(T)$			$\beta(T)$	$\xi(T)$
T	$i=0$	$i=1$	$i=2$		
0	0.623	-0.298	-0.326	1.000	∞
0.1	0.623	-0.298	-0.326	1.000	$> 10^3$
0.2	0.623	-0.298	-0.326	1.000	$> 10^3$
0.3	0.642	-0.295	-0.336	0.998	499.5
0.4	0.655	-0.292	-0.339	0.989	90.4
0.5	0.667	-0.289	-0.345	0.969	31.8
0.6	0.678	-0.284	-0.353	0.939	15.9
0.7	0.690	-0.279	-0.362	0.902	9.7
0.8	0.700	-0.272	-0.371	0.860	6.6
0.9	0.709	-0.265	-0.380	0.816	4.9
1.0	0.716	-0.258	-0.389	0.773	3.9
1.1	0.722	-0.251	-0.399	0.731	3.2
1.2	0.728	-0.244	-0.408	0.691	2.7
1.3	0.733	-0.240	-0.417	0.653	2.3
1.4	0.738	-0.240	-0.426	0.617	2.0
1.5	0.742	-0.240	-0.434	0.584	1.8

Table 2.3 Values of the coefficients $\alpha_i(T)$ and $\beta(T)$ to an accuracy of 10^{-3}.

2.5 Summary

The correlation behavior of the triangular Ising antiferromagnet has been studied in detail through numerical evaluation of exact analytical results and Monte Carlo simulation. The precision of existing approximations for on-axis correlations for finite temperatures, are found to be unsuitable for high precision calculations. A lattice partitioning is defined that describes the symmetry of high precision off-axis correlations. The correlation function is shown to be not exactly rotationally invariant at all temperatures, but to be approximately rotationally invariant within a given small error. This allows an accurate description of the correlation function in terms of only radial separation and the sublattice. The region of separation-temperature space where correlations are significant is identified, and simple approximations are derived that accurately describe the correlation function in this region. These latter expressions will be useful to those using the TIA to quantitatively model various systems.

Chapter 3

The two-point correlation function for the fully frustrated square Ising model

3.1 Introduction

The fully frustrated square Ising model (FFS), introduced in Section 1.2.5, is a geometrically frustrated system with complicated organizational properties. As with the TIA described in Chapter 2, it serves as an important archetype for studies of more complicated geometrically frustrated systems [Bra06, WNF+06]. The correlation behavior of the FFS provides a basic description of its cooperative properties, and an accurate description of the correlation function is useful in some applications. The few analytic results available and the existing on-axis approximations were reviewed in Section 1.2.5. Although much is known about the correlation behaviour of the FFS, there are some significant gaps. A number of aspects of the correlation function of the FFS, in particular the off-axis behaviour and the accuracy of approximate expressions, are poorly understood. In this chapter a number of these aspects of the correlation function for the FFS are addressed.

For pairs of sites on the lattice axes and on the diagonal, at both zero and non-zero temperatures, exact expressions have been developed, but these are not convenient to evaluate except for the diagonal correlation function at zero temperature [WZ82]. Leading order asymptotic (in separation) expressions have been developed, but their precision has not been investigated [For80, WZ82]. The lack of numerical calculations means that currently there is little information available on the quantitative behaviour of the correlation function. For all temperatures, the on-axis correlation function exhibits two behaviours for odd and even separations. The diagonal correlation function also exhibits two behaviours for odd and even separations. There is no information in the literature on the correlation func-

tion for pairs of sites not on a lattice axis. The continuation of the behaviours described above off the axes and the diagonal is unknown, as is the extent to which the FFS correlation function is rotationally invariant. Applications of the FFS as a model of various systems requires numerical calculation of the correlation function for any separation (on-axis or off-axis) at any temperature. There is currently no convenient means of performing such calculations.

In this chapter some of the shortcomings in current knowledge of the correlation function for the FFS are addressed. This is achieved through a combination of known exact results for the on-axis case at $T = 0$, numerical integration of known analytic expressions at finite temperature, and through Monte Carlo simulation for off-axis separations. Symmetry relationships for the general (off-axis) correlation functions are derived in Section 3.2 and it is shown that all correlations can be defined in terms of one set of correlation functions. Exact results are reviewed and the precision of existing approximations is evaluated for the on-axis and diagonal cases at zero and finite temperatures in Section 3.3. The off-axis correlation behaviour is examined in some detail in Section 3.4. A sublattice description of the off-axis correlation function is derived from high precision Monte Carlo results. Rotational invariance and the correlation length are studied as a function of temperature. Concluding remarks are made in Section 3.5.

3.2 Symmetry relationships

The FFS model with nearest-neighbor interactions is defined by the Hamiltonian Eq. (1.52) and illustrated in Fig. 1.11. The system has ferromagnetic interactions in horizontal rows, and ferromagnetic and anti-ferromagnetic vertical interactions in alternating columns assumed to be equal in magnitude. The rescaled temperature parameter Eq. (1.9) is used to describe the systems state in this chapter.

The correlation coefficients are defined as follows. The definition of the Hamiltonian Eq. (1.52) implies that the origin of the lattice is on a ferromagnetic column (Fig. 1.11). There are therefore two sets of correlation coefficients, depending on whether the reference spin is on a ferromagnetic or antiferromagnetic column. These two cases are denoted with superscripts $+$ and $-$, respectively, and the correlation coefficients are then defined by

$$\rho^{+}_{xy} = \langle s_{00} s_{xy} \rangle, \tag{3.1a}$$

$$\rho^{-}_{xy} = \langle s_{10} s_{x+1,y} \rangle, \tag{3.1b}$$

where $\langle \cdot \rangle$ is the ensemble average over all configurations and $x, y \in \mathbb{Z}$. Note that the use here of $+$ and $-$ is consistent with, but more general than, that of Wolff and Zittartz [WZ82]

since they considered only axial correlations.

A number of symmetry relationships between ρ^+_{xy} and ρ^-_{xy} are derived here. First, it is clear that the correlation coefficients satisfy mirror symmetry in the x and y axes so only the quadrant $x \geq 0$, $y \geq 0$ needs to be considered. It is convenient to consider the four cases for x and y individually odd or even.

For x and y both odd, the lattice symmetry implies that

$$\rho^+_{xy} = \rho^-_{xy}, \quad x \text{ and } y \text{ odd.} \tag{3.2}$$

Applying the gauge transformation described by Wolff and Zittartz [WZ82] in which the spins at the intersections of ferromagnetic and antiferromagnetic bonds are flipped (Fig. 3.1) shows that

$$\left.\begin{aligned} \rho^+_{xy} &= -\rho^+_{yx}, \\ \rho^-_{xy} &= -\rho^-_{yx}, \\ \rho^+_{xy} &= \rho^-_{yx}, \end{aligned}\right\} \; x \text{ and } y \text{ odd.} \tag{3.3}$$

Using Eqs. (3.2) and (3.3) shows that

$$\rho^+_{xy} = \rho^-_{xy} = 0, \quad x \text{ and } y \text{ odd.} \tag{3.4}$$

For x and y both even, using the above gauge transformation shows that

$$\rho^+_{xy} = \rho^+_{yx} = \rho^-_{xy} = \rho^-_{yx}, \quad x \text{ and } y \text{ even.} \tag{3.5}$$

For x odd and y even, the gauge transformation shows that

$$\rho^+_{xy} = \rho^+_{yx} = \rho^-_{xy} = -\rho^-_{yx}, \quad x \text{ odd, } y \text{ even.} \tag{3.6}$$

For x even and y odd, the gauge transformation shows that

$$\rho^+_{xy} = \rho^+_{yx} = -\rho^-_{xy} = \rho^-_{yx}, \quad x \text{ even, } y \text{ odd.} \tag{3.7}$$

Equations (3.4)-(3.7) summarize the symmetry relationships of the correlations. Eq. (3.4) defines a sublattice on which the correlations are zero. Note that ρ^+_{xy} has even symmetry in the line $x = y$, and that ρ^-_{xy} has even symmetry in $x = y$ if x and y are either both odd or both even, and odd symmetry otherwise. Note also that ρ^+_{xy} is related to ρ^-_{xy}, the relationship depending on x and y being odd and/or even. In view of the these relationships it is necessary to calculate only ρ^+_{xy} for $y \leq x$, as all other correlations can be calculated from

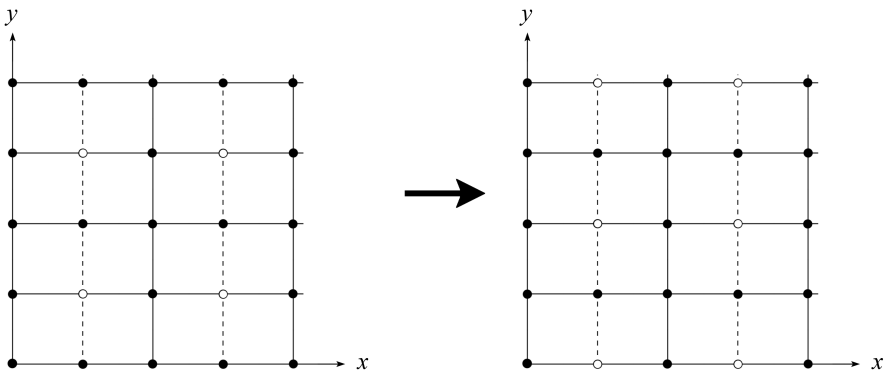

Figure 3.1 Gauge transformation where all spins along antiferromagnetic columns are flipped which leaves the physical properties of the FFS invariant.

these. Only these correlations are considered further, and for simplicity we denote ρ^+_{xy} by ρ_{xy}.

It is instructive to compare these symmetry results with those of Wolff and Zittartz [WZ82] for the axial correlations (keeping in mind their opposite definitions of horizontal and vertical). They show that their "horizontal" (ρ^+_{0y} and ρ^-_{0y} here) and their "vertical" (ρ^+_{x0} and ρ^-_{x0} here) satisfy

$$\rho^+_{x0} = \rho^+_{0x} = (-1)^x \rho^-_{0x}, \tag{3.8}$$

which is a special case of Eqs. (3.5) and Eqs. (3.6). Note that they do not distinguish between ρ^+_{x0} and ρ^-_{x0}. They also show that

$$\rho^+_{xx} = \rho^-_{xx} = 0, \quad x \text{ odd}, \tag{3.9}$$

which is a special case of Eq. (3.4).

3.3 Axial correlation functions

In this section, the results of Wolff and Zittartz [WZ82] for the horizontal and diagonal correlation functions denoted ρ_{x0} and ρ_{xx}, respectively, are reviewed. The set $\{\rho_{x0}, \rho_{xx}\}$ are referred as the axial correlation functions. At $T = 0$, ρ_{xx} and ρ_{x0} are given by Eqs. (1.59) and (1.61), respectively. At finite temperature ρ_{x0} and ρ_{xx} have the asymptotic form given by Eqs. (1.63) and (1.64). Their calculation utilizes the similarity between a Toeplitz determinant and the Wiener-Hopf sum formula which only holds when x [and hence n, the size of the Toeplitz determinant Eq. (A.34)] is large, and when $T \gg 0$ [Wu66]. By the use of Szego's theorem, the asymptotic behaviour of the Toeplitz determinant as $n \to \infty$ can be inferred. Eqs. (1.63) and (1.64) are therefore expected to break down for small x, and also

for $T \to 0$. To study the accuracy of these expressions, the exact expressions Eqs. (A.34) and (A.35) with the integrands Eqs. (1.54) and (1.55) are evaluated.

It is useful to examine the behaviour of Eqs. (1.63) and (1.64) as $T \to 0$. At $T = 0$, Eq. (1.64) reduces to

$$\rho_{xx}(T=0) \sim \begin{cases} 0, & x = 2m-1 \\ (2/\pi)^{1/2}\, x^{-1/2}, & x = 2m, \end{cases} \tag{3.10}$$

which shows the same functional form as Eq. (1.59) but a discrepancy between the prefactors of $1/\sqrt{\pi} = 0.5642$ versus $(0.6450)^2 = 0.4160$. Similarly, at $T = 0$, Eq. (1.63) reduces to

$$\rho_{x0}(T=0) \sim \begin{cases} 2^{1/4}\pi^{-1/2}x^{-1/2}, & x = 2m-1 \\ 2^{3/4}\pi^{-1/2}x^{-1/2}, & x = 2m, \end{cases} \tag{3.11}$$

showing the same functional form as Eq. (1.61) but with the same discrepancy between the prefactors as above. A similar discrepancy occurs for the TIA, as seen in Section 2.2.2.

3.3.1 Numerical integration

The diagonal correlation function at $T = 0$ can be calculated using Eq. (1.58), but the horizontal correlation function at $T = 0$ and both the diagonal and horizontal correlation functions for $T > 0$ need to be calculated by numerical integration of Eq. (A.35) and evaluation of the determinant. Eq. (A.35) is written in real form for the purposes of integration. The integrands Eqs. (1.54) and (1.55) can be written in the form

$$\varphi(\omega) = e^{-in\omega}\frac{A(\omega)}{|A(\omega)|}. \tag{3.12}$$

Substituting this form of the integrand into Eq. (A.35) and following the analysis of Section 2.2.1, Eq. (A.35) has the real form

$$a_n = \frac{1}{\pi}\int_0^\pi \frac{\cos[(n+1)\omega]\Re[A(\omega)] + \sin[(n+1)\omega]\Im[A(\omega)]}{|A(\omega)|}d\omega. \tag{3.13}$$

In the case of the diagonal correlation function, $A(\omega) = (1 + z_0^2\exp(2i\omega))$ so that

$$\Re[A(\omega)] = 1 + z_0^2\cos 2\omega, \tag{3.14a}$$

$$\Im[A(\omega)] = z_0^2\sin 2\omega, \tag{3.14b}$$

$$|A(\omega)| = \left(1 + 2z_0^2\cos 2\omega + z_0^4\right)^{\frac{1}{2}}. \tag{3.14c}$$

For the horizontal correlation function,

$$A(\omega) = (1 - z_1^2 \exp(2i\omega))(1 + z_2 \exp(i\omega))(1 - z_2 \exp(-i\omega)),$$

and

$$\Re[A(\omega)] = 1 - z_2^2 - z_1^2 \cos 2\omega + z_1^2 z_2^2 \cos 2\omega + 2z_1^2 z_2 \sin\omega \sin 2\omega, \tag{3.15a}$$

$$\Im[A(\omega)] = 2z_2 \sin\omega - z_1^2 \sin 2\omega + z_1^2 z_2^2 \sin 2\omega - 2z_1^2 z_2 \sin\omega \cos 2\omega, \tag{3.15b}$$

$$|A(\omega)| = \left(\left[1 - 2z_2^2 \cos 2\omega + z_2^4\right]\left[1 - 2z_1^2 \cos 2\omega + z_1^4\right]\right)^{\frac{1}{2}}. \tag{3.15c}$$

Numerical integration was performed using an adaptive Gauss-Lobatto quadrature algorithm described in Section 2.2.1, using an error tolerance of 1×10^{-6}. Calculations were repeated using various tolerance values and the results showed that this value is sufficient.

3.3.2 Numerical results

The axial correlation functions at $T = 0$ were calculated for $1 \leq x \leq 20$ and are shown in Fig. 3.2. The diagonal correlation function was calculated using Eq. (1.58) and is shown by the filled circles in Fig. 3.2(a). The alternating positive and zero correlations described above are evident. The approximation Eq. (1.59) was calculated and is shown as the crosses in Fig. 3.2(a). The maximum error in the approximation is 0.01 and decreases with increasing x. The approximation Eq. (3.10) was also calculated and was found to be less accurate than Eq. (1.59). The prefactor 0.5642 derived for finite temperatures is therefore inappropriate for the ground state. The correlation function was also calculated using numerical integration of Eqs. (3.13) with Eq. (3.14) and the results agree with the exact values with an error of less than 1×10^{-5}. This indicates that the adaptive quadrature method is suitable for calculating accurate correlation functions where the a_n cannot be determined analytically. Since high precision values of the correlation function may be useful in other studies, the values of ρ_{xx} for $x \leq 20$ calculated by Eq. (1.58) are listed in Table 3.1.

The horizontal correlation function at $T = 0$, calculated using Eq. (A.34) and numerical integration of Eq. (3.13) with Eq. (3.15), is shown by the filled circles in Fig. 3.2(b). Given the precision of the numerical integration, these results are treated as exact. Two distinct curves for x odd and even are evident. The approximation Eq. (1.61) was calculated and is shown as the crosses in Fig. 3.2(b). The maximum error of the approximation is 0.02 and decreases with increasing x. The approximation Eq. (3.11) was also calculated and was again found to be less accurate than Eq. (1.61). The values of ρ_{x0} calculated by numerical integration for $x \leq 20$ are listed in Table 3.1.

For finite temperature, the correlation function was calculated using Eq. (A.34) and numerical integration of Eq. (3.13). Results for $T = 0.5$ and $T = 1.0$ are shown by the filled circles

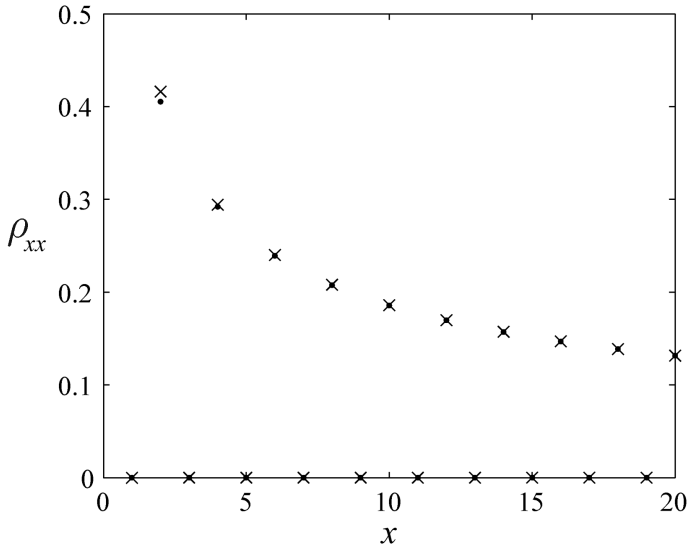

(a)

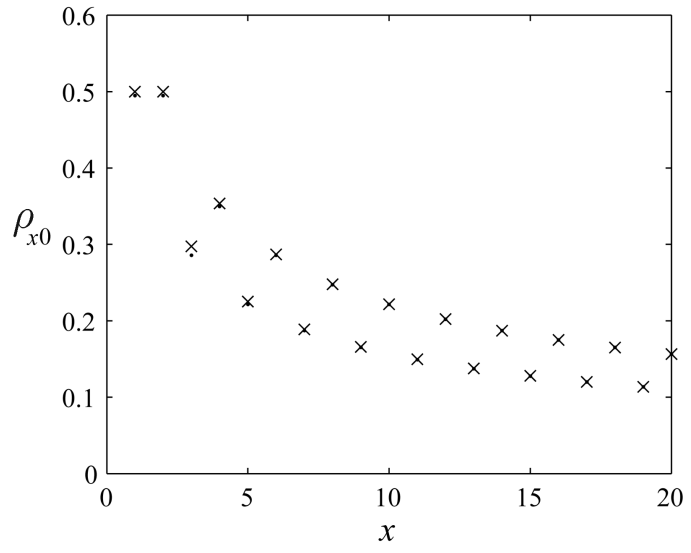

(b)

Figure 3.2 (a) Diagonal correlation function at $T = 0$ calculated using Eq. (1.58) (•), and using the approximation Eq. (1.59) (×). (b) Horizontal correlation function at $T = 0$ calculated exactly by numerical integration of Eqs. (3.13) with Eq. (3.15) (•), and using the approximation Eq. (1.61) (×).

	$\rho_{x0}(T)^1$		$\rho_{xx}(T)^1$	
x	$T=0$	$T=0.5$	$T=0$	$T=0.5$
0	1	1	1	1
1	0.50000	0.49849	0	0
2	0.50000	0.49038	0.40528	0.38977
3	0.29736	0.28746	0	0
4	0.35369	0.33344	0.29201	0.26349
5	0.22532	0.20805	0	0
6	0.28707	0.25768	0.23938	0.20023
7	0.18867	0.16530	0	0
8	0.24700	0.21086	0.20761	0.15988
9	0.16576	0.13725	0	0
10	0.22159	0.17786	0.18582	0.13115
11	0.14967	0.11681	0	0
12	0.20218	0.15281	0.16970	0.10943
13	0.13754	0.10096	0	0
14	0.18713	0.13292	0.15714	0.09237
15	0.12797	0.08819	0	0
16	0.17501	0.11665	0.14702	0.07862
17	0.12016	0.07764	0	0
18	0.16499	0.10306	0.13861	0.06737
19	0.11363	0.06877	0	0
20	0.15651	0.09153	0.13150	0.05801

[1] The precision of ρ_{x0} and ρ_{xx} is 1×10^{-5}

Table 3.1 Values of ρ_{x0} and ρ_{xx} for $T = 0$ and 0.5.

in Figs. 3.3 and 3.4 for the diagonal and horizontal correlation functions, respectively. The values for $x \leq 20$ and $T = 0.5$ are listed in Table 3.1. The correlation coefficient falls off more rapidly with x for increasing T as expected. The correlations were also calculated using the asymptotic expressions Eq. (1.63) and (1.64) which are shown by the crosses in Figs. 3.3 and 3.4. The maximum error for the diagonal correlation function is 0.14 for $T = 0.5$ and 0.07 for T=1.0, and for the horizontal correlation function is 0.15 for $T = 0.5$ and 0.07 for $T = 1.0$. The short-range correlations are shown versus temperature in Fig. 3.5. They are seen to be approximately constant for $T \leq 0.3$, in common with the behaviour of the TIA shown in Fig. 2.4.

In summary, the asymptotic approximations Eq. (1.59) and Eq. (1.61) for $T = 0$ are quite accurate, but the approximations Eq. (1.63) and Eq. (1.64) are not particularly accurate for $T < 1.0$.

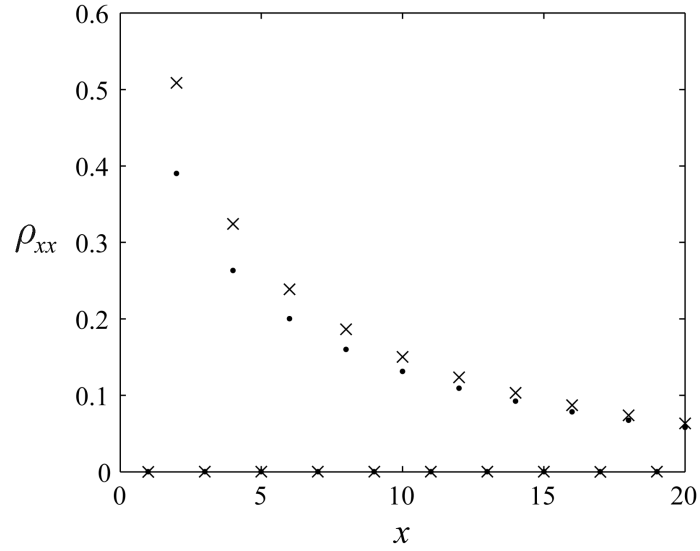

(a)

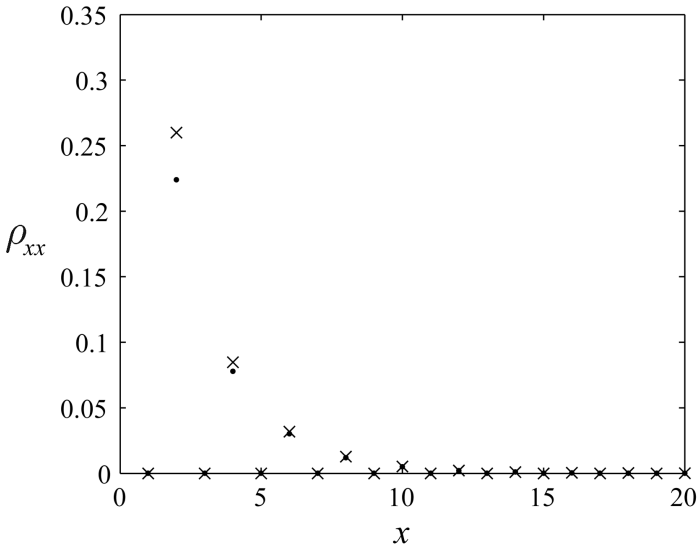

(b)

Figure 3.3 Diagonal correlation function calculated exactly by numerical integration (•) and using the approximation Eq. (1.64) (×), for (a) $T = 0.5$ and (b) $T = 1.0$.

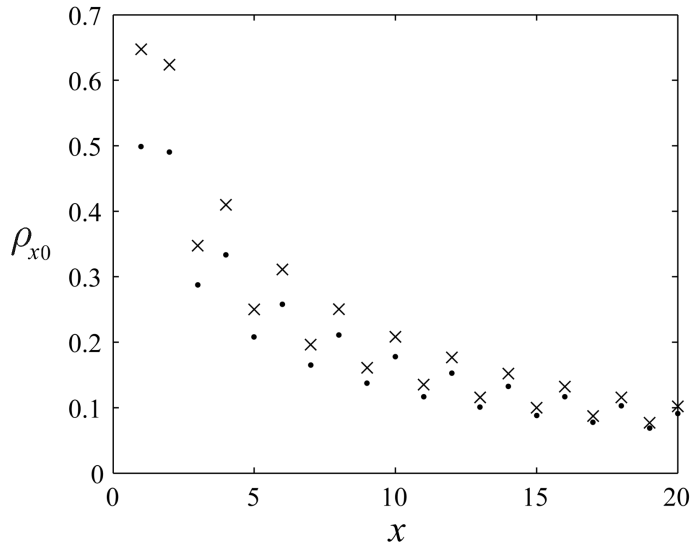

(a)

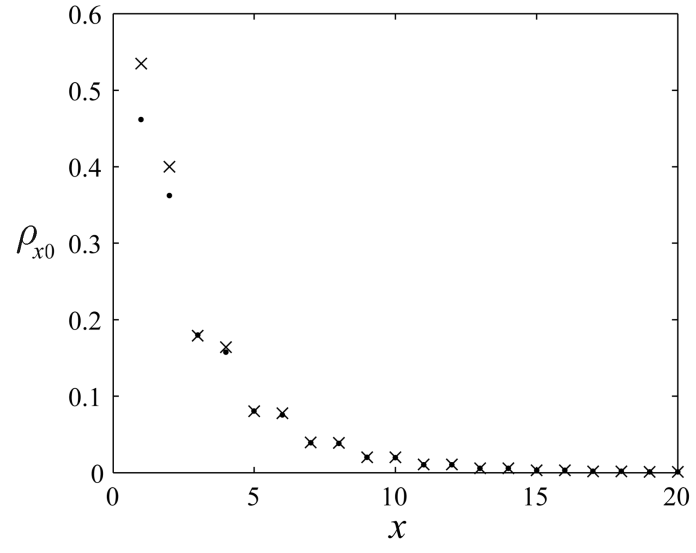

(b)

Figure 3.4 Horizontal correlation function calculated exactly by numerical integration (•) and using the approximation Eq. (1.63) (×) for (a) $T = 0.5$ and (b) $T = 1.0$.

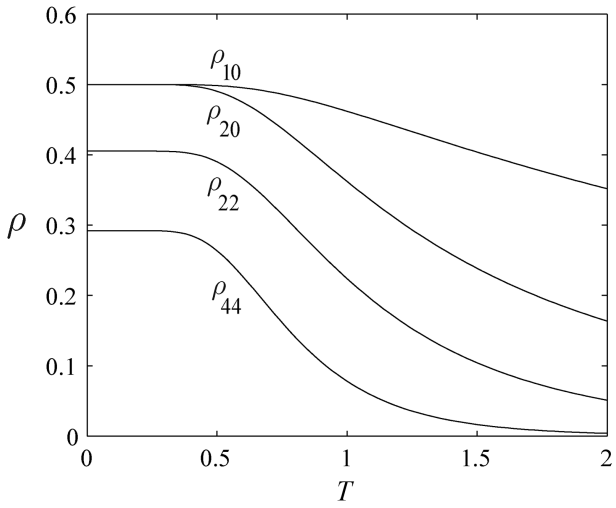

Figure 3.5 Low-order on-axis correlation coefficients versus temperature.

3.4 Off-axis correlation function

Little is known concerning the general correlation function ρ_{xy} apart from the special axial cases considered in the previous section. An important question is the extent to which ρ_{xy} is rotationally invariant, i.e. depends only on the distance

$$r_{xy} = \left(x^2 + y^2\right)^{1/2} \tag{3.16}$$

between the sites $(0, 0)$ and (x, y). The behaviour of the axial correlations for odd and even separations described in Section 3.3 is suggestive of a sublattice structure for ρ_{xy}, as was observed for the TIA discussed in Section 2.3. These aspects are examined in detail in this section.

3.4.1 Monte Carlo simulation

Since analytical results are not available for calculating the off-axis correlation coefficients, they were calculated using Monte Carlo (MC) simulation. MC simulation near the ground state of the FFS can be difficult, and was performed at all temperatures using an algorithm developed specifically for the FFS model by Kandel, Ben-Av and Domany (KBD) [KBAD90]. The algorithm of Zhang and Yang [ZY94] described in Section 2.3.1 applies the framework of the KBD algorithm to the TIA, with the adjustment that freeze-delete decisions are made on triangular plaquettes. The key concepts of the KBD algorithm were discussed in Section 2.3.1 and are described in detail in Refs. [KBAD90, CH94], so the al-

gorithm is only briefly outlined here.

The KBD algorithm begins partitioning the lattice into two sets of square plaquettes in a checkerboard fashion, one of which is chosen at random for each Monte Carlo sweep. Bonds between spins of a single plaquette are labelled as frozen or deleted depending on the orientation of spins in the square plaquette. Due to the lattice geometry, it is not possible for all four bonds, or just two bonds, of a plaquette to be satisfied. If three bonds of a plaquette are satisfied, the two bonds satisfied that are parallel to each other are frozen with probability $p = 1 - \exp(4K)$ while the other two bonds are deleted, and otherwise, all four bonds are deleted with probability $p = \exp(4K)$. If only one bond of the plaquette is satisfied, all four bonds are deleted with probability $p = 1$. Clusters of connected frozen bonds are then flipped in a Swendsen-Wang manner, followed by a Metropolis sweep to preserve ergodicity.

The FFS was simulated on an $L \times L$ lattice with toroidal boundary conditions, as depicted in Fig. 2.6 for the TIA. The lattice size L is multiple of 2 to avoid dislocations in on-axis periodicity across the boundaries. Generally $L = 180$ was used. Thermalization times used were generally 1×10^5 sweeps. Decorrelation times τ_{decorr} were calculated and correlation values calculated by sampling every τ_{decorr} sweeps and averaging over 1×10^4 samples. Standard deviations of correlation coefficients calculated from the MC simulations were typically about 2×10^{-4}. Comparison of on-axis correlation coefficients with those calculated by numerical integration gave a maximum absolute difference of 2×10^{-3}.

3.4.2 Off-axis sublattice structure

The form of the axial correlation functions presented in the previous section suggests that they belong to three sets that are smoothly varying functions of distance, i.e. (1) ρ_{xx} for x odd, (2) ρ_{x0} for x odd and (3) ρ_{xx} and ρ_{x0} for x even, where Eq. (1.62) has been used. This suggests, as is the case for the TIA in Section 2.3.2, that the off-axis correlations can be partitioned into three sublattices with a smoothly varying function of distance on each sublattice. This possibility was investigated by calculating the correlations ρ_{xy} for different temperatures and plotting them versus r_{xy}. The results are shown in Fig. 3.6 where the axial correlations are shown by open circles and those within each sublattice are joined by cubic spline interpolation (Appendix C), and the off-axis correlations are shown by dots. Inspection of the figure shows that the off-axis correlations do, indeed, fall close to the three curves defined by the axial correlations. Inspection of the indices (x, y) for ρ_{xy} on

each curve shows that the three sets, denoted sublattices 0, 1 and 2, are defined by

$$(x,y) \in \begin{cases} \text{sublattice } 0, & \text{for } x \text{ and } y \text{ even,} \\ \text{sublattice } 1, & \text{for } x \text{ and } y \text{ odd,} \\ \text{sublattice } 2, & \text{when } x \text{ and } y \text{ have different parity.} \end{cases} \tag{3.17}$$

The three sublattices are illustrated in Fig. 3.7. Sublattices 0 and 1 are square lattices with a lattice spacing of 2, and sublattice 2 is a square lattice with a lattice spacing of $\sqrt{2}$ and rotated by $45°$. The correlations are zero on sublattice 1, and are two different smoothly varying functions of r_{xy} on sublattices 0 and 2. The sublattices are consistent with the axial correlation behaviour. The maximum errors between the curves and the off-axis correlations in Fig. 3.6 are 0.04, 0.04 and 0.05, for $T = 0.0$, 0.5 and 1.0, respectively.

Referring to the symmetry relationships Eqs. (3.4)-(3.7) shows that on sublattices 0 and 1, $\rho^+_{xy} = \rho^-_{xy}$ and has even symmetry about $x = y$. On sublattice 2, ρ^+_{xy} has even symmetry and ρ^-_{xy} odd symmetry about $x = y$, and $\rho^+_{xy} = \pm\rho^-_{xy}$ depending on the parity of x and y.

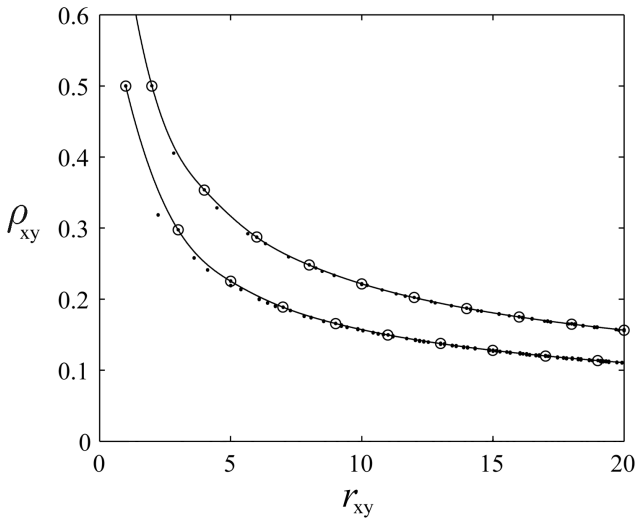
0.6
0.5
0.4
0.3
0.2
0.1
0
ρ_{xy}
0
5
10
15
20
r_{xy}

(a)

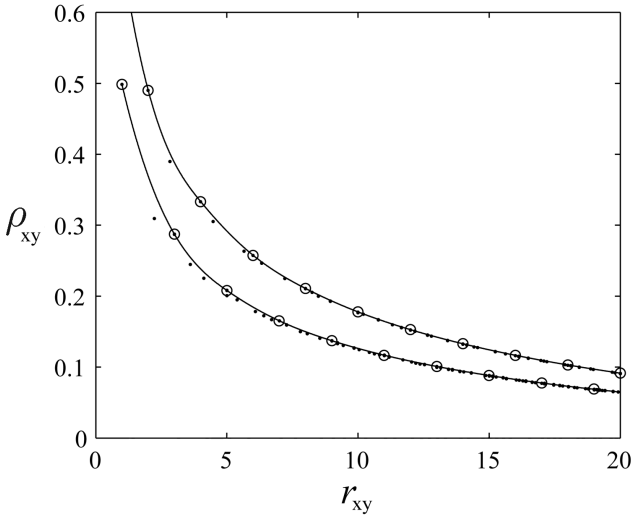
0.6
0.5
0.4
0.3
0.2
0.1
0
ρ_{xy}
0
5
10
15
20
r_{xy}

(b)

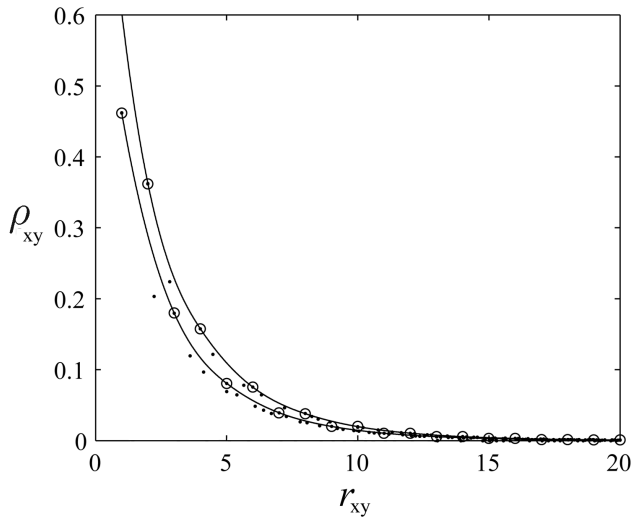

(c)

Figure 3.6 Axial correlation coefficients $\odot$ with spline interpolation (-), and the off-axis correlation coefficients ρ_{xy} calculated by MC simulation, (•), for (a) $T = 0$, (b) $T = 0.5$ and (c) $T = 1.0$. The upper curves are for sublattice 0, the lower curves for sublattice 2.

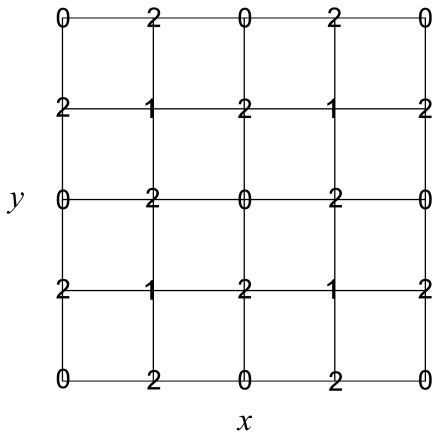

Figure 3.7 Sublattice partitioning of the off-axis correlation function.

3.4.3 Approximations

Figure 3.6 suggests that the off-axis correlations may be well-approximated by smooth interpolation in r of the on-axis values. Since the analytical expression Eq. (1.58) is available for the diagonal correlations at $T = 0$, the ground state is considered first.

For $T = 0$, writing the correlation function in terms of $r = r_{xy}$ as $\rho_i(r)$ where $i = 0, 1, 2$ denotes the sublattice, Eq. (1.61) suggests that $\rho_0(r) \approx 2^{1/2}\rho_2(r)$. Therefore, in Fig. 3.8 the correlations $\rho_0(r)$ and $2^{-1/2}\rho_2(r)$ are plotted versus $r^{-1/2}$, for all values of $r < 50$, together with the line $\rho(r) = (0.6450)^2 2^{3/4} r^{-1/2}$. Inspection of the figure shows that the correlations are a good fit to the line and the maximum difference is 0.05. The deviations of the values from the line for large r are comparable to the precision of the MC simulations described above. Eq. (1.61) can therefore be used to describe all the ground state correlations within this error. Using Eq. (1.58) with $r = 2^{1/2}x$, instead of Eq. (1.61), gives a slightly better representation with a maximum error of 0.04.

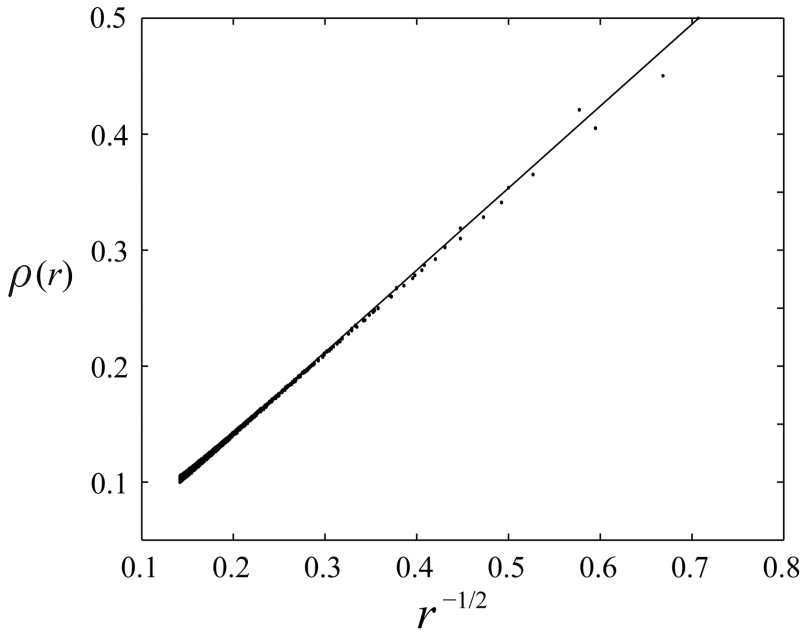

Figure 3.8 Ground state correlations $\rho_0(r)$ and $2^{-1/2}\rho_2(r)$ versus $r^{-1/2}$ and the line $\rho(r) = (0.6450)^2 2^{3/4} r^{-1/2}$.

For $T > 0$, the approximate expressions given in Section 1.2.5 do not provide high precision values for the axial correlations. Therefore, accurate values for all the correlations for $T > 0$ must be obtained by evaluating Eqs. (A.34) and (1.55) using numerical integration followed by interpolation. As described above, this gives a maximum error of 0.04 for $T = 0.5$ and 0.05 for $T = 1.0$.

3.4.4 Rotational invariance as a function of temperature

The results presented above show good rotational invariance at $T = 0$ and approximate rotational invariance for $0 < T \leq 1.0$. For larger temperatures the correlations are small and deviations from rotational invariance in terms of differences between correlations at the same radii are small. This is shown in Fig. 3.9(a) where the difference between the diagonal correlation coefficients ρ_{xx} and those on the horizontal axis calculated at the same value of r by linear interpolation on sublattice 0, denoted $\Delta(r, T)$, is shown versus temperature for $x = 2, 4, 6$. The differences are seen to be small and decrease with increasing temperature. Since the correlations are small, it is informative to investigate the ratio, rather than the difference, at the same radii. Some information on the ratio can be obtained using the asymptotic expressions Eqs. (1.63) and (1.64) for large x and large T for the diagonal and horizontal correlation coefficients. Using these expressions shows that the ratio of the diagonal to horizontal correlation coefficients on sublattice 0 for the same value of r, denoted $R(r, T)$, is

$$R(r,T) = (2\alpha)^{-1/4}(1+\alpha)^{-1/4} z_1^{-r} z_0^{r/\sqrt{2}}, \quad r \gg 0, T \gg 0. \tag{3.18}$$

Note that, as discussed in Section 3.3, Eqs. (1.63) and (1.64) have the correct behaviour at $T = 0$ except for the prefactors, and since the prefactors cancel in $R(r, T)$, Eq. (3.18) is expected to be accurate for all T. Using the definitions of α, z_0 and z_1 shows that

$$\begin{aligned} \alpha(T) &\sim 1 + 4\exp(-4/T), && T \to 0 \\ z_0(T) &\sim 1 - 2^{3/2}\exp(-2/T), && T \to 0 \\ z_1(T) &\sim 1 - 2\exp(-2/T), && T \to 0 \end{aligned} \tag{3.19}$$

and

$$\begin{aligned} \alpha(T) &\sim (T/2)^2, && T \to \infty \\ z_0(T) &\sim 2/T^2, && T \to \infty \\ z_1(T) &\sim 1/T, && T \to \infty. \end{aligned} \tag{3.20}$$

Substituting Eq. (3.19) into Eq. (3.18) gives

$$R(r,T) \sim \frac{1}{1 + (3/2)\exp(-4/T)}, \quad T \to 0, \tag{3.21}$$

i.e. $R(r,T) \sim 1$ for $T \to 0$, confirming rotational invariance for small temperatures. Substituting Eq. (3.20) into Eq. (3.18) gives

$$R(r,T) \sim 2^{5/4}\, 2^{r/\sqrt{2}}\, T^{-((\sqrt{2}-1)r+1)}, \quad T \to \infty. \tag{3.22}$$

The exponent of T in Eq. (3.22) is negative so that $R(r,T) \to 0$ as $T \to \infty$, the decay rate increasing with increasing r, and thus rotational invariance breaks down for large T. The ratio of the correlation coefficients ρ_{22}, ρ_{44} and ρ_{66} to those on the horizontal axis calculated at the same value of r by linear interpolation from the adjacent sites on sublattice 0 is plotted in Fig. 3.9(b). The anticipated behaviour is observed with the ratio being close to 1 for $T < 1$, except for a small deviation for the smallest value of r, and approaching zero for large T. However, as noted above, since the difference between the correlations is small for large T, an assumption of rotational invariance will generally be satisfactory for most numerical applications.

3.4.5 Correlation length

The correlation length is a useful parameter that describes the spatial scale of the correlations. For the FFS the correlation length grows rapidly as the temperature approaches zero, and approaches zero as $T \to \infty$. The correlation length $\xi(T)$ is defined here in terms of the physical distance r, i.e., referring to Eqs. (1.63) and (1.64), by

$$\rho(r,T) \sim B(T)\, r^{-1/2} e^{-r/\xi(T)}, \quad r \to \infty, \tag{3.23}$$

where $B(T)$ is a constant. Since the correlation function is rotationally invariant for small T but not for large T, the same behaviour for the correlation lengths is anticipated. Note that the inaccurate prefactors in Eqs. (1.63) and (1.64) for small T do not effect the correlation length. Referring to Eq. (1.64), the correlation length on sublattice 0 on the diagonal axis, denoted $\xi_d(T)$, is given by

$$\xi_d(T) = -\frac{2^{1/2}}{\ln(z_0(T))}. \tag{3.24}$$

Similarly, referring to Eq. (1.63), the correlation lengths on sublattices 0 and 2 on the horizontal axis are identical, and are denoted here by $\xi_h(T)$ and given by

$$\xi_h(T) = -\frac{1}{\ln(z_1(T))}. \tag{3.25}$$

The correlation lengths in the horizontal and diagonal directions are calculated using Eqs. (3.24) and (3.25) and shown versus temperature in Fig. 3.10. It is evident that the correlation lengths are almost identical for $T < 1$ but diverge for larger T.

More information on the correlation lengths can be obtained by studying $\xi_d(T)$ and $\xi_h(T)$

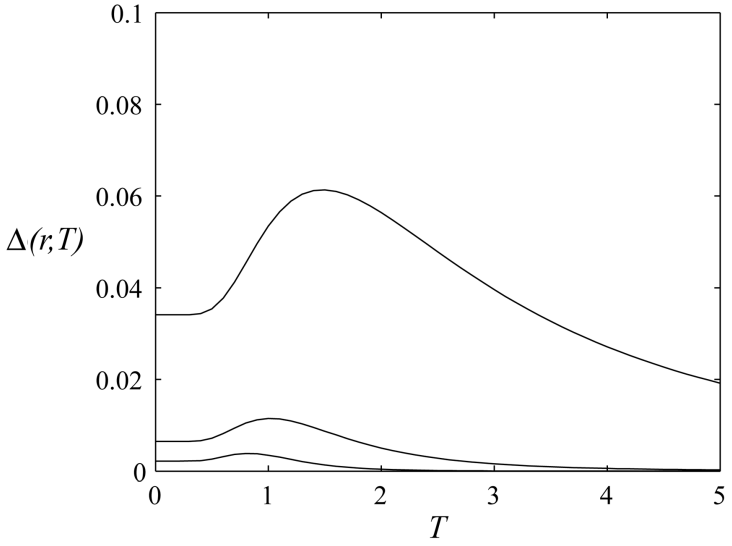

(a)

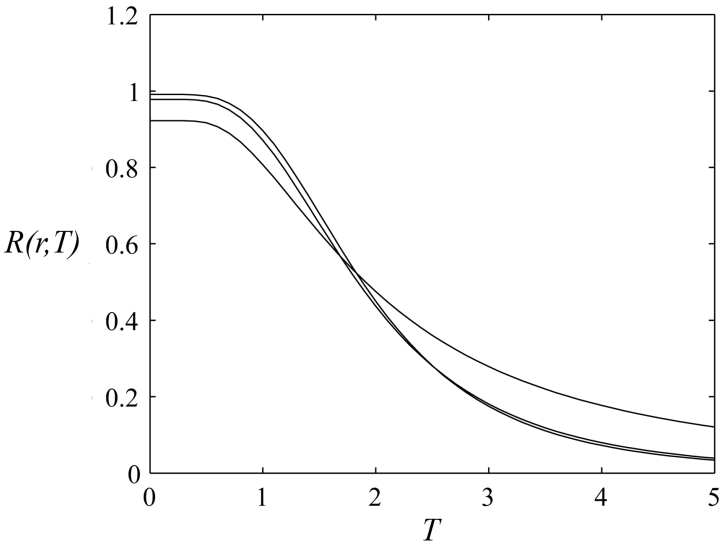

(b)

Figure 3.9 (a) Difference $\Delta(r,T)$ between the diagonal and horizontal correlation function for the same radii versus temperature (upper curve $r = 2\sqrt{2}$, middle curve $r = 4\sqrt{2}$, lower curve $r = 6\sqrt{2}$). (b) Ratio $R(r,T)$ of the diagonal to horizontal correlation function for the same radii versus temperature (lower curve on left $r = 2\sqrt{2}$, middle curve on left $r = 4\sqrt{2}$, upper curve on left $r = 6\sqrt{2}$).

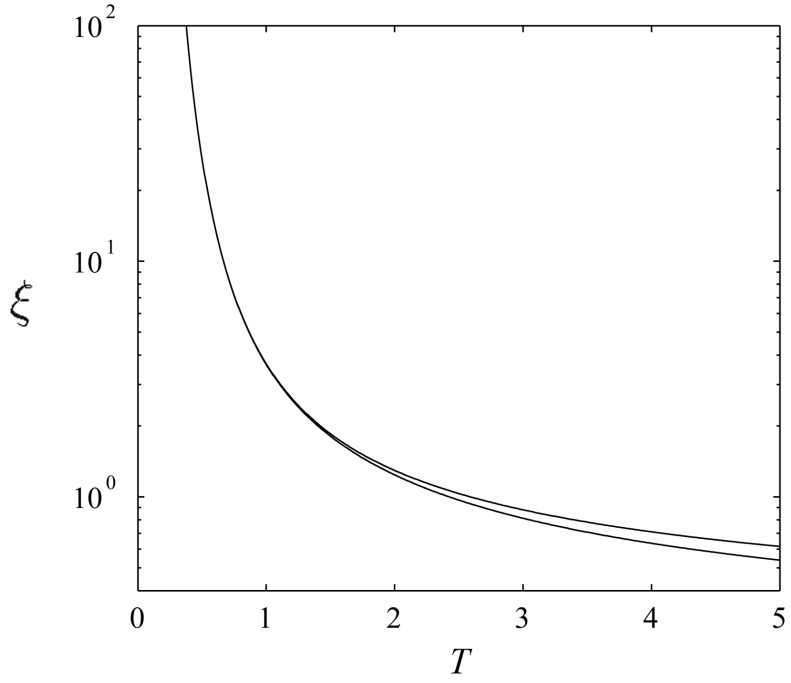

Figure 3.10 Diagonal (lower curve) and horizontal (upper curve) correlation lengths versus temperature.

for small and large temperatures. Consider first the small T behaviour. Substituting Eq. (3.19) into Eqs. (3.24) and (3.25) gives

$$\begin{aligned} \xi_d(T) &\sim (1/2)\exp(2/T), \quad T \to 0, \\ \xi_h(T) &\sim (1/2)\exp(2/T), \quad T \to 0. \end{aligned} \tag{3.26}$$

Thus the correlation lengths are the same in the horizontal and diagonal directions for $T \to 0$. Consider now the large T behaviour. Substituting Eq. (3.20) into Eqs. (3.24) and (3.25) gives

$$\begin{aligned} \xi_d(T) &\sim 2^{-1/2}[\ln(T)]^{-1}, \quad T \to \infty, \\ \xi_h(T) &\sim [\ln(T)]^{-1}, \qquad\quad T \to \infty. \end{aligned} \tag{3.27}$$

Equation. (3.27) shows that the diagonal correlation length is smaller, by a factor of $1/\sqrt{2}$, than the horizontal correlation length, and thus the correlation length is not rotationally invariant, for large temperatures. However, this will generally be of little numerical significance since the correlation lengths are so small for these temperatures.

3.5 Conclusions

The correlation behavior of the fully frustrated square Ising model has been studied in detail through numerical evaluation of exact analytical results and Monte Carlo simulation. There are two sets of correlation functions as a result of two unique origins. Symmetry relationships for the general correlation functions are derived. These show that the two sets are related and that all correlations can be described in terms of one set in a 45° sector. As is seen with the TIA, the correlations are approximately constant for $T < 0.4$. The approximate expressions for the axial correlations are quite accurate for $T = 0$ and large temperatures but not as accurate for $0 < T < 1$. The lattice can be partitioned into 3 sublattices such that the correlation function is zero on one sublattice and is, to a good approximation, a smoothly varying function on the other two sublattices. The correlation function is to a good approximation rotationally invariant for $0 < T < 1$ within each sublattice and within the symmetry relationships described in Section 3.2. For larger temperatures the correlation function is not rotationally invariant. However, since the correlations for these temperatures are so small, an assumption of rotational invariance would generally have no detrimental effect on numerical calculations using correlation coefficients. Therefore, an accurate description of the correlation function can be obtained in terms of only radial separation and the sublattice, and interpolation from the axial values. The correlation length is rotationally invariant in terms of physical distance in the lattice for $T < 1$, but not for large T.

Chapter 4

Cylindrically averaged diffraction by disordered polycrystalline fibres

4.1 Introduction

Diffraction by disordered polycrystalline fibres is an ensemble average over the realizations of the disordered system, and is cylindrically averaged over the variable orientations of crystallite arrays about the fibre axis. Two methods can be used to calculate the diffraction from such systems. One is to generate an ensemble of system realizations, calculate the diffraction from each and then average the diffraction numerically. This process, in general, can be computationally intensive and is susceptible to undersampling of the configuration space. The other, more favorable method is to perform the ensemble averaging analytically by formulating expressions for the diffraction from a model structure. Theory for calculating the diffraction from systems with a variety of types of disorder has been developed. These include uncorrelated and correlated lattice disorder, where the positions of molecules are distorted from the lattice sites [SM96a, SM96b], and uncorrelated substitution disorder, where different molecule types are substituted at random at sites of the crystallite [SM95]. Extensive analysis of the diffraction from quasicrystals, structures which exhibit local order but lack long-range translational symmetry, have also been performed [BH99].

As described in Section 1.6, the myosin lattice of vertebrate muscle forms a disordered polycrystalline fibre in which the myosin filaments follow the statistics of the triangular Ising antiferromagnet (TIA). X-ray fibre diffraction patterns from muscle are therefore described by cylindrically averaged diffraction from a system exhibiting correlated substitution disorder. The general theory for diffraction by such a system is developed in this

chapter.

The disorder in the crystallites in such a fibre is described by the two-point correlation function for the two kinds of scatterers in the two-dimensional lattice transverse to the fibre axis. Two-point correlation functions for two simple geometrically frustrated systems, the triangular Ising antiferromagnet (TIA) and the fully frustrated square Ising model (FFS), were extensively studied in Chapters 2 and 3. In this chapter, the term spin used in the context of the TIA and FFS is replaced by the term scatterer. The TIA and FFS are considered simple because there are only two possible scatterer types within the fibre. Theory is developed to describe diffraction from a system with any number of scatterer types exhibiting correlated substitution disorder. Lattice disorder is incorporated into the calculations, allowing diffraction from systems with combined lattice and correlated substitution disorder to be calculated. The theory developed is investigated by numerical calculation to characterize the effects of correlated substitution disorder in fibres with TIA-type statistics. The theory developed in this chapter is used in Chapter 5 to study diffraction by the myosin lattice of vertebrate muscle.

In the next section theory is developed for calculating the cylindrically averaged diffraction by an ensemble of crystallites containing helical molecules with correlated substitution disorder. In Section 4.3 these results are applied to the case of TIA disorder. In Section 4.4 simulated fibre diffraction patterns are calculated using simple helical molecules to study the characteristics of the diffraction. Concluding remarks are made in Section 4.5.

4.2 Theory

A disordered polycrystalline fibre is considered as described in Section 1.5.3. Such a fibre consists of crystalline domains, or crystallites, that aggregate parallel to the fibre axis, and are randomly positioned in the lateral plane and randomly rotated about the fibre axis. A large coherence length along the z-direction is assumed so that the diffraction vanishes except on the planes $Z = l/c$ where l is an integer. Assuming that $F_{jk}(\mathbf{R})$ and $\mathbf{d}_{jk}$ have stationary statistics, and that $F_{jk}(\mathbf{R})$ and $\mathbf{d}_{jk}$ are independent, the cylindrically averaged intensity is given by Eq. (1.155) with the ensemble averaged intensity given by Eq. (1.156).

4.2.1 Correlated substitution disorder

Consider first the case where there is substitution disorder but no lattice disorder, i.e. $\mathbf{d}_{jk} = 0$ and $\langle \exp\left[i2\pi\mathbf{R}\cdot(\mathbf{d}_{jk}-\mathbf{d}_{00})\right]\rangle_d = 1$. Yoon [Yoo09] showed that Eq. (1.156) then reduces to

$$I(\mathbf{R}) = \langle N\rangle \sum_j \sum_k t(\mathbf{r}_{jk}) \left[|\langle F(\mathbf{R})\rangle_d|^2 + \rho_{jk}(\langle |F(\mathbf{R})|^2\rangle_d - |\langle F(\mathbf{R})\rangle_d|^2)\right] \exp(i2\pi\mathbf{R}\cdot\mathbf{r}_{jk}), \quad (4.1)$$

where ρ_{jk} is the two-point correlation between the molecules, or equivalently between the scattering factors, at sites separated by indices (j,k). For Q kinds of molecule with scattering factors $F^{(\alpha)}(\mathbf{R})$, with $\alpha = 1,2,\ldots,Q$, each occurring with probability P_α, the averages in Eq. (4.1) are

$$\langle |F(\mathbf{R})|^2 \rangle_d = \sum_\alpha P_\alpha \left| F^{(\alpha)}(\mathbf{R}) \right|^2, \tag{4.2}$$

and

$$|\langle F(\mathbf{R}) \rangle_d|^2 = \left| \sum_\alpha P_\alpha F^{(\alpha)}(\mathbf{R}) \right|^2. \tag{4.3}$$

The Q molecules are assumed to have the same u_v helix symmetry. The scattering factor $F(\mathbf{R}) = F(R,\psi,l/c)$ of a molecule is written in the standard form in Eq. (1.145) with Fourier-Bessel structure factors $G_{nl}(R)$ given by Eq. (1.146). Substituting Eq. (1.145) into the averages in Eqs. (4.2) and (4.3) and assuming equal probabilities for each molecule gives

$$\left\langle |F(\mathbf{R})|^2 \right\rangle_d = \frac{1}{Q} \sum_n \sum_m \exp\left(i[n-m][\psi + \pi/2]\right) \sum_\alpha G_{nl}^{(\alpha)}(R) G_{ml}^{(\alpha)*}(R), \tag{4.4}$$

and

$$|\langle F(\mathbf{R}) \rangle_d|^2 = \frac{1}{Q^2} \sum_n \sum_m \exp\left(i[n-m][\psi + \pi/2]\right) \sum_\alpha G_{nl}^{(\alpha)}(R) \sum_\beta G_{ml}^{(\beta)*}(R), \tag{4.5}$$

where the $G_{nl}^{(\alpha)}(R)$ denote the Fourier-Bessel structure factors of the α^{th} molecule.

Using Eqs. (1.128) and (4.1), the cylindrically averaged diffraction from the fiber is

$$\begin{aligned} I_l(R) \quad = \quad & \frac{\langle N \rangle}{2\pi} \sum_j \sum_k t(\mathbf{r}_{jk}) \int_0^{2\pi} \Big\{ |\langle F(\mathbf{R}) \rangle_d|^2 \\ & + \rho_{jk} \left[\left\langle |F(\mathbf{R})|^2 \right\rangle_d - |\langle F(\mathbf{R}) \rangle_d|^2 \right] \Big\} \exp(i 2\pi \mathbf{R} \cdot \mathbf{r}_{jk}) \mathrm{d}\psi. \end{aligned} \tag{4.6}$$

Following Yoon [Yoo09] it is useful to separate the diffracted intensity into "Bragg" and "diffuse" components, i.e.

$$I_l(R) = I_l^B(R) + I_l^D(R), \tag{4.7}$$

where

$$I_l^B(R) = \frac{\langle N \rangle}{2\pi} \sum_j \sum_k t(\mathbf{r}_{jk}) \int_0^{2\pi} |\langle F(\mathbf{R}) \rangle_d|^2 \exp(i 2\pi \mathbf{R} \cdot \mathbf{r}_{jk}) \mathrm{d}\psi, \tag{4.8}$$

and

$$I_l^D(R) = \frac{\langle N \rangle}{2\pi} \sum_j \sum_k \rho_{jk} t(\mathbf{r}_{jk}) \int_0^{2\pi} \left[\left\langle |F(\mathbf{R})|^2 \right\rangle_d - |\left\langle F(\mathbf{R}) \right\rangle_d|^2 \right] \exp(i2\pi \mathbf{R} \cdot \mathbf{r}_{jk}) \mathrm{d}\psi. \quad (4.9)$$

As a result of the Ewald sum in Eq. (4.8), the Bragg diffraction is concentrated around the reciprocal lattice points with fixed reflection profiles and is zero elsewhere, and thus has the character of diffraction from an undistorted system. The diffuse diffraction depends on the form of the correlation function, is continuous and exists at all positions in reciprocal space. The diffuse diffraction is smoothly varying for weak correlations and forms broad peaks at the reciprocal lattice points that become increasingly sharp as the correlations strengthen. The effect is to broaden the "Bragg" reflections in the full diffraction pattern. The separation into Bragg and diffuse diffraction is discussed further by Yoon [Yoo09].

Substituting Eqs. (4.4) and (4.5) into Eqs. (4.8) and (4.9), and noting that since $\mathbf{r}_{jk}$ is perpendicular to the z-axis,

$$\mathbf{R} \cdot \mathbf{r}_{jk} = R r_{jk} \cos(\psi - \phi_{jk}), \quad (4.10)$$

where ϕ_{jk} is the angle between the vector $\mathbf{r}_{jk}$ and the x-axis, and $r_{jk} = |\mathbf{r}_{jk}|$, allows the integral over ψ to be evaluated. Eqs. (4.8) and (4.9) then become

$$I_l^B(R) = \frac{\langle N \rangle}{Q^2} \sum_j \sum_k t(\mathbf{r}_{jk}) \sum_n \sum_m h_{jkmn}(R) \sum_\alpha G_{nl}^{(\alpha)}(R) \sum_\beta G_{ml}^{(\beta)*}(R), \quad (4.11)$$

and

$$\begin{aligned} I_l^D(R) &= \frac{\langle N \rangle}{Q^2} \sum_j \sum_k t(\mathbf{r}_{jk}) \rho_{jk} \\ &\quad \times \sum_n \sum_m h_{jkmn}(R) \sum_\alpha G_{nl}^{(\alpha)}(R) \left[(Q-1) G_{ml}^{(\alpha)*}(R) - \sum_{\beta \neq \alpha} G_{ml}^{(\beta)*}(R) \right], \end{aligned} \quad (4.12)$$

where the quantity $h_{jkmn}(R)$ is the integral over ψ given by

$$h_{jkmn} = \frac{1}{2\pi} \int_0^{2\pi} \exp\left(i[n-m][\Psi + \pi/2]\right) \exp\left(i2\pi R r_{jk} \cos(\Psi - \phi_{jk})\right) \mathrm{d}\Psi. \quad (4.13)$$

With the change of variables $\Psi' = \Psi - \phi_{jk}$, Eq. (4.13) becomes

$$\begin{aligned} h_{jkmn} &= \frac{1}{2\pi} \int_0^{2\pi} \exp\left(i2\pi R r_{jk} \cos \Psi'\right) \exp\left(i[n-m][\Psi' + \phi_{jk} + \pi/2]\right) \mathrm{d}\Psi' \\ &= \frac{1}{2\pi} \exp\left(i[n-m][\phi_{jk} + \pi/2]\right) \int_0^{2\pi} \exp\left(i2\pi R r_{jk} \cos \Psi'\right) \exp\left(i[n-m]\Psi'\right) \mathrm{d}\Psi'. \end{aligned} \quad (4.14)$$

With the definition for the n-th order Bessel function of the first kind [Bow38],

$$J_n(z) = \frac{1}{2\pi i^n} \int_0^{2\pi} \exp(iz\cos\psi)\exp(in\psi)\mathrm{d}\psi, \tag{4.15}$$

Eq. (4.14) reduces to

$$\begin{aligned} h_{jkmn} &= \frac{i^{(n-m)}}{2\pi}\exp(i[n-m]\psi_{jk}) \int_0^{2\pi} \exp(i[n-m]\Psi')\exp(i2\pi R r_{jk}\cos\Psi')d\Psi' \\ &= J_{m-n}(2\pi R r_{jk})\exp\left(i[n-m]\psi_{jk}\right). \end{aligned} \tag{4.16}$$

Equations (4.11) and (4.12) describe the intensity diffracted by a fibre containing crystallites of helical molecules exhibiting correlated substitution disorder. The Q molecules may, in general, be different. However, in many cases there will be a single molecule that adopts a number of different positions relative to the crystal lattice. Two special cases are considered where there is one molecule that adopts one of two positions.

In the first case, the first molecule is in a reference position and has Fourier-Bessel structure factors $G_{nl}(R)$, and the second molecule is the same but is rotated by $\Delta\phi$ about, and shifted by Δz along, the z-axis relative to the first. Therefore, $G^{(1)}_{nl}(R) = G_{nl}(R)$ and referring to Eq. (1.146)

$$G^{(2)}_{nl}(R) = G_{nl}(R)\exp(i[2\pi l\Delta z/c - n\Delta\phi]), \tag{4.17}$$

and substitution into Eqs. (4.11) and (4.12) gives

$$\begin{aligned} I^B_l(R) &= \frac{\langle N\rangle}{4}\sum_j\sum_k t(\mathbf{r}_{jk})\sum_n\sum_m h_{jkmn}(R)G_{nl}(R)G^*_{ml}(R) \\ &\quad\times\left[1+\exp(i[2\pi l\Delta z/c - n\Delta\phi])\right]\left[1+\exp(-i[2\pi l\Delta z/c - m\Delta\phi])\right], \end{aligned} \tag{4.18}$$

and

$$\begin{aligned} I^D_l(R) &= \frac{\langle N\rangle}{4}\sum_j\sum_k t(\mathbf{r}_{jk})\rho_{jk}\sum_n\sum_m h_{jkmn}(R)G_{nl}(R)G^*_{ml}(R) \\ &\quad\times\left[1-\exp(i[2\pi l\Delta z/c - n\Delta\phi])\right]\left[1-\exp(-i[2\pi l\Delta z/c - m\Delta\phi])\right]. \end{aligned} \tag{4.19}$$

The nature of the Bragg and diffuse diffraction depends on the values of Δz and $\Delta\phi$. For example, the diffuse diffraction vanishes if

$$2\pi l\Delta z/c - n\Delta\phi = 2\pi p, \quad \forall n \tag{4.20}$$

where p is an integer. For example, if $\Delta z = 0$ and $\Delta\phi = (2\pi sv/u)$, where s is an integer,

then the left-hand side of Eq. (4.20) reduces to

$$-n\Delta\phi = \left(m - \frac{l}{u}\right) 2\pi s, \tag{4.21}$$

where the helix selection rule, Eq. (1.141), has been used. If l is a multiple of u then the right-hand side of Eq. (4.21) is a multiple of 2π so that the diffuse diffraction vanishes on these layer lines. Similar reasoning shows that if $\Delta\phi = 0$ and $\Delta z = c/s$ for any integer s, then the diffuse diffraction vanishes on layer lines l that are a multiple of s. Other combinations of Δz and $\Delta\phi$ give similar effects.

Similarly, inspection of Eq. (4.18) shows that the Bragg diffraction vanishes if

$$2\pi l\Delta z/c - n\Delta\phi = (2p+1)\pi, \quad \forall n \tag{4.22}$$

where p is an integer. For example, if $\Delta\phi = 0$ and $\Delta z = c/(2s)$ for any integer s, then the Bragg diffraction vanishes on layer lines l that are an odd multiple of s. Examples of these characteristics are shown in Section 4.4.

In the second case, the second molecule is rotated by 180° about a line in the xy-plane relative to the first. This is often referred to as "directional disorder" and the two molecules referred to as being "up" and "down". The second molecule can be described as being the first molecule rotated by 180° about the x-axis followed by an appropriate rotation $\Delta\phi$ and shift Δz. The Fourier-Bessel structure factor of the second molecule is then

$$G^{(2)}_{nl}(R) = G^*_{nl}(R)\exp(i[2\pi l\Delta z/c - n\Delta\phi]), \tag{4.23}$$

and substitution into Eqs. (4.11) and (4.12) gives

$$\begin{aligned} I^B_l(R) &= \frac{\langle N\rangle}{4}\sum_j\sum_k t(\mathbf{r}_{jk})\sum_n\sum_m h_{jkmn}(R)\left[G_{nl} + G^*_{nl}\exp(i[2\pi l\Delta z/c - n\Delta\phi])\right] \\ &\quad \times \left[G^*_{ml} + G_{ml}\exp(-i[2\pi l\Delta z/c - m\Delta\phi])\right], \end{aligned} \tag{4.24}$$

and

$$\begin{aligned} I^D_l(R) &= \frac{\langle N\rangle}{4}\sum_j\sum_k t(\mathbf{r}_{jk})\rho_{jk}\sum_n\sum_m h_{jkmn}(R)\left[G_{nl} - G^*_{nl}\exp(i[2\pi l\Delta z/c - n\Delta\phi])\right] \\ &\quad \times \left[G^*_{ml} - G_{ml}\exp(-i[2\pi l\Delta z/c - m\Delta\phi])\right]. \end{aligned} \tag{4.25}$$

4.2.2 Lattice disorder

Lattice disorder corresponds to non-zero vectors $\mathbf{d}_{jk}$ that describe distortions of the lattice, i.e. deviations in the positions of the molecules away from the sites of the undistorted lattice. Correlated lattice disorder is expected to occur to at least some degree in most real systems. Models for correlated lattice disorder and the cylindrically averaged diffraction have been discussed in detail by Stroud and Millane [SM96a, SM96b]. In that model, a two-dimensional lattice is distorted into three dimensions, which is appropriate for a system containing rigid, orientated molecules as is considered here. Correlations are therefore in the lateral direction only but the distortions are in three dimensions. The correlations are described by two circularly symmetric imposed correlation fields $\rho_{\text{lat}}(r)$ and $\rho_{\text{axial}}(r)$ that describe correlations between the lateral and axial distortions of the lattice, respectively. The Cartesian components of the distortions are assumed to be independently Gaussian distributed with the covariances of the components in the lateral plane being equal. The lateral and axial single site variances are denoted σ^2_{lat} and σ^2_{axial}, respectively. It can then be shown that [SM96a]

$$\langle \exp\left[i2\pi\mathbf{R}\cdot(\mathbf{d}_{jk}-\mathbf{d}_{00})\right]\rangle_d = w_{\text{lat}}(R,r_{jk})w_{\text{axial}}(Z,r_{jk}), \tag{4.26}$$

where

$$w_{\text{lat}}(R,r) = \exp\left(-4\pi^2R^2\sigma^2_{\text{lat}}\left[1-\rho_{\text{lat}}(r)\right]\right), \tag{4.27}$$

and

$$w_{\text{axial}}(Z,r) = \exp\left(-4\pi^2R^2\sigma^2_{\text{lat}}\left[1-\rho_{\text{axial}}(r)\right]\right). \tag{4.28}$$

Substituting Eq. (4.26) into Eq. (1.156) and with the analysis of the previous section, the effects of correlated lattice disorder can be easily incorporated, and Eqs. (4.11) and (4.12) are replaced by

$$\begin{aligned} I_l^B(R) &= \frac{\langle N\rangle}{Q^2}\sum_j\sum_k w_{\text{lat}}(R,r_{jk})w_{\text{axial}}(l/c,r_{jk})t(\mathbf{r}_{jk}) \\ &\quad\times\sum_n\sum_m h_{jkmn}(R)\sum_\alpha G_{nl}^{(\alpha)}(R)\sum_\beta G_{ml}^{(\beta)*}(R), \end{aligned} \tag{4.29}$$

and

$$\begin{aligned} I_l^D(R) &= \frac{\langle N\rangle}{Q^2}\sum_j\sum_k w_{\text{lat}}(R,r_{jk})w_{\text{axial}}(l/c,r_{jk})t(\mathbf{r}_{jk})\rho_{jk} \\ &\quad\times\sum_n\sum_m h_{jkmn}(R)\sum_\alpha G_{nl}^{(\alpha)}(R)\left[(Q-1)G_{ml}^{(\alpha)*}(R)-\sum_{\beta\neq\alpha}G_{ml}^{(\beta)*}(R)\right]. \end{aligned} \tag{4.30}$$

Note, however, that now the separation into Bragg and diffuse diffraction is not useful since Eq. (4.29) contains correlations through the terms $w_{\text{lat}}(R, r_{jk})$ and $w_{\text{axial}}(l/c, r_{jk})$. It is therefore appropriate to consider just the total diffraction $I_l(R) = I_l^B(R) + I_l^D(R)$ as is done by Stroud and Millane [SM96a]. Briefly, the effect of correlated lattice disorder is to broaden the Bragg reflections, the degree of broadening increasing with increasing distance from the origin of reciprocal space (resolution). At high resolution adjacent peaks broaden into one another producing slowly varying (diffuse) diffraction. The degree of broadening and the rate at which it increases with resolution depends on the interplay between the single site variances and the correlation lengths. The reader is referred to Stroud and Millane [SM96a] for the details. Lattice disorder is not considered further here, suffice that it can be included if required by using Eqs. (4.29) and (4.30).

4.2.3 Lattice symmetry

As noted by Stroud and Millane [SM96a], the symmetry of the lattice can be used to reduce the number of terms in the summations in Eqs. (4.11) and (4.12). If the correlation function ρ_{jk} and the autocorrelation of the shape function are both circularly symmetric then the (j, k) terms in Eqs. (4.11) and (4.12) for which r_{jk} is the same can be combined. The triangular lattice is considered here and the convention that the angle between **a** and **b** is $\pi/3$ is adopted. Combining the six symmetry related lattice points with the same r_{jk} allows the summations to be restricted to the region $j \geq 0$ and $k \geq 0$, i.e. $0 \leq \phi_{jk} < \pi/3$, and Eqs. (4.11) and (4.12) can be written as

$$\begin{aligned} I_l^B(R) &= \frac{\langle N \rangle}{Q^2} \sum_{j \geqslant 0} \sum_{k \geqslant 0} t(r_{jk}) \sum_n \sum_m J_{m-n}(2\pi R r_{jk}) \\ &\quad \times \sum_\alpha G_{nl}^{(\alpha)}(R) \sum_\beta G_{ml}^{(\beta)*}(R) \exp\left(i[n-m]\phi_{jk}\right) \sum_{p=0}^{5} \exp\left(i[n-m]p\pi/3\right), \end{aligned} \tag{4.31}$$

and

$$\begin{aligned} I_l^D(R) &= \frac{\langle N \rangle}{Q^2} \sum_{j \geq 0} \sum_{k \geq 0} t(r_{jk}) \rho_{jk} \sum_n \sum_m J_{m-n}(2\pi R r_{jk}) \\ &\quad \times \sum_\alpha G_{nl}^{(\alpha)}(R) \left[(Q-1) G_{ml}^{(\alpha)*}(R) - \sum_{\beta \neq \alpha} G_{ml}^{(\beta)*}(R) \right] \\ &\quad \times \exp\left(i[n-m]\phi_{jk}\right) \sum_{p=0}^{5} \exp\left(i[n-m]p\pi/3\right), \end{aligned} \tag{4.32}$$

where $t(\mathbf{r}_{jk}) \equiv t(r_{jk})$ with the assumption of circularly symmetry. Since

$$\sum_{p=0}^{5} \exp\left(i[n-m]p\pi/3\right) = \begin{cases} 6, \text{ if } n-m \text{ is divisible by 6} \\ 0, \text{ otherwise,} \end{cases} \tag{4.33}$$

all terms in Eqs. (4.31) and (4.32) for which $n-m$ is not divisible by six vanish. Furthermore, the terms in Eqs. (4.31) and (4.32) corresponding to r_{jk} that have reflection symmetry in the line $\phi = \pi/6$ can be combined and the summation over k restricted to the interval $0 \leq k \leq j$. Since only terms for which $n-m$ are divisible by 6 contribute to the intensity, $n-m$ is always even and the terms related by an interchange of the indices m and n are identical. Utilizing all of the above allows Eqs. (4.31) and (4.32) to be reduced to

$$\begin{aligned} I_l^B(R) &= \frac{\langle N \rangle}{Q^2} \sum_{j\geq 0} \sum_{k=0}^{j} t(r_{jk}) \sum_{n} {\sum_{m\geq n}}^{(6)} \epsilon_{n-m} \Theta_{n-m}(\phi_{jk}) J_{m-n}(2\pi R r_{jk}) \\ &\quad \times \sum_{\alpha} G_{nl}^{(\alpha)}(R) \sum_{\beta} G_{ml}^{(\beta)*}(R), \end{aligned} \tag{4.34}$$

and

$$\begin{aligned} I_l^D(R) &= \frac{\langle N \rangle}{Q^2} \sum_{j\geq 0} \sum_{k=0}^{j} t(r_{jk}) \rho_{jk} \sum_{n} {\sum_{m\geq n}}^{(6)} \epsilon_{n-m} \Theta_{n-m}(\phi_{jk}) J_{m-n}(2\pi R r_{jk}) \\ &\quad \times \sum_{\alpha} G_{nl}^{(\alpha)}(R) \left[(Q-1) G_{ml}^{(\alpha)*}(R) - \sum_{\beta \neq \alpha} G_{ml}^{(\beta)*}(R) \right], \end{aligned} \tag{4.35}$$

where

$$\Theta_p(\phi_{jk}) = \begin{cases} 1, & j = k = 0 \\ 6(-1)^{p/6}, & k = j \text{ and } j \neq 0 \\ 12\exp(ip\phi_{jk}), & 0 < k < j, \end{cases} \tag{4.36}$$

$$\epsilon_i = \begin{cases} 1, & n = 0 \\ 2, & n \neq 0, \end{cases} \tag{4.37}$$

the notation

$${\sum_{m}}{\sum_{n}}^{(i)}$$

denotes the double summation over pairs of indices n and m for which $n-m$ is divisible by the integer i, and both n and m satisfy the helix selection rule. The same simplifications can be applied to Eqs. (4.18), (4.19), (4.24) and (4.25) for the cases of a single molecule adopting one of two positions.

4.3 Cylindrically averaged diffraction by the triangular Ising antiferromagnet

The TIA, introduced in Section 1.2.4, is a disordered system on a triangular lattice. Emperical expressions that give accurate values for the correlation function for the TIA were given in Chapter 2. The regular and cylindrically averaged diffraction by the TIA in two dimensions has been described previously [Yoo09]. These results are extended here to the case of a three-dimensional fibre containing helical molecules. In the next two subsections, the key properties of the TIA and its diffraction are reviewed. In the third subsection, the results of Section 4.2 are applied to describe cylindrically averaged diffraction by the TIA.

4.3.1 Diffraction by the triangular Ising antiferromagnet

The TIA is a disordered system on a triangular lattice. A triangular lattice spacing of unity is used and an internal angle of $\pi/3$ so that the unit cell vectors in Cartesian coordinates are given by

$$\begin{aligned} \mathbf{a} &= (1,0), \\ \mathbf{b} &= (1/2,\sqrt{3}/2). \end{aligned} \tag{4.38}$$

The sites of the triangular lattice are indexed by the indices h and k and have a position denoted $\mathbf{r}_{hk}$, where

$$\mathbf{r}_{hk} = h\mathbf{a} + k\mathbf{b}. \tag{4.39}$$

The integers (h,k) are an oblique coordinate system where the unit cell, shown in Fig. 4.1(a), is a rhombus but the lattice forms a triangular net. As a result of the positive correlations, there tends to be small, ordered crystalline domains with the same molecule (or molecular position) at each site, sometimes referred to as "superlattice" domains, that are rhombic in shape. These domains, illustrated in Fig. 4.1(b), behave as small crystals with unit cell vectors

$$\begin{aligned} \mathbf{a}_s &= (3/2,-\sqrt{3}/2), \\ \mathbf{b}_s &= (3/2,\sqrt{3}/2), \end{aligned} \tag{4.40}$$

where the subscript s denotes superlattice, and a lattice spacing of $\sqrt{3}$. The sites of the superlattice are indexed by the indices h and k and have a position denoted $\mathbf{r}_{s,hk}$, where

$$\mathbf{r}_{s,hk} = h\mathbf{a}_s + k\mathbf{b}_s. \tag{4.41}$$

The unit cell vectors for the triangular lattice and superlattice are related by

$$\begin{aligned} \mathbf{a}_s &= 2\mathbf{a} - \mathbf{b}, \\ \mathbf{b}_s &= \mathbf{a} + \mathbf{b}. \end{aligned} \tag{4.42}$$

Diffraction by the TIA is described in detail by Yoon [Yoo09] and consists of a Bragg component and a diffuse component. The Bragg reflections lie on the two-dimensional reciprocal lattice which is also triangular and has reciprocal unit cell vectors

$$\begin{aligned} \check{\mathbf{a}} &= (1, -1/\sqrt{3}), \\ \check{\mathbf{b}} &= (0, 2/\sqrt{3}), \end{aligned} \tag{4.43}$$

and a lattice spacing of $2/\sqrt{3} \sim 1.155$. The sites of the reciprocal lattice are indexed by the indices p and q with position vector

$$\mathbf{R}_{pq} = p\check{\mathbf{a}} + q\check{\mathbf{b}}. \tag{4.44}$$

The reciprocal lattice and the reciprocal unit cell vectors are shown in Fig. 4.1(c). The effect of a finite crystallite size is to broaden the Bragg reflections about the reciprocal lattice points, with their widths inversely proportional to the crystallize size. The Bragg diffraction is equivalent to that from an ordered system with an average molecule at each site.

The diffuse component exists everywhere in reciprocal space and is smoothly varying. However, for small temperatures the long range correlations produce peaks in the diffuse diffraction. The most significant effect is due to the rather large positive correlations on sublattice 0 at low temperatures. Therefore, at low temperatures, the diffuse diffraction peaks at the sites of the corresponding reciprocal superlattice which has reciprocal unit cell vectors

$$\begin{aligned} \check{\mathbf{a}}_s &= (1/3, -1/\sqrt{3}), \\ \check{\mathbf{b}}_s &= (1/3, 1/\sqrt{3}), \end{aligned} \tag{4.45}$$

and a lattice spacing of $2/3$. These superlattice reflections are formed from a concentration of the diffuse scattering at the reciprocal superlattice points. As the temperature increases the correlations become weaker and the intensity of the superlattice reflections diminishes and the peaks broaden. At high temperatures only slowly varying diffraction is present. The reciprocal lattice points are a subset of the reciprocal superlattice points. Yoon [Yoo09] showed that at the reciprocal lattice points, the diffuse diffraction vanishes for small temperatures.

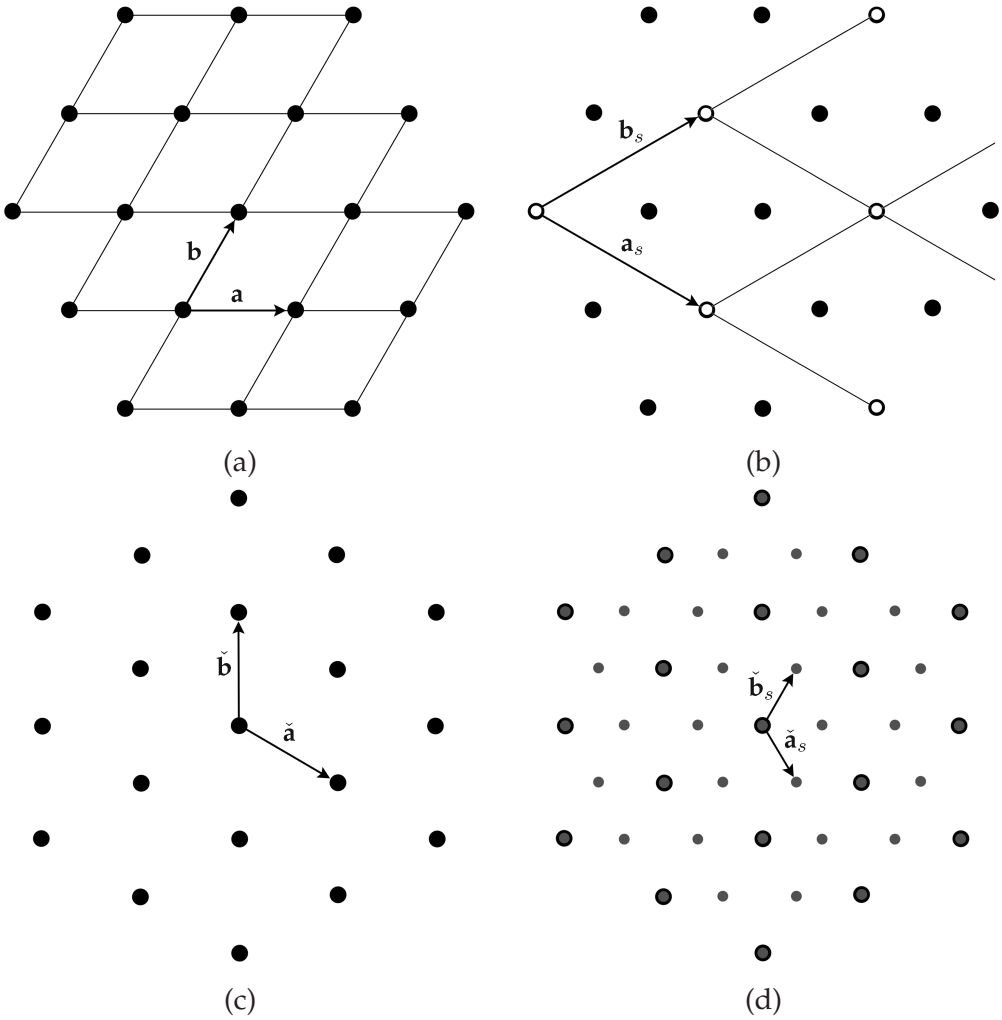

Figure 4.1 Lattices and the corresponding reciprocal lattices. (a) The triangular lattice and (c) the reciprocal lattice. (b) The lattice sites shown by the filled and open circles, and the superlattice sites shown by open circles. (d) The reciprocal lattice (open black circles) and the reciprocal superlattice (filled grey circles).

4.3.2 Cylindrically averaged diffraction

To summarise, the model developed here for the fibre is a collection of many orientated crystalline domains randomly rotated about the fibre axis. Within each crystallite, at each lattice site there is a helical molecule in one of two positions. The second-order statistics of the two positions are defined by the correlation function ρ_{jk} of the TIA. The diffraction from the fiber can be calculated using Eqs. (4.18) and (4.19) if there is no directional disorder and using Eqs. (4.24) and (4.25) if there is directional disorder, by simply substituting for ρ_{jk} that for the TIA.

Example calculations of the diffraction are shown in the next section, but some qualitative characteristics can be obtained by considering cylindrical averaging of the characteristics of the diffraction by the TIA described in the previous subsection. The Bragg diffraction peaks at the cylindrically averaged reciprocal lattice points, i.e. at the radii R_{pq} given by

$$R_{pq} = \frac{2}{\sqrt{3}}\sqrt{p^2 - pq + q^2}, \tag{4.46}$$

and the amplitude will be modulated by the average of the diffraction by the two molecules. For small temperatures the diffuse diffraction will peak at the cylindrically averaged reciprocal superlattice points, i.e. at the radii $R_{s,pq}$ given by

$$R_{s,pq} = \frac{2}{3}\sqrt{p^2 - pq + q^2}, \tag{4.47}$$

the peaks reducing in amplitude and broadening into a slowly varying function as the temperature increases. The diffuse diffraction will be modulated by a function related to the difference between the diffraction by the two molecules. The radii of the reciprocal lattice and reciprocal superlattice points are listed in Table 4.1 for $R < 3$ and illustrated in Fig. 4.2 for $R < 5$. Note that the former are a subset of the latter.

4.4 Simulations

4.4.1 Methods

In order to study characteristics of the cylindrically averaged diffraction from the TIA, the theory described above was used to calculate diffraction patterns at various temperatures and with various relative molecular positions. Directional disorder is not considered and so Eqs. (4.18) and (4.19) are used. A circular crystallite shape function of radius r_c was used which gives the autocorrelation

$$t(r) = 2r_c^2\alpha - r_c r\sin(\alpha), \tag{4.48}$$

$(p,q)_s$	$R_{s,pq}$	(p,q)
(1,0)	0.667	
(2,1)	1.155	(1,0)
(2,0)	1.333	
(3,1)	1.764	
(3,0)	2	(2,1)
(4,2)	2.309	(2,0)
(4,1)	2.404	
(4,0)	2.667	
(5,2)	2.906	

Table 4.1 Coordinates $(p,q)_s$ of the superlattice reflections and their radii $R_{s,pq}$ for $R_{s,pq} < 3$. If there is a reciprocal lattice point at the same radius its indices are given in the right column.

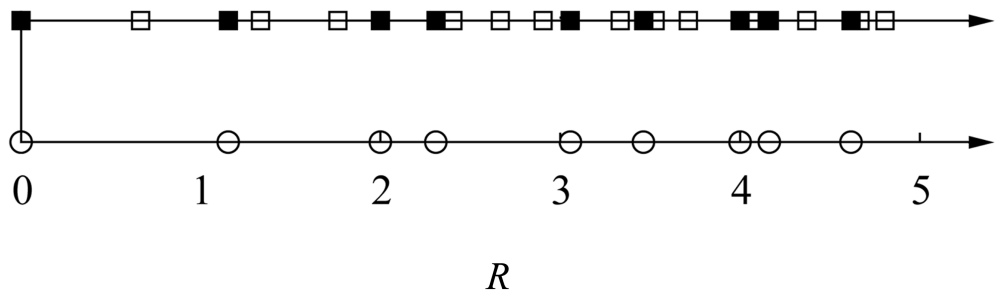

Figure 4.2 The cylindrically projected reciprocal lattice points (○) and reciprocal superlattice points (□ and ■). Reciprocal superlattice points that have the same radii as a reciprocal lattice point are denoted (■).

where

$$\alpha = \cos^{-1}\left(\frac{r}{2r_c}\right). \tag{4.49}$$

Programs were written to calculate fibre diffraction patterns based on Eqs. (4.34) and (4.35). A main program calls two functions to precalculate quantities required to calculate the intensities. The first function calculates the functions $t(r_{jk})$, ρ_{jk} and $J_{m-n}(2\pi R r_{jk})$ for the values of j, k, m, n required using the symmetry described above and as in Eqs. (4.34) and (4.35), and for values of R with an appropriate spacing ΔR. These values are stored in tables in the main environment and recalled by subsequent calculations. Although the helix selection rule has an infinite number of solutions, for a given value of R only orders n such that

$$|n| \leq 2\pi R r_0 + 2, \tag{4.50}$$

contribute significantly to the diffraction [CRK70, Mak82] and the sums in Eqs. (4.18) and (4.19) are limited to these values. A second function calculates the Fourier Bessel structure factors $G_{nl}(R)$ with a spacing ΔR, which are stored in tables in the main environment. The $I_l(R)$ are then calculated within the main environment. For a crystallite containing 250 helices of 5_1 symmetry, computation times were approximately 15 seconds on a intel® Core™ 2 CPU 6600 at 2.40GHz.

4.4.2 Results

For the simulations, a lattice spacing of unity was used and molecules with 5_1 helix symmetry were used to avoid interaction with the 6-fold symmetry of the lattice. For simplicity, the helix repeat unit is a point scatterer on the x-axis at a distance r_0 from the helix axis. Referring to Eq. (1.146), the Fourier-Bessel structure factors are then

$$G_{nl}(R) = J_n(2\pi R r_0). \tag{4.51}$$

A value of $r_0 = 0.4$ was used for the simulations. Since $v = 1$, the helix selection rule Eq. (1.141) reduces to

$$n = l - um, \tag{4.52}$$

for any integer m and on each layer line the contributing adjacent Bessel orders are spaced by u. The diffracted intensity was calculated over the range $0 \leq R \leq 6$ in steps of $\Delta R = 0.01$. A crystallite size $r_c = 9$ was used.

The diffraction pattern with no disorder is shown in Fig. 4.3. Each curve represents one layer line l as shown. The diffracted intensity consists only of Bragg reflections. The peak positions correspond to the values of R_{hk} listed in Table 4.1. The amplitudes of the Bragg reflections are modulated by the Bessel functions that contribute on each layer line and

they show the usual behaviour of fibre diffraction patterns in which there is diffraction on the meridian ($R = 0$ axis) only when l is a multiple of u (5 in this case) since they are the only layer lines where the zero order Bessel function contributes. The diffraction shows an overall decrease in amplitude with increasing R as a result of cylindrical averaging. The ripples near $R = 0$ are due to a fixed crystallite size and would average out for a real fiber that contains crystallites of varying in size.

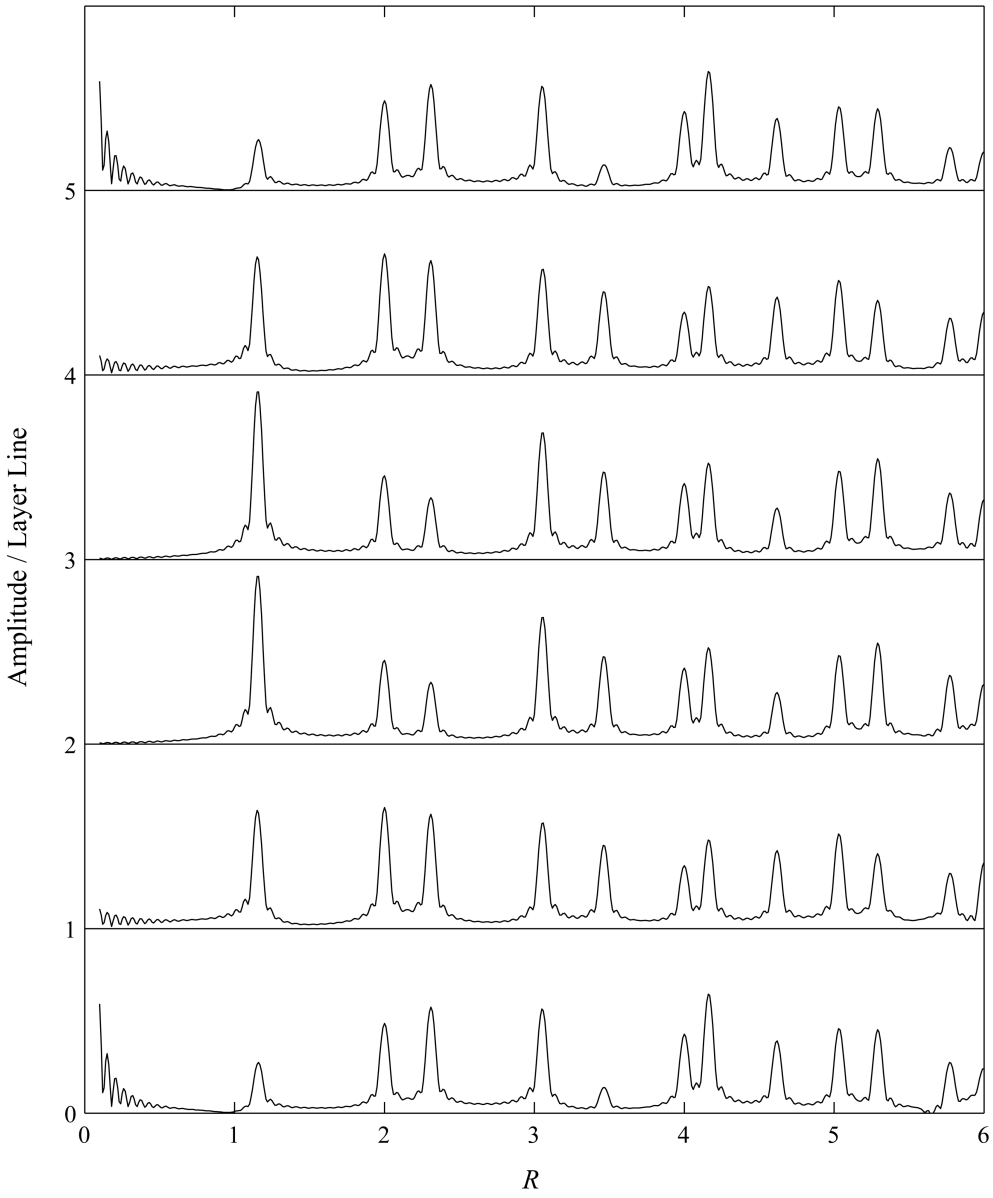

Figure 4.3 Layer line amplitudes for the TIA with no disorder.

Diffraction patterns are first calculated for the TIA for $\Delta\phi = \pi/2$ and $\Delta z = 0$, and variable temperature. The total diffracted amplitude and the diffuse component alone are shown as the two curves in Figs. 4.4-4.6, for $T = 0, 1.0$ and 2.0. The difference between the two curves therefore represents the Bragg diffraction. Comparison of Fig. 4.4 ($T = 0$) with Fig. 4.3 shows that the total diffraction is more intricate with many new peaks and considerable smooth background diffraction. These new features are introduced by the diffuse diffraction as shown in the figure. The peaks in the diffuse diffraction occur at the positions $R_{s,pq}$ of the reciprocal superlattice listed in Table 4.1. Five of the superlattice "row lines" are shown in Fig. 4.4 and the diffuse diffraction peaks are evident at these values of $R_{s,pq}$. Note that at low temperatures the diffuse diffraction does not peak at the reciprocal lattice points. The TIA disorder therefore introduces significant changes into the diffraction pattern over that for an ordered system. The new diffuse component is of significant amplitude and introduces many new peaks into the diffraction pattern. At $T = 1.0$ (Fig. 4.5), the diffraction pattern is similar, but the superlattice reflections in the diffuse component are reduced in amplitude and are broadened slightly. This is due to the weakening of the correlations with increasing temperature. At $T = 2.0$ [Fig. 4.6], only a few peaks are discernable in the diffuse diffraction and it approaches the slowly varying diffuse diffraction characteristics of a system with uncorrelated disorder. Note however that the overall amplitude of the diffuse diffraction remains the same and is independent of temperature. A diffraction pattern with the same parameters at $T = 0$ but with twice the crystallite radius is shown in Fig. 4.7. The effect of the larger crystallite size is to sharpen the peaks of both the Bragg and diffuse diffraction and close inspection shows that the diffuse diffraction is weakened relative to the amplitudes of the Bragg peaks.

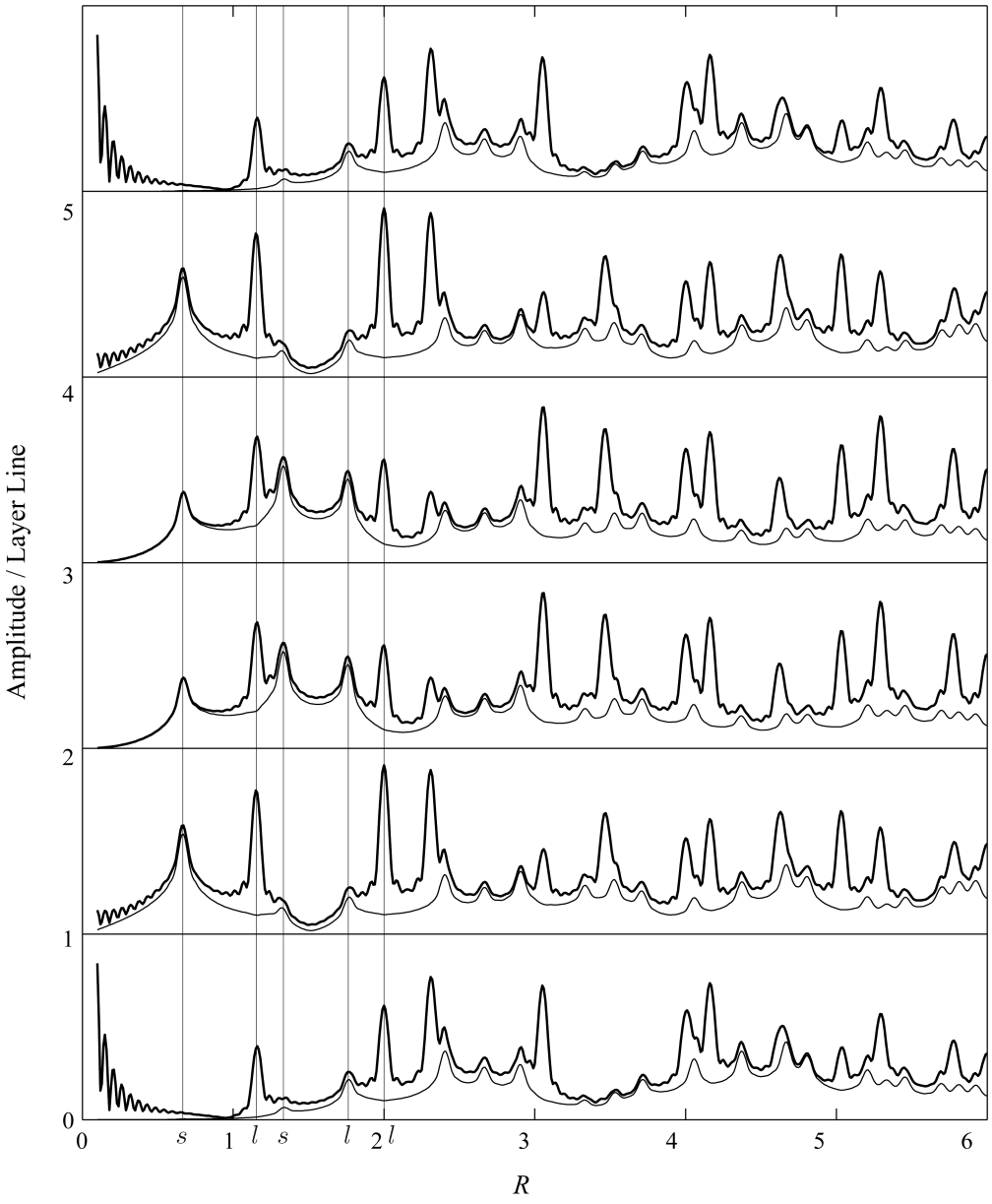

Figure 4.4 Layer line amplitudes for the TIA with $\Delta\phi = \pi/2$, $\Delta z = 0$ and $T = 0$. Thick lines represent the total diffraction with thin lines representing diffuse components. Vertical lines denote the positions of the reciprocal lattice (l) and superlattice row lines (s).

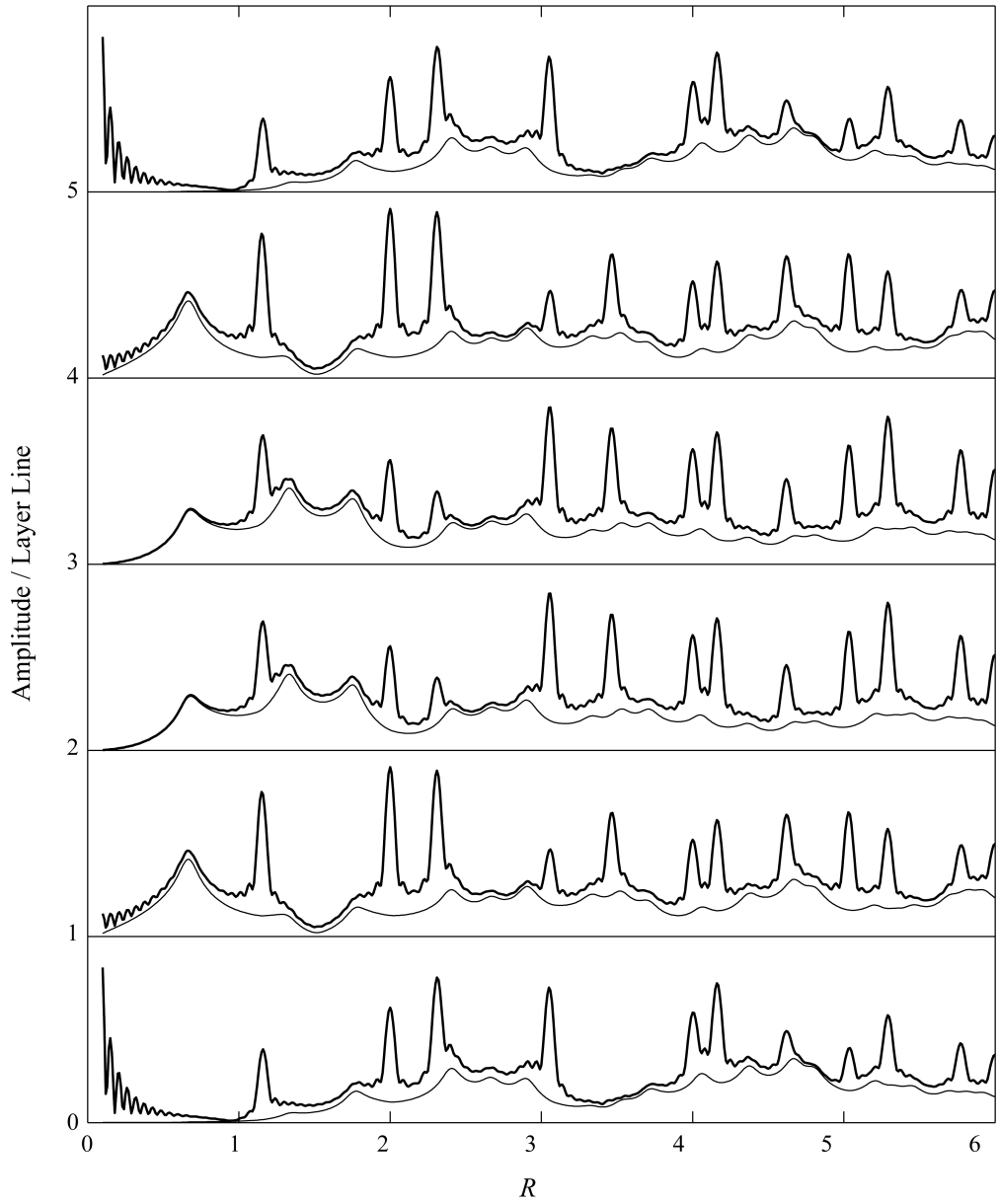

Figure 4.5 Layer line amplitudes for the TIA with $\Delta\phi = \pi/2$, $\Delta z = 0$ and $T = 1.0$. Thick lines represent the total diffraction with thin lines representing diffuse components.

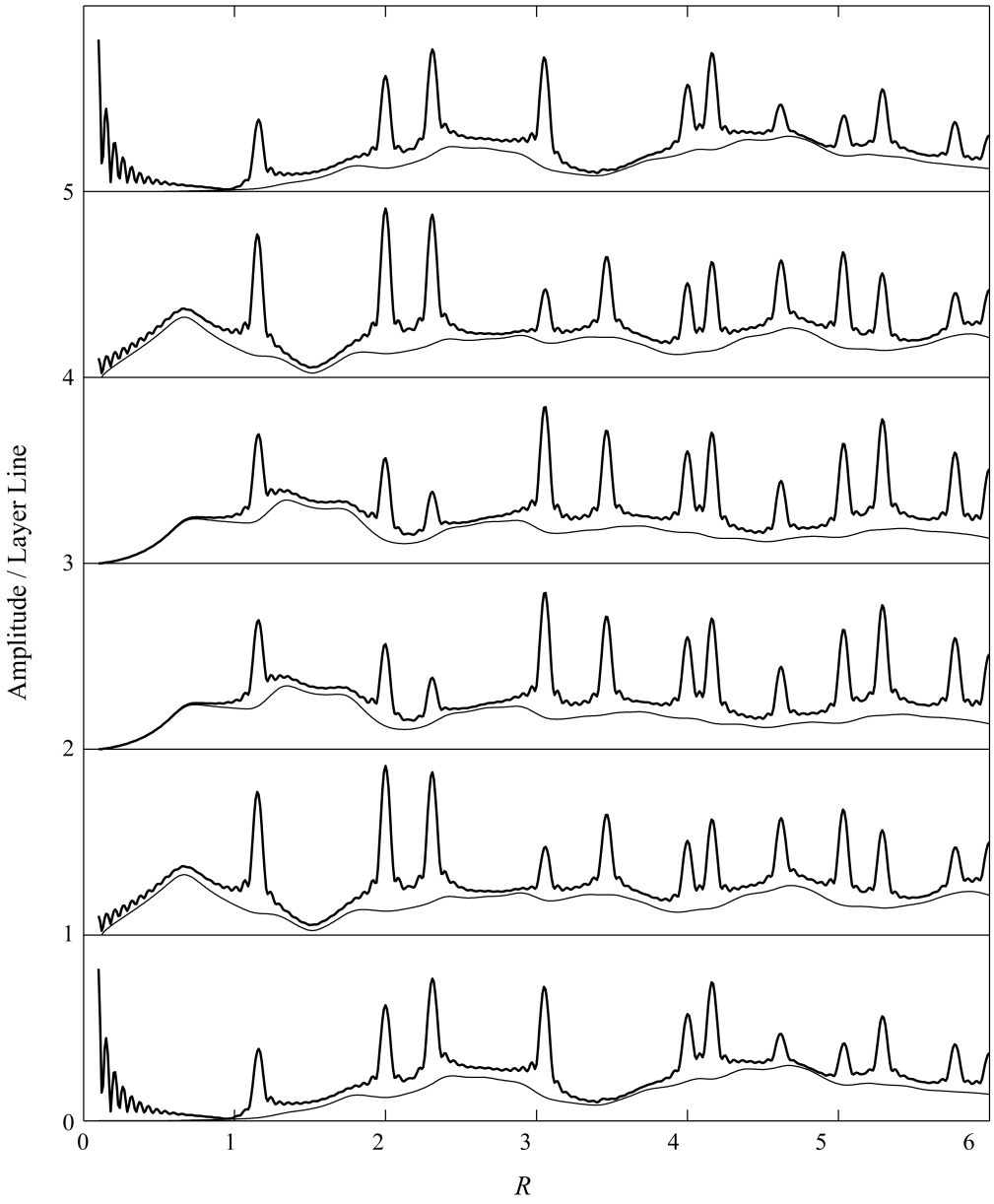

Figure 4.6 Layer line amplitudes for the TIA with $\Delta\phi = \pi/2$, $\Delta z = 0$ and $T = 2.0$. Thick lines represent the total diffraction with thin lines representing diffuse components.

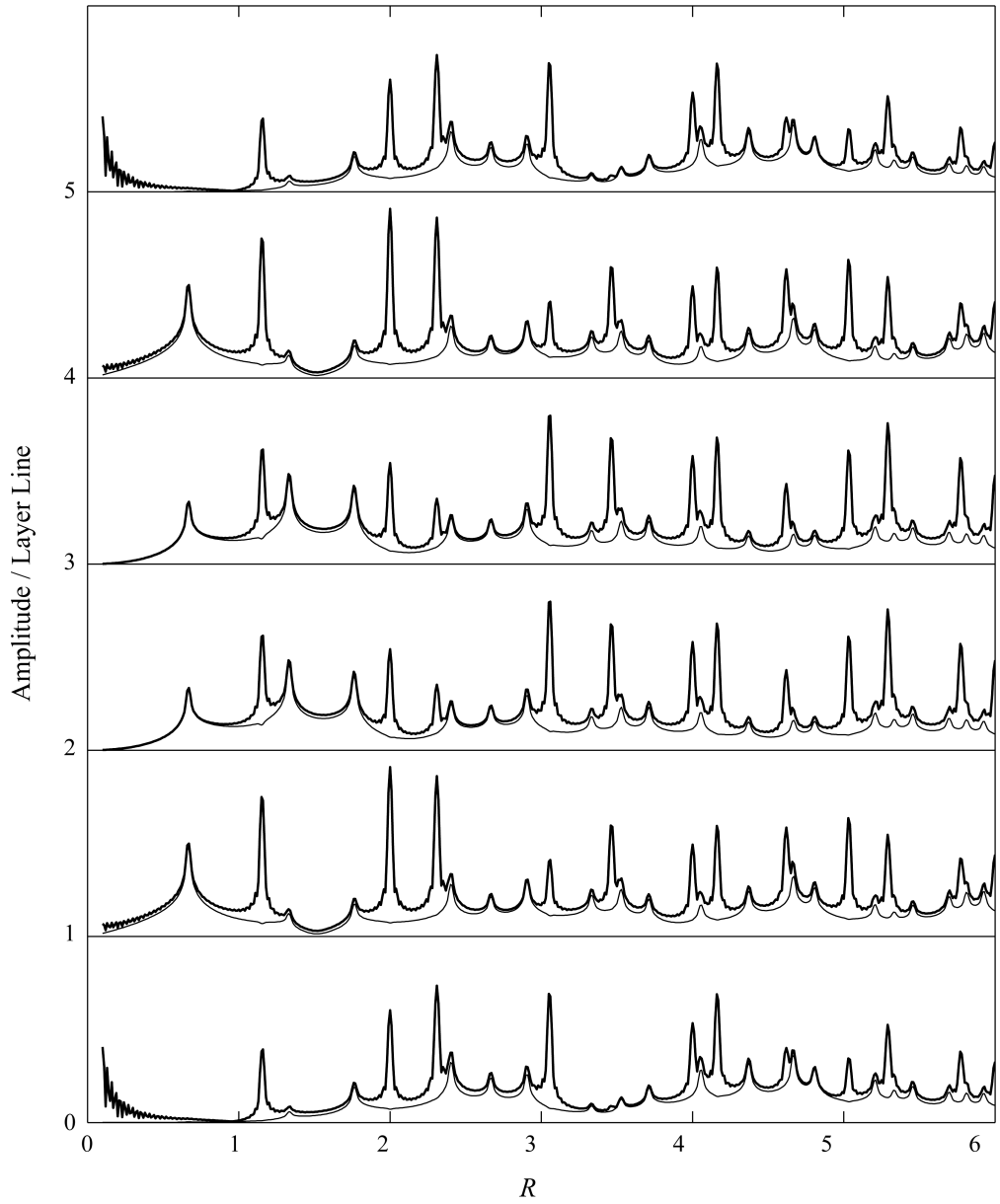

Figure 4.7 Layer line amplitudes for the TIA with $\Delta\phi = \pi/2$, $\Delta z = 0$, $T = 0$ and $r_c = 18$. Thick lines represent the total diffraction with thin lines representing diffuse components.

Consider now the case $\Delta\phi = 2\pi/5$ and $\Delta z = 0$ for which the diffraction pattern for $T = 0$ is shown in Fig. 4.8. This is an example of the case where $\Delta\phi$ is a multiple of $(2\pi v/u)$ as discussed in Section 4.2.1. The diffraction pattern has similar features to Fig. 4.4 except that, as anticipated, the diffuse component vanishes on layer lines 0 and 5, leaving only the Bragg component. Note also that the Bragg component on layer lines 2 and 3 is attenuated compared to that in Fig. 4.4. This can be understood as follows. Consider the weight factor

$$\alpha(\Delta\phi, \Delta z, l, m, n) = [1 + \exp(i[2\pi l\Delta z/c - n\Delta\phi])]\,[1 + \exp(-i[2\pi l\Delta z/c - m\Delta\phi])]\,, \quad (4.53)$$

for the Bragg diffraction in Eq. (4.18). Substituting $\Delta\phi = 2\pi/5$, $\Delta z = 0$, $l = 2$ and using the helix selection rule to evaluate m and n shows that $\alpha(2\pi/5, 0, 2, m, n) = 2(1 + \cos(4\pi/5)) = 0.382$ so that the Bragg diffraction is weighted down as observed. The same applies for $l = 3$.

The case when $\Delta\phi = 0$ and $\Delta z = c/10$ is shown in Fig. 4.9. This diffraction pattern shows a number of the characteristics described in Section 4.2.1. First, with $\Delta z = c/s$ for $s = 10$, the diffuse component vanishes on layer lines that are multiple of 10 and so only on the equator in this case. Second, with $\Delta z = c/(2s)$ for $s = 5$ the Bragg component vanishes on layer lines that are an odd multiple of s and so $l = 5$ in this case. The Bragg intensity on layer line 4 is attenuated because Eq. (4.53) reduces to $\alpha(0, c/10, 4, m, n) = 2(1 + \cos(4\pi/5)) = 0.382$. The diffuse component on layer line 1 appears attenuated which can be understood by considering the weight factor

$$\beta(\Delta\phi, \Delta z, l, m, n) = [1 - \exp(i[2\pi l\Delta z/c - n\Delta\phi])]\,[1 - \exp(-i[2\pi l\Delta z/c - m\Delta\phi])]\,, \quad (4.54)$$

for diffuse scattering in Eq. (4.18). Substituting $\Delta\phi = 0$, $\Delta z = c/10$ and $l = 1$, Eq. (4.54) becomes $\beta(0, c/10, 1, m, n) = 2(1 - \cos(\pi/5)) = 0.382$. The diffuse component on layer line 2 and the Bragg component on layer line 3 appear slightly attenuated. Substituting $\Delta\phi = 0$, $\Delta z = c/10$ and $l = 3$ into Eq. (4.53) gives $\alpha(0, c/10, 3, m, n) = 2(1 + \cos(3\pi/5)) = 1.382$, less than the mean value of the weight factor of 2. Similarly, substituting $\Delta\phi = 0$, $\Delta z = c/10$ and $l = 2$ into Eq. (4.54) gives $\beta(0, c/10, 2, m, n) = 2(1 - \cos(2\pi/5)) = 1.382$.

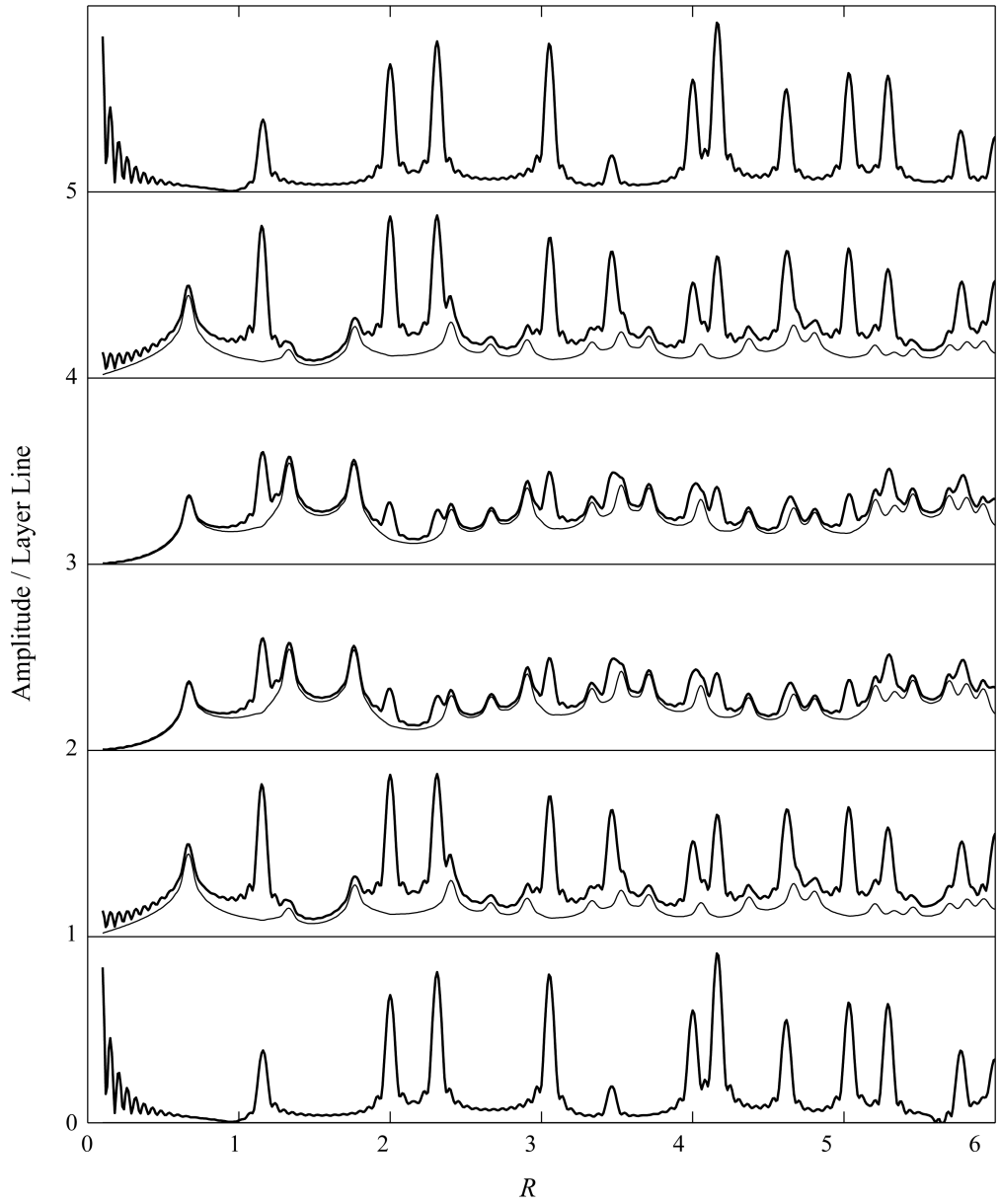

Figure 4.8 Layer line amplitudes for the TIA with $\Delta\phi = 2\pi/5$, $\Delta z = 0$ and $T = 0$. Thick lines represent the total diffraction with thin lines representing diffuse components.

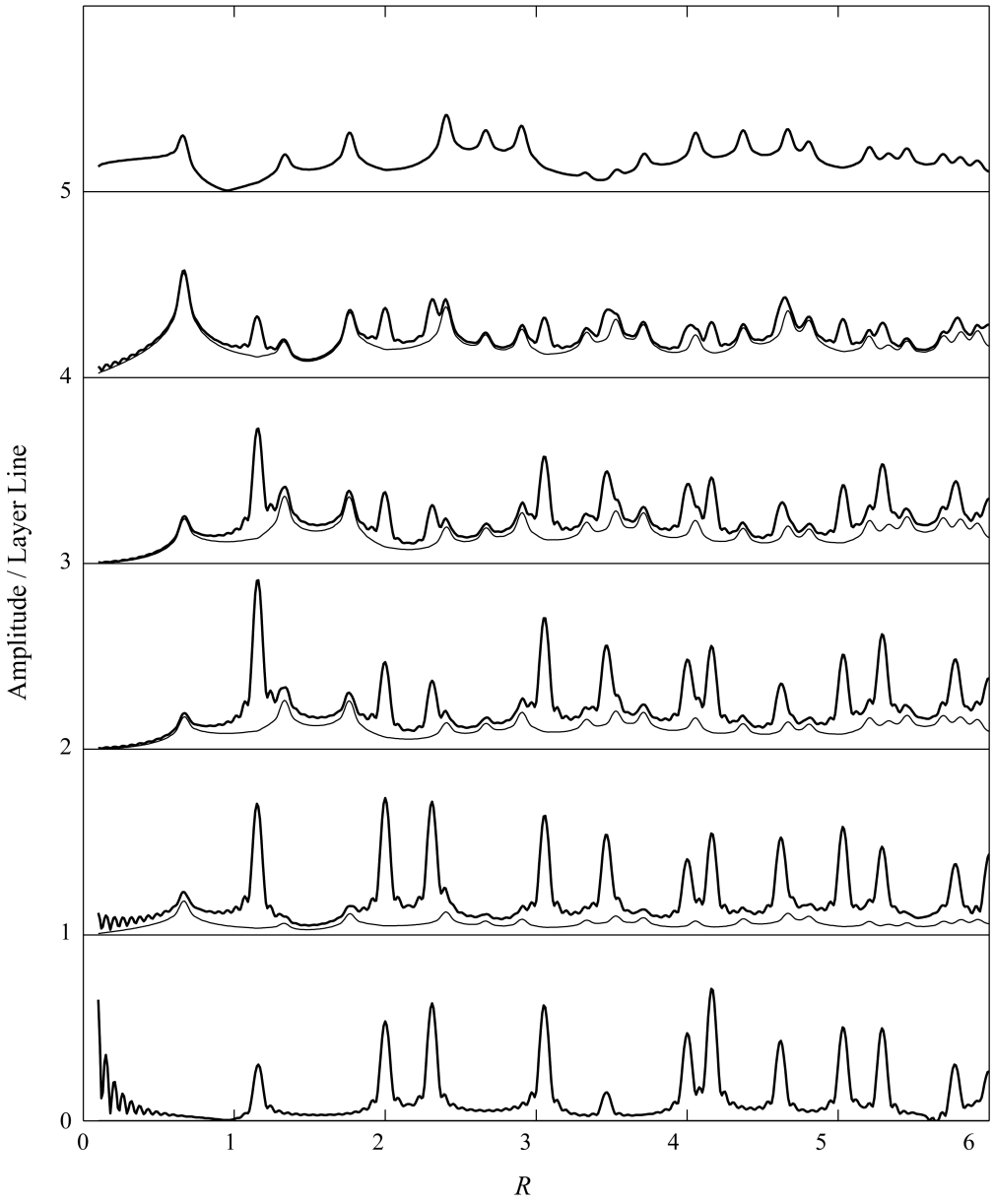

Figure 4.9 Layer line amplitudes for the TIA with $\Delta\phi = 0$, $\Delta z = c/10$ and $T = 0$. Thick lines represent the total diffraction with thin lines representing diffuse components.

4.5 Conclusions

Theory has been developed for calculating the cylindrically averaged diffraction from polycrystalline fibres of helical molecules, in which the constituent crystallites contain correlated substitution disorder. Correlations between molecules are described by the spatial correlation function of the molecules at two sites in the two-dimensional lattice transverse to the fibre axis. Expressions for diffraction by fibres with circularly symmetric correlation statistics are derived which allow for efficient numerical calculation of cylindrically averaged intensities. Any number of scatterer types and lattice disorder can be easily incorporated into the calculation. Simplifications for crystalline arrays with hexagonal lattice symmetry are made, reducing the number of terms to be computed in the calculation.

The theory developed was used to calculate the diffraction by polycrystalline fibres with TIA-type interactions between scatterers, where the TIA two-point correlation function, developed in Chapter 2, was used. Simulations were performed using a circular crystallite containing 250 helices with 5_1 symmetry and point repeating units. Helices could be one of two possible types, simply related by rotational and axial shifts. The relationship between the temperature of the TIA and the calculated diffuse diffraction was explored, showing that superlattice peaks diminish and diffuse diffraction increases with increasing temperature (weakening correlations). Values of the rotational and axial shifts between scatterer types were varied and the effects on the calculated diffraction explored. For certain pairs of values for the axial and rotational shifts, diffuse and Bragg components of the diffraction diminish, or extinguish entirely, along certain layer-lines.

Chapter 5

X-ray diffraction by the myosin lattice of vertebrate muscle

5.1 Introduction

X-ray fibre diffraction is a valuable tool for determining the structure and structural transitions of contractile and regulatory proteins during muscular contraction [Hux69, HFB+80, HFK+83, HK85, KHFH86, MFBD+94, LPG+95]. An aspect still under study are the conformal changes undergone by myosin subfragment S1, referred to as the myosin "head", during the process of contraction. Myosin heads have two primary domains that each have many degrees of freedom [RHW+93]. Myosin heads in the rigor state are strongly bound to actin filaments to form an actin-myosin complex [HDM+96]. In the rest state, the myosin heads are unbound and the diffraction effects from actin proteins are easily accounted for. Models for the conformation of myosin heads are refined by fitting calculated diffraction intensities to observed X-ray diffraction patterns.

The uniform filament orientations in simple-lattice specimens make it relatively straightforward to calculate their X-ray fibre diffraction patterns. Such calculations have been used as the basis for a number of high-resolution, structural studies of bony fish muscle, a specimen with simple lattice arrangement, culminating in a high-precision model [HS86, HHDS97, SCC+98, AKS06]. However, structural studies of superlattice muscles, such as frog sartorius muscle, requires the calculation of diffraction patterns that take the myosin disorder into account. So far, methods have not been available for calculating the diffraction from specimens exhibiting this kind of disorder. The only attempt to incorporate the superlattice disorder into diffraction calculations is that of Koubassova et al. [KT02, KBFT08]. They have modelled the superlattice in rabbit muscle (a superlattice species) by

an ordered system in which one superlattice cell forms the unit cell (Fig. 5.2). Note that they described this in terms of an equivalent hexagonal unit cell (shown by dashed lines in Fig. 5.2). The model is not disordered however and corresponds to 3 interdigitated superlattices, two of which have up molecules and one has down molecules. Since the model is not disordered the diffraction is easily calculated. The no-three-alike rules are obeyed without exception in this model, as opposed to with the frequencies described in Section 1.6.4, and the superlattice arrangement extends over the whole array. This corresponds to a single configuration of the highly degenerate TIA ground state and is therefore inconsistent with the semi-systematic ordering observed in electron micrographs [LMS81, MG00]. Statistical averaging over all configurations at the appropriate temperature is required to properly describe myosin superlattice diffraction.

In this chapter, the methods for calculating cylindrically averaged diffraction by the TIA described in Chapter 4 are applied to the myosin superlattice structure. The ultimate goal is to develop a framework for structure determination studies on vertebrate muscle exhibiting superlattice arrangements of the myosin filaments. The disordered myofibril structure model used, incorporating high-precision results for the two-point correlation function of the TIA from Chapter 2 is described in Section 5.2. A low resolution model of the myosin filament and its incorporation into the diffraction calculations is described in Section 5.3. Simulated X-ray fibre diffraction patterns and comparison with experimental fibre diffraction patterns are presented in Section 5.4. Concluding remarks are made in Section 5.5.

5.2 Modelling the muscle fibre

5.2.1 Fibre structure

A cross-section of a vertebrate muscle fibre, shown in Fig. 5.1 by an electron micrograph of a transverse section through the so-called "bare region" of the A-band, appears polycrystalline with myofibrils representing each crystallite. In this study, the myofibrils are considered to be sufficiently large so that their properties can be described statistically. The average myofibril cross-section profile is approximated to be circular in shape with an average radius of $r_c \simeq 1\,\mu$m estimated from micrographs of frog sartorius muscle. Likewise, a sufficient sample of myofibril orientations about the fibre axis is assumed such that a uniform distribution of orientations is obtained. Diffraction from actin filaments is well understood and can be accounted for in X-ray fibre diffraction patterns [EEO69].

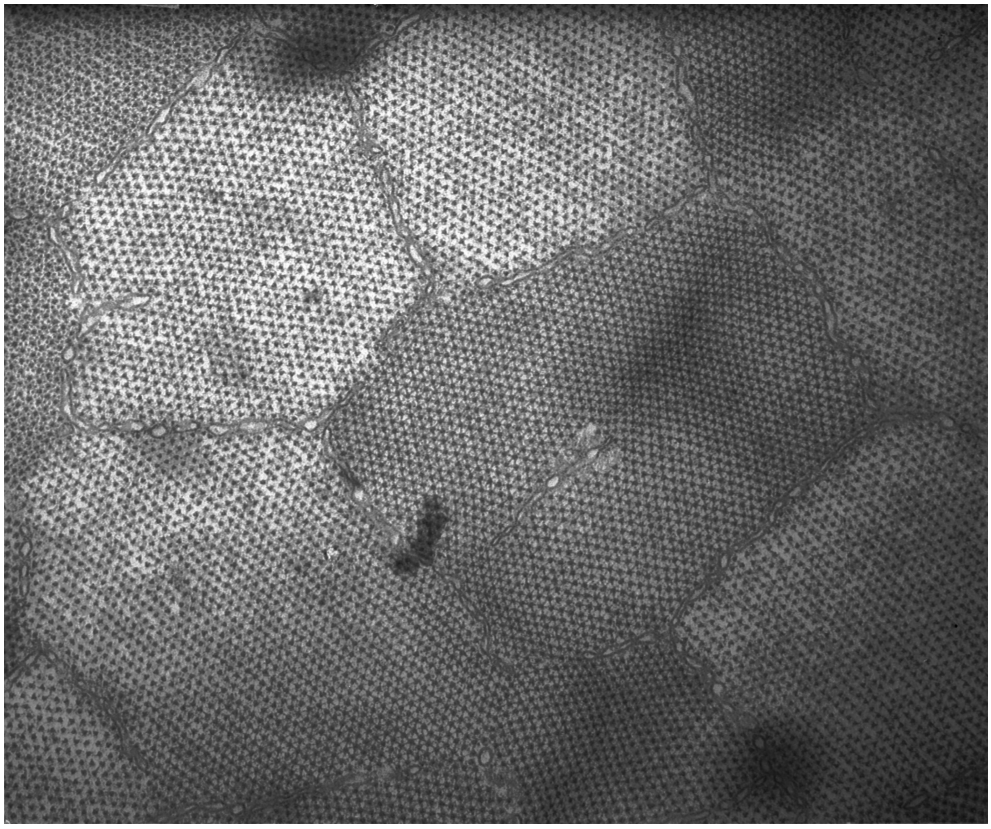

Figure 5.1 Electron micrograph of a thin section through the bare region of the A-band of frog sartorius muscle. Tightly packed myofibrils and their constituent myosin filaments are clearly visible. (Image provided by Dr. Pradeep Luther, Imperial College London).

5.2.2 Myosin superlattice disorder

The myosin superlattice disorder has been shown to be well represented by a finite temperature triangular Ising antiferromagnet by Yoon [Yoo09]. Metropolis Monte Carlo simulations of the TIA were performed over a range of temperatures and various disorder parameters calculated. Simulated values were then compared with values measured from electron micrographs. An effective temperature T_{eff} was defined as the temperature at which best agreement between the sets of values is obtained. Correlations were described by the first order term of the asymptotic expression Eq. (1.48) given by

$$\rho(r, T_{\text{eff}}) \sim \left(\frac{\pi}{2}\sin\theta\right)^{-1/2} |z|^r r^{-1/2} \cos\left(2\pi r/3\right), \tag{5.1}$$

with θ given by Eq. (1.49) and r defined by Eq. (2.11) with rotational invariance assumed. Several aspects of this analysis require review in light of the results of Chapter 2. Metropolis Monte Carlo is not suited for simulations at low temperatures (close to the critical temperature $T_c = 0$), suffering from critical slowing and getting trapped in metastable regions of configuration space. Eq. (5.1) was shown to be insufficiently accurate for small T and small separations r in Section 2.2.2 and it assumes only two forms of the radial correlation function, merging sublattices 1 and 2. Rotational invariance was also assumed, a property shown in Section 2.3.2 to be quite accurate. These calculations were therefore revisited using the more accurate correlation function results described in Chapter 2.

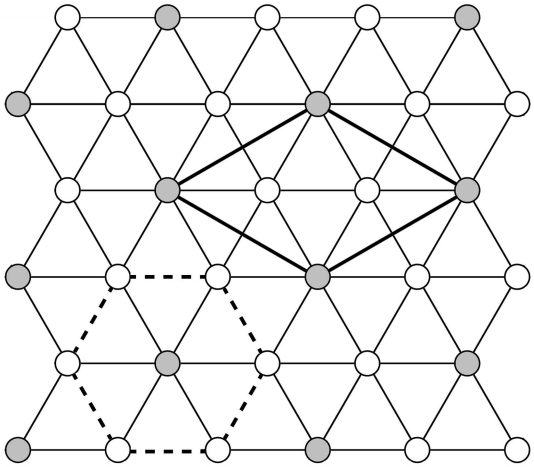

Figure 5.2 A region of the periodic model for the myosin filament array used by Koubassova et al. [KT02]. The hexagonal superlattice unit cell is identified by the dashed lines and the superlattice cell is shown by full lines.

The effective temperature of the myosin lattice was determined by calculating the correlation function of the TIA, using Eq. (2.14), and comparing it to the correlations mea-

sured from micrographs, as a function of temperature. The fit between the calculated and measured correlation functions was determined by calculating the root mean square error (RMSE),

$$E_{\text{RMS}}(T) = \sqrt{\frac{1}{K}\sum_{j=1}^{K}[\rho(r_j, T) - \rho_M(r_j)]^2}, \tag{5.2}$$

where $\rho(r_j, T)$ is the calculated correlation function from the TIA, $\rho_M(r_j)$ is the correlation function determined from micrographs and K is the number of distances in the range $0 \leq r \leq 10$. The measured correlation functions were derived from frog sartorius myosin arrays [Yoo09]. The effective temperature T_{eff} is then that at which $E_{\text{RMS}}(T)$ is a minimum. The RMSE calculated over the range $0 \leq T \leq 2$ is shown in Fig. 5.3. A minimum occurs at $T_{\text{eff}} = 1.2$, similar to the value determined by Yoon [Yoo09] of $T_{\text{eff}} = 1.1$. Note that Yoon chooses a coupling strength of $J = -1/2$ and thus reports an effective temperature of half this value, i.e. 0.56. The correlation function at $T_{\text{eff}} = 1.2$ is given by Eq. (2.14) with $\{\alpha_0, \alpha_1, \alpha_2\} = \{0.727, -0.245, -0.407\}$ and $\beta = 0.699$ and is shown by in Fig. 5.4 with the correlation values extracted from myosin arrays represented by errorbars.

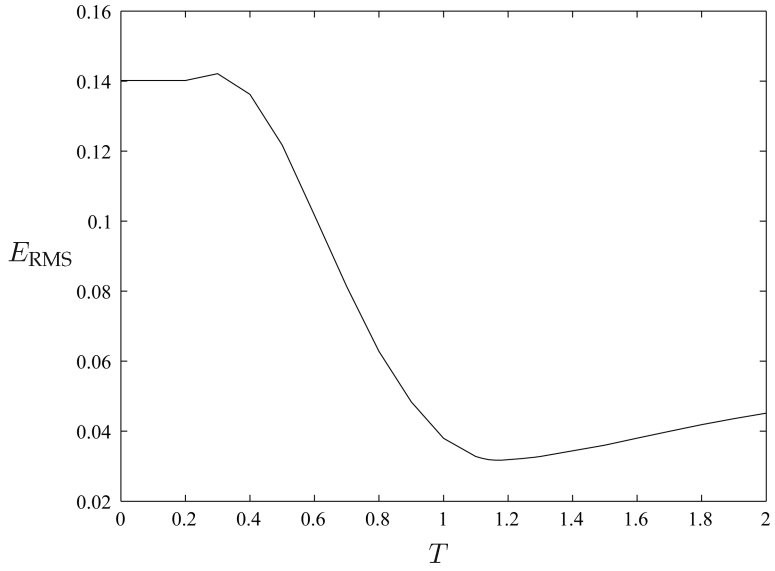

Figure 5.3 RMSE values between Eq. (2.14) at various temperatures and correlation values measured from myosin arrays [Yoo09].

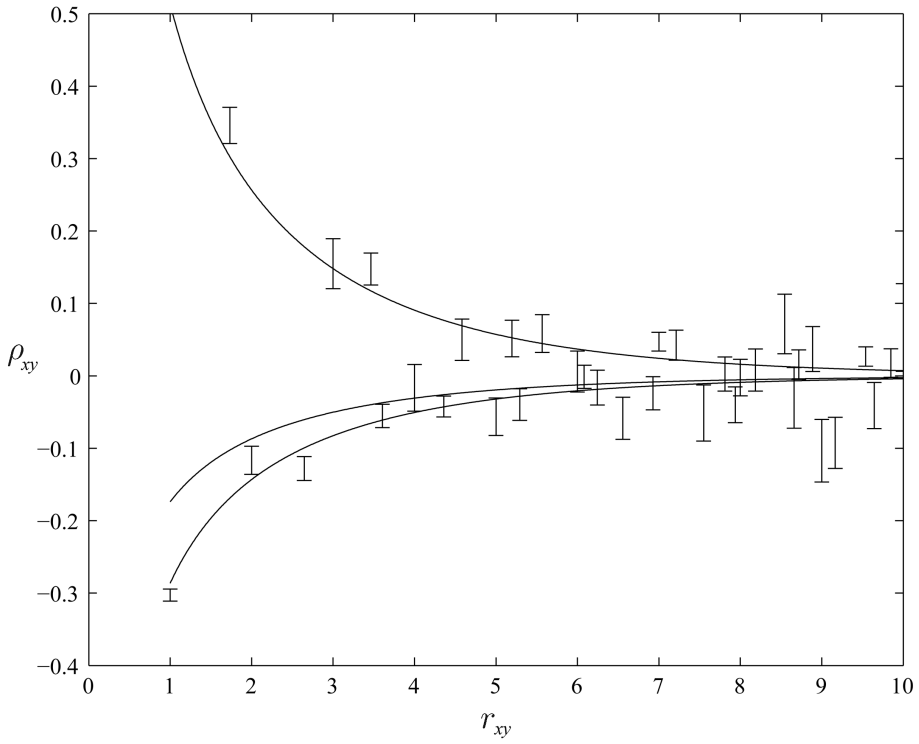

Figure 5.4 The correlation function Eq. (2.14) (full lines) at T=1.2 and correlation values from myosin arrays (error bars).

5.2.3 Myosin filament structure

The myosin filament structure was described in Sec. 1.6.1. The structure is described here in more detail for the purpose of developing a simple model with which to calculate the diffraction. The filament is composed of an approximately cylindrical filament stem of diameter of ~ 15 nm, and myosin head pairs which are arranged around the stem as three strands, each has, to a first approximation, 9_1 helical symmetry and a c-repeat (pitch) of $c = 128.7$ nm. The axial separation between head pairs is then $128.7/9 = 14.3$ nm. In frog sartorius muscle a perturbation from 9_1 helical symmetry is observed in which the structure is described as a 3_1 helix, of the same pitch, with a repeating unit of 3 myosin head pairs. The axial separations of the heads in one repeat unit are 15.7 nm, 11.6 nm and 15.7 nm, rather than 14.3 nm [SHES82]. The 9_1 and 3_1 models are referred to here as models A and B and are illustrated in Fig. 5.5.

The myosin filament consists of three strands (either model A or B) that are rotated by $120°$ and $240°$, relative to a reference strand, about the helix axis with no axial shift. Three heads pairs at the same value of z are referred to as a "crown". In the A model, the crowns are spaced by 14.3 nm in z, and the three 9_1 helices then reduce to a 1_1 helix with three crowns, or 9 head pairs, forming the helix repeat unit, and a c-repeat of $128.7/3 = 42.9$ nm [Fig. 5.5(a)]. In the B model, the three 3_1 helices reduce to a 1_1 helix with 3 crowns (9 head pairs) forming the helix repeat, and a c-repeat of 42.9 nm [Fig. 5.5(b)].

A single myosin head can be described as an approximately pear-shaped structure, about 19 nm in length and 5nm at its widest point [EO78], illustrated in Fig. 5.6 (a) and (b) by a 50-sphere model [HHDS97]. The myosin head has a centre of mass at approximately 12.3 nm-13.8 nm from the filament axis. A single head consists of a motor domain which contains the actin binding sites, and a lever arm which positions the motor domain along the actin filament. The position of each domain can be described in terms of rotation, slew, tilt and translational parameters [RHW$^+$93, HHDS97, HAK$^+$03]. The vector joining two heads within a repeating unit can vary in length and orientation also. The three head pairs within a crown can have different sets of values of these parameters. The number of degrees of freedom within a myosin crown in these kinds of models which have a sensitivity to measured data better than 1 nm is about 40 [AKS06].

The objective here is to study the overall effect of the superlattice disorder on fibre diffraction patterns. For this purpose, a low resolution model of the myosin filament is used. The myosin head pair is approximated as a sphere of radius $r_m = 5$ nm of uniform electron density and centered at $r_0 = 13$ nm from the filament axis as shown in Fig. 5.6 (a) and (b). The filament stem is approximated by a cylinder of uniform density and radius $r_s = 7.5$ nm. A single crown of this model is shown in Fig. 5.6(c). Without loss of generality, the myosin

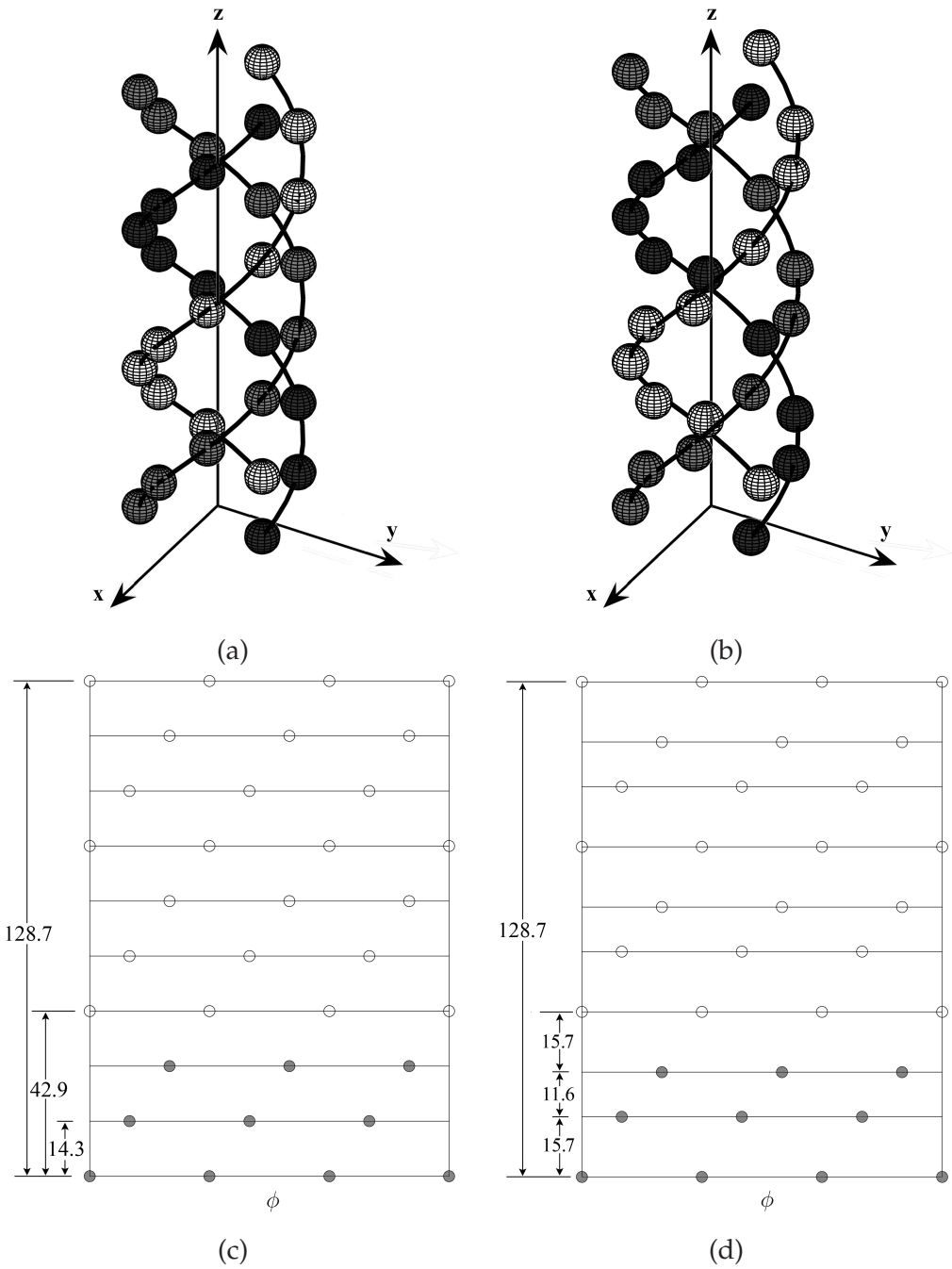

Figure 5.5 The myosin filament structure of model A [(a) and (c)] and model B [(b) and (d)]. The three helices are shown in (a) and (b), and the radial nets in (c) and (d).

stem is placed at the origin. There is one rotational degree of freedom which is defined as the angle ϕ_0 between the line joining the axis of the myosin and the centre of the sphere representing one of the head pairs to the **a**-axis [Fig. 5.6(c)].

5.3 Diffraction from the vertebrate muscle model

The theory for diffraction by polycrystalline fibres of helical molecules subject to TIA disorder developed in Chapter 4 is applied to the myosin superlattice array.

5.3.1 Calculation of layer-line intensities

First consider model A. Referring to Eq. (1.146), the Fourier-Bessel structure factor for the filament is

$$\begin{aligned} G_{nl}^{(\mathrm{A})}(R) &= f_0(|\mathbf{R}|)J_n(2\pi Rr_0)\sum_{j=0}^{2}\sum_{k=0}^{2}\exp\left(-in[\phi_0 + j2\pi/3 + k2\pi/9]\right)\exp(ikl2\pi/3) \\ &= f_0(|\mathbf{R}|)J_n(2\pi Rr_0)\exp(-in\phi_0)\sum_{j=0}^{2}\exp(-inj2\pi/3)\sum_{k=0}^{2}\exp(ik2\pi[l/3 - n/9]) \\ &= f_0(|\mathbf{R}|)J_n(2\pi Rr_0)\exp(-in\phi_0)\Phi_n\Lambda_{nl}, \end{aligned} \tag{5.3}$$

where $f_0(|\mathbf{R}|)$ is the scattering factor of a sphere given by Eq. (B.10),

$$\begin{aligned} \Phi_n &= 1 + \exp(-in2\pi/3) + \exp(-in4\pi/3) \\ &= \begin{cases} 3, & \text{for } n = 3p,\ \forall p \in \mathbb{Z} \\ 0, & \text{otherwise,} \end{cases} \end{aligned} \tag{5.4}$$

and

$$\begin{aligned} \Lambda_{nl} &= 1 + \exp(in2\pi[l/3 - n/9]) + \exp(in4\pi[l/3 - n/9]) \\ &= \begin{cases} 3, & \text{for } n = 3l - 9p,\ \forall p \in \mathbb{Z} \\ 0, & \text{otherwise.} \end{cases} \end{aligned} \tag{5.5}$$

So Eq. (5.3) reduces to

$$G_{nl}^{(\mathrm{A})}(R) = \begin{cases} 9f_0(|\mathbf{R}|)J_n(2\pi Rr_0)\exp(-in\phi_0), & \text{for } n = 3l - 9p,\ \forall p \in \mathbb{Z} \\ 0, & \text{otherwise,} \end{cases} \tag{5.6}$$

and noting that $|\mathbf{R}| = (R^2 + l^2/c^2)^{1/2}$.

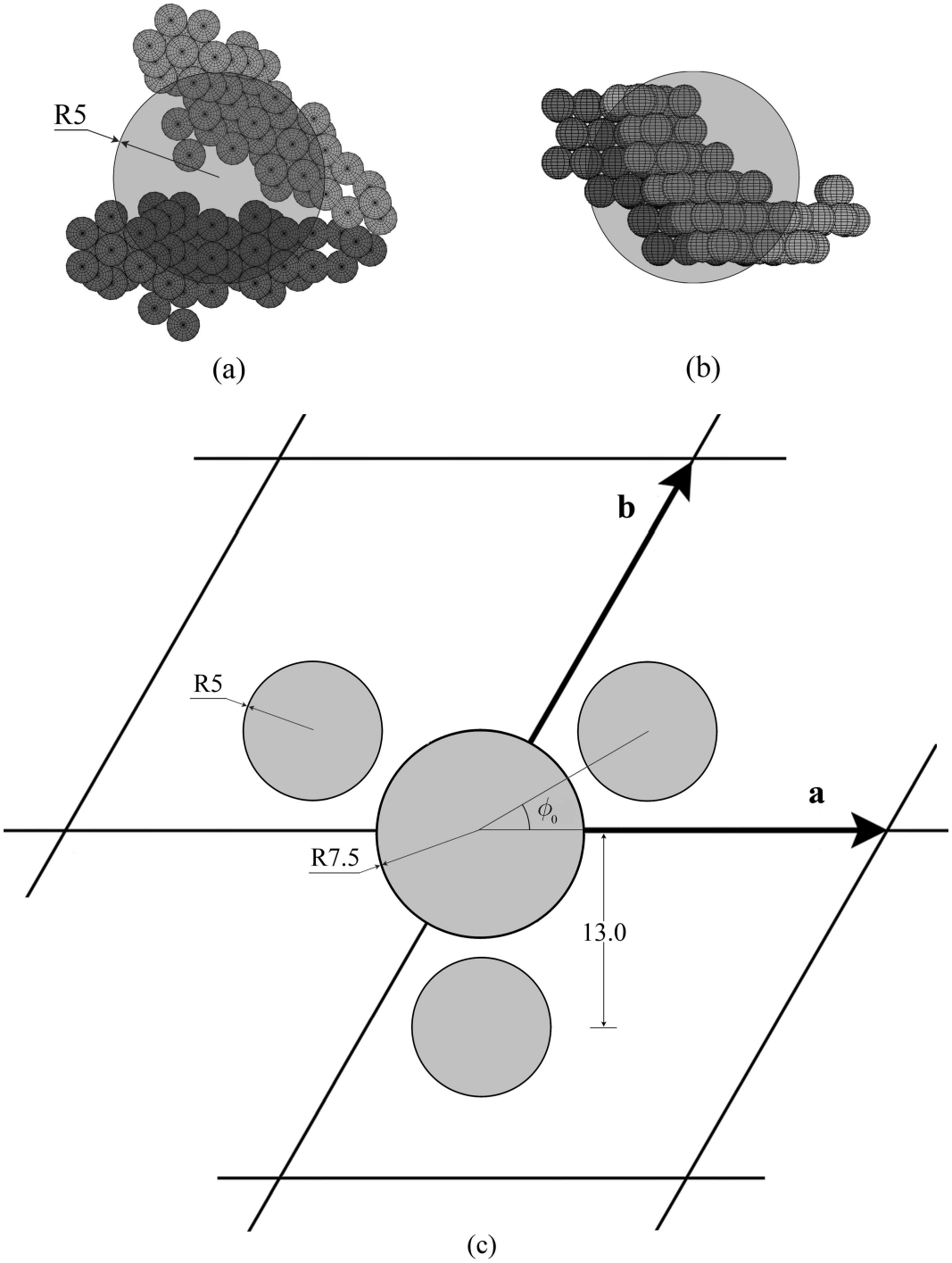

Figure 5.6 The myosin head pair repeating unit approximated by a sphere of radius $r_m = 5\,\text{nm}$, shown (a) in top view and (b) front view. A single crown from the model of myosin is shown in (c) with the rotation ϕ_0 and stem radius $r_s = 7.5\,\text{nm}$ are also indicated. Dimensions are in nm.

Since the two filament positions differ by a rotation of $\Delta\phi = \pi/3$, using the terminology of Chapter 4 and Eq. (4.17), gives

$$G_{nl}^{(2A)}(R) = G_{nl}^{(A)}(R)\exp(-in\pi/3). \tag{5.7}$$

Using the analysis of Section 4.2.3 for a hexagonal lattice and substituting $\Delta\phi = \pi/3$ and $\Delta z = 0$ into Eqs. (4.18) and (4.19) gives the Bragg and diffuse diffracted intensities as

$$\begin{aligned} I_l^B(R) &= \frac{\langle N\rangle}{4}\sum_{j\geq 0}\sum_{k=0}^{j} t(r_{jk})\sum_n \sum_{m\geq n}^{(6)} \epsilon_{n-m}\Theta_{n-m}(\phi_{jk})J_{m-n}(2\pi R r_{jk}) \\ &\quad \times G_{nl}^{(A)}(R)G_{ml}^{(A)*}(R)\left[1+\exp(-in\pi/3)\right]\left[1+\exp(im\pi/3)\right], \end{aligned} \tag{5.8}$$

and

$$\begin{aligned} I_l^D(R) &= \frac{\langle N\rangle}{4}\sum_{j\geq 0}\sum_{k=0}^{j} t(r_{jk})\rho_{jk}\sum_n \sum_{m\geq n}^{(6)} \epsilon_{n-m}\Theta_{n-m}(\phi_{jk})J_{m-n}(2\pi R r_{jk}) \\ &\quad \times G_{nl}^{(A)}(R)G_{ml}^{(A)*}(R)\left[1-\exp(-in\pi/3)\right]\left[1-\exp(im\pi/3)]\right], \end{aligned} \tag{5.9}$$

where $\Theta_p(\phi_{jk})$ is given by Eq. (4.36), ϵ_i by Eq. (4.37), $t(r_{jk})$ by Eq. (4.48), and the contributing n (and m) are those that satisfy

$$n = 3l - 9p, \quad \forall p \in \mathbb{Z}. \tag{5.10}$$

Consider now the case for model B. Referring to Fig. 5.5(d), without loss of generality, the crowns are defined to be at $z = 0$, $z = (1+\epsilon)c/3$ and $z = (2-\epsilon)c/3$ where c is the c-repeat 42.9 nm, and for frog sartorius muscle $\epsilon = 1.4/14.3 \simeq 0.1$. Using Eq. (1.146), the Fourier-Bessel structure factor for the filament is

$$\begin{aligned} G_{nl}^{(B)}(R) &= f_0(|\mathbf{R}|)J_n(2\pi R r_0)\sum_{j=0}^{2}\sum_{k=0}^{2}\exp\left(-in[\phi_0 + j2\pi/3 + k2\pi/9]\right)\exp(iz_k l 2\pi) \\ &= f_0(|\mathbf{R}|)J_n(2\pi R r_0)\exp(-in\phi_0)\sum_{j=0}^{2}\exp(-inj2\pi/3)\sum_{k=0}^{2}\exp(i2\pi[z_k l - nk/9]) \\ &= f_0(|\mathbf{R}|)J_n(2\pi R r_0)\exp(-in\phi_0)\Phi_n\tilde{\Lambda}_{nl}, \end{aligned} \tag{5.11}$$

where Φ_n is given by Eq. (5.4),

$$\begin{aligned} z_0 &= 0, \\ z_1 &= (1+\epsilon)/3, \\ z_2 &= (2-\epsilon)/3, \end{aligned} \tag{5.12}$$

and

$$\tilde{\Lambda}_{nl} = \sum_{k=0}^{2} \exp(i2\pi[z_k l - nk/9]). \tag{5.13}$$

Using Eqs. (5.12) and (5.13), $\tilde{\Lambda}_{nl}$ simplifies to

$$\begin{aligned} \tilde{\Lambda}_{nl} = 1 \quad &+ \quad \exp(i2\pi[l/3 - n/9 + l\epsilon/3]) \\ &+ \quad \exp(i4\pi[l/3 - n/9 + l\epsilon/3]) \exp(-i2\pi l\epsilon), \end{aligned} \tag{5.14}$$

so that Eq. (5.11) reduces to

$$G_{nl}^{(\mathrm{B})}(R) = \begin{cases} 3f_0(|\mathbf{R}|) J_n(2\pi R r_0) \exp(-in\phi_0) \tilde{\Lambda}_{nl}, & \text{for } n = 3p,\ \forall p \in \mathbb{Z} \\ 0, & \text{otherwise.} \end{cases} \tag{5.15}$$

With $\epsilon = 0$, $\tilde{\Lambda}_{nl}$ reduces to Λ_{nl} of Eq. (5.5). The Bragg and diffuse intensities for model B have the same form as Eqs. (5.8) and (5.9) but with $G_{nl}^{(\mathrm{B})}(R)$ and $G_{nl}^{(\mathrm{B})*}(R)$ replacing $G_{nl}^{(\mathrm{A})}(R)$ and $G_{nl}^{(\mathrm{A})*}(R)$, and the contributing Bessel orders n (and m) being those that satisfy

$$n = 3p, \quad \forall p \in \mathbb{Z}. \tag{5.16}$$

5.3.2 Diffraction data

The measured diffraction data used here are those given by Iwamoto et al. [IWFY03]. They present intensity profiles along myosin layer lines, that can be used for comparison with the calculated diffraction. The measured X-ray fibre diffraction pattern obtained by Iwamoto et al. [IWFY03] is shown in Fig. 5.7. The diffraction pattern is the summed data from 38 individual exposures using 6 different specimens of intact bullfrog sartorius muscle in the rest state. Each exposure was performed at high gain to amplify weak features then background scattering was subtracted [IOSF02]. The reader is referred to Ref. [IOSF02] for further details on the data collection and the estimation of the background. Iwamoto et al. [IWFY03] present intensity profiles extracted from the data shown in Fig. 5.7 along layer lines M1 through to M5. They also present the intensity profile along layer line M0 for which the data is not shown in Fig. 5.7. The layer lines are reproduced in Fig. 5.8, after being converted from intensity to amplitude. The amplitudes were normalized such that the largest peak on the equator at $R \simeq 0.026\,\mathrm{nm}^{-1}$, corresponding to the $(1, 0)$ reciprocal lattice point, is equal to unity. The radii of expected reciprocal lattice and superlattice reflections are obtained by multiplying radii in the second column of Table 4.1 by $1/a$.

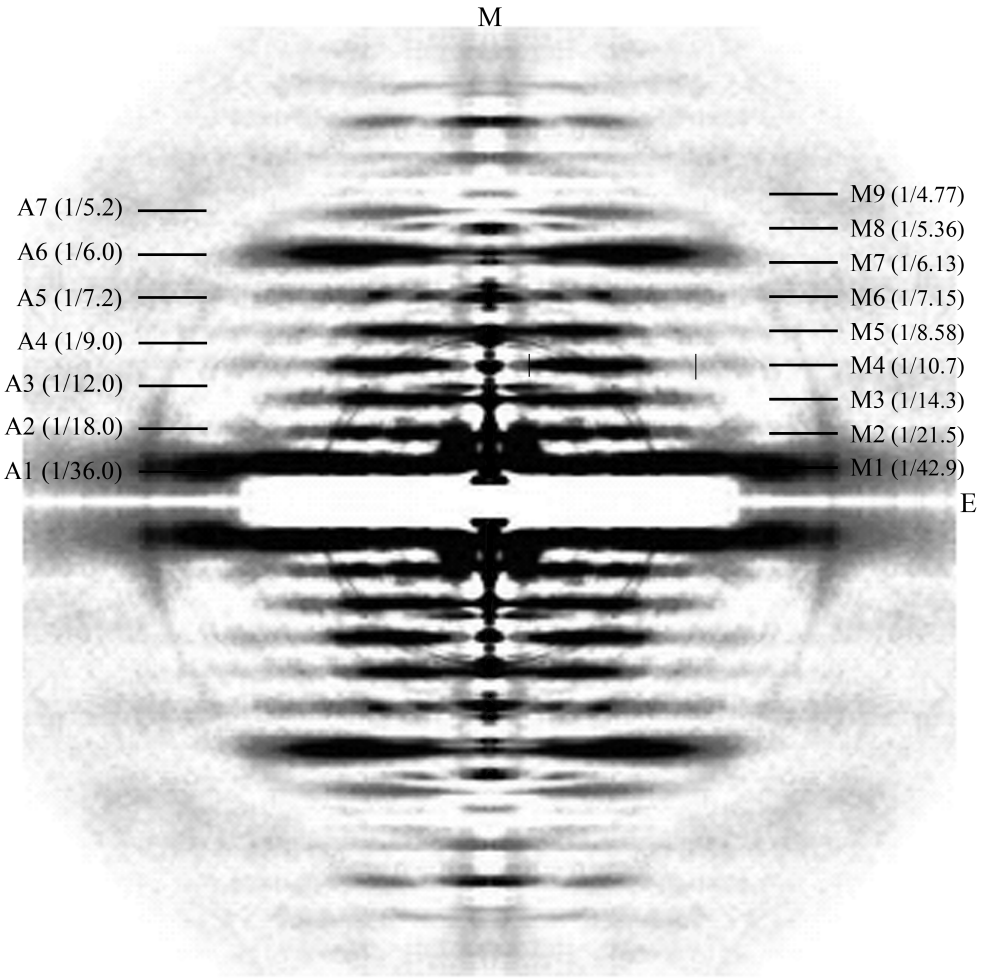

Figure 5.7 Diffraction pattern from frog sartorius muscle fibre in the relaxed state, obtained by Iwamoto et al. [IWFY03]. M1 through to M9 denote the first to 9th-order myosin layer lines with a crystallographic repeat of 42.9 nm and A1 through to A7 denote the first to 7th-order actin layer lines. The values in parentheses are positions of layer lines along the Z-axis.

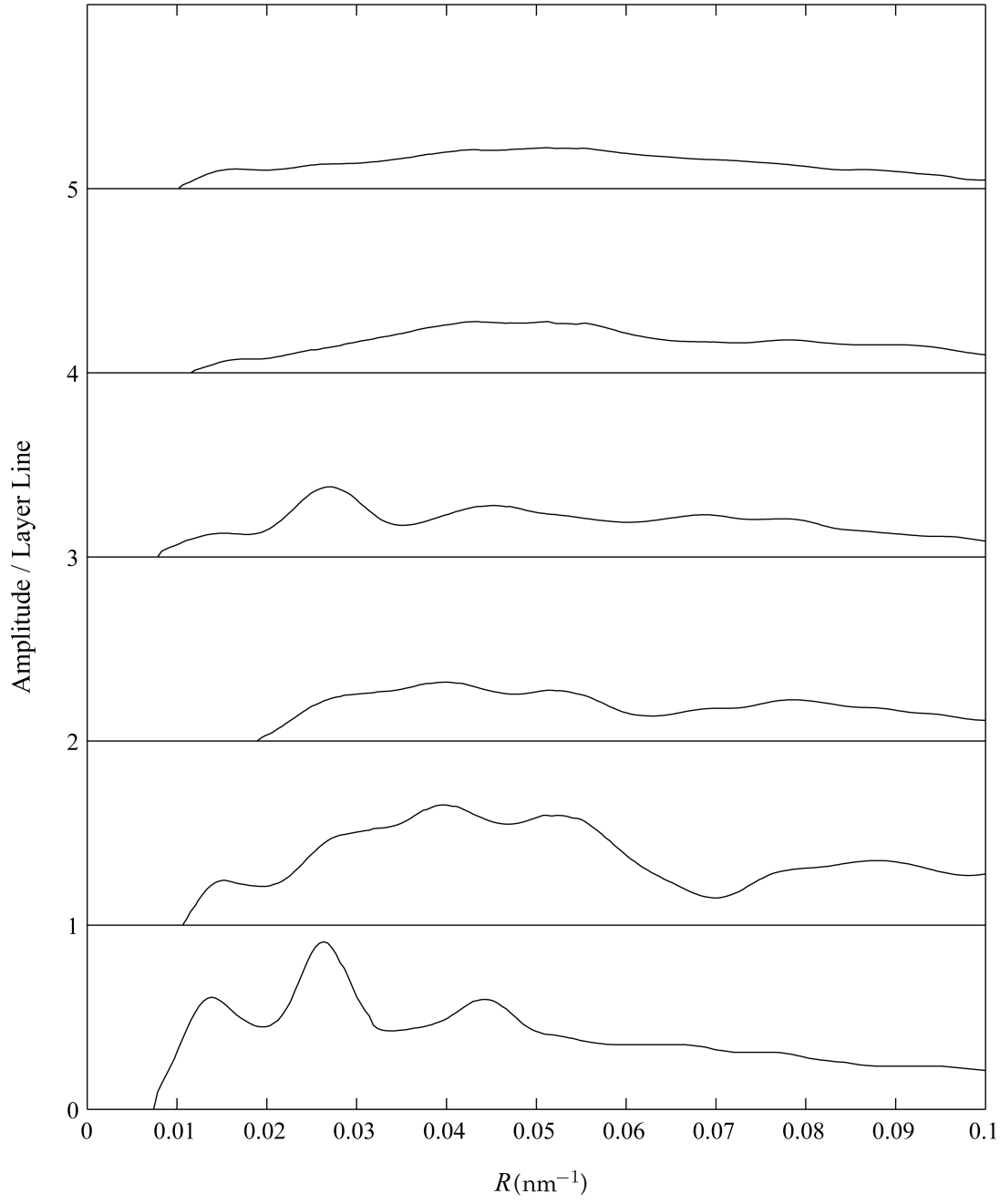

Figure 5.8 Amplitudes along the centres of the myosin layer lines in Fig. 5.7 [IWFY03].

5.3.3 Coherence length and disorientation

The data in Fig. 5.8 are traces of the amplitude through the centres of the layer lines. The layer line amplitudes $I_l(R)$ calculated using the equations in Chapter 4 must therefore be converted to equivalent traces for comparison. The differences are due to smearing of the layer lines due to coherence length and disorientation. The effects of coherence length and disorientation are described in Section 1.5.4. At low resolution there is no layer line overlap and each layer line can be treated independently.

Equation (1.165) describes the diffraction in terms of angular smearing dominated by disorientation. It is convenient here to resolve the smearing of each layer line into components along the R and Z directions. The intensity in the vicinity of the layer line, denoted $\tilde{I}_l(R,Z)$, can then be written as

$$\begin{aligned}\tilde{I}_l(R,Z) &= I_l(R)\delta(Z-l/c) \otimes \left[\frac{1}{\sqrt{2\pi}(\alpha_0\rho\cos\sigma)}\exp\left(-\frac{R^2}{2(\alpha_0\rho\cos\sigma)^2}\right)\right] \\ &\quad \otimes \left[\frac{1}{\sqrt{2\pi}[1/l_c^2+(\alpha_0\rho\sin\sigma)^2]^{1/2}}\exp\left(-\frac{Z^2}{2[1/l_c^2+(\alpha_0\rho\sin\sigma)^2]}\right)\right].\end{aligned} \tag{5.17}$$

The intensity along the centre of the layer line, $\tilde{I}_l(R) = \tilde{I}_l(R, l/c)$, is then, aside from some constant factors,

$$\tilde{I}_l(R) = \begin{cases} I_l(R)(1/l_c^2+\alpha_0^2R^2)^{-1/2} \otimes \left[(l/c)^{-1}\exp\left(-R^2/[2(\alpha_0 l/c)^2]\right)\right], & l \neq 0 \\ I_l(R)(1/l_c^2+\alpha_0^2R^2)^{-1/2}, & l = 0. \end{cases} \tag{5.18}$$

The intensity along the centre of the layer line is therefore reduced by the factor $(1/l_c^2 + \alpha_0^2R^2)^{-1/2}$ as a result of smearing along Z due to finite coherence length and disorientation, and is smeared along R due to disorientation. The calculated intensities $I_l(R)$ are therefore converted to $\tilde{I}_l(R)$ using Eq. (5.18) before comparison with the measured traces in Fig. 5.8.

The conversion of $I_l(R)$ to $\tilde{I}_l(R)$ requires estimates of l_c and α_0. These parameters were estimated by matching Gaussian profiles to profiles of the grey levels across profiles in Fig. 5.7. This involves an implicit assumption that the grey level represents intensity although the effect of this assumption for this purpose is expected to be small. The cross-sectional profile versus Z on the $l = 4$ layer at $R = 0.028\,\text{nm}^{-1}$ is shown in Fig. 5.9(a) ($\times$'s). In this region where $\sigma \approx 16^\circ$ is small, the effects of disorientation are small and l_c can be estimated by fitting a Gaussian [full curve in Fig. 5.9(a)], giving $l_c = 350\,\text{nm}$. The profile on the $l = 4$ layer line at $R = 0.14\,\text{nm}^{-1}$ is shown in Fig. 5.9(b) ($\times$'s). Fitting a Gaussian profile [full curve in Fig. 5.9(b)] to this profile gives $1/l_c^2 + (\alpha_0 R)^2 = 2.4 \times 10^{-5}\,\text{nm}^{-2}$. Substituting the value of l_c determined above gives the estimate $\alpha_0 = 2.0^\circ$.

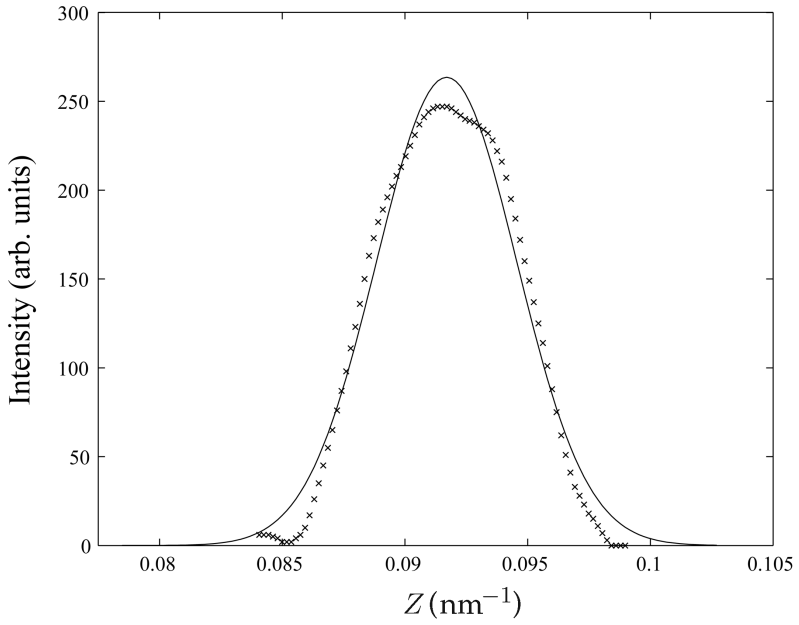

(a)

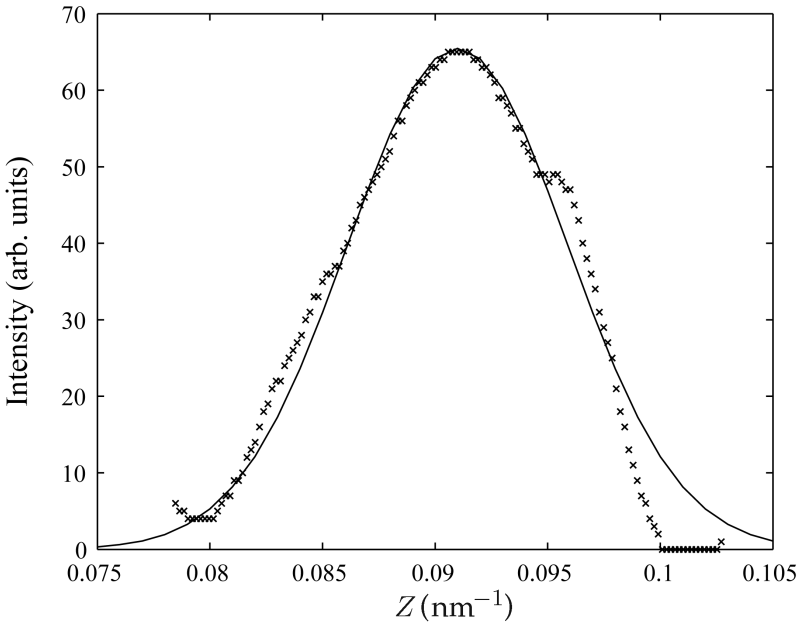

(b)

Figure 5.9 Intensity profiles ($\times$'s) through the myosin layer line M4 as a function of Z at fixed (a) $R = 0.028\,\mathrm{nm}^{-1}$, and (b) $R_l = 0.14\,\mathrm{nm}^{-1}$. The full lines show the Gaussian profiles fitted to data.

5.4 Simulations

5.4.1 Methods

Layer line intensities $I_l(R)$ were calculated as described in Section 4.4.1 and converted to layer line cross sections $\tilde{I}_l(R)$ using Eq. (5.18) and the amplitudes compared with the data in Fig. 5.8. The myosin filament model consisting of spheres as described in Section 5.2.3 is used. Both models A and B are considered. Expressions for the diffraction given in Section 5.3.1 are used and the scattering factor for a sphere, given by Eq. (B.10) in Appendix B. The orders of n in Eqs. (5.10) and (5.16) are truncated by the condition Eq. (4.50).

The calculated amplitudes presented represent the total of the Bragg and diffuse components, i.e. the square root of the sum of Eqs. (5.8) and (5.9). The myosin filament stem is represented as a cylinder of radius $r_0 = 7.5\,\text{nm}$ and the diffraction from a cylinder [calculated in Appendix B and given by Eq. (B.15)], is included in the diffraction on the equator. The diffraction from the cylinder contributes only Bragg reflections on the equator. Calculated amplitudes are normalized using the convention stated in Section 5.3.2, that is, the amplitude of the peak at $R_{1,0} \simeq 0.026\,\text{nm}^{-1}$ on the equator is set to unity. The reference rotation ϕ_0 is found to have only a small effect on the diffraction and is set to zero for most of the simulations.

5.4.2 Results

A suitable crystallite radius was found to be $r_c = 200\,\text{nm}$. First, for reference, calculated diffraction patterns for no disorder (i.e. only one filament rotation) and with random disorder ($T = \infty$) are shown in Figs. 5.10 and 5.11, respectively. The measured layer-line intensities of Fig. 5.8 are represented by the dashed lines. Inspection of Fig. 5.10 shows that for no disorder (i.e. a simple lattice), the diffraction consists of Bragg peaks only. The amplitudes of the Bragg peaks resemble the amplitudes in the diffraction pattern but the model is clearly unsatisfactory as it does not produce the observed diffuse diffraction. For random (uncorrelated) disorder (Fig. 5.11), the Bragg reflections are suppressed at low resolution on layer lines 1, 2 and 4 and diffuse diffraction appears. Note the absence of diffuse diffraction on layer line 3. Overall, the match with the measured diffraction pattern is improved, but there are no Bragg or superlattice peaks on layer lines 1 and 2 at low resolution. Note that disorder does not affect diffraction on the equator.

The diffracted amplitude calculated for the TIA at $T = T_{\text{eff}} = 1.2$ is shown in Fig. 5.12. Agreement is improved with the appearance of peaks at the superlattice radii on layer lines 1 and 2. Note that the $l = 3$ layer-line amplitudes in Figs 5.12 and 5.10 are nearly identical. This result suggests that the $l = 3$ layer-line amplitude is not significantly influenced by

the myosin superlattice disorder and testing disorder models based on this layer-line, as done by Koubassova et al. [KT02, KBFT08], would be inconclusive.

Although the fit in Fig. 5.12 is quite good there are some discrepancies. There is an excess of Bragg diffraction over diffuse diffraction on layer lines 0 and 1 at high resolution compared to that observed. This could be due to the presence of lattice disorder. Lattice disorder is easily incorporated into the model, as done in Section 4.2.2 where the effects on the diffracted intensity are also discussed. Uncorrelated lattice disorder suppresses Bragg diffraction at high resolution and introduces diffuse diffraction. The lateral site variance is dependent on the species being considered and can be estimated from electron micrographs such as Fig. 5.1, with a value $\sigma_{\text{lat}} \sim 1.9\,\text{nm}$ being estimated in rabbit muscle [KT02]. Lattice disorder with $\sigma_{\text{lat}} = 1.2\,\text{nm}$ was incorporated into the diffraction calculation using Eqs. (4.29) and (4.30) and the result is shown in Fig. 5.13. An improvement is seen at high resolution on layer lines 0 and 1 although the effect is quite small. The lattice disorder is retained in subsequent calculations.

Using the same parameters as above but for model B (i.e. breaking the 9_1 symmetry of a single strand) with $\epsilon = 0.1$ gives the calculated amplitudes shown in Fig. 5.14. Small variations are introduced, the most being an increase in diffuse diffraction on layer line 3. This gives a better match to the data on this layer line so model B is used from here on. The agreement between the calculated and measured diffraction is now quite good.

It is worth considering the effects of a non-zero value of ϕ_0 on the diffraction. The full range of possible values for ϕ_0 is $-30^\circ < \phi_0 < 30^\circ$. Varying ϕ_0 showed that the diffuse diffraction on layer lines 1, 2, 4, and 5 decreases with increasing $|\phi_0|$ and reaches a minimum at $|\phi_0| = 30^\circ$, and is a maximum for $\phi_0 = 0^\circ$. This tended to make the match to the data worse so the value ϕ_0 was retained. A value of $\phi_0 = -10^\circ$ comparable to values determined in Ref. [AKS06] for bony fish muscle does not give diffraction that is significantly different to that for $\phi_0 = 0^\circ$.

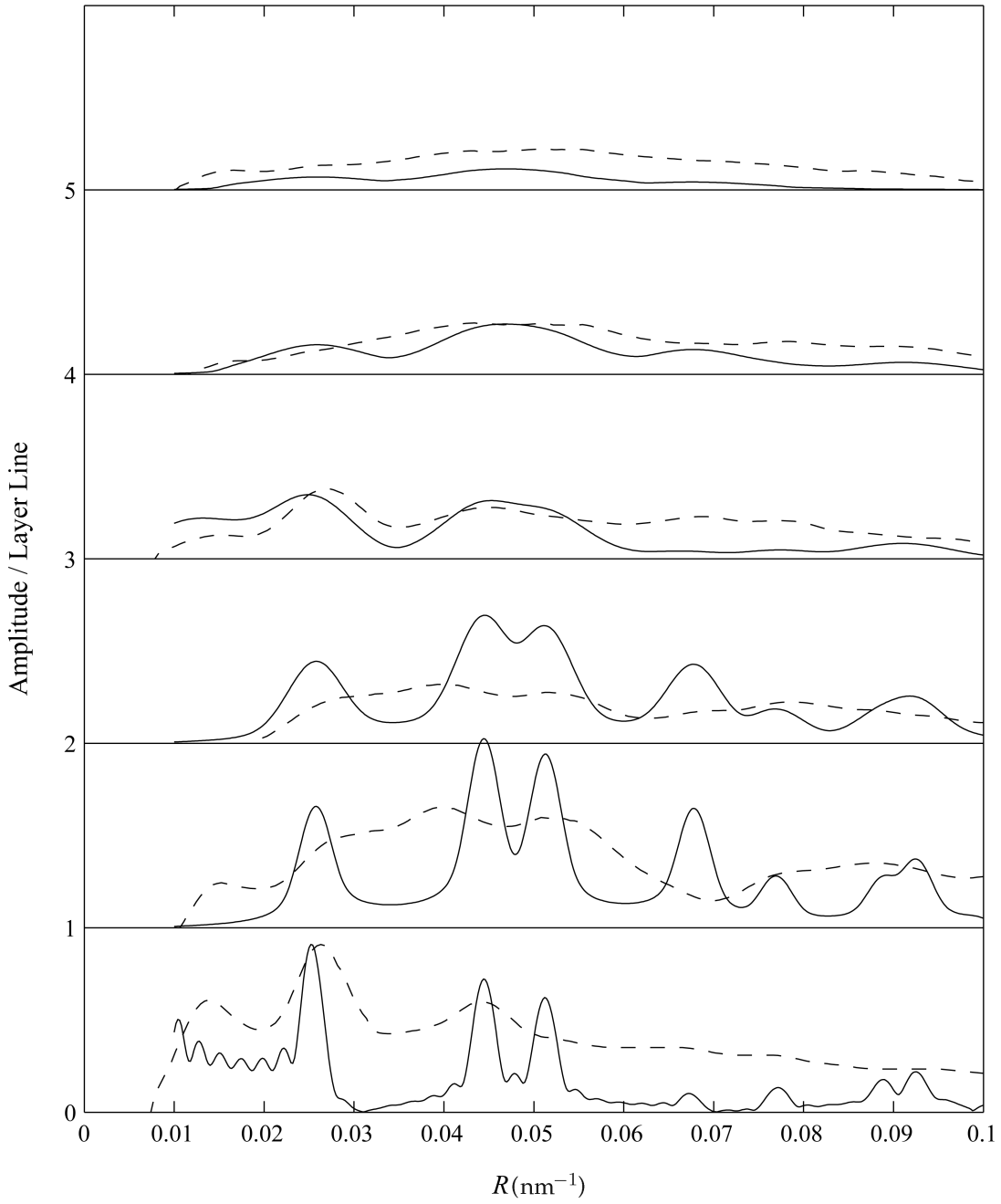

Figure 5.10 Calculated layer line amplitudes (full lines) from a myosin filament array with no disorder and measured amplitudes (broken lines).

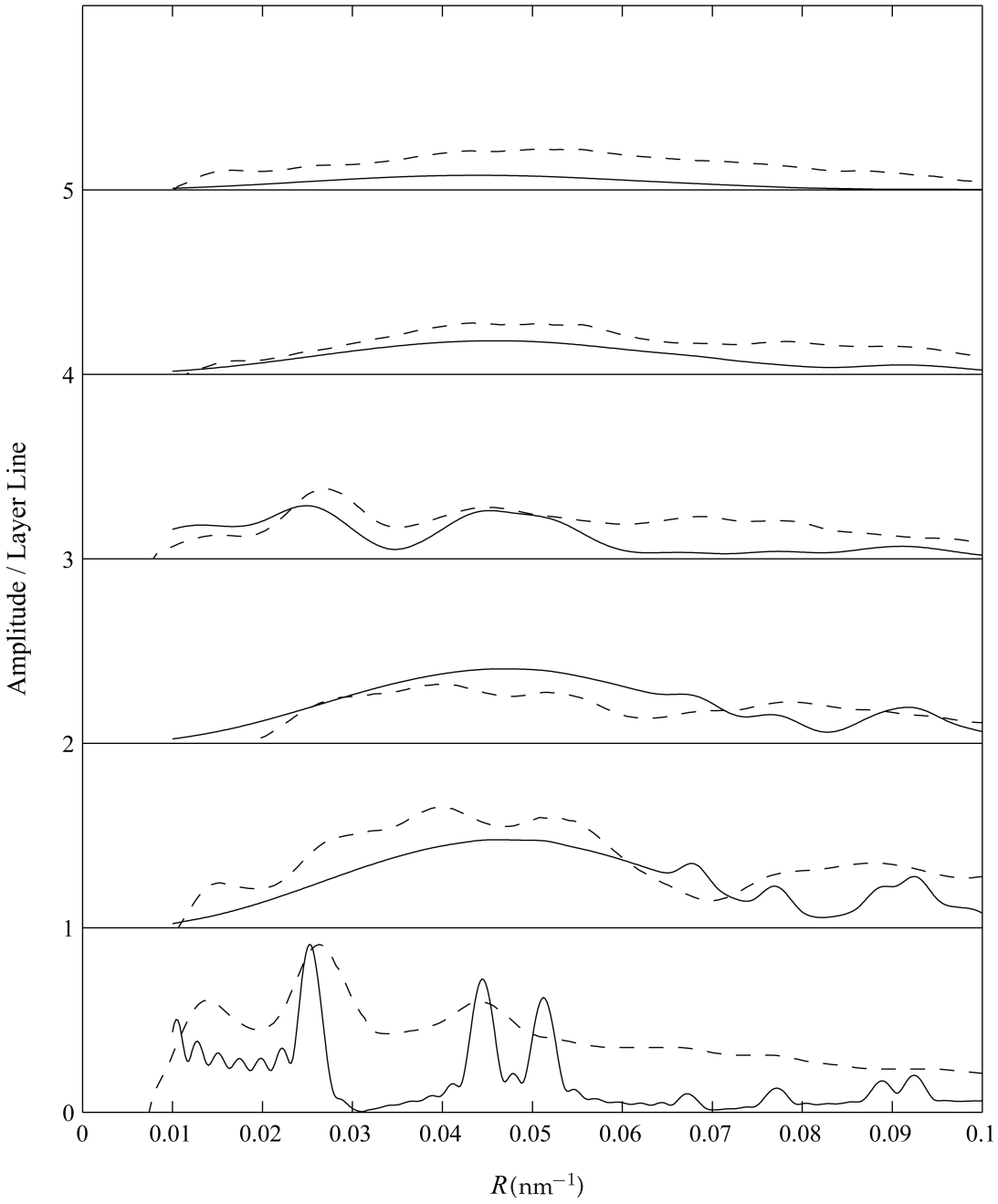

Figure 5.11 Calculated layer line amplitudes (full lines) from a myosin filament array with uncorrelated substitution disorder and measured amplitudes (broken lines).

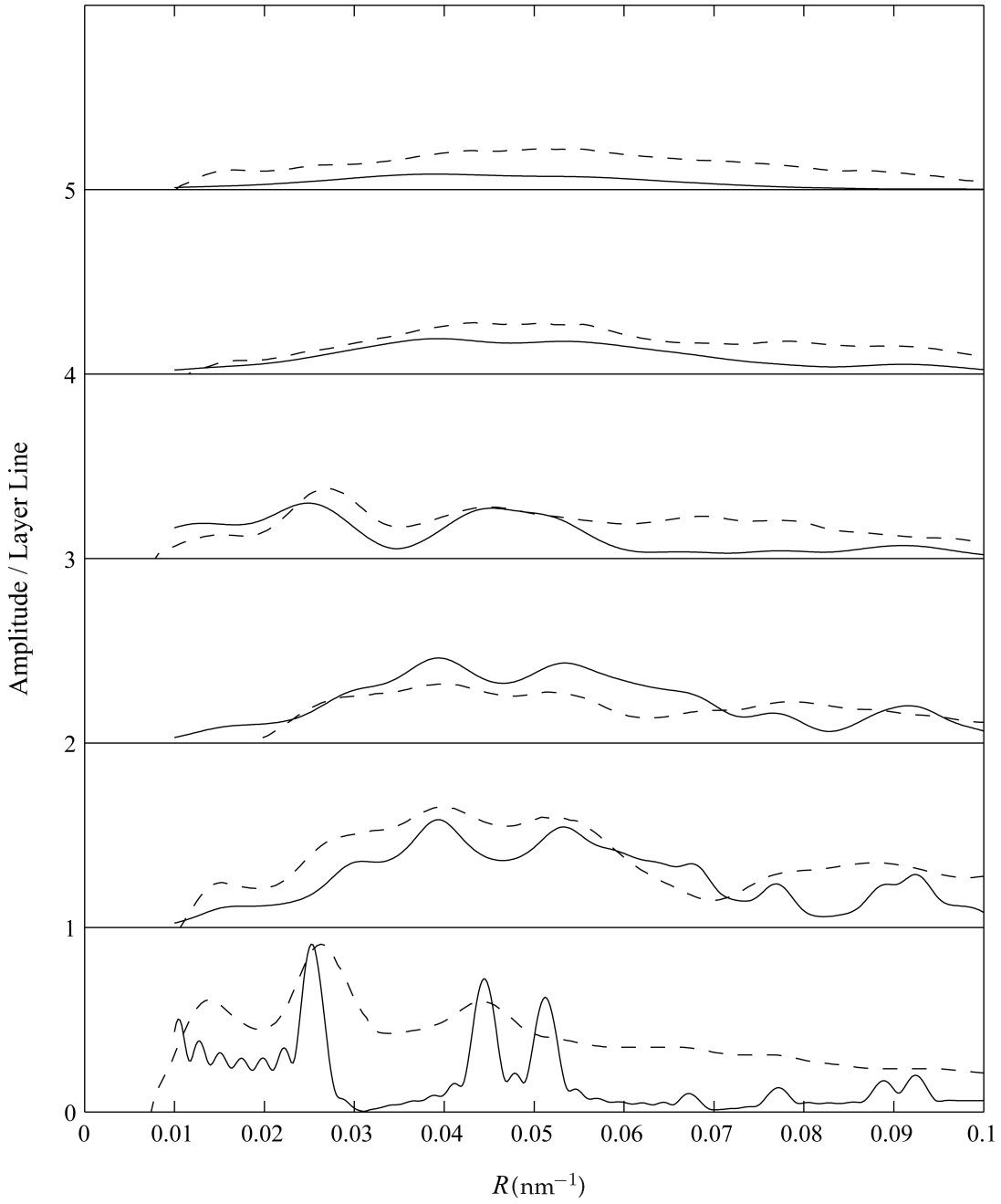

Figure 5.12 Calculated layer line amplitudes (full lines) for the TIA model of the myosin filament array at $T_{\mathrm{eff}} = 1.2$, and the measured amplitudes (broken lines).

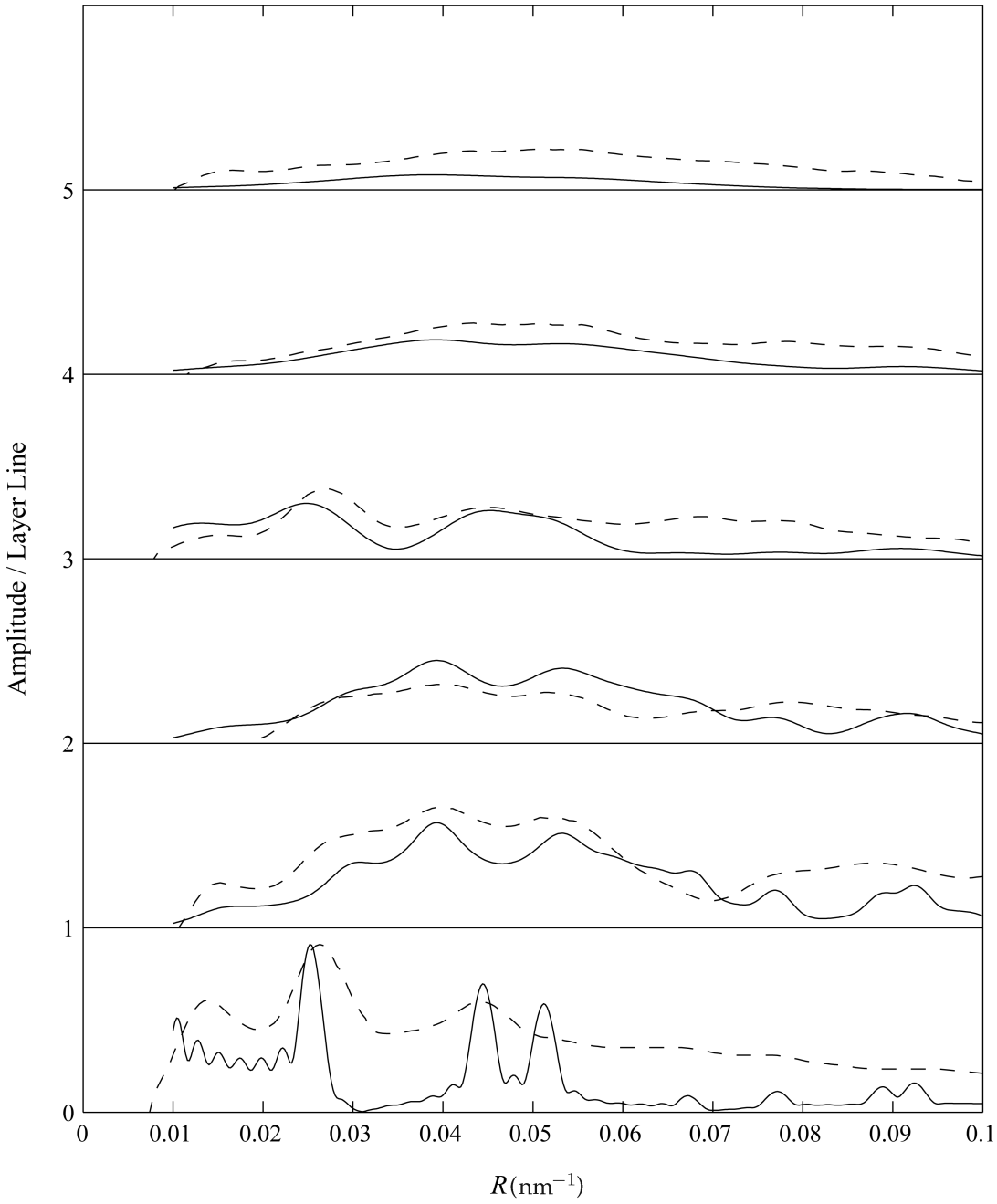

Figure 5.13 Calculated layer line amplitudes (full lines) for the TIA model of the myosin filament array with uncorrelated lattice disorder. Measured amplitudes are shown by the broken lines.

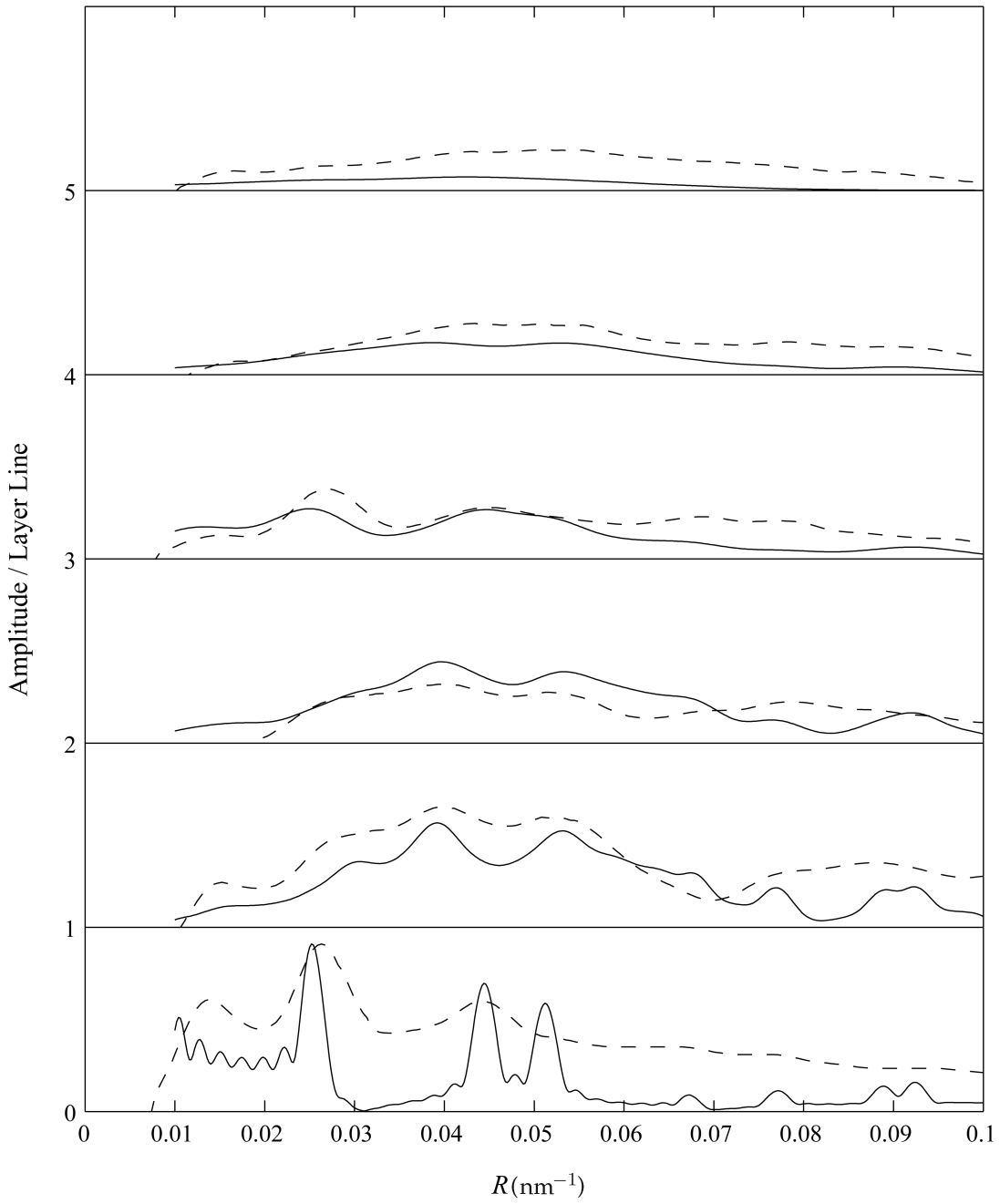

Figure 5.14 Calculated layer line amplitudes (full lines) for model B. Measured amplitudes are shown by the broken lines.

Referring to Fig. 5.14, the calculated diffraction is too weak on layer lines 4 and 5. This can be increased by increasing the molecular transform at high resolution, which in this case corresponds to decreasing r_m. The effect of reducing the radius of the sphere representing myosin head pair to $r_m = 4\,\text{nm}$ is shown in Fig. 5.15. The diffraction on the higher layer lines is increased and a better match to the data is obtained. This also indicates that a higher resolution model of the myosin head is required to improve modelling of higher order layer line intensities.

A quantitative measure of the agreement between the calculated and measured diffraction amplitudes is provided by calculating the R-factor, which was calculated for Figures 5.10-5.15. The R-factor indicates the "goodness of fit" and the smaller the R-factor, the better the fit. The R-factor between the calculated and measured amplitudes is given by

$$\mathcal{R} = \frac{\sum_{l=1}^{5} \sum_i \left| kA_l(R_i) - \hat{A}_l(R_i) \right|}{\sum_{l=1}^{5} \sum_i \hat{A}_l(R_i)}, \tag{5.19}$$

where $A_l(R_i)$ and $\hat{A}_l(R_i)$ are calculated and measured amplitude values, respectively, the subscript i indicates the values of R_i at which the amplitudes are sampled, and k is a scale factor that is adjusted to minimize the R-factor. The equator is excluded for the reasons described above. The R-factors for the models corresponding to Figures 5.10-5.15 are given in Table 5.1. The R-factor shows poor agreement for the model incorporating no disorder and an improved fit if uncorrelated substitution disorder is assumed. The R-factor reduces only slightly when TIA-type disorder is assumed rather than uncorrelated substitution disorder. The considerable improvement in agreement on layer line 1 seen in Fig. 5.12 is evidently not reflected in the R-factor. Introducing uncorrelated lattice disorder causes the R-factor to increase slightly, indicating that the disorder model used is inadequate for frog sartorius muscle. A significant decrease in the R-factor is seen if model B for the axial separation of myosin heads is used, indicating that this model is a more accurate description. The R-factor reduces considerably when the radius of the sphere representing the myosin head is reduced to $r_m = 4\,\text{nm}$, indicating that this is a better estimate of the head dimensions.

The agreement between the calculated and measured diffraction is now quite good and is considered satisfactory for the low resolution model of the myosin filament that has been used. An R-factor of 0.34 is acceptable for low resolution modelling of this kind. The main discrepancy is on the equator where the diffraction will also be due to other material in the muscle fibre with c-repeats different to that of myosin.

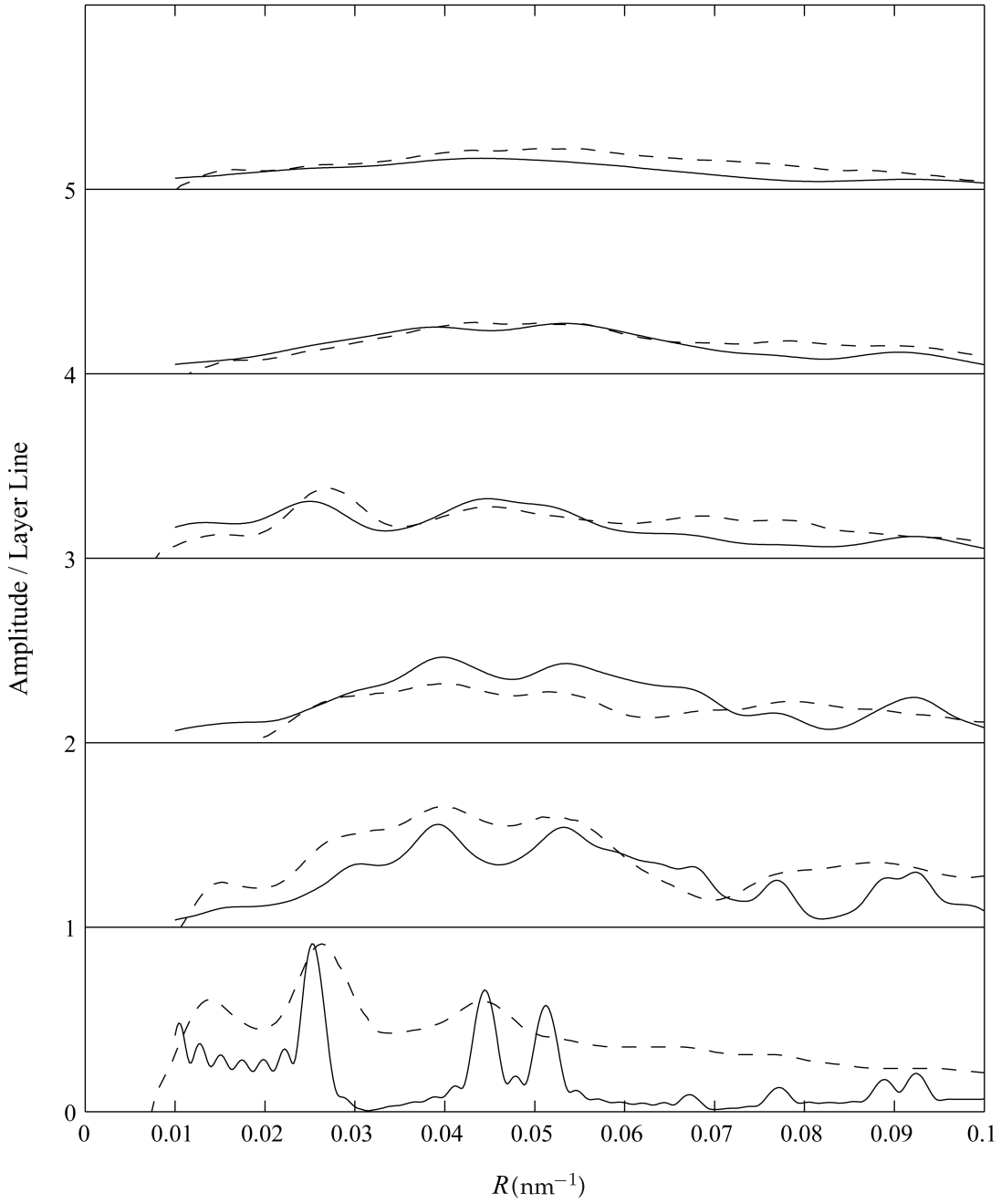

Figure 5.15 Calculated layer line amplitudes (full lines) for model B with $r_m = 4\,\mathrm{nm}$. Measured amplitudes are shown by the broken lines.

Model	Figure	$\mathcal{R}$
No disorder	5.10	0.540
Uncorrelated disorder	5.11	0.426
TIA	5.12	0.424
TIA (with lattice disorder)	5.13	0.432
TIA (Model B)	5.14	0.415
TIA ($r_m = 4\,\mathrm{nm}$)	5.15	0.339

Table 5.1 R-factors calculated for the models corresponding to Figures 5.10-5.15.

5.5 Conclusions

The theory for diffraction by fibres containing helical molecules with correlated substitution disorder developed in Chapter 4, and the high precision form of the TIA correlation function derived in Chapter 2, have been used to calculate diffracted intensities from a low-resolution model of the myosin filaments in vertebrate muscle fibres. The calculated diffraction shows the effects of the myosin superlattice disorder with diffuse diffraction and superlattice peaks. Comparison with layer line traces from a measured diffraction pattern shows quite good agreement. There are discrepancies on the equator and at high resolution where not all of the diffuse scattering is accounted for, probably due to other diffracting material and maybe other forms of disorder. An obvious candidate for diffuse scattering to consider is correlated lattice disorder in myosin filament packing. This would have the effect of broadening and diminishing Bragg reflections at large R which, as a result, increases the intensity of the superlattice reflections relative to the Bragg reflections. This could be incorporated into the calculation without too much difficulty.

Chapter 6

Summary and Suggestions for Future Research

In this thesis, the two-point correlation functions of two archetypical geometrically frustrated systems, the triangular Ising antiferromagnet (TIA) and the fully frustrated Ising model (FFS), were studied. Theory was developed for the calculation of cylindrically averaged diffraction from polycrystalline fibres with correlated substitution disorder. This theory was used to calculate the diffraction from polycrystallites with TIA-type interactions between scatterers, allowing the effects of the disorder to be explored. A model for a type of disorder observed in the myosin filament array of higher vertebrate muscle was developed that utilized the TIA correlation function developed earlier. This was used in calculations of cylindrically averaged diffraction from such specimens and comparison with experimental data.

For the TIA and FFS, it was shown that the lattice can be partitioned into 3 sublattices such that the two-point correlation function is a smoothly varying function on each sublattice. Accurate descriptions of each correlation function in terms of only radial separation and the sublattice were developed from a combination of cluster Monte Carlo techniques and numerical integration of known exact results. It was found that both correlation functions are approximately constant for a rescaled temperature $T < 0.4$ and are, to a good approximation, rotationally invariant within a given small error for $0 < T < 1$. Rotational invariance of the FFS correlation function was shown to break down for larger temperatures. Simple approximations were derived that accurately describe the TIA correlation function in the region of separation-temperature space where correlations are significant. The highly accurate methods developed for calculating the correlation functions will be useful to those using the systems to quantitatively model various systems.

Theory for calculating the cylindrically averaged diffraction from polycrystalline fibres containing helical molecules with correlated substitution disorder was developed. The analysis was kept sufficiently general to describe diffraction from any number of scatterer types and so that lattice disorder could be included into the model. Simplifications due to triangular lattice symmetry and having only two scatterer types were made. This was used to calculate the diffraction from fibres with TIA-type interactions between the two scatterers, and the effects of different relationships between the two scatterers was explored. Particular values lead to extinction of Bragg or diffuse diffraction on particular layer-lines. A low resolution model for the myosin filament of higher vertebrate muscle was developed and incorporated into diffraction calculations. Adjustment of parameters of the model gave good agreement with observed diffraction data.

The primary continuation of the work presented in this thesis is its application to higher resolution structural studies of superlattice muscle from X-ray fibre diffraction data. This will involve incorporation of the expressions for the diffraction derived here into muscle structure refinement programs that use high-resolution structures of myosin subfragment -1, actin and the acto-S1 complex. Determination of the myosin head configurations within higher vertebrate muscle at rest and during contraction will overcome current methods that do not incorporate the effects of the disorder.

Other possible extensions to the work described here include:

1. Development of a functional expression for the FFS correlation function could be useful in structural studies of systems that exhibit FFS-type statistics.

2. Further exploration of the high temperature TIA and FFS correlation behaviour to clarify the extent of rotational invariance of the correlation functions with temperature. In particular, one sublattice of the TIA shows a reversal in sign of the correlation function at high temperatures.

3. The relationship between lattice symmetry and the extinction of cylindrically averaged Bragg and diffuse diffraction from polycrystallites with correlated substitution disorder could be further explored.

4. Study of the extent and nature of lattice disorder in the frog sartorius muscle from the electron micrographs would be worthwhile.

Appendix A

Appendix A: The Pfaffian solution

In the expansion of the product of Eq. (1.30), all terms containing an odd number of s variables vanish. The remaining terms can be interpreted to represent polygons with a variable number of horizontal, vertical and diagonal nearest-neighbour links. Determining the partition function can then be expressed as a counting problem. Kasteleyn [Kas63] showed that the partition function Eq. (1.30) can be evaluated by constructing a Pfaffian $\mathrm{Pf}^2(\mathbf{A}) = |\mathbf{A}|$ and calculating the square of the partition function,

$$Z^2 = (2\cosh K_1 \cosh K_2)^{2N} |\mathbf{A}|. \tag{A.1}$$

Calculation of the Pfaffian equates to counting dimer coverings on the corresponding "bathroom tile" or cluster lattice, shown in Fig. A.1(b), constructed by replacing each site of the square lattice [Fig. A.1(a)] by a cluster of four sites. The arrows indicate directions which enforce a correct counting of polygons on the tile lattice.

The skew-symmetric matrix $\mathbf{A}$ is a $4N \times 4N$ matrix with 4×4 submatrix elements obtained by inspection of Fig. A.1(b). The entry $\mathbf{A}(x, y; x, y)$ is constructed by writing down parities of bonds that connect cluster points associated with the site x, y relative to the arrowhead directions. With the convention that bond directions are considered in the order right, left, up, down,

$$\mathbf{A}(x, y; x, y) = \begin{bmatrix} 0 & 1 & -1 & -1 \\ -1 & 0 & 1 & -1 \\ 1 & -1 & 0 & 1 \\ 1 & 1 & -1 & 0 \end{bmatrix}. \tag{A.2}$$

The element $\mathbf{A}(x, y; x + 1, y)$ is constructed by writing down bond strengths and their rel-

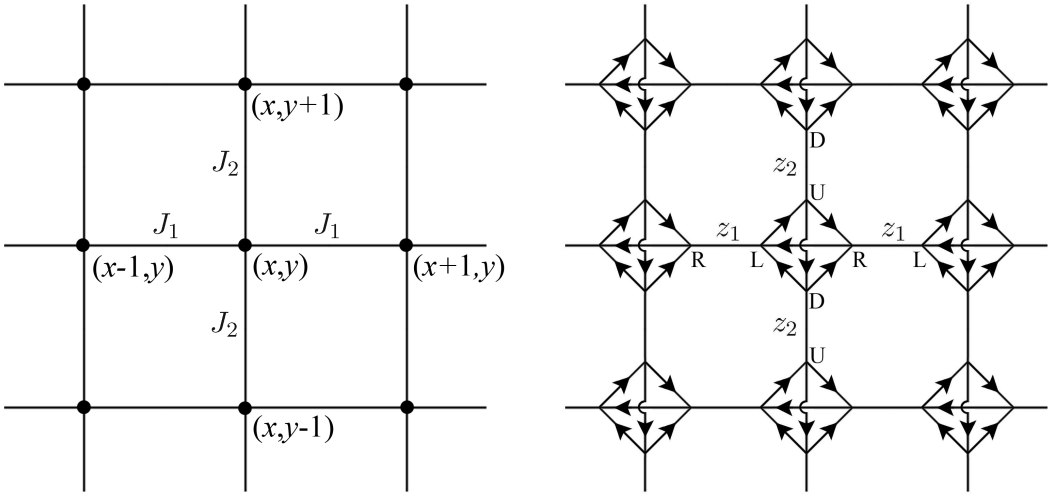

Figure A.1 A region of the SL Ising model in (a), and the corresponding "bathroom tile" lattice in (b). The arrows give a possible set of directions which force a correct counting of polygons on the lattice.

ative parities connecting cluster points associated with the sites (x, y) and $(x + 1, y)$ giving

$$\mathbf{A}(x, y; x + 1, y) = \begin{bmatrix} 0 & 0 & 0 & 0 \\ 0 & 0 & 0 & 0 \\ 0 & 0 & 0 & z_2 \\ 0 & 0 & 0 & 0 \end{bmatrix}. \tag{A.3}$$

Similarly, the other 4×4 elements are given by

$$\mathbf{A}(x, y; x, y + 1) = \begin{bmatrix} 0 & z_1 & 0 & 0 \\ 0 & 0 & 0 & 0 \\ 0 & 0 & 0 & 0 \\ 0 & 0 & 0 & 0 \end{bmatrix}, \tag{A.4}$$

$$\mathbf{A}(x + 1, y; x, y) = \begin{bmatrix} 0 & 0 & 0 & 0 \\ 0 & 0 & 0 & 0 \\ 0 & 0 & 0 & 0 \\ 0 & 0 & -z_2 & 0 \end{bmatrix}, \tag{A.5}$$

and

$$\mathbf{A}(x,y+1;x,y) = \begin{bmatrix} 0 & 0 & 0 & 0 \\ -z_1 & 0 & 0 & 0 \\ 0 & 0 & 0 & 0 \\ 0 & 0 & 0 & 0 \end{bmatrix}, \tag{A.6}$$

where $z_i = \tanh K_i$ as in Eq. (1.30). The skew-symmetric matrix $\mathbf{A}$ can then be evaluated by solving $D\mathbf{u} = \lambda\mathbf{u}$ where is a $4N$-component eigenvector

$$\begin{aligned} \mathbf{A}(x,y;x,y)\mathbf{u}_{xy} + \mathbf{A}(x,y;x+1,y)\mathbf{u}_{x+1,y} + \mathbf{A}(x+1,y;x,y)\mathbf{u}_{x-1,y} & \\ +\mathbf{A}(x,y;x,y+1)\mathbf{u}_{x,y-1} + \mathbf{A}(x,y-1;x,y)\mathbf{u}_{x,y+1} &= \lambda\mathbf{u}_{xy}, \end{aligned} \tag{A.7}$$

where the $\mathbf{u}_{xy}$ are 4-component vectors. The system can be diagonalized by a Fourier-type unitary transform

$$\mathbf{u}_{xy} = \exp\left(\frac{i2\pi(px+qy)}{N}\right)\mathbf{u}^{(pq)}, \tag{A.8}$$

where $1 \le p \le m$ and $1 \le q \le n$ are integers. Eq. (A.7) becomes

$$\begin{aligned} \Big(\mathbf{A}(x,y;x,y) + \mathbf{A}(x,y;x+1,y)\alpha_p &+ \mathbf{A}(x+1,y;x,y)\alpha_q \\ +\mathbf{A}(x,y;x,y+1)\alpha_{-p} &+ \mathbf{A}(x,y-1;x,y)\alpha_{-q}\Big).\mathbf{u}^{(pq)} = \lambda\mathbf{u}^{(pq)}, \end{aligned} \tag{A.9}$$

where $\alpha_q = \exp(i\phi_1)$ and $\alpha_p = \exp(i\phi_2)$ with $\phi_1 = 2\pi p/m$ and $\phi_2 = 2\pi q/n$. The determinant $|\mathbf{A}|$ can therefore be obtained from the determinant of

$$\begin{aligned} \mathbf{A}(\phi_1,\phi_2) &= \mathbf{A}(0,0;0,0) + \mathbf{A}(0,0;1,0)e^{i\phi_1} + \mathbf{A}(0,0;-1,0)e^{-i\phi_1} \\ &\quad +\mathbf{A}(0,0;0,1)e^{i\phi_2} + \mathbf{A}(0,0;0,-1)e^{-i\phi_2} \\ &= \begin{bmatrix} 0 & 1+z_1e^{i\phi_2} & -1 & -1 \\ -1-z_1e^{-i\phi_2} & 0 & 1 & -1 \\ 1 & -1 & 0 & 1+z_2e^{i\phi_1} \\ 1 & 1 & -1-z_2e^{-i\phi_1} & 0 \end{bmatrix}. \end{aligned} \tag{A.10}$$

For $N \to \infty$, it can be shown that

$$\ln|\mathbf{A}| \sim \frac{N}{(2\pi)^2}\int_\pi^\pi\int_\pi^\pi \ln|\mathbf{A}(\phi_1,\phi_2)|\mathrm{d}\phi_1\mathrm{d}\phi_2, \tag{A.11}$$

where

$$|\mathbf{A}(\phi_1,\phi_2)| = (1+z_1^2)(1+z_2^2) - 2z_2(1-z_1^2)\cos\phi_1 - 2z_1(1-z_2^2)\cos\phi_2. \tag{A.12}$$

Substitution of Eq. (A.12) and Eq. (A.11) into Eq. (A.1) and rearranging gives the expression

Eq. (1.31) derived by Onsager.

The two-point correlation function between the pair of spins at sites $(0,0)$ and $(x,0)$ given by Eq. (1.32) was calculated by Montroll et al. [MPW63]. The factor $s_{00}s_{x0}$ in Eq. (1.32) can be written as the product

$$\begin{aligned} s_{00}s_{x0} &= (s_{00}s_{10})(s_{10}s_{20})(s_{20}s_{30})\ldots(s_{x-1,0}s_{x0}) \\ &= \prod_{j=1}^{x}(s_{j-1,0}s_{j0}). \end{aligned} \tag{A.13}$$

Because $s_{xy}^2 = 1$, it follows that

$$s_{j0}s_{j+1,0}(1 + z_1 s_{j0}s_{j+1,0}) = z_1(1 + z_1^{-1}s_{j0}s_{j+1,0}), \tag{A.14}$$

and Eq. (1.32) can be rearranged to give

$$\begin{aligned} Zz_1^{-x}\langle s_{00}s_{x0}\rangle &= (\cosh K_1 \cosh K_2)^N \sum_{s_{jk}=\pm 1} \\ &\quad \times \prod_{j=1}^{x}(1 + z_1^{-1}s_{j-1,0}s_{j,0}) \prod_{j=x+1}^{m-1}(1 + z_1 s_{j0}s_{j+1,0}) \\ &\quad \times \prod_{j=0}^{m-1}\prod_{k=1}^{n-1}(1 + z_1 s_{jk}s_{j+1,k})(1 + z_2 s_{jk}s_{j,k+1}). \end{aligned} \tag{A.15}$$

Eq. (A.15) has the same form as Eq. (1.30) and a skew-symmetric matrix $\mathbf{A} + \underline{\delta}$ where the only non-zero elements in the skew-symmetric matrix $\underline{\delta}$ are the $2x$ values of j in Eq. (A.15) where $j < x$, which involve products of terms of the order $\mathcal{O}(z_1^{-1})$. Using Eq. (A.1), the correlation $\langle s_{00}s_{x0}\rangle$ is defined by

$$|\mathbf{A}|z_1^{-2x}\langle s_{00}s_{x0}\rangle^2 = |\mathbf{A} + \underline{\delta}|, \tag{A.16}$$

which can be rearranged to give

$$\langle s_{00}s_{x0}\rangle^2 = z_1^{2x}|\mathbf{I} + \mathbf{A}^{-1}\underline{\delta}|. \tag{A.17}$$

Eq. (A.17) can then be simplified considerably by replacing the determinant of the $4N \times 4N$ matrix by the determinant of a $2x \times 2x$ matrix

$$|\mathbf{I} + \mathbf{A}^{-1}\underline{\delta}| = |\mathbf{I} + \mathbf{Q}\mathbf{y}|, \tag{A.18}$$

where $\mathbf{y}$ is the sub-matrix of $\underline{\delta}$ consisting only of the rows and columns with non-zero elements, and the same rows and columns are taken from $\mathbf{A}^{-1}$ to construct $\mathbf{Q}$. The deter-

minant $|\mathbf{I} + \mathbf{Qy}|$ can be rewritten

$$|\mathbf{I} + \mathbf{Qy}| = |\mathbf{y}^{-1} + \mathbf{Q}||\mathbf{y}|. \tag{A.19}$$

Because $\mathbf{y}$ and, therefore its inverse $\mathbf{y}^{-1}$, are skew-symmetric, so is $\mathbf{y}^{-1} + \mathbf{Q}$. The right-hand side of Eq. (A.19) can be written as the Pfaffian product

$$|\mathbf{y}^{-1} + \mathbf{Q}||\mathbf{y}| = [P(\mathbf{y}^{-1} + \mathbf{Q})P(\mathbf{y})]^2, \tag{A.20}$$

and

$$\langle s_{00} s_{x0} \rangle = \pm z_1^x P(\mathbf{y}^{-1} + \mathbf{Q})P(\mathbf{y}). \tag{A.21}$$

The non-zero elements of $\mathbf{y}$ are given by

$$\underline{\delta}(0, j; 0, j+1) = z_1^{-1} - z_1, \tag{A.22a}$$

$$\underline{\delta}(0, j+1; 0, j) = -(z_1^{-1} - z_1), \tag{A.22b}$$

and $\mathbf{y}$ can be written as

$$\mathbf{y} = (z_1^{-1} - z_1) \begin{bmatrix} \mathbf{0} & \mathbf{I} \\ \mathbf{\text{-}I} & \mathbf{0} \end{bmatrix}. \tag{A.23}$$

The sub-matrix $\mathbf{Q}$ is given by

$$\mathbf{Q} = \begin{bmatrix} \mathbf{0} & \mathbf{S} \\ \mathbf{\text{-}S} & \mathbf{0} \end{bmatrix}, \tag{A.24}$$

where $\mathbf{S}$ is the $x \times x$ matrix

$$\mathbf{S} = \begin{bmatrix} [1,0] & [2,0] & [3,0] & \dots & [x,0] \\ [0,0] & [1,0] & [2,0] & \dots & [x-1,0] \\ [-1,0] & [0,0] & [1,0] & \dots & [x-2,0] \\ \vdots & \vdots & \vdots & \ddots & \vdots \\ [2-x,0] & [3-x,0] & [4-x,0] & \dots & [1,0] \end{bmatrix}, \tag{A.25}$$

The elements $[\beta, 0]$ are elements from the inverse matrix $\mathbf{A}^{-1}$ defined by

$$\begin{aligned} \mathbf{A}^{-1}(j,k;x,y) &\equiv [x-j, y-k] \\ &= \frac{1}{(2\pi)^2} \int_\pi^\pi \int_\pi^\pi \exp\left(i[(j-x)\phi_1 + (k-y)\phi_2]\right) \mathbf{A}^{-1}(\phi_1, \phi_2) \mathrm{d}\phi_1 \mathrm{d}\phi_2, \end{aligned} \tag{A.26}$$

where $\mathbf{A}^{-1}(\phi_1, \phi_2)$ is the inverse of the matrix $\mathbf{A}(\phi_1, \phi_2)$ given by

$$\mathbf{A}^{-1}(\phi_1,\phi_2) = \frac{1}{|\mathbf{A}(\phi_1,\phi_2)|} \begin{bmatrix} 2iz_2\sin\phi_1 & b+\bar{b}-ab\bar{b} & 2-a\bar{b} & 2-ab \\ -\bar{b}-b+\bar{a}\bar{b}b & -2iz_2\sin\phi_1 & -2+\bar{a}\bar{b} & 2-\bar{a}b \\ -2+\bar{a}b & 2-ab & -2iz_1\sin\phi_2 & a+\bar{a}-a\bar{a}b \\ -2+\bar{a}\bar{b} & -2+a\bar{b} & -\bar{a}-a+\bar{a}a\bar{b} & 2iz_1\sin\phi_2 \end{bmatrix}, \tag{A.27}$$

with

$$a = 1 + z_1\exp(i\phi_2),$$

$$b = 1 + z_2\exp(i\phi_1).$$

The Pfaffians of Eq. (A.21) then have the form

$$P(\mathbf{y}) = (z_1^{-1} - z_1)^x, \tag{A.29}$$

$$P(\mathbf{y}^{-1} + \mathbf{Q}) = |-(z_1^{-1} - z_1)^{-1}\mathbf{I} + \mathbf{S}|, \tag{A.30}$$

which, after substitution into Eq. (A.21) gives

$$\langle s_{00}s_{x0}\rangle = \pm|z_1\mathbf{I} - (1-z_1^2)\mathbf{S}|. \tag{A.31}$$

By defining

$$a_0 = z_1 - (1-z_1^2)[1,0], \tag{A.32a}$$

$$a_n = -(1-z_1^2)[1+n,0], \tag{A.32b}$$

$$a_{-n} = -(1-z_1^2)[1-n,0], \tag{A.32c}$$

with $n = 1, 2, \ldots, x-1$, Montroll et al. [MPW63] reduced the calculation of the correlation function to the Toeplitz determinant

$$\langle s_{00}s_{x0}\rangle \equiv \rho_{x0} = \pm\det(a)_x, \tag{A.33}$$

with

$$\det(a)_x = \begin{vmatrix} a_0 & a_1 & a_2 & \ldots & a_{x-1} \\ a_{-1} & a_0 & a_1 & \ldots & a_{x-2} \\ a_{-2} & a_{-1} & a_0 & \ldots & a_{x-3} \\ \vdots & \vdots & \vdots & \ddots & \vdots \\ a_{1-x} & a_{2-x} & a_{3-x} & \ldots & a_0 \end{vmatrix}. \tag{A.34}$$

By a change of variables, the integral Eq. (A.26) can be simplified such that matrix elements

are given by

$$a_n = \frac{1}{2\pi}\int_{-\pi}^{\pi} \exp(-in\omega)\varphi(\omega)\mathrm{d}\omega, \tag{A.35}$$

with the function $\varphi(\omega)$ defined by the equation

$$\varphi(\omega) = \left[\frac{(1 - z_1\tilde{z}_2\exp(i\omega))(1 - (\tilde{z}_2/z_1)\exp(-i\omega))}{1 - z_1\tilde{z}_2\exp(-i\omega))(1 - (\tilde{z}_2/z_1)\exp(i\omega))}\right]^{1/2}, \tag{A.36}$$

with $\varphi(\omega) > 0$ and

$$\tilde{z}_2 = \frac{(1 - z_2)}{(1 + z_2)}. \tag{A.37}$$

By symmetry, the same result is obtained for the correlation between the pair of spins at sites $(0, 0)$ and $(0, y)$ but with the roles of z_1 and z_2 reversed.

Appendix B

Appendix B: Scattering factors of objects with uniform density

B.1 Point scatterer

For a single spherically symmetric repeating unit centered at $(r_0, 0, 0)$, the Fourier-Bessel structure factor Eq. (1.146) simplifies to

$$\begin{aligned} G_{nl}(R) &= f_0(|\mathbf{R}|)J_n(2\pi R r_0)\exp\left[i(2\pi l z_0/c - n\varphi_0)\right] \\ &= f_0(|\mathbf{R}|)J_n(2\pi R r_0), \end{aligned} \tag{B.1}$$

where the scattering factor $f_0(|\mathbf{R}|)$ is given by

$$f_0(|\mathbf{R}|) = \int_{-\infty}^{\infty} \rho(|\mathbf{r}|)\exp(i2\pi\mathbf{R}\cdot\mathbf{r})\mathrm{d}\mathbf{r}. \tag{B.2}$$

For a density function $\rho(\mathbf{r})$ consisting of a single point,

$$\rho(\mathbf{r}) = \delta(|\mathbf{r}|), \tag{B.3}$$

$f_0(|\mathbf{R}|) = 1$ and Eq. (B.1) reduces to

$$G_{nl}(R) = J_n(2\pi R r_0). \tag{B.4}$$

B.2 Spherical scatterer

Consider a sphere of constant electron density such that $\rho(\mathbf{r}) = 1$ for $0 \leq |\mathbf{r}| \leq r_m$ and 0 elsewhere. Because a sphere is centro-symmetric the scattering factor is a function of $|R|$ only, where

$$\mathbf{R} = \{|\mathbf{R}|, \Theta, \Phi\}, \tag{B.5}$$

and

$$\begin{aligned} |\mathbf{R}| &= \sqrt{X^2 + Y^2 + Z^2} \\ &= \sqrt{R^2 + (l/c)^2}. \end{aligned} \tag{B.6}$$

In real-space $\mathbf{r}$ has the spherical coordinates $\{|\mathbf{r}|, \theta, \phi\}$ and the inner product of Eq. (B.2) simplifies to

$$\mathbf{R} \cdot \mathbf{r} = |\mathbf{R}||\mathbf{r}| \cos\theta. \tag{B.7}$$

Substituting Eq. (B.7) into Eq. (B.2) and using spherical polar coordinates gives

$$f_0(|\mathbf{R}|) = \int_0^{2\pi} \mathrm{d}\phi \int_0^{\pi} \sin\theta \mathrm{d}\theta \int_0^{r_m} |\mathbf{r}|^2 \exp(i2\pi|\mathbf{R}||\mathbf{r}|\cos\theta)\mathrm{d}|\mathbf{r}|. \tag{B.8}$$

Defining $u = \cos\theta$, $\mathrm{d}u = -\sin\theta\mathrm{d}\theta$

$$\begin{aligned} f_0(|\mathbf{R}|) &= 2\pi \int_0^{r_m} |\mathbf{r}|^2 d|\mathbf{r}| \int_{-1}^{1} \exp(i2\pi|\mathbf{R}||\mathbf{r}|u)du \\ &= 2\pi \int_0^{r_m} |\mathbf{r}|^2 d|\mathbf{r}| \left[\frac{\exp(i2\pi|\mathbf{R}||\mathbf{r}|u)}{i|\mathbf{R}||\mathbf{r}|}\right]_{-1}^{1} \\ &= 4\pi \int_0^{r_m} |\mathbf{r}|^2 \frac{\sin(2\pi|\mathbf{R}||\mathbf{r}|)}{2\pi|\mathbf{R}||\mathbf{r}|} d|\mathbf{r}|. \end{aligned} \tag{B.9}$$

Letting $u = 2\pi|\mathbf{R}||\mathbf{r}|$ and integrating by parts gives

$$f_0(|\mathbf{R}|) = \frac{1}{2\pi^2|\mathbf{R}|^3} \left[\sin(2\pi|\mathbf{R}|r_m) - (2\pi|\mathbf{R}|r_m)\cos(2\pi|\mathbf{R}|r_m)\right], \tag{B.10}$$

and the Fourier-Bessel structure factor Eq. (1.146) becomes

$$G_{nl}(R) = \frac{J_n(2\pi R r_0)}{2\pi^2|\mathbf{R}|^3} \left[\sin(2\pi|\mathbf{R}|r_m) - (2\pi|\mathbf{R}|r_m)\cos(2\pi|\mathbf{R}|r_m)\right]. \tag{B.11}$$

B.3 Cylindrical scatterer

The electron density function of a circular cylinder of unit density is $\rho(\mathbf{r}) = 1$ for $0 \leq |r| \leq r_c$ and 0 elsewhere for $\forall z$. In cylindrical polar coordinates, the inner product of Eq. (B.2)

simplifies to

$$\mathbf{R}\cdot\mathbf{r} = Rr\cos(\psi-\phi) + Zz. \tag{B.12}$$

The scattering factor $f_0(\mathbf{R})$ is then given by

$$f_0(\mathbf{R}) = \int_{-\infty}^{\infty}\int_0^{2\pi}\int_0^{r_c} \exp\left(i2\pi Rr\cos(\psi-\phi)\right)\exp\left(i2\pi Zz\right) r\mathrm{d}r\mathrm{d}\phi\mathrm{d}z. \tag{B.13}$$

Performing the integral over z gives

$$f_0(\mathbf{R}) = \delta(Z)\int_0^{2\pi}\int_0^{r_c} \exp\left(i2\pi Rr\cos(\psi-\phi)\right) r\mathrm{d}r\mathrm{d}\phi. \tag{B.14}$$

Let $u=\psi-\phi$ so that $\mathrm{d}u=\mathrm{d}\phi$, gives

$$\begin{aligned} f_0(\mathbf{R}) &= \delta(Z)\int_{\psi}^{2\pi+\psi}\int_0^{r_c} \exp\left(i2\pi Rr\cos(u)\right) r\mathrm{d}r\mathrm{d}u \\ &= \delta(Z)\int_0^{2\pi}\int_0^{r_c} \exp\left(i2\pi Rr\cos(u)\right) r\mathrm{d}r\mathrm{d}u \\ &= \delta(Z)2\pi\int_0^{r_c} J_0(2\pi Rr_c) r\mathrm{d}r \\ &= \delta(Z)\frac{r_c}{R}J_1(2\pi Rr_c), \end{aligned} \tag{B.15}$$

and the only non-zero Fourier-Bessel structure factor, $G_{n0}(R)$, is given by

$$G_{n0}(R) = \frac{r_c}{R}J_1(2\pi Rr_c)J_n(2\pi Rr_0). \tag{B.16}$$

Appendix C

Appendix C: Cubic spline interpolation

C.1 Definition

A cubic spline $S : [x_0, x_n] \to \mathbb{R}$ is a piecewise cubic polynomial consisting of n cubic pieces, where $x_0 < x_1 < \cdots < x_{n-1}$, i.e.

$$S_i(x) = a_i + b_i(x - x_i) + c_i(x - x_i)^2 + d(x - x_i)^3, \quad x_i \geq x < x_{i+1}, \tag{C.1}$$

for $i = 0, 1, \ldots, n-1$, where a_i, b_i, c_i and d_i are $4n$ unknown coefficients. The n points x_i are referred to as "knots". The spline interpolates a set of points $\{y_0, y_1, \ldots, y_n\}$ such that

$$S(x_i) = y_i, \quad \text{for } i = 0, 1, \ldots, n-1. \tag{C.2}$$

A cubic spline satisfies the conditions that $S(x)$, $S'(x)$ and $S''(x)$ be continuous on the interval $[x_0, x_n]$, i.e.

$$\begin{aligned} S_i(x_i) &= y_i, \\ S_i(x_{i+1}) &= y_{i+1}, \end{aligned} \tag{C.3}$$

for $i = 0, 1, \ldots, n-1$, and

$$S_i'(x_{i+1}) = S_i'(x_{i+1}), \tag{C.4a}$$

$$S_i''(x_{i+1}) = S_i''(x_{i+1}), \tag{C.4b}$$

for $i = 0, 1, \ldots, n-2$. These conditions give $4n - 2$ equations in total relating the $4n$ coefficients of Eq. (C.1).

The derivatives $S_i'(x)$ and $S_i''(x)$ have the form

$$S_i'(x) = b_i + 2c_i(x - x_i) + 3d_i(x - x_i)^2, \tag{C.5a}$$

$$S_i''(x) = 2c_i + 6d_i(x - x_i). \tag{C.5b}$$

Introducing the notation $h_i = x_{x+1} - x_i$ and defining $m_i = S_i''(x_i)$, Eq. (C.5b) reduces to $S_i''(x_i) = 2c_i$ and

$$c_i = \frac{m_i}{2}. \tag{C.6}$$

Using Eq. (C.5b), the continuity condition Eq. (C.4b) reduces to

$$m_i + 6h_i d_i - m_{m+1} = 0,$$

which rearranges to give

$$d_i = \frac{m_{i+1} - m_i}{6h_i}. \tag{C.7}$$

The conditions Eq. (C.3) combine to give

$$y_i + h_i b_i + h_i^2 c_i + h_i^3 d_i = y_{i+1},$$

and, after substituting Eqs. (C.6) and (C.7), rearranges to give

$$b_i = \frac{y_{i+1} - y_i}{h_i} - \frac{h_i}{2} m_i - \frac{h_i}{6}(m_{i+1} - m_i). \tag{C.8}$$

From the continuity condition Eq. (C.4a),

$$b_i + 2h_i c_i + 3h_i^2 d_i = b_{i+1}, \tag{C.9}$$

which, after substitution of Eqs. (C.6)-(C.8) and arranging, gives

$$h_i m_i + 2(h_i + h_{i+1}) m_{i+1} + h_{i+1} m_{i+2} = 6\left(\frac{y_{i+2} - y_{i+1}}{h_{i+1}} - \frac{y_{i+1} - y_i}{h_i}\right), \tag{C.10}$$

for $i = 0, 1, \ldots, n-2$. Eq. (C.10) describes $n-1$ linear equations for $n+1$ unknown variables, so two more equations are required to solve the $(n+1) \times (n+1)$ system. The missing equations are obtained by applying constraints on the derivatives at the endpoints x_0 and x_n.

C.2 "Not-a-knot" endpoint conditions

There is no unique choice on the conditions imposed on the derivatives at the endpoints. "Not-a-knot" endpoint conditions used in this thesis, force third derivative continuity

across the knots x_1 and x_{n-1} of the spline, i.e.

$$S_0'''(x_1) = S_1'''(x_1), \tag{C.11a}$$

$$S_{n-2}'''(x_{n-1}) = S_{n-1}'''(x_{n-1}). \tag{C.11b}$$

With $S_i'''(x) = 6d_i$ and using Eq. (C.7), the third derivative conditions reduce to

$$m_1 - m_0 = m_2 - m_1, \tag{C.12a}$$

$$m_{n-1} - m_{n-2} = m_n - m_{n-1}. \tag{C.12b}$$

These two equations along Eq. (C.10) combine to form the $(n+1) \times (n+1)$ linear system

$$\begin{bmatrix} -1 & 2 & -1 & \dots & \dots & 0 \\ h_0 & 2(h_0+h_1) & h_1 & 0 & \dots & \vdots \\ 0 & h_1 & 2(h_1+h_2) & h_2 & 0 & \vdots \\ \vdots & 0 & \ddots & \ddots & \ddots & 0 \\ 0 & \dots & 0 & h_{n-2} & 2(h_{n-2}+h_{n-1}) & h_{n-1} \\ 0 & \dots & \dots & -1 & 2 & 1- \end{bmatrix} \begin{bmatrix} m_0 \\ m_1 \\ m_2 \\ \vdots \\ m_{n-1} \\ m_n \end{bmatrix}$$

$$= 6 \begin{bmatrix} 0 \\ \frac{y_2-y_1}{h_1} - \frac{y_1-y_0}{h_0} \\ \frac{y_3-y_2}{h_2} - \frac{y_2-y_1}{h_1} \\ \vdots \\ \frac{y_n-y_{n-1}}{h_{n-1}} - \frac{y_{n-1}-y_{n-2}}{h_{n-2}} \\ 0 \end{bmatrix}. \tag{C.13}$$

Values for m_i can be then be found by back substitution, which then can be related to the coefficients b_i, c_i and d_i using the relations Eqs. (C.6)-(C.8).

Bibliography

[ABC+79] G. Andre, R. Bidaux, J. P. Carten, R. Conte, and L. de Seze. "Frustration in periodic systems : Exact results for some 2D Ising models.," *J. Phys.*, vol. 40, pp. 479–488, 1979.

[AC97] G. Aeppli and P. Chandra. "Seeking a simple complex system.," *Science*, vol. 275, pp. 177, 1997.

[AKS06] H. A. AL-Khayat and J. M. Squire. "Refined structure of bony fish muscle myosin filaments from low-angle x-ray diffraction data.," *J. Struct. Biol.*, vol. 155, pp. 218–229, 2006.

[Bal71] C. J. Ball. *An introduction to the theory of diffraction*. Pergamon Press, New York, USA, 1971.

[Bax82] R. J. Baxter. *Exactly solved models in statistical mechanics*. Academic Press, London, UK, 1982.

[BD76] C. Bays and S. D. Durham. "Improving a poor random number generator.," *Communications of the ACM.*, vol. 31, pp. 59–64, 1976.

[BH99] M. Baake and M. Hoffe. "Diffraction of random tilings: Some rigorous results.," *J. Stat. Phys*, vol. 99, pp. 219–261, 1999.

[Bow38] F. Bowman. *Introduction to Bessel functions*. Longmans, London, UK, 1938.

[Bra78] R. N. Bracewell. *The Fourier transform and its applications*. McGraw-Hill, 1978.

[Bra06] S. T. Bramwell. "Great moments in disorder.," *Nature*, vol. 439, pp. 273–274, 2006.

[BY86] K. Binder and A. P. Young. "Spin glasses: Experimental facts, theoretical concepts, and open questions.," *Rev. Mod. Phys.*, vol. 58, pp. 801–976, 1986.

[CCV52] W. Cochran, F. H. C. Crick, and V. Vand. "The structure of synthetic polypeptides. I. the transform of atoms on a helix.," *Acta Cryst.*, vol. 5, pp. 581–586, 1952.

[CH94] P. D. Coddington and L. Han. "Generalized cluster algorithms for frustrated spin models.," *Phys. Rev. B*, vol. 50, pp. 3058–3067, 1994.

[Cho84] T. C. Choy. "Triangular Ising model: Complete expressions for even spin correlations in an exact evaluation of $P(h,T)$.," *J. Math. Phys.*, vol. 25, pp. 3558–3562, 1984.

[CP04] R. W. Craig and R. Padrón. "Molecular Structure of the Sarcomere," in *Myology*, A. G. Engel, Ed., pp. 129–166. McGraw-Hill, 3rd edition, 2004.

[CRK70] R. A. Crowther, D. J. De Rosier, and A. Klug. "The reconstruction of a three-dimensional structure from projections and its application to electron microscopy.," *Proc. R. Soc. London Ser. A*, vol. 317, pp. 319–340, 1970.

[Cul78] B. D. Cullity. *Elements of X-ray Diffraction.* Addison-Wesley, Menlo Park, CA, 2 edition, 1978.

[CW67] H. Cheng and T. T. Wu. "Theory of Toeplitz determinants and the spin correlations of the two-dimensional Ising model. III.," *Phys. Rev.*, vol. 164, pp. 719–735, 1967.

[DD83] V. S. Dotsenko and V. S. Dotsenko. "Critical behaviour of the phase transition in the 2D Ising model with impurities.," *Adv. Phys.*, vol. 32, pp. 129–172, 1983.

[dG89] H. de Graaf. "On the calculation of small-angle diffraction patterns from disordered lattices.," *Acta Cryst. A*, vol. 45, pp. 861–870, 1989.

[DKR+97] D. Davidović, S. Kumar, D. H. Reich, J. Siegel, S. B. Field, R. C. Tiberio, R. Hey, and K. Ploog. "Magnetic correlations, geometrical frustration, and tunable disorder in arrays of superconducting rings.," *Phys. Rev. B*, vol. 55, pp. 6518–6540, 1997.

[Dre94] J. Drenth. *Principles of Protein X-Ray Crystallography*. Springer-Verlag, 1994.

[EEO69] S. Ebashi, M. Endo, and I. Otsuki. "Control of muscle contraction," *Quarterly reviews of biophysics*, vol. 2, pp. 351–384, 1969.

[EO78] A. Elliot and G. Offer. "Shape and flexibility of the myosin molecule.," *J. Mol. Biol.*, vol. 123, pp. 505–519, 1978.

[Eve03] H. G. Evertz. "The loop algorithm," *Advances in Physics*, vol. 52, pp. 1–66, 2003.

[Fis59] M. E. Fisher. "The susceptibility of the plane Ising model.," *Physica*, vol. 25, pp. 521–524, 1959.

[Fis63] M. E. Fisher. "Lattice statistics - a review and an exact isotherm for a plane lattice gas.," *J. Math. Phys.*, vol. 4, pp. 278–286, 1963.

[For80] G. Forgacs. "Ground-state correlations and universality in two-dimensional fully frustrated systems.," *Phys. Rev. B*, vol. 22, pp. 4473–4480, 1980.

[GG00] W. Gander and W. Gautschi. "Adaptive quadrature - revisited.," *BIT.*, vol. 40, pp. 84–101, 2000.

[GH05] M. A. Geeves and K. C. Holmes. "The molecular mechanism of muscle contraction," *Advances in Protein Chemistry*, vol. 71, pp. 161–193, 2005.

[Gib02] J. W. Gibbs. *Elementary Principles of Statistical Mechanics*. Yale University Press, 1902.

[GPS01] H. Goldstein, C. P. Poole, and J. L. Safko. *Classical Mechanics*. Addison Wesley, San Francisco, 3 edition, 2001.

[Gre01] J. E. Greedan. "Geometrically frustrated magnetic materials," *Journal of Materials Chemistry*, vol. 11, pp. 37–53, 2001.

[GRS96] W. R. Gilks, S. Richardson, and D. J. Spiegelhalter. *Markov Chain Monte Carlo in Practice*. CRC Press, 1996.

[GS58] U. Grenander and G. Szego. *Toeplitz Forms and their Applications.* Cambridge University Press, Cambridge, England., 1958.

[Gui63] A. Guinier. *X-ray Diffraction in Crystals, Imperfect Crystals and Amorphous Bodies*. W. H. Freeman and Company, 1963.

[HAK+03] K. C. Holmes, I. Angert, F. J. Kull, W. Jahn, and R.R. Schroder. "Electron cryo-microscopy shows how strong binding of myosin to actin releases nucleotide.," *Nature*, vol. 25, pp. 423–427, 2003.

[Har90] J. R. Harris. *Electron microscopy in Biology.* Oxford University Press, Oxford, 1990.

[Has70] W. K. Hastings. "Monte Carlo sampling methods using Markov chains and their applications.," *Biometrika*, vol. 57, pp. 97–109, 1970.

[HB62] R. Hosemann and S. N. Bagchi. *Direct Analysis of Diffraction by Matter*. North-Holland Publishing, 1962.

[HB67] H. E. Huxley and W. Brown. "The low-angle x-ray diagram of vertebrate striated muscle and its behaviour during contraction and rigor.," *J. Mol. Biol.*, vol. 30, pp. 383–434, 1967.

[HDM+96] J. J. Harford, R. C. Denny, E. Morris, R. Mendelson, and J. M. Squire. "3-D reconstruction from fibre x-ray diffraction patterns: Myosin-decorated actin filaments.," *Fibre Diffraction Review*, vol. 5, pp. 27–29, 1996.

[HFB+80] H. E. Huxley, A. R. Faruqi, J. Bordas, M. Koch, and J. R. Milch. "The use of synchrotron radiation in time-resolved x-ray diffraction studies of myosin layer-line reflections during muscle contraction.," *Nature*, vol. 284, pp. 140–143, 1980.

[HFK+83] H. E. Huxley, A. R. Faruqi, M. Kress, J. Bordas, and M. H. J. Koch. "Changes in the x-ray reflections from contracting muscle during rapid mechanical transients and their structural implications.," *J. Mol. Biol.*, vol. 169, pp. 469–506, 1983.

[HG60] C. A. Hurst and H. S. Green. "New solution of the Ising problem for a rectangular lattice," *J. Chem. Phys*, vol. 33, pp. 1059–1062, 1960.

[HHDS97] L. Hudson, J. J. Harford, R. C. Denny, and J. M. Squire. "Myosin head configuration in relaxed fish muscle: Resting state myosin heads must swing axially by up to 150 Å or turn upside down to reach rigor.," *J. Mol. Biol.*, vol. 273, pp. 440–455, 1997.

[HK76] J. Hoshen and R. Kopelman. "Percolation and cluster distribution. i. cluster multiple labeling technique and critical concentration algorithm.," *Phys. Rev. B*, vol. 14, pp. 3438–3445, 1976.

[HK85] H. E. Huxley and M. Kress. "Crossbridge behaviour during muscle contraction.," *J. Muscle Res. Cell Motil.*, vol. 6, pp. 153–161, 1985.

[HL74] K. C. Holmes and J. Barrington Leigh. "The effect of disorientation on the intensity distribution of non-crystalline fibres I. Theory.," *Acta Cryst. A*, vol. 30, pp. 635–638, 1974.

[Hou50] R. M. F. Houtappel. "Order-disorder in hexagonal lattices.," *Physica*, vol. 16, pp. 425–455, 1950.

[HS50] K. Husimi and I. Syozi. "The statistics of honeycomb and triangular lattice. i.," *Prog. Theor. Phys*, vol. 5, pp. 177–186, 1950.

[HS86] J. J. Harford and J. M. Squire. "Crystalline myosin cross-bridge array in relaxed bony fish muscle. Low-angle x-ray diffraction from plaice fin muscle and its interpretation.," *Biophys. J.*, vol. 50, pp. 145–155, 1986.

[HS97] J. J. Harford and J. M. Squire. "Time-resolved diffraction studies of muscle using synchrotron radiation.," *Rev. Prog. Phys.*, vol. 60, pp. 1723–1787, 1997.

[Hua63] K. Huang. *Statistical mechanics*. Wiley-Interscience Publication, 1963.

[Hux57] H. E. Huxley. "The double array of filaments in cross-striated muscle," *Journal of Biophysical and Biochemical Cytology*, vol. 3, pp. 631–648, 1957.

[Hux69] H. E. Huxley. "The mechanism of muscular contraction.," *Science*, vol. 164, pp. 1356–1366, 1969.

[Hux74] A. F. Huxley. "Muscular contraction," *Journal of Physiology (London)*, vol. 243, pp. 1–43, 1974.

[HWZ81] P. Hoever, W. F. Wolff, and J. Zittartz. "Random layered frustration models.," *Z. Phys. B*, vol. 41, pp. 43, 1981.

[HZ81] P. Hoever and J. Zittartz. "Thermodynamics of some layered Ising models.," *Z. Phys. B*, vol. 44, pp. 129, 1981.

[IOSF02] H. Iwamoto, K. Oiwa, T. Suzuki, and T. Fujisawa. "States of thin filament regulatory proteins as revealed by combined cross-linking/x-ray diffraction techniques.," *J. Mol. Biol.*, vol. 317, pp. 707–720, 2002.

[Isi24] E. Ising. *Beitrag zur Theorie des Ferro- und Paramagnetismus*. Ph.D. thesis, University of Hamburg, 1924.

[IWFY03] H. Iwamoto, J. Wakayama, T. Fujisawa, and N. Yagi. "Static and dynamic x-ray diffraction recordings from living mammalian and amphibian skeletal muscles.," *Biophys. J.*, vol. 85, pp. 2492–2506, 2003.

[JF97] J. L. Jacobsen and H. C. Fogedby. "Monte Carlo study of correlations near the ground state of the triangular antiferromagnetic Ising model.," *Physica A*, vol. 246, pp. 563–575, 1997.

[Kas63] P. W. Kasteleyn. "Dimer statistics and phase transitions.," *J. Math. Phys.*, vol. 4, pp. 287–293, 1963.

[KBAD90] D. Kandel, R. Ben-Av, and E. Domany. "Cluster dynamics for fully frustrated systems.," *Phys. Rev. Lett.*, vol. 65, pp. 941–944, 1990.

[KBFT08] N. A. Koubassova, S. Y. Bershitsky, M. A. Ferenczi, and A. K. Tsaturyan. "Direct modelling of x-ray diffraction pattern from contracting skeletal muscle.," *Biophys. J.*, vol. 95, pp. 2880–2894, 2008.

[KDR+88] D. Kandel, E. Domany, D. Ron, A. Brandt, and E. Loh. "Simulations without critical slowing down.," *Phys. Rev. Lett.*, vol. 60, pp. 1591–1594, 1988.

[KHFH86] M. Kress, H. E. Huxley, A. R. Faruqi, and J. Hendrix. "Structural changes during activation of frog muscle studied by time-resolved x-ray diffraction.," *J. Mol. Biol.*, vol. 188, pp. 325–342, 1986.

[KK05] N. Kasai and M. Kakudo. *X-Ray Diffraction by Macromolecules*. Springer-Verlag, Berlin, Germany, 2005.

[KO49] B. Kaufmann and L. Onsager. "Crystal statistics. II. Partition function evaluated by spinor analysis.," *Phys. Rev.*, vol. 76, pp. 1232–1243, 1949.

[KT02] N. A. Koubassova and A. K. Tsaturyan. "Direct modelling of x-ray diffraction pattern from skeletal muscle in rigor.," *Biophys. J.*, vol. 83, pp. 1082–1097, 2002.

[KW52] M. Kac and J. C. Ward. "A combinatorial solution of the two-dimensional Ising model.," *Phys. Rev.*, vol. 88, pp. 1332–1337, 1952.

[LB05] D. P. Landau and K. Binder. *A Guide to Monte Carlo Simulations in Statistical Physics*. Cambridge University Press, New York, NY, 2 edition, 2005.

[L'E88] P. L'Ecuyer. "Efficient and portable combined random number generators.," *Communications of the ACM*, vol. v.31 n.6, pp. 742–751, 1988.

[Lie86] R. Liebmann. *Statistical Mechanics of Periodic Frustrated Ising Systems*. Springer-Verlag, Berlin, Germany, 1986.

[Liu02] J. S. Liu. *Monte Carlo Strategies in Scientific Computing*. Springer-Verlag, Berlin, 2002.

[LLP80] L. D. Landau, E. M. Lifshits, and L. P. Pitaevski. *Statistical physics.* Pergamon Press, New York, 1980.

[LMS81] P. K. Luther, P. M. G. Munro, and J. M. Squire. "Three-dimensional structure of the vertebrate muscle A-band. III. M-region structure and myosin filament symmetry.," *J. Mol. Biol.*, vol. 151, pp. 703–730, 1981.

[LO80] L. Longa and A. M. Oleś. "Rigorous properties of the two-dimensional Ising model with periodically distributed frustration.," *J. Phys. A: Math. Gen.*, vol. 13, pp. 1031–1042, 1980.

[LPG+95] V. Lombardi, G. Piazzesi, M. A. Gerenczi, H. Thirlwell, I. Dobbie, and M. Irving. "Elastic distortion of myosin heads and repriming of the working stroke in muscle.," *Nature*, vol. 374, pp. 553–555, 1995.

[LS80] P. K. Luther and J. M. Squire. "Three-dimensional structure of the vertebrate muscle A-band. II. The myosin filament superlattice.," *J. Mol. Biol.*, vol. 141, pp. 409–439, 1980.

[LSF96] P. K. Luther, J. M. Squire, and P. L. Forey. "Evolution of the simple lattice and superlattice A-band in vertebrate skeletal muscle.," *J. Morphol.*, vol. 229, pp. 325–335, 1996.

[MA86] R. P. Millane and S. Arnott. "Digital processing of x-ray diffraction patterns from oriented fibres.," *J. Macromol. Sci. Phys., volume =*, 1986.

[Mak78] L. Makowski. "Processing of x-ray diffraction data from partially orientated specimens.," *J. Appl. Cryst.*, vol. 11, pp. 273–283, 1978.

[Mak82] L. Makowski. "The use of continuous diffraction data as a phase constraint. II. Application to fiber diffraction data.," *J. Appl. Cryst.*, vol. 15, pp. 546–557, 1982.

[MC06] R. P. Millane and R. M. Clare. "Triangular Ising antiferromagnet: Boundary conditions, ground state entropy, and vortices," *Physical Review E*, vol. 74, pp. 051101, 2006.

[MD01] R. P. Millane and D. L. Dorset. *International Tables for Crystallography, Vol. B*, pp. 466–481. International Union of Crystallography, 2nd edition, 2001.

[Mez03] M. Mezard. "Passing messages between disciplines.," *Science*, vol. 301, pp. 1685–1686, 2003.

[MFBD+94] M. L. Martin-Fernandez, J. Bordas, G. Diakun, J. Harries, J. Lowy, G. R. Mant, A. Svensson, and E. Towns-Andrews. "Time-resolved x-ray diffraction studies of myosin head movements in live frog sartorius muscle during isometric and isotonic contractions.," *J. Muscle Res. Cell Motil.*, vol. 15, pp. 319–348, 1994.

[MG00] R. P. Millane and A. Goyal. "Analysis of the disordered myosin lattice in muscle.," *Fibre Diffraction Review*, vol. 9, pp. 6–11, 2000.

[Mil90] R. P. Millane. "Phase Retrieval in Crystallography and Optics.," *Journal of the Optical Society of America A*, vol. 7, pp. 394–411, 1990.

[Mil91] R. P. Millane. "An alternative approach to helical diffraction.," *Acta Crystallogr.*, vol. 47, pp. 449–451, 1991.

[MPW63] E. W. Montroll, R. B. Potts, and J. C. Ward. "Correlations and spontaneous magnetization of the two-dimensional Ising model.," *J. Math. Phys.*, vol. 4, pp. 308–322, 1963.

[MRR+53] N. Metropolis, A. W. Rosenbluth, M. N. Rosenbluth, A. H. Teller, and E. Teller. "Equation of state calculations by fast computing machines.," *J. Chem. Phys.*, vol. 21, pp. 1087–1092, 1953.

[MS01] R. Moessner and S. L. Sondhi. "Ising models of quantum frustration.," *Phys. Rev. B*, vol. 63, pp. 224401, 2001.

[MU49] N. Metropolis and S. Ulam. "The Monte Carlo Method," *Journal of the American Statistical Association*, vol. 44, no. 247, pp. 335–341, 1949.

[NB99] M. E. J. Newman and G. T. Barkema. *Monte Carlo Methods in Statistical Physics*. Oxford University Press, Oxford, UK, 1999.

[New50] G. F. Newell. "Crystal statistics of a two-dimensional triangular Ising lattice.," *Phys. Rev.*, vol. 79, pp. 876–882, 1950.

[NHB84] B. Nienhuis, H. J. Hilhorst, and H. W. J. Blote. "Triangular SOS models and cubic-crystal shapes.," *J. Phys. A: Math. Gen.*, vol. 17, pp. 3559–3581, 1984.

[Nor97] J. R. Norris. *Markov Chains.* Cambridge University Press, New York, NY, 1997.

[Ons44] L. Onsager. "Crystal statistics. I. A two-dimensional model with an order-disorder transition.," *Phys. Rev.*, vol. 65, pp. 117–149, 1944.

[Par88] G. Parisi. *Statistical field theory.* Addison-Wesley Pub. Co., Redwood City, Calif., 1988.

[Pau35] L. Pauling. "The structure and entropy of ice and of other crystals with some randomness of atomic arrangement," *Journal of American Chemistry Society*, vol. 57(12), pp. 2680–2684, 1935.

[PAY06] J. H. H. Perk and H. Au-Yang. "Some recent results on pair correlation functions and susceptibilities in exactly solvable models.," *J. Phys. Conf. Ser.*, vol. 42, pp. 231–238, 2006.

[PB89] M. Plischke and B. Bergersen. *Equilibrium statistical physics.* Prentice Hall, Englewood Cliffs, N.J., 1989.

[Pes73] P. H. Peskun. "Optimum Monte Carlo sampling using Markov chains," *Biometrika*, vol. 60, pp. 607–612, 1973.

[Pes82] I. Peschel. "On the correlation functions of fully frustrated two-dimensional Ising systems.," *Z. Phys. B*, vol. 45, pp. 339–344, 1982.

[Pic77] D. K. Pickard. "A curious binary lattice process," *J. Appl. Prob*, vol. 14, pp. 717–731, 1977.

[Pic78] D. K. Pickard. "Unilateral Ising models," *Suppl. Adv. Appl. Prob.*, vol. 10, pp. 58–64, 1978.

[Pic80] D. K. Pickard. "Unilateral Markov fields," *Adv. Appl. Prob.*, vol. 12, pp. 655–671, 1980.

[Ple88] V. N. Plechko. "Grassman path-integral solution for a class of triangular type decorated Ising models.," *Physica A*, vol. 152, pp. 51–97, 1988.

[PS01] N. Prokof'ev and B. Svistunov. "Worm algorithms for classical statistical models.," *Phys. Rev. Lett*, vol. 87, pp. 160601, 2001.

[PTVF92] W. H. Press, S. A. Teukolsky, W. T. Vetterling, and B. P. Flannery. *Numerical Recipes in C: The Art of Scientific Computing*. Cambridge University Press, New York, NY, 2nd edition, 1992.

[PW55] R. B. Potts and J. C. Ward. "The combinatrial method and the two-dimensional Ising model.," *Prog. Theor. Phys*, vol. 13, pp. 38–46, 1955.

[Ram03] A. P. Ramirez. "Geometric frustration: Magic moments.," *Nature (London)*, vol. 421, pp. 483–484, 2003.

[RHW+93] I. Rayment, H. M. Holden, M. Whittaker, C. B. Yohn, M. Lorenz, K. C. Holmes, and R. A. Milligan. "Three-dimensional structure of myosin subfragment-1: A molecular motor.," *Science*, vol. 261, pp. 50–58, 1993.

[SAKKL05] J. M. Squire, H. A. Al-Khayat, C. Knupp, and P. K. Luther. "Molecular architecture in muscle contractile assemblies," *Advances in Protein Chemistry*, vol. 71, pp. 17–87, 2005.

[SCC+98] J. M. Squire, M. Cantino, M. Chew, R. C. Denny, J. J. Harford, L. Hudson, and P. K. Luther. "Myosin rod-packing schemes in vertebrate muscle thick filaments.," *J. Struct. Biol.*, vol. 122, pp. 128–138, 1998.

[SHES82] J. M. Squire, J. J. Harford, A. C. Edman, and M. Sjostrom. "Fine structure of the A-band in cryo-sections. III. crossbridge distribution and the axial structure of the human C-zone.," *J. Mol. Biol.*, vol. 155, pp. 467–494, 1982.

[SLM90] J. M. Squire, P. K. Luther, and P. Morris. "Organisation and Properties of the Striated Muscle Sarcomere," in *Molecular mechanisms in muscular contraction*, J. M. Squire, Ed., pp. 1–48. CRC Press, Boca Raton, Florida, USA, 1990.

[SM72] M. J. Stephen and L. Mittag. "A new representation of the solution of the Ising model.," *J. Math. Phys.*, vol. 13, pp. 1944–1951, 1972.

[SM95] W. J. Stroud and R. P. Millane. "Diffraction by disordered polycrystalline fibers.," *Acta Cryst.*, vol. A51, pp. 771–790, 1995.

[SM96a] W. J. Stroud and R. P. Millane. "Cylindrically averaged diffraction by disordered lattices.," *Proc. R. Soc. London Ser. A*, vol. 452, pp. 151–173, 1996.

[SM96b] W. J. Stroud and R. P. Millane. "Diffraction by polycrystalline fibers with correlated disorder.," *Acta Cryst.*, vol. A52, pp. 812–829, 1996.

[SML64] T. D. Schultz, D. C. Mattis, and E. H. Lieb. "Two-dimensional Ising model as a soluble problem of many fermions.," *Rev. Mod. Phys.*, vol. 36, pp. 856–871, 1964.

[Squ72] J. M. Squire. "General model of myosin filament structure. II. Myosin filaments and cross-bridge interactions in vertebrate striated and insect flight muscles," *Journal of Molecular Biology*, vol. 72, pp. 125–138, 1972.

[SSL+91] M. Sjostrom, J. M. Squire, P. K. Luther, E. Morris, and A. C. Edman. "Cryoultramicrotomy of muscle: Improved preservation and resolution of muscle ultrastructure using negatively stained ultrathin cryosections.," *J. Microsc.*, vol. 163, pp. 29–42, 1991.

[Ste64] J. Stephenson. "Ising model spin correlations on the triangular lattice. I.," *J. Math. Phys.*, vol. 5, pp. 1009–1024, 1964.

[Ste70] J. Stephenson. "Ising model spin correlations on the triangular lattice. III. isotropic antiferromagnetic lattice.," *J. Math. Phys.*, vol. 11, pp. 413–419, 1970.

[Str93] W. J. Stroud. *Theory and simulation of diffraction by disordered polycrystalline fibers*. Ph.D. thesis, Purdue University, 1993.

[Stu74] G. J. Stubbs. "The effect of disorientation on the intensity distribution of noncrystalline fibres. II. Applications.," *Acta Cryst. A*, vol. 31, pp. 639–645, 1974.

[SW87] R. H. Swendsen and J. S. Wang. "Nonuniversal critical dynamics in Monte Carlo simulations.," *Phys. Rev. Lett.*, vol. 58, pp. 86–88, 1987.

[Tho65] C. J. Thompson. "Algebraic derivation of the partition function of a two-dimensional Ising model.," *J. Math. Phys*, vol. 6, pp. 1392–1395, 1965.

[Vil77] J. Villain. "Spin glass with non-random interactions.," *J. Phys. C*, vol. 10, pp. 1717–1734, 1977.

[Wan50] L. Wannier. "Antiferromagnetism. the triangular Ising net.," *Phys. Rev.*, vol. 79, pp. 357–364, 1950.

[WB95] T. R. Welberry and B. D. Butler. "Diffuse X-ray Scattering from Disordered Crystals," *Chemical Reviews*, vol. 95, pp. 2369–2403, 1995.

[WC82] T. R. Welberry and C. E. Carroll. "Gaussian growth-disorder models and optical transform methods.," *Acta Crystallographica*, vol. A38, pp. 761–772, 1982.

[Wel77] T. R. Welberry. "A further solution for a two-dimensional model of crystal-growth disorder," *J. Appl. Cryst*, vol. 10, pp. 344–348, 1977.

[Wel04] T. R. Welberry. *Diffuse X-ray Scattering and Models of Disorder*. Oxford Univeristy Press, 2004.

[WG73] T. R. Welberry and R. Galbraith. "A two-dimensional model of crystal-growth disorder," *J. Appl. Cryst*, vol. 6, pp. 87–96, 1973.

[WG75] T. R. Welberry and R. Galbraith. "The effect of non-linearity on a two-dimensional model of crystal-growth disorder," *J. Appl. Cryst*, vol. 8, pp. 636–644, 1975.

[WH81] J. S. Wray and K. C. Holmes. "X-ray diffraction studies of muscle," *Annual Review of Physiology*, vol. 43, pp. 553–565, 1981.

[WHf95] M. Woolfson and F. Hai-fu. *Physical and non-physical methods of solving crystal structures*. Cambridge University Press, 1995.

[WHZ81] W. F. Wolff, P. Hoever, and J. Zittartz. "Layered inhomogeneous Ising models with frustration on a square lattice.," *Z. Phys. B*, vol. 42, pp. 259, 1981.

[WMC80] T. R. Welberry, G. H. Miller, and C. E. Carroll. "Paracrystal and Growth-Disorder models," *Acta Crystallographica*, vol. A36, pp. 921–929, 1980.

[WMTB76] T. T. Wu, B. M. McCoy, C. A. Tracy, and E. Barouch. "Spin-spin correlation functions for the two-dimensional Ising model: Exact theory in the scaling region.," *Phys. Rev. B*, vol. 13, pp. 316–374, 1976.

[WNF+06] R. F. Wang, C. Nisoli, R. S. Freitas, J. Li, W. McConville, B. J. Cooley, M. S. Lund, N. Samarth, C. Leighton, V. H. Crespi, and P. Schiffer. "Artificial spin ice in a geometrically frustrated lattice of nanoscale ferromagnetic islands.," *Nature (London)*, vol. 439, pp. 303–306, 2006.

[Wol89] U. Wolff. "Collective Monte Carlo updating for spin systems.," *Phys. Rev. Lett.*, vol. 62, pp. 361–364, 1989.

[Wu66] T. T. Wu. "Theory of Toeplitz determinants and the spin correlations of the two-dimensional Ising model. I.," *Phys. Rev.*, vol. 149, pp. 380–401, 1966.

[WZ82] W. F. Wolff and J. Zittartz. "Correlations in inhomogeneous Ising models. I. General methods, the fully-frustrated square lattice and the Chessboard model.," *Z. Phys. B*, vol. 47, pp. 341–352, 1982.

[YBK+09] C. H. Yoon, B. Bodvarsson, S. Klim, M. Morkelbjerg, S. Mortensen, J. Chen, J. R. Maclaren, P. K. Luther, J. M. Squire, P. J. Bones, and R. P. Millane. "Determination of myosin filament orientations in electron micrographs of muscle cross-sections.," *Image Processing, IEEE Transactions on*, vol. 18, pp. 831–839, 2009.

[YNS86] C. S. O. Yokoi, J. F. Nagle, and S. R. Salinas. "Dimer pair correlations on the brick lattice.," *J. Stat. Phys.*, vol. 44, pp. 729–747, 1986.

[Yoo09] C. H. Yoon. *Image analysis and diffraction by the myosin lattice of vertebrate muscle.* Ph.D. thesis, University of Canterbury, 2009.

[Zim79] John M. Ziman. *Models of disorder*, p. 17. Cambridge University Press, Cambridge, UK, 1979.

[ZY94] G. M. Zhang and C. Z. Yang. "Cluster Monte Carlo dynamics for the antiferromagnetic Ising model on a triangular lattice.," *Phys. Rev. B*, vol. 50, pp. 12546–12549, 1994.